

X-ray fluorescence scanning of discrete samples – a new tool for the geochemical characterization of loess-paleosol sequences

Dissertation

A dissertation submitted to

Fachbereich 8

University of Bremen

for the degree

Doctor of Natural Science (Dr. rer. nat.)

submitted by

M.Sc. Jörn Profe

Bremen, December 2017

Referees

First referee: Prof. Dr. Bernd Zolitschka
Institute of Geography
University of Bremen, Germany

Second referee: Prof. Dr. Markus Fuchs
Institute of Geography
Justus Liebig University Gießen, Germany

Public thesis defense: 26.03.2018

*“All truths are easy to understand
once they are discovered:
the point is to discover them.”*

Galileo Galilei

Table of Contents

Table of Contents	i
Abstract	iv
Zusammenfassung	vi
1. Introduction	1
2. Loess – unde venistis?	5
2.1. Origin and formation	5
2.2. Paleosol formation	15
2.3. The temporal perspective	16
2.4. Loess-paleosol sequences: review of geochemical proxies	20
3. X-ray fluorescence – theory and application	26
4. Study I – Schwalbenberg II	33
4.1. Introduction	35
4.2. Study site	36
4.3. Methods	38
4.3.1. Sampling	38
4.3.2. XRF analyses	38
4.3.3. Organic carbon	39
4.3.4. Magnetic susceptibility	40
4.3.5. Grain-size	40
4.3.6. Trend analysis	41
4.3.7. Correlation analysis	41
4.4. Results and discussion	41
4.4.1. XRF data quality	41
4.4.2. Rock magnetic properties	42
4.4.3. Br counts as proxy for organic carbon	45
4.4.4. Inorganic geochemical parameters	48
4.4.4.1. Weathering indices	48
4.4.4.1.1. Ca/Sr	48
4.4.4.1.2. Rb/Sr, Ba/Sr, Rb/K	50
4.4.4.2. Provenance indices	51
4.4.4.2.1. Ti/Zr, Ti/Al	51
4.4.4.2.2. Si/Al	54
4.4.5. Paleoenvironmental implications and relations to other regional climate archives	55
4.5. Conclusion	59
4.6. Supplementary material	60
5. Study II – Susak	61
5.1. Introduction and regional setting	63

5.2.	Material and methods	66
5.2.1.	Sampling and stratigraphic description	66
5.2.2.	XRF scanning of discrete samples	67
5.2.3.	Chemostratigraphy	69
5.2.4.	Standard addition calibration	70
5.2.5.	Total organic carbon and calcium carbonate content	70
5.2.6.	Grain-size analysis	71
5.3.	Results	71
5.3.1.	Data quality	71
5.3.2.	Bok N	72
5.3.3.	Bok O	75
5.3.4.	Bok P	78
5.4.	Discussion	81
5.4.1.	Reliability of XRF scanning-derived element ratios	81
5.4.1.1.	Bok N	81
5.4.1.2.	Bok O	83
5.4.1.3.	Bok P	84
5.4.2.	Bromine and chlorine	85
5.4.3.	Chemostratigraphy vs. lithostratigraphy	87
5.4.4.	Paleoenvironmental implications	89
5.5.	Conclusions	92
5.6.	Supplementary material	93
6.	Study III – Süttő	94
6.1.	Introduction	96
6.2.	Regional setting and previous work	97
6.3.	Materials and methods	99
6.3.1.	Material	99
6.3.2.	Methods	100
6.3.2.1.	Laboratory analyses	100
6.3.2.1.1.	XRF scanning of discrete samples	100
6.3.2.1.2.	Quantitative XRF measurements	100
6.3.2.1.3.	Bulk powder X-ray diffraction (XRD)	101
6.3.2.1.4.	Total organic carbon and calcium carbonate determination	101
6.3.2.2.	Data analyses	101
6.3.2.2.1.	Multivariate statistics	101
6.3.2.2.2.	Element ratios	102
6.3.2.2.3.	Correlation analysis	102
6.3.2.3.	Geochemical reference	102
6.4.	Results and discussion	103
6.4.1.	Data quality control	103
6.4.2.	Chemostratigraphy	106
6.4.3.	Weathering trends	109
6.4.4.	UCC, sediment recycling and dust provenance	112
6.4.5.	Proxy correlation analysis	117
6.4.6.	Bulk loess mineralogy	119
6.4.7.	Paleoenvironmental implications	119
6.4.7.1.	Weathering	119
6.4.7.2.	Dust provenance and tectonics	121
6.4.8.	XRF scanning vs. WD-XRF	123
6.5.	Conclusions	124
6.6.	Supplementary material	125

7. Concluding remarks and outlook	131
7.1. Weathering indices	131
7.2. Provenance indices	133
7.3. Grain-size indices	135
7.4. Chemostratigraphy and multivariate statistics	136
8. References	139
Acknowledgements	viii
Erklärung	ix

Abstract

Loess-paleosol sequences (LPS) are among the most important terrestrial archives of paleoclimate for the Quaternary and provide valuable information about past environmental changes on millennial to multi-millennial time scales. Magnetic susceptibility and grain-size are proven as reliable proxies for pedogenesis and wind activity. Thus, to analyse these proxies, LPS are sampled in high spatial resolutions down to 2 cm. In contrast, geochemical data indicating weathering intensity, dust provenance and grain-size dynamics are often acquired with 10 cm resolution at best by using time- and cost-intensive quantitative analytical methods. However, results derived from X-ray fluorescence (XRF) scanning in the marine and lacustrine realm demonstrate that determining qualitative, relative changes in the elemental composition of a profile is generally sufficient to track paleoenvironmental changes at a high spatial resolution down to 100 μm .

With the design of sample holders that allow measurements of discrete samples with an ITRAX XRF core-scanner, it becomes possible to exploit the unused potential of high-resolution samples previously taken for grain-size analysis as to geochemistry. Consequently, the aim of this study is to benchmark XRF scanning of discrete samples against other proxy data to evaluate the potential of high-resolution qualitative geochemistry unravelling weathering intensity, dust source changes and grain-size variations. For this purpose, three well-studied European LPS (Schwalbenberg II, Germany; Susak, Croatia; Süttő, Hungary) have been considered. They cover different time periods from Marine Isotope Stage (MIS) 7 to MIS 2 and are predominantly influenced either by oceanic, continental or Mediterranean climate respectively.

The results show that Rb/Sr and Ba/Sr track weathering intensity best unless secondary calcification is present. The presence of secondary calcification can be estimated by Ca/Sr while micromorphology is required for robust validation. In contrast, Rb/K that represents K-feldspar weathering, suffers from difficulties that are related to the reliable measurement of small concentration changes of K by XRF scanning of discrete samples. Moreover, the results indicate that there are no reliable element proxies available for magnetic susceptibility and total organic carbon. Changes in weathering-inert elements (Al, Ti, Zr) identify dust source alterations, albeit the LPS studied here have experienced sediment recycling and transport-induced fractionation rather than dust source changes. It turns out that the element ratios Zr/Rb and Si/Al are ambiguous proxies for grain-size variations due to weak correlations of element ratios with specific grain-size fractions at the examined LPS. This is likely due to sediment recycling and sorting effects that superimpose element-grain-size correlations.

Applying multivariate statistics to XRF scanning-derived qualitative element data enable the establishment of a chemostratigraphy that when compared to the lithostratigraphy facilitates the correlation of specific horizons across profiles. This may become necessary as there is often no profile available that covers the complete stratigraphy. Differences between the chemo- and lithostratigraphy may point to important transition zones that require further

detailed investigations with other methods. Additional principal component and biplot analyses allow identification of dominant processes that control element variability and thus enable the identification of element ratios that describe the determined processes best. In conclusion, this thesis carefully examines XRF scanning of discrete samples as a versatile and cost- and time-efficient tool for the geochemical characterization of LPS. It is expected that this study fosters its widespread application on terrestrial paleoenvironmental archives.

Zusammenfassung

Löss-Paläoboden-Sequenzen (LPS) sind eines der wichtigsten terrestrischen Paläoklimaarchive des Quartärs, die wertvolle Informationen über vergangene Paläoumweltänderungen mit einer tausend- bis mehrtausendjährigen zeitlichen Auflösung enthalten. Die magnetische Suszeptibilität und die Korngröße sind ausgewiesene Proxies für Pedogenese und Windaktivität, weshalb sie in einer hohen räumlichen Auflösung von bis zu 2 cm beprobt werden. Im Gegensatz dazu werden geochemische Daten quantitativ mit zeit- und kostenintensiven Methoden bei einer maximalen räumlichen Auflösung von 10 cm erhoben, obwohl Verwitterungsintensität, Staubherkunft und Korngrößen-änderungen aus ihnen abgeleitet werden können. Allerdings zeigen marine und lakustrine Röntgenfluoreszenz(XRF)scannerdaten, dass qualitative geochemische Daten ausreichen um Paläoumweltveränderungen nachzuvollziehen.

Die Entwicklung von Einzelprobenhaltern für den ITRAX XRF Kernscanner erlaubt das bisher ungenutzte Potential der zuvor für Korngrößenanalysen genommenen Proben für die geochemische Charakterisierung von LPS zu nutzen. Deshalb ist das Ziel dieser Studie die Methode des XRF Scannens an Einzelproben mithilfe anderer zur Verfügung stehender Proxydaten zu prüfen, um das Potential qualitativer Elementdaten als Proxy für Verwitterungsintensität, Staubherkunft und Korngrößenvariabilität zu evaluieren. Dazu wurden drei gut untersuchte LPS ausgewählt, die jeweils andere Zeitperioden zwischen den marinen Isotopenstadien (MIS) 7 und MIS 2 umfassen und entweder überwiegend von ozeanischem, kontinentalem oder mediterranem Klima beeinflusst sind.

Die Ergebnisse zeigen, dass Rb/Sr und Ba/Sr die Verwitterungsintensität zuverlässig anzeigen, sofern keine sekundäre Aufkalkung stattfindet. Das Auftreten sekundärer Aufkalkung kann mithilfe von Ca/Sr abgeschätzt werden, wenngleich mikromorphologische Befunde für eine zweifelsfreie Aussage über das Vorhandensein von sekundärer Aufkalkung notwendig sind. Im Gegensatz dazu beeinträchtigen Rb/K Schwierigkeiten beim Messen kleiner Unterschiede in den K-Konzentrationen. Zudem weisen die Ergebnisse daraufhin, dass es keine Elementverhältnisse als Proxy für magnetische Suszeptibilität oder organischen Gesamtkohlenstoff gibt. Anhand verwitterungsresistenter Elemente (Al, Ti, Zr) werden Änderungen der Staubherkunft untersucht. Allerdings scheinen die betrachteten LPS eher von Sedimentrecycling und transportinduzierter Fraktionierung und weniger von einem Wechsel in der Staubherkunft betroffen zu sein. Aufgrund schwacher Korrelationen mit spezifischen Korngrößenfraktionen stellt sich heraus, dass die Elementverhältnisse Zr/Rb und Si/Al durch Sedimentrecycling beeinflusst werden und deshalb keine eindeutigen Korngrößenproxies sind.

Die Anwendung multivariater Statistik auf qualitative Elementdaten erlaubt die Erstellung einer Chemostratigraphie im Vergleich zur Lithostratigraphie und erleichtert damit die Korrelation einzelner Horizonte über mehrere Profile hinweg. Eine solche Korrelation wird dann notwendig, wenn es keine Profile gibt, die die gesamte Stratigraphie umfassen. Mögliche Unterschiede zwischen Chemo- und Lithostratigraphie weisen auf wichtige

Übergangshorizonte hin, die zur genauen Charakterisierung weiterer detaillierterer Analysen bedürfen. Der Einsatz von Hauptkomponenten- und Biplotanalysen ermöglicht zusätzlich die Identifikation von Prozessen, die die Elementdaten hauptsächlich beeinflussen. Daraus lassen sich Elementverhältnisse ableiten, die die zuvor identifizierten Prozesse am besten widerspiegeln. Zusammengefasst wird in dieser Arbeit detailliert die Eignung des XRF Scannens von Einzelproben als vielseitiges, zeit- und kostengünstiges Werkzeug zur geochemischen Charakterisierung von LPS überprüft.

1. Introduction

Loess-paleosol sequences (LPS) are important but complex terrestrial paleoenvironmental archives (e.g. Muhs, 2018). Loess, the parent material of LPS, covers about 10 % of the Earth's surface (Pécsi, 1990; Sprafke and Obreht, 2016) and allows tracing terrestrial paleoenvironmental change back to 5 Ma in the Tarim basin (e.g. Liu, 1988; Varga, 2011). The investigation of Chinese LPS reveals large-scale climatic changes during the Quaternary (Kukla, 1987; Liu, 1988). Even fluctuations on millennial time scales are reported and related to Dansgaard-Oeschger cycles recorded in Greenland ice cores (Antoine et al., 2013; Antoine et al., 2009; Rousseau et al., 2017b; Sun et al., 2012). However, such correlations are often prevented by luminescence chronologies with typical error margins of several thousand years for Late Pleistocene LPS (Frechen and Schirmer, 2011; Kadereit et al., 2013). Recent developments in dating techniques may overcome this problem for LPS younger than 50 ka by radiocarbon dating of earthworm calcite granules from paleosols (Moine et al., 2017). This chronologic advancement was developed at Nussloch where it clearly attributes tundra gleys to individual Greenland interstadials at Nussloch (Rousseau et al., 2017a). Due to the location of LPS along preferred pathways of human dispersal to Western Central Europe, especially the study of Carpathian LPS adjacent to the river Danube and its tributaries experienced a renaissance in recent years (Bösken et al., 2017; Fitzsimmons et al., 2012; Marković et al., 2016; Marković et al., 2015; Obreht et al., 2017; Obreht et al., 2015; Zeeden et al., 2017; Zeeden et al., 2016). These studies fostered multi-proxy and multidisciplinary investigations and thereby provide excellent archives to examine potential interdependencies between human dispersal and paleoclimatic conditions. In light of the ongoing climate change, such knowledge is of urgent need to gain detailed extensive knowledge about past environmental change.

LPS are analyzed for their stratigraphy, color, grain-size distributions, rock magnetic properties, micromorphology, mineralogy, geochemistry, calcium carbon and organic carbon contents, morphology of secondary carbonates, malacology, pollen and biomarkers in order to unravel weathering intensity, dust source changes, sedimentation dynamics and vegetation cover as well as to quantify paleo-temperatures and paleo-precipitation (e.g. Ahmad and Chandra, 2013; Antoine et al., 2009; Antoine et al., 2001; Bábek et al., 2011; Banak et al., 2016; Baumgart et al., 2013; Bayat et al., 2017; Buggle et al., 2011; Buggle and Zech, 2015; Gocke et al., 2014; Koeniger et al., 2014; Novothny et al., 2011; Prud'Homme et al., 2015; Prud'homme et al., 2018; Schatz et al., 2015; Schatz et al., 2011; Schirmer, 2012; Sprafke et al., 2014; Terhorst et al., 2015; Zech et al., 2013b). While LPS are often sampled in 2 cm resolution for grain-size and magnetic susceptibility (MS) (e.g. Novothny et al., 2011; Wacha et al., 2017), other proxies are determined at a much coarser spatial resolution (e.g. micromorphology, Sprafke et al., 2014). Since geochemistry provides valuable information about weathering intensity, dust provenance, sediment recycling and grain-size dynamics at LPS, its common sampling resolution of 10 cm at best is remarkable (Hošek et al., 2015; Mikulčić Pavlaković et al., 2011; Obreht et al., 2015). Conventional XRF and spectrometric techniques denote standard methods for the acquisition of quantitative element data from LPS (e.g. Buggle et al., 2008; Mikulčić Pavlaković et al., 2011). In

contrast, in the marine and lacustrine realm, it has been state-of-the-art for more than a decade to acquire qualitative element data with the X-ray fluorescence (XRF) core-scanner technology in high-spatial resolution down to 100 μm (Davies et al., 2015; Rothwell and Croudace, 2015a, b). Because relative variations in the elemental composition along a sediment core proved to be sufficient to explain paleoclimate variations in most cases (Weltje et al., 2015), there is no need to apply time- and labor-intensive techniques in order to acquire quantitative element data. First studies using the ITRAX XRF core-scanner to analyze U-channels derived from the Chinese Loess Plateau with a resolution of 0.5 cm highlight the potential and the need for spatial high-resolution XRF data in paleoenvironmental reconstructions based on LPS (Liang et al., 2012; Sun et al., 2016). Therefore, making the samples previously taken for grain-size and MS at a spatial resolution of 2 cm available, would improve the geochemical characterization of LPS. A high-resolution geochemical framework would facilitate correlation across different profiles and would provide the possibility for a geochemical comparison to lithostratigraphy. Differences may indicate important transition zones that require further investigations by more elaborated methods such as micromorphology.

The objective of this thesis is to evaluate XRF scanning of discrete samples as a cost- and time-efficient tool for the geochemical characterization of LPS with regard to weathering intensity, dust provenance, sedimentation dynamics and grain-size variability. The design of sample holders that allow discrete sample measurement in scanning mode with an ITRAX XRF core-scanner (Ohlendorf, 2018) is a prerequisite to exploit the potential of previously taken samples for geochemistry. Using homogenized and dry samples minimizes the effects of water content, grain-size and surface roughness which otherwise adversely affect the recorded XRF spectra from wet split core surfaces (Jarvis et al., 2015; Rothwell and Rack, 2006; Tjallingii et al., 2007). Three quasi-continuously sampled and well-studied LPS (Fig. 1-1, Schwalbenberg II, Germany; Susak, Croatia; Süttő, Hungary) has been selected to benchmark XRF scanning of discrete samples against other available proxy data. The LPS cover different time periods with varying temporal resolutions and are situated in different climatic regions to demonstrate universal applicability of this method. Proxy data for evaluation comprise e.g. grain-size, MS, micromorphology, secondary carbonates, mineralogy and quantitative XRF data. The LPS Schwalbenberg II is located at the Middle Rhine valley in Germany and is dominated by a North Atlantic oceanic climate. It provides a detailed record of the MIS 3 and the transition to MIS 2 (Schirmer, 2000a, 2012). The LPS Susak is situated on the Island of Susak in the north-eastern Adriatic Sea and is characterized by a Mediterranean climate. This is a unique position for a LPS that records paleoenvironmental changes driven by trans- and regressions of the Adriatic Sea accompanied by various extensions of the paleo river Po. The studied profiles encompass the time period from MIS 7 to MIS 4 (Durn et al., 2017b; Wacha et al., 2011a; Wacha et al., 2011b). In contrast, the LPS Süttő is located in the northwestern part of the Carpathian basin in Hungary at the transition zone between oceanic and continental climate. It comprises the time period from MIS 6 to MIS 2 (Novothy et al., 2011; Rolf et al., 2014).

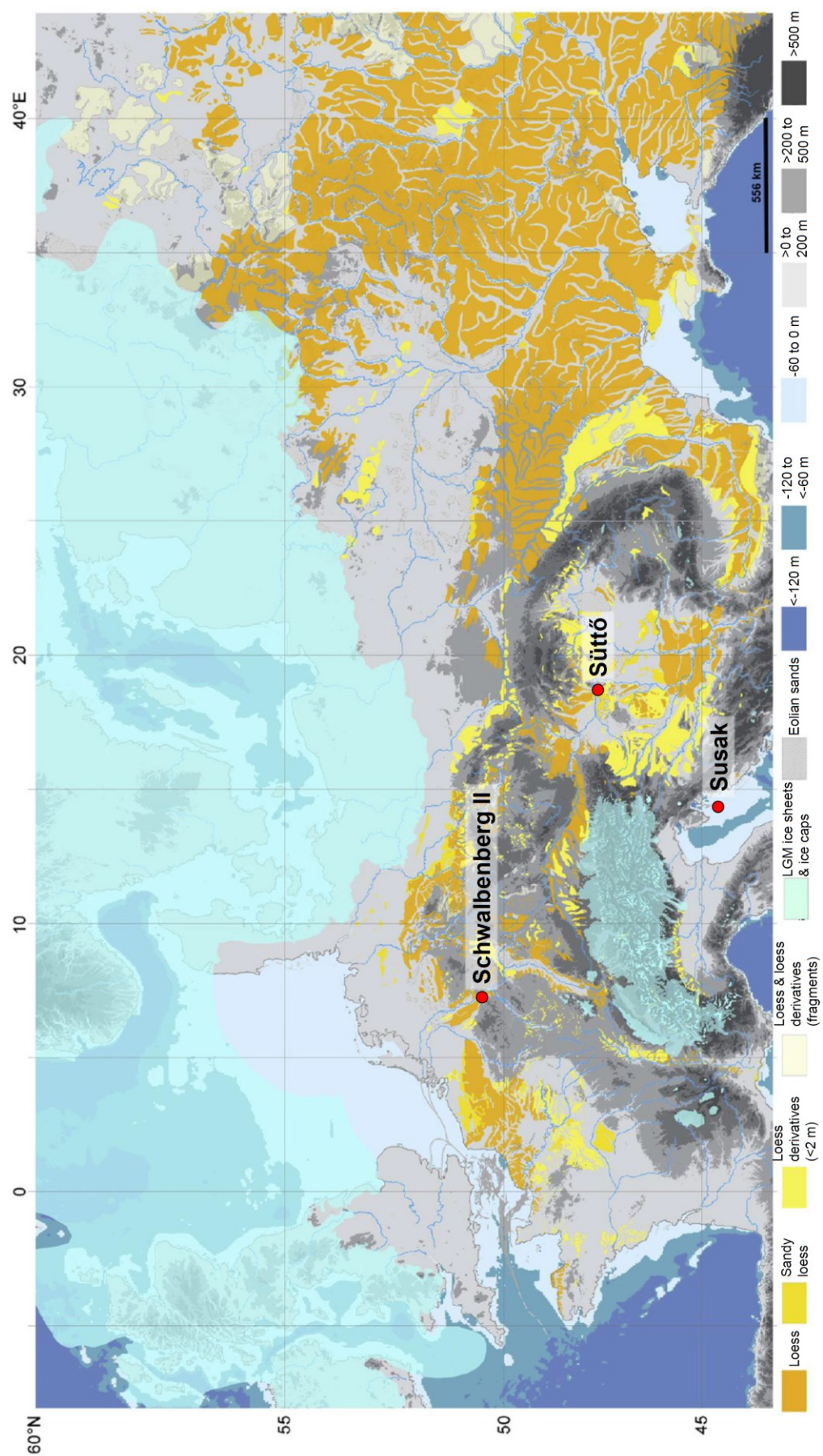


Fig. 1-1: European loess map that shows the positions of the three investigated loess-paleosol sequences with the extensions of the Last Glacial Maximum ice sheets and ice caps (modified after: Antoine et al., 2013: 18; Haase et al., 2007: 1310; Rousseau et al., 2017a: 100).

The thesis is structured as follows: Chapter 2 and 3 summarize basic knowledge about loess and the XRF method to provide a robust theoretical framework for the three subsequent paper manuscripts benchmarking XRF scanning of discrete samples. In addition, chapter 3 addresses the cost- and time-efficiency of XRF scanning of discrete samples in comparison to conventional XRF analysis. Chapter 4 evaluates XRF scanning-derived element data as proxies for weathering intensity, dust provenance, grain-size, MS and total organic carbon (TOC) at the LPS Schwalbenberg II. Based on dynamics of weathering-inert elements at the transition to MIS 2, a conceptual framework is suggested that explains the indicated dust source change as local sediment recycling in agreement with observations from the Eifel Lake Sediment Archive (ELSA). Chapter 5 demonstrates, taking Susak as an example, how a high-resolution chemostratigraphy helps to correlate horizons across profiles, and allows the identification of a pedocomplex that was not recognized as such by field observations. According to the lessons learned on Susak, Chapter 6 supplements the chemostratigraphy by principal component analysis (PCA) and biplot analysis in order to identify the dominant processes controlling variations in the elemental composition at the LPS Süttő. Hence, element ratios describing the identified processes best can be deduced from biplot analysis. Detailed verification of XRF scanning data with quantitative XRF data brings out difficulties in reliably detecting K with the ITRAX XRF core-scanner and highlights the usefulness of Zr as proxy for sediment recycling. Finally, Chapter 7 concludes the findings of the three paper manuscripts by linking them thematically and presenting further research questions.

2. Loess – unde venistis?

2.1. Origin and formation

Loess is a silt-sized clastic yellowish eolian material that covers about 10 % of the Earth's surface (Pécsi, 1990; Pye, 1995; Smalley, 1966). It is one of the most complex and most important terrestrial paleoenvironmental archives on Earth (e.g. Muhs, 2018). This paramount importance becomes obvious in a nearly two centuries lasting scientific discussion of what loess and its origin actually is (Smalley et al., 2001; Sprafke and Obreht, 2016; Zöller and Semmel, 2001). According to Sprafke and Obreht (2016), the term loess was first introduced by Leonhard (1824 cited in Sprafke and Obreht, 2016) for a dusty loamy material observed at the outcrop Haarlass near Heidelberg. Studying the loess of the river Rhine and the Rodderberg volcano in Germany in the 1830s led to an intensive loess research by Charles Lyell and Leonard Horner from a geological point of view (Smalley and Kels, 2018). At this time, vertical walls of loess easily erodible by water as well as fertile loess soils prone to deflation were recognized (Smalley and Kels, 2018). In his worldwide-sold book "Principles of Geology" Volume Three Lyell (1833 cited in Smalley and Markovic, 2018) devoted a chapter to loess which spread the idea of loess to the worldwide scientific community and thereby fostered loess research elsewhere (Smalley and Markovic, 2018; Smalley et al., 2001). Lyell considered the origin of loess to be alluvial or lacustrine (Smalley and Markovic, 2018; Sprafke and Obreht, 2016). Although Richthofen might not have been the first researcher suggesting an eolian origin of loess (Sprafke and Obreht, 2016), his detailed observations about the Chinese loess plateau as a geographer (Richthofen, 1882 cited in Smalley and Markovic, 2018) are acknowledged as the classical eolian theory on loess (Smalley and Markovic, 2018; Sprafke and Obreht, 2016). However, Richthofen described loess without providing a theory for the mechanisms of its origin (Smalley et al., 2001).

At the end of the 19th century John Hardcastle investigated the Timaru loess on the Southern Island of New Zealand in order to develop a concept of loess formation (Hardcastle, 1889). By conceptualizing fundamental processes relevant for particle production that finally form loess deposits, Hardcastle revolutionized the understanding of loess, invented the loess stratigraphy and pioneered the field of paleoclimatology (Smalley and Fagg, 2015). At this time three competing opinions existed about the origin of loess: marine, eolian and volcanic (Hardcastle, 1889). First, he postulated four prerequisites that are still valid today to form the observed loess deposits at Timaru: "(1) a source of wind-borne dust, (2) winds to transport the dust, (3) vegetation to entrap it, and (4) sufficient time for its accumulation." (Hardcastle, 1889: 406). Based on a detailed description of field observations in a stratigraphic way, he explained his dust-heap theory as to the source of dust as follows:

"There was only one source possible in these latitudes for such a quantity of dust; and a mere hint as to its nature will suffice. If we consider the loess to belong to the great Ice Age there is no difficulty. The dust was 'rock-meal,' produced by the great ice mill, and spread out by rivers of sludge for the winds to dry, and pick up, and bear away, losing more or less of their load whenever they passed over a vegetated region" (Hardcastle, 1889: 413).

This quote highlights the idea of an event-sequence that involves particle production and subsequent multiple cycles of particle transport and deposition with final eolian transport and deposition. For this reason, Smalley and Fagg (2015) consider this concept as cutting-edge for the provenance-transportation-deposition (PTD) approach introduced by Smalley (1966) and thus propose to call such an event-sequence the Hardcastle sequence. In addition, Hardcastle (1889) already recognized the importance of glacier action in producing silt-sized material more than half a century before it became common knowledge in the theory of glacial loess by the work of Ian Smalley (Smalley, 1966). Rephrasing the original quote of Hardcastle in terms of the PTD approach leads to: “P1 = material formed by glacial action, T1 = carried by rivers, D1 = and deposited on floodplains, T2 = then transported by wind action, D2 = to form a loess deposit” (Smalley and Fagg, 2015: 52). The same mechanism as described for the Timaru loess formation was suggested for the formation of loess at the river Rhine and for loess formation in North America (Hardcastle, 1889). In its most elaborated form, Smalley et al. (2014) added the term “change” (C) to the PTD approach to account for phases of pedogenesis after deposition and for re-deposition by slope processes.

In his second revolutionary article, Hardcastle (1890) focused on the relevance of the sequence of different layers found in the Timaru loess as a climate register. For example, drought veins are representative for dry climate in a way that different layers were related to different types of climate. “Deposited upon areas elevated above the reach of rivers, this growing dust-heap played the part of an observant bystander, taking notes of certain climatic phenomena as they successively arose” (Hardcastle, 1890: 326f.). This quote impressively summarizes Hardcastle’s understanding of a loess sequence as a paleoclimate archive nearly a century before serious lessons were learned from the evolving field of paleoclimatology by e.g. comparison of Pleistocene LPS with marine sediment cores (Kukla, 1977). Furthermore, Hardcastle inspired researchers in Hungary to study Quaternary climate at the Paks LPS in relation to the Milankovitch climate-cycle theory in the 1930s (Horváth and Bradák, 2014).

The next example reviews the Russian way of thinking on loess at the beginning of the 20th century – Vladimir Afanas’evich Obruchev vs. Lev Semenovich Berg. While Obruchev lived in Eastern Russia and was aware of the Central Asian and Chinese loess deposits, Berg lived in Western Russia (today’s Ukraine) and was strongly influenced by the new emerging field of soil science led by Dokuchaev (Smalley and Jary, 2004). Correspondingly, Obruchev followed the idea of eolian deposition similar to Richthofen and thus drafted the concept of “desert” loess whereas Berg attributed the formation of loess to in-situ processes such as pedogenesis transforming non-loess into loess (Jefferson et al., 2003; Smalley and Jary, 2004; Sprafke and Obreht, 2016). Due to political issues, Berg’s theory was favored in Russia, but suffered from limited scientific discussion abroad, in turn, directed the focus on the sedimentological perspective of loess in Western Europe and North America (Smalley and Jary, 2004; Sprafke and Obreht, 2016).

In the middle of the 20th century LPS were the backbone of Quaternary stratigraphy in Europe although no universal definition of loess was accepted (Pye, 1984; Sprafke and

Obreht, 2016). Besides eolian deposition, Kukla (1987) and Liu (1988) recognized post-depositional processes such as cementation and secondary calcification (loessification) as a necessity to provide loess with its typical properties: homogeneity, porosity, metastability and collapsibility (Pye, 1984; Smalley and Jary, 2004; Smalley and Markovic, 2017; Sprafke and Obreht, 2016). Finally, in the outgoing 20th century, the work of Pye (1984, 1995) and Pécsi (1990) can be considered as the last attempts to provide holistic definitions of loess. Pye (1984) simplified the definition of loess to a silt-sized, windblown, quartz-dominated deposit typically characterized as: homogeneous, non-stratified and porous. He further subdivided loess into primary loess, reworked loess and weathered loess. The third refers to pedogenetically-altered loess whereas the second refers to loess affected by re-deposition due to slope or water interaction. In addition, loess-like deposits refer to sediments that are similar to loess but deposited by non-eolian processes (Pye, 1984). In contrast to Pye (1984), Pécsi (1990: 1) claimed that “loess is not just the accumulation of dust”. He defined ten criteria qualifying a deposit as loess amongst which carbonate contents $\geq 1\%$, slight diagenesis and partly slight cementation are mandatory additional to the criteria of Pye (1984). According to Sprafke and Obreht (2016), the term diagenesis by Pécsi (1990) refers to loessification as defined above. Pye (1995) discussed the work of Pécsi (1990) in his introduction and argued against an unnecessary complication of defining loess by prescribing e.g. a certain amount of carbonates. There are several examples of deposits (Timaru loess, New Zealand; Bignell loess, Nebraska USA; Alaskan loess) that are poor in calcium carbonate but nevertheless show the typical characteristics of loess (Muhs et al., 2003; Pye, 1995). According to Pécsi (1990) such kinds of deposits might be named “loam of similar properties”, whereas Muhs and Bettis III (2003) stated that loessification in terms of diagenetic cementation by carbonates is an unnecessary restriction for the formation and definition of loess. In this context, Iriondo and Kröhling (2007) introduced tropical loess, volcanic loess in Ecuador, trade-wind associated loess in Venezuela and Brazil as well as gypsum loess in Spain. All these deposits are similar to the classical glacial loess with the same characteristics required to be termed as loess but related to climates different from periglacial and desert scenarios (Iriondo and Kröhling, 2007; Sprafke and Obreht, 2016). Realizing that not only continental ice sheets are able to produce considerable amounts of silt, Smalley et al. (2009) reconsidered the idea of glacial loess and reframed the European loess deposits as mountain loess originating from the Alps rather than as glacial loess originating from the periglacial environments of the Fennoscandian ice sheet. Confusion may arise about the terms “desert” and “mountain loess”. Mountain loess may incorporate the action of small-scale glaciers but also refers to frost and gravitational weathering frequently occurring in high mountain environments providing a large amount of silt-sized material. Accordingly, the loess in Central Asia fits better to the explanation of mountain loess where the desert serves as a loess reservoir from which the final eolian transport takes place to the Chinese loess plateau (Smalley et al., 2009). Therefore, desert loess only refers to loess that is completely produced, transported and deposited in desert or peri-desert environments (Smalley and Markovic, 2017; Smalley et al., 2009).

Furthermore, Murton et al. (2015) suggest yedoma silt as one category of cold-climate loess exemplified on Northeast Siberia. Yedoma silt refers to ice-rich silts in permafrost-

dominated periglacial regions affected by syngenetic freezing (Schirmer et al., 2013). This material is common for non-glaciated areas in Northern Siberia and Alaska being representative for a circumpolar permafrost region characterized by eolian activity. Comparing sedimentological and geocryological evidence from Duvanny Yar (Northeast Siberia), with observations from Alaska and Northwest Europe eolian activity, remains the sole reasonable explanation for their formation. With regard to the origin of loess, glacial fed rivers transported glacier-grinded silt material onto floodplains from where it was deflated by dust storms allowing loess deposition in the Kolyma Lowland (Murton et al., 2015). Eventually, Sprafke and Obreht (2016) indicate that a satisfying loess definition should elaborate more on the process of loessification and should include both the process of eolian deposition and the contemporaneous or subsequent process of loessification to avoid inclusion of many non-loess deposits (Sprafke and Obreht, 2016) by an oversimplified definition of loess being just windblown silt-sized particles (Muhs, 2013). While Smalley et al. (2009) understand loess as a sediment and geomorphological entity Sprafke and Obreht (2016) ask whether loess is a sediment, rock or soil. Answering this question requires clarity on loessification and related processes such as the role of carbonate in comparison to clay to form loess, the role of specific grain-size in loessification and whether loessification is different from pedogenesis or diagenesis. Since the desired clarity does not exist, Sprafke and Obreht (2016: 206) suggest loess as “something complex in between” and advise to term it just loess instead of a sediment, rock or soil.

To fully understand how loess and LPS work, the different stages from particle production to final particle deposition (Figs. 2-1 and 2-2) and LPS evolution are reviewed. Besides the process of glacial grinding (Smalley, 1966), Pye (1995: 657) lists eight processes responsible for the formation of silt-sized particles: disintegration of silt-sized sedimentary rocks, frost, salt and chemical weathering, eolian and fluvial abrasion and crushing, clay aggregation and biological processes (Figs. 2-1 and 2-2). Smalley and Markovic (2017) raise the question what the fundamental process is that enables the formation of predominantly silt-sized quartz particles. Based on eutectic reactions in rock melts, there is a crystalline transformation from high quartz to low quartz when the melt cools. This transformation introduces tensile stress and thus defects to the quartz structure. Consequently, a sand-sized quartz grain released from its parent rock is susceptible to further disintegration. Against this background, it may not only be the continental ice sheets producing silt particles by the “ice mill” but the smaller mountain glaciers as well (Smalley and Markovic, 2017). In addition, model experiments demonstrate that glacial grinding produces flat, blade-shaped particles necessary for the metastable structure of loess deposits (Smalley and Markovic, 2017). Wright et al. (1998) performed laboratory experiments to estimate the effectiveness of some of the aforementioned processes in the production of silt-sized particles (Table 2-1). Their results reveal that fluvial tumbling is the most effective followed by eolian abrasion and glacial grinding. Frost weathering is the least effective process with a time period of 1.35 Ma needed to reduce 1 kg of sand-sized particles to 1 kg of silt-sized particles (Wright, 2001b; Wright et al., 1998). Fluvial tumbling seems to be the most effective process (Wright et al., 1998) and thus draws attention to a long neglected process involved in loess formation – the fluvial transport by rivers (Lindé and Mycielska-Dowgiallo, 1980). However, the experiment represented high-energy

turbulent flow conditions with a sediment load that consisted of mixed grain-sizes (Wright, 2001b). Therefore, silt production is controlled by the duration of particles' exposure to high-energy flow conditions rather than the transport distance (Wright and Smith, 1993). Comparing fluvial comminution with the effectiveness of glacial grinding and eolian abrasion, the latter two might be of similar effectiveness due to spatial or environmental reasons.

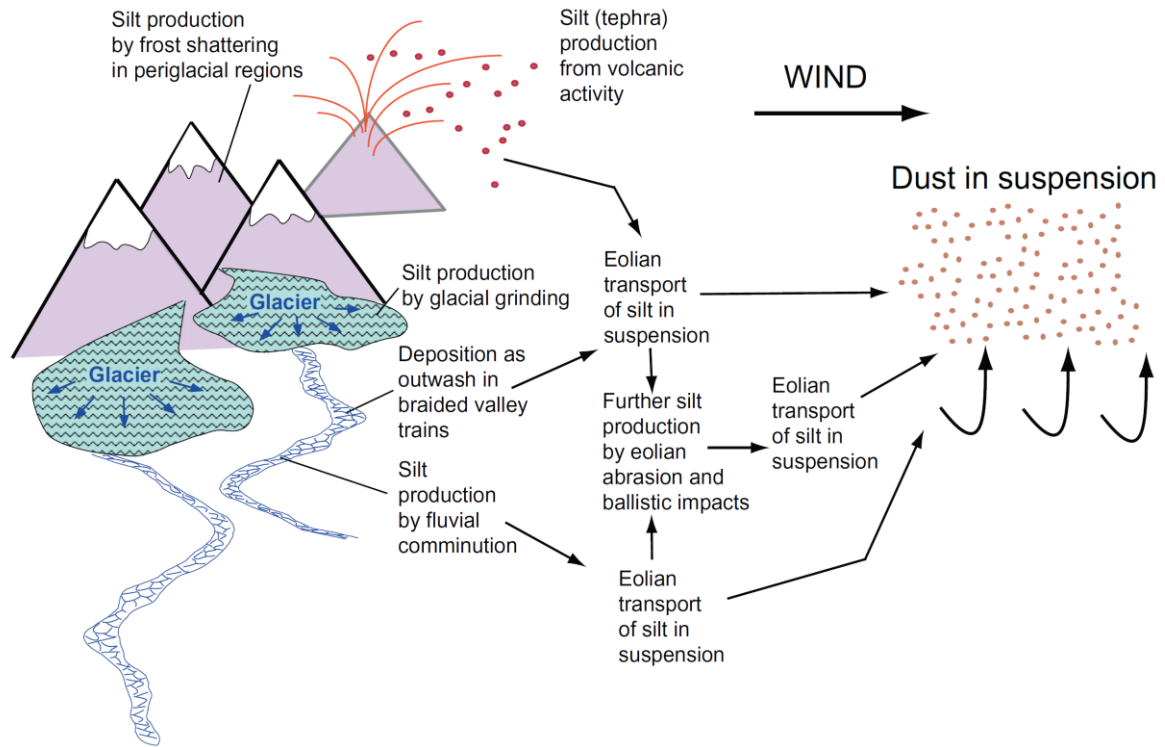


Fig. 2-1: Concept to explain the formation and transport pathways of dust in glacial environments (Muhs, 2013: 5).

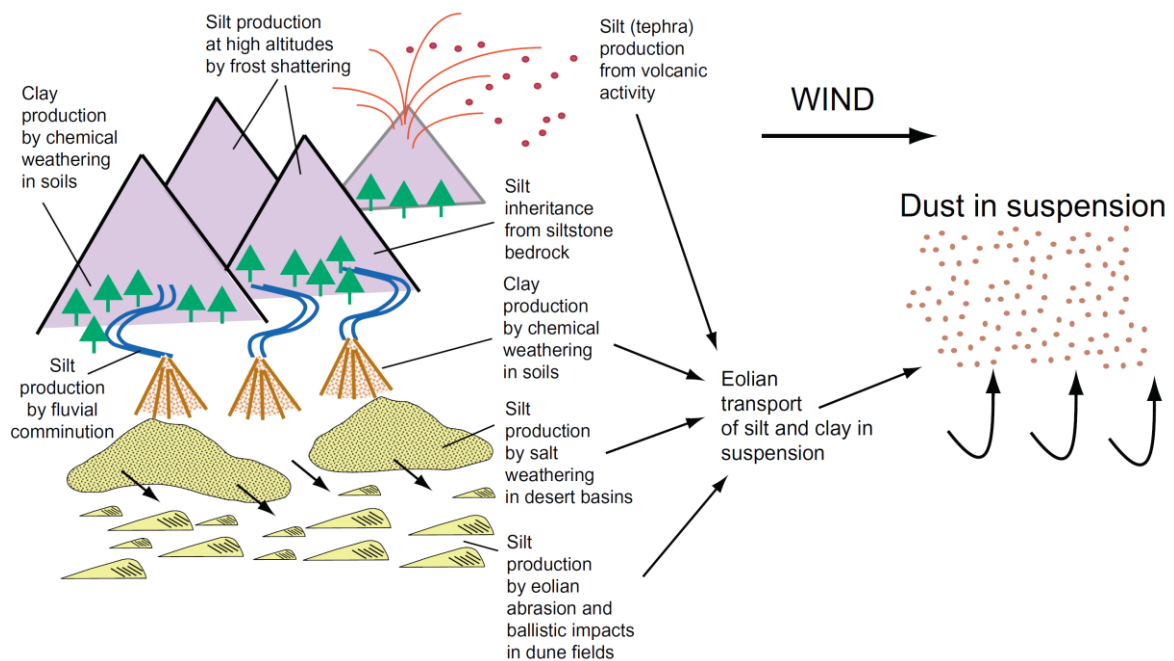


Fig. 2-2: Concept to explain dust production and transport pathways of dust in non-glacial environments (Muhs, 2013: 7).

Table 2-1: The relative effectiveness of silt producing mechanisms as determined from the amount of silt produced from 1 kg of the original sample (Wright, 2001b: 12).

Run type	Amount of material < 63 µm produced (g/kg)	Run duration	Rate of production of material < 63 µm (g/h)	Time needed to reduce 1 kg of original material to silt
Glacial grinding	47.4	24 h	1.98	506 h
Eolian abrasion: vein quartz	287	96 h	2.99	334.5 h
Eolian abrasion: fluvial sands	63.5	204 h	0.31	3212 h
Eolian abrasion: Pannonian sands	179	128 h	1.40	715 h
Fluvial tumbling: spheres	900	32 h	28.31	36 h
Salt weathering: Na ₂ SO ₄	41.6	40 cycles	0.04	2.64 a
Frost weathering: -12 – +15°C	0.44	360 cycles	5.1 * 10 ⁻⁵	1.35 Ma

Taking the example of glacier coverage during the Last Glacial Maximum, glacial grinding likely produced a substantial amount of fine material due to the size of the glaciers (Wright, 2001b). Moreover, laboratory experiments do not reflect all aspects of subglacial comminution processes (Wright, 2001b), and thus may underestimate their effectiveness. The production of silt under glacial conditions may also include the incorporation of previously weathered, reworked, silt-sized material, thereby distinctly increasing the output of silt-sized particles from continental ice sheets (Wright, 2001b). Similarly, eolian abrasion and salt weathering in desert environments (Fig. 2-2) provide reasonable explanations for the production of silt in water-sparse environments on long timescales (Wright, 2001b). Slow processes such as frost or insolation weathering may act as a constant minor stress upon rocks weakening their structure and finally causing rock slope failure events that contribute to large amounts of small particles (Wright, 2001b). In glacial periods, these small particles may subsequently be carried by glaciers. The first production stage of silt-sized particles represents the P1 event in the Hardcastle sequence.

After particles are produced, they are transported by rivers (Fig. 2-1, T1 in the Hardcastle sequence, Smalley and Markovic, 2017). Smalley et al. (2009) emphasize river transport as a mandatory step in material preparation associated with loess deposits. It is considered to be more important than material production by glacial grinding as the fluvial transport confines the location of the loess deposit due to subsequent final ineffective eolian short-distance transport (Smalley et al., 2009). Furthermore, additional silt-sized particles might be produced during fluvial transport as documented by laboratory experiments (Wright, 2001b; Wright and Smith, 1993; Wright et al., 1998). In this line of thinking, Smalley et al. (2009) summarize the PhD thesis of Hill (2005) with regard to the provenance of the Rhine loess ending with the statement that Belgium loess is likely of Alpine origin. The rationale behind this is the production of large amounts of sediment load by glacial grinding and physical weathering in the Alps and subsequent transport by the Rhine. On its way to the

river mouth into the North Sea, this transported material might be “diluted” by the admixture of non-Alpine material while likely further comminuted by fluvial action (Smalley et al., 2009). Despite potential dilution, Alpine material is well traceable down to the Rhine delta (Bernet et al., 2004). The stage of temporal deposition on floodplains or glacial outwash plains (Smalley et al., 2009) is termed D1 in the Hardcastle sequence (Smalley and Markovic, 2017).

The final steps include short-distance eolian transport (T2 in the Hardcastle sequence) and final deposition in terms of falling particles (D2 in the Hardcastle sequence) (Smalley and Fagg, 2015; Smalley and Markovic, 2017). Smalley et al. (2009) consider eolian transport as ineffective since particles in the size-range of loess are not effectively carried in suspension by air. Although this assumption explains the observed rapid thinning of loess deposits away from their associated dust reservoirs (D1), it challenges 80 μm as the optimal size for eolian particle transport (Smalley and Markovic, 2017). Furthermore, it contradicts concepts of Saharan dust entrapment in Carpathian loess sequences (Varga et al., 2016) and dust contributions from the Fennoscandian ice sheet and the North Sea shelf area to the loess sequences of Northern Central Europe (Antoine et al., 2013; Lehmkühl et al., 2016). Nonetheless, given the example of the LPS Nussloch (Germany), Rousseau et al. (2017b) distinguish between coarse material originating from the Rhine floodplain and fine material likely originating from distant sources such as the English Channel. Contributions of fine material from distant sources is consistent with dust model results for the European loess belt (Rousseau et al., 2014; Sima et al., 2013).

Eolian sediment transport involves creeping, saltation and suspension (Fig. 2-3, Pye, 1995). Particles may settle due to gravitation, downward turbulent diffusion, advection towards the surface and wet deposition by precipitation (Pye, 1995). Reduced wind speed together with increased surface roughness favor deposition. Unless either moist and/or rough bare grounds where small particles may infiltrate below the surface or vegetation cover do not exist permanent settlement of particles is likely prevented by frequent resuspension events (Pye, 1995). Vegetation cover is the most effective in trapping of silt-sized particles since vegetation compensates for accretion of dust by vertical growth allowing the formation of thick vertical deposits over time (Pye, 1995; Tsoar and Pye, 1987).

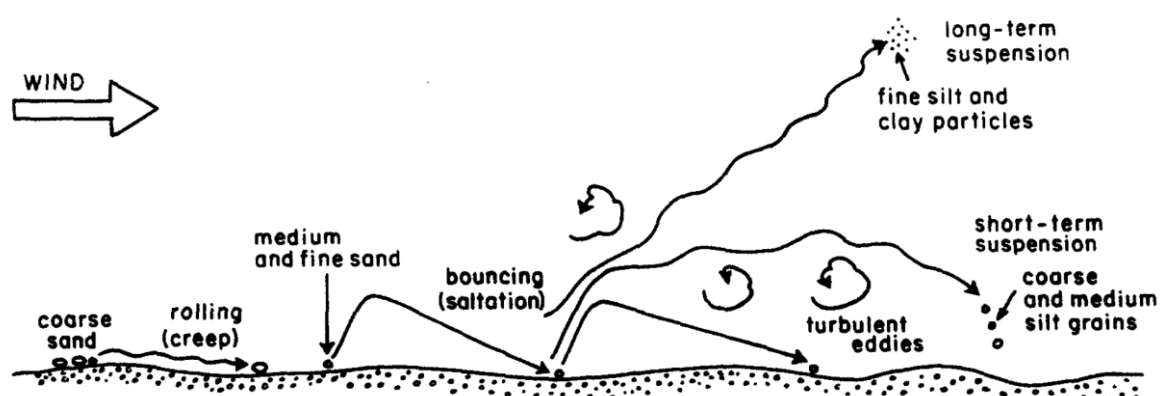


Fig. 2-3: Sketch illustrating eolian particle transport (Pye, 1995: 661).

Typical landforms related to loess deposits in a periglacial environment encompass proximal sand dunes or loess deposits with a fining and thinning trend towards larger distances from their source (Fig. 2-4, Pye, 1995). Accordingly, the LPS Susak consists of rather coarse-grained loess due to its proximal location adjacent to the paleo-Po delta (Wacha et al., 2017), possibly a transitional state between A and C (Fig. 2-4). Topographic obstacles reduce wind speed and thus favor luv-sided loess deposits (Fig. 2-4D) as exemplified on the Rhine loess, e.g. the LPS Schwalbenberg II and Nussloch (Lehmkuhl et al., 2016) as well as on the Danube loess, e.g. the LPS Süttő (Novothny et al., 2011). Wright (2001a) combines the described processes immanent to loess deposit formation in a framework to explain Hungarian loess deposition (Fig. 2-5). Due to the special location of the Carpathian Basin, the Danube serves as a carrier that transports previously conditioned material from the Alps, the Moravian mountains and the Carpathians into the Carpathian Basin (Smalley and Leach, 1978). Temporary deposition on the Danube floodplains during glacial periods together with topographically-determined atmospheric circulation patterns allows nearly ubiquitous loess deposition in the Carpathian basin (Sebe et al., 2011; Wright, 2001a).

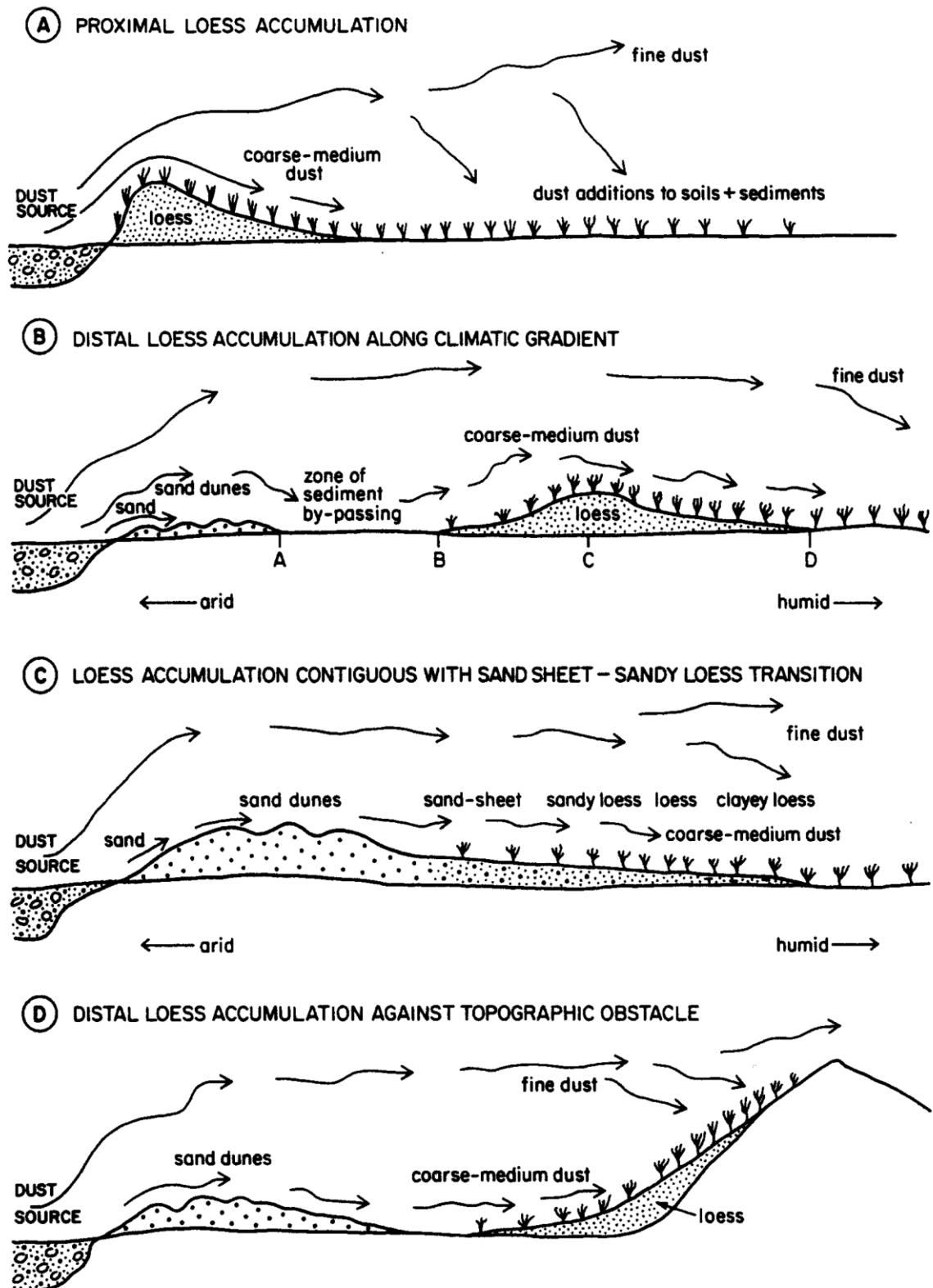


Fig. 2-4: Schematic models showing four conditions under which loess deposits may form: (A) accumulation of proximal loess on a well-vegetated surface adjacent to a dust source; (B) formation of distal loess on the vegetated semi-arid margin of a desert, accompanied by formation of eolian sand deposits proximal to the dust source; (C) formation of loess which is joined to proximal sand dunes and sand sheets by a transitional sandy loess zone; (D) accumulation of distal loess deposit against a topographic barrier (Pye, 1995: 664).

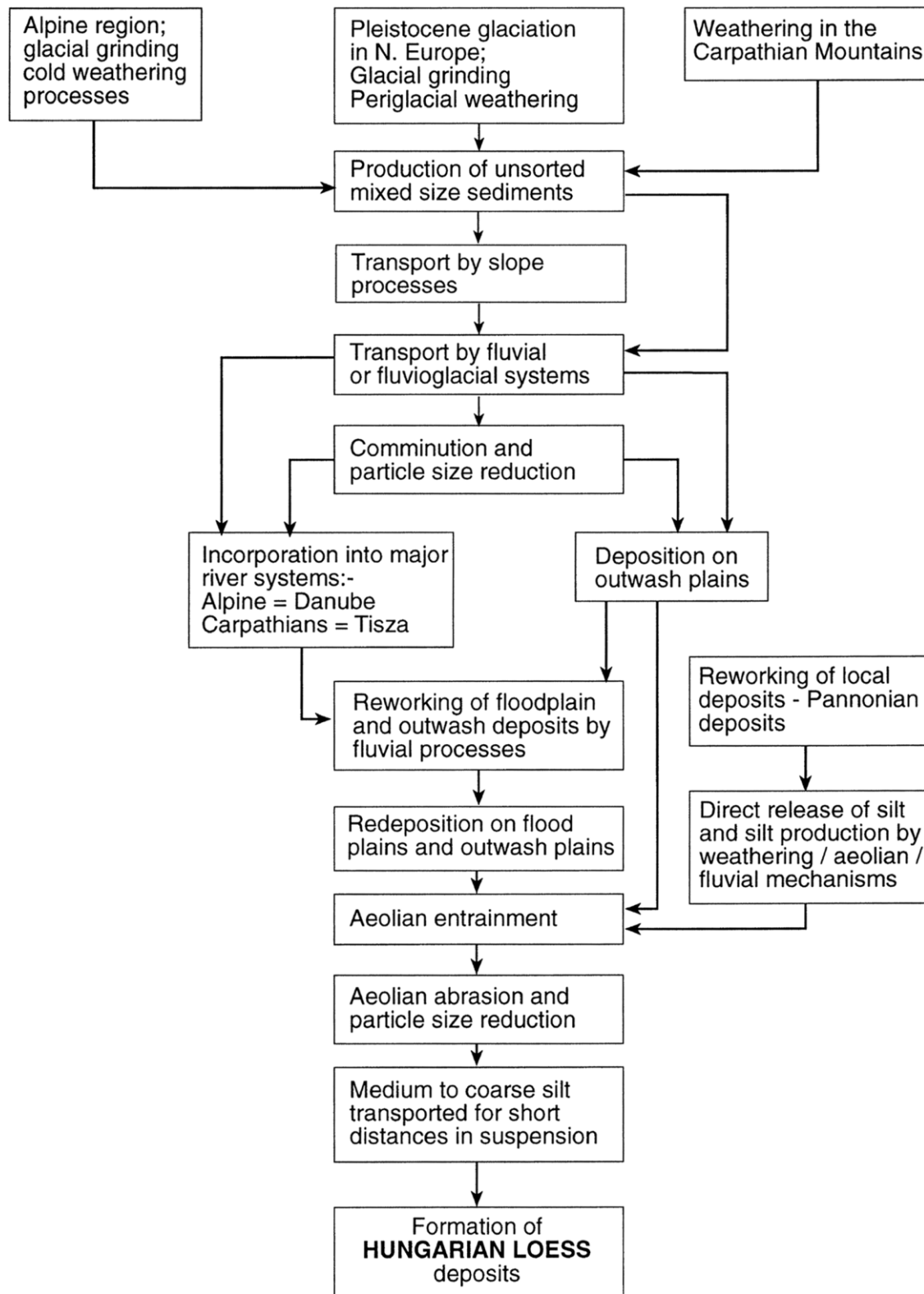


Fig. 2-5: Hungarian loess in a nutshell according to the processes involved in loess formation (Wright, 2001a: 243).

2.2. Paleosol formation

Understanding complex pathways of dust deposition, draws attention to the process of pedogenesis shaping a LPS ideally as an alternating sequence between loess and paleosols. In general, dust deposition and pedogenesis are competitive processes (e.g. Ferraro, 2009) unless climatic conditions prevent pedogenesis completely. Global or continental climatic variations control loess deposition (Rousseau et al., 2017b) while soils are a function of the interdependent factors climate, organisms, relief, parent material and time (Stockmann et al., 2011). Organisms in particular play important roles on different scales: e.g. there is flora- and fauna-induced bioturbation at the macro scale (Lavelle et al., 2016). Whereas microorganisms are involved in the establishment of localized anaerobic conditions favoring manganese precipitation (Keiluweit et al., 2016), or in the production of very small superparamagnetic iron particles being responsible for increased MS in soils (Fassbinder et al., 1990; Lovley et al., 1987). Therefore, specific climatic conditions permit a variety of soils to develop in loess. Subsequently, typical soil types preserved in European LPS are briefly discussed. Cold permafrost-dominated climate favors cryosols or gelic gleysols as incipient soils. Frequent freeze-thaw cycles and/or active layer dynamics may induce stagnant conditions in the active layer and sediment mixing by cryoturbation (Scheffer and Schachtschabel, 2002). Such soil formation is rapid, occurring within timescales from decades to centuries (Targulian and Krasilnikov, 2007), as evidenced for the Nussloch LPS correlating tundra gleysols with Greenland Interstadials (Rousseau et al., 2017a). Arctic brown paleosols or cambisols require more stable climatic conditions and longer timescales, in the range of thousands of years, to develop (Targulian and Krasilnikov, 2007). Cambisol formation involves leaching of the topsoil, i.e. the removal of alkaline ions (Na, Ca, Sr, Mg, K) by percolating water (Nesbitt et al., 1980), and brunification (Scheffer and Schachtschabel, 2002). Therefore, cambisols are either related to long-lasting Greenland interstadials (Rousseau et al., 2017a) or temperate-continental climatic conditions during interglacials accompanied by rubification under Mediterranean conditions (Obrecht et al., 2016). In contrast, chernozems reflect arid continental climates with a steppe-like vegetation cover. Limited precipitation and cold winters are responsible for the typical humus accumulation in the topsoil and contemporaneous bioturbation of unweathered loess and organic matter (Scheffer and Schachtschabel, 2002). Consequently, they may develop rather quickly within 2000 years (Scheffer and Schachtschabel, 2002). Central European LPS such as Dolní Věstonice show a chernozem-complex towards MIS 4 (Antoine et al., 2013) while chernozems represent the last interglacial (MIS 5e) at Carpathian LPS (Obrecht et al., 2016) and at the northern foreland of the Harz mountains in Germany (Lehmkuhl et al., 2016). Luvisols occur under temperate humid climatic conditions, often associated with interglacials (Antoine et al., 2013; Schirmer, 2016). Of the considered soil types, luvisols are the most developed. The typical process accompanying luvisol formations is clay translocation from the top to the subsoil forming a characteristic Bt horizon (Scheffer and Schachtschabel, 2002). Often truncated luvisols are preserved as paleosols in LPS (e.g. Antoine et al., 2013; Sprafke et al., 2014). Especially related to transitions from interglacial to glacial conditions accompanied by several returns to warmer climatic conditions, pedocomplexes may form as illustrated by Sprafke et al. (2014) for the Paudorf LPS in Austria (Fig. 2-6). Alternating phases of erosion, accumulation, reworking and pedogenesis

can lead to situations where the current pedogenesis affects weathered material that has already undergone a previous cycle of pedogenesis (Fig. 2-6). Consequently, such a pedocomplex may indicate misleading weathering intensity compared to the actual paleoenvironmental conditions active at the time of soil formation due to pedogenesis in a previously developed paleosol (Sprafke et al., 2014).

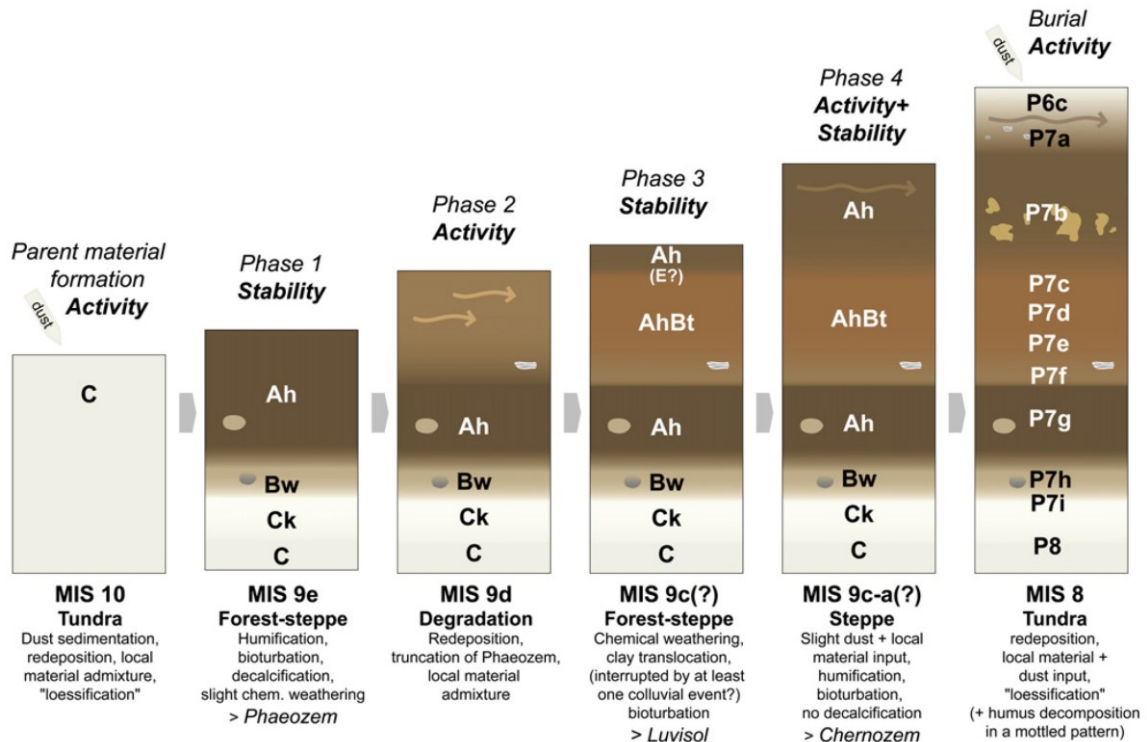


Fig. 2-6: Simplified genetic model for the lower pedocomplex (P7) during MIS 9. Main processes and average environments are indicated for each phase. A forest-steppe environment is assumed, degrading to a steppe ecosystem in the final phase. The formation of the luvisol is caused by ongoing weathering of decalcified and pre-weathered substrate (Sprafke et al., 2014: 68).

2.3. The temporal perspective

Recognizing the cyclic succession of loess and paleosols in Chinese (Liu, 1988) and European loess sequences (Pécsi, 1982), was a milestone in establishing the continental Quaternary stratigraphy (Zöller, 2010). Attempts to correlate terrestrial LPS with emerging marine sediment and ice core records fostered the awareness about the existence of large-scale climate fluctuations in time (Kukla, 1977, 1987). The most complete quaternary and oldest records are located in China (Zöller, 2010) with a maximum age of 5 Ma in the Tarim Basin (Varga, 2011). Each study that aims at reconstructing paleoenvironmental conditions requires independent numerical age control to unambiguously correlate events recorded in LPS on the one hand to events recorded in marine sediment and polar ice cores on the other hand (cf. Blaauw, 2012). However, robust numerical dating techniques covering the LPS time frame were in their infancy at the time of understanding the importance of LPS as terrestrial paleoenvironmental archive. This strongly supported the development of luminescence dating (for deposits < 400 ka) and magnetostratigraphy over the past decades (Zöller, 2010). The latter subdivides into paleomagnetism and MS.

Paleomagnetism makes use of variations in intensity, declination and inclination of the Earth's magnetic field with particular focus on reversals on longer time scales. It covers the time period from 100 a to 10 Ma (Hambach et al., 2008; Liu et al., 2015). MS as a rock magnetic property and parameter of environmental magnetism detects cyclic changes along LPS often related to paleosols, thus allowing indirect dating of LPS by correlating MS profiles across LPS to other proxy data measured at different paleoenvironmental archives (Hambach et al., 2008; Liu et al., 2015). Today, luminescence dating is the key technique to provide numerical age control for Middle and Late Pleistocene loess (Zöller, 2010). However, luminescence ages exhibit error margins in the range of 10 % (Moine et al., 2017; Zöller and Semmel, 2001) and more (e.g. Frechen and Schirmer, 2011), challenging an unambiguous correlation of loess stratigraphies that predominantly rely on luminescence chronologies with Dansgaard-Oeschger cycles (Antoine et al., 2009; Profe et al., 2016). Therefore, ^{14}C radiocarbon ages may refine luminescence chronologies for the youngest 50 ka as long as e.g. organic matter remains or earthworm calcite granules are preserved and available in sufficient amounts for dating (Moine et al., 2017; Zöller, 2010).

The rationale behind luminescence dating is that electrons trapped in crystal defects accumulate over time as a function of natural nuclear radiation after burial (Fig. 2-7). For dating of sediments, quartz and feldspar grains are used. Exposure to sunlight or heat releases trapped electrons and thus zeroes the “luminescence clock” (Fig. 2-7, Preusser et al., 2008). This behavior is used in the laboratory to measure luminescence radiation emitted by quartz or feldspar grains when stimulated by heat (thermoluminescence, TL), visible light (optical-stimulated luminescence, OSL) or infrared radiation (infrared-stimulated luminescence, IRSL) (Fig. 2-7, Preusser et al., 2008). The luminescence age (eq. 1) is estimated based on the relationship between the measured luminescence signal (paleodose) and the nuclear radiation over time (dose rate) (Preusser et al., 2008 and references therein).

$$\text{Age} = \frac{\text{measured luminescence signal (Paleodose)}(\text{Gy})}{\text{nuclear radiation over time (Dose rate)}\left(\frac{\text{Gy}}{\text{a}}\right)} \quad (1)$$

Paleodoses are either retrieved by the additive or regenerative dose approach. The latter measures the luminescence signal of the sample first, and subsequently applies different doses to the sample in the laboratory to estimate the paleodose. In contrast, the first approach adds defined doses to multiple aliquots of the sample prior to measurement of the luminescence signal to estimate the natural luminescence signal by extrapolation (Preusser et al., 2008 and references therein). However, the additive dose approach is susceptible to fitting errors while the regenerative dose approach may suffer from zeroing-induced changes in luminescence properties of the sample (Preusser et al., 2008). In loess research, TL was state-of-the-art until the mid-1990s whereas IRSL approaches dominate today (Roberts, 2008; Zöller, 2010). TL is particularly prone to age overestimation due to incomplete bleaching while IRSL and TL approaches applied to feldspars are particularly prone to age underestimation due to anomalous fading (Preusser et al., 2008; Roberts, 2008). Anomalous fading describes a non-thermal loss of signal with time. In case of irradiation and subsequent stimulation in the laboratory minerals affected by anomalous

fading release too much signal since there is not enough time between irradiation and measurement to lose the same amount of signal as during natural luminescence signal accumulation. Because temperature triggers this non-thermal signal loss over time, pre-heating strategies are reported to compensate best for anomalous fading (Preusser et al., 2008; Roberts, 2008). Dose rates are estimated by measuring or approximating the nuclear radiation in the sample or at the position from which the sample was taken. Radionuclides of K and U contribute most to the natural nuclear radiation necessary for luminescence accumulation in the sample (Preusser et al., 2008).

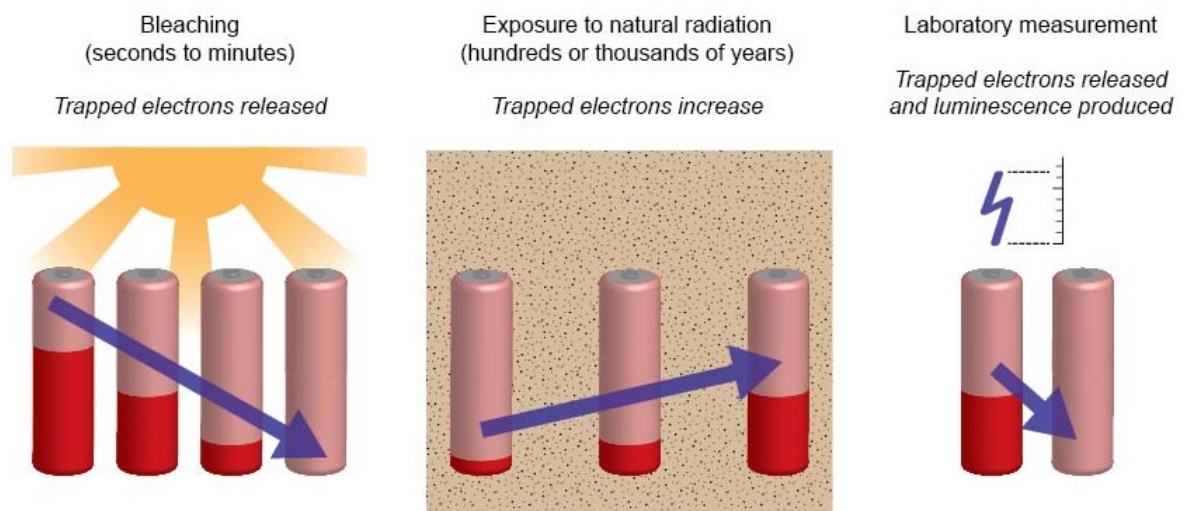


Fig. 2-7: Sketch expressing luminescence dating as a rechargeable battery. Exposure to sunlight or heat releases trapped electrons and the battery is depleted. After burial exposure to natural radiation accumulates luminescence signal in sediments and recharges the battery. In the laboratory, the emission of light by releasing the stored energy (depleting the battery) is recorded (Duller, 2008: 4).

Since luminescence requires dark conditions to accumulate with time, luminescence ages represent sedimentation ages, i.e. in case of paleosols they reflect maximum ages after which pedogenesis may have started. Under ideal conditions, in LPS time passes from the bottom to top during loess deposition so that the oldest loess is located at the bottom and the youngest loess at the top (Fig. 2-8). During phases of pedogenesis, ideally accompanied by cessation of dust deposition, time storage reverses from top to bottom, i.e., the material that is affected by pedogenesis for the longest period of time is located at the top (Fig. 2-8). Subsequent loess deposition involves a jump in time from the bottom of pedogenesis to the bottom of the new loess layer and passes again from bottom to top (Rousseau et al., 2017b). High-resolution luminescence studies enable the calculation of sediment or mass accumulation rates (e.g. Frechen, 2003; Roberts, 2008).

The completeness and continuity of LPS are still matters of debate and strongly depend on the researcher's viewpoint. While an LPS is considered to be complete if most of the MIS are represented by at least one stratigraphic unit, most LPS would represent quasi-complete and quasi-continuous terrestrial records serving as terrestrial counterparts of marine sediment cores (Muhs, 2018). In contrast, if millennial to centennial-scale resolution was required e.g. to study Dansgaard-Oeschger cycles, most LPS would be incomplete and discontinuous, except for special locations such as loess gredas (Lehmkuhl et al., 2016),

i.e., loess dunes (Leger, 1990). One important example for the time period MIS 3 to MIS 2 is the loess greda Nussloch at the eastern margin of the Upper Rhine valley (Moine et al., 2017; Rousseau et al., 2017a). Nussloch has been studied for more than half a century and ranges among the best studied LPS in Europe (Lehmkuhl et al., 2016; Zöller and Semmel, 2001). Based on high-resolution grain-size and MS data combined with a very detailed stratigraphy, Antoine et al. (2001) and Antoine et al. (2009) correlate the observed changes at Nussloch with alterations in the $\delta^{18}\text{O}$ and dust records of Greenland ice cores. Antoine et al. (2009) conclude that grain-size changes at Nussloch mirror Dansgaard-Oeschger events, however, the established chronology at that time allowed doubts about this correlation as discussed by Kadereit et al. (2013). Recently, earthworm calcite granules are identified as important proxy for paleoenvironmental conditions as the calcite produced by earthworms originates from nutrient uptake in the form of litter (Moine et al., 2017; Prud'Homme et al., 2015). This excludes old dead carbon sources and qualifies carbon derived from earthworm calcite granules as an ideal target material for radiocarbon dating (Moine et al., 2017). Earthworms live in the upper decimeters of a soil and adapt to climate fluctuations very quickly as they are abundant in tundra gleys but absent in unweathered loess (Prud'Homme et al., 2015). Applying this technique to Nussloch confirms previous results by an independent high-resolution (each paleosol) radiocarbon chronology allowing an unambiguous correlation of stratigraphic units to single Greenland interstadials (Moine et al., 2017). Knowledge about the duration of Greenland interstadials derived from transitions recorded in ice cores together with knowledge about different soil types that developed during different interstadials foster new insights into the relationship between climate, time and pedogenesis. The results show that tundra gleys predominantly developed during short interstadials (< 1000 a) while arctic brown soils are limited to longer interstadials (1600-4200 a) (Rousseau et al., 2017a). The next steps are to use the stable oxygen and carbon isotopes in earthworm calcite granules to investigate their potential as quantitative paleo-temperature and paleo-precipitation proxies (e.g. Prud'homme et al., 2018).

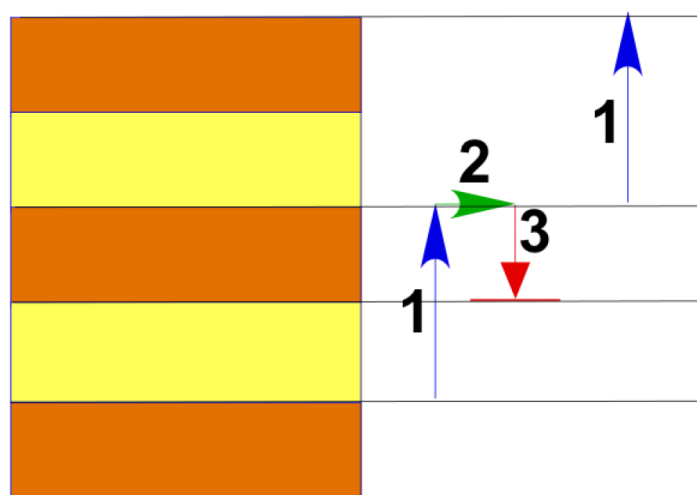


Fig. 2-8: Ideal schematic stratigraphic evolution of time in a loess-paleosol sequence. Orange: paleosol, yellow: loess. Blue arrow (1): time evolution during loess deposition from bottom to top. Green arrow (2): phase of stability where dust deposition ideally ceases. Red arrow (3): time evolution during pedogenesis from top to bottom (modified after Rousseau et al., 2017b: 1187).

2.4. Loess-paleosol sequences: review of geochemical proxies

After providing a brief overview of numerical dating in loess, the next step is to review proxies applied on LPS to unravel paleoenvironmental dynamics with particular emphasis on geochemical proxies. Grain-size and MS analyses are the most common applied analyses on LPS with the highest spatial resolution up to 2 cm. Although grain-size variations are often interpreted as a proxy for wind activity, they are a function of wind strength and particle aridity at emission, sediment availability and mixture of different dust sources (e.g. Antoine et al., 2009; Kadereit et al., 2013; Újvári et al., 2016). Fine sand and coarse silt deposits are related to saltation while medium silt is associated with transport in low suspension accompanied by cyclonic activity and fine silt particles are attributed to long distance transport in suspension (Vandenberghe, 2013). MS may represent dust source changes, weathering intensity and paleoenvironmental conditions (e.g. Maher, 2011). In a nutshell, there are two contrasting scenarios for the behavior of MS in paleosols: MS can be either lower or higher than in unweathered loess (e.g. Maher, 2011). Comparing MS with geochemical weathering indices, Bokhorst et al. (2009) find consistency between them at Ukrainian and Serbian LPS whereas Bloemendal et al. (2008) and Bábek et al. (2011) report inconsistencies. Geochemical weathering indices do not seem to react individually to different soil types as it is the case for MS (Bábek et al., 2011).

The analyses of geochemical composition in loess-paleosol sequences has been pioneered by Chinese loess researchers to study loess origin and paleoclimate (Liu, 1988; Muhs, 2018). Considering chemical elements to unravel paleoenvironmental conditions and sedimentation dynamics from LPS, basic knowledge about element behavior in relation to the aforementioned environmental processes is indispensable. Each chemical element is characterized by an individual ionic potential (IP), i.e. the ratio of ionic radius and ionic charge, determining its behavior towards environmental conditions (Goldschmidt, 1937). Elements with $IP < 3$ and $IP > 12$ form soluble cations and anionic complexes whereas elements with $3 < IP < 12$ form insoluble hydrolysates (Fig. 2-9). In the case of weathering, atoms are released into solution and interact with water molecules. While elements with intermediate IP are able to deprotonate water molecules in order to form covalent bounds with oxygen and thus constitute fast-precipitating insoluble hydrolysates, elements with lower IP become fully hydrated and elements with high IP form water soluble anionic complexes (Buggle et al., 2011; Goldschmidt, 1937). Although pH-value and redox conditions may influence the behavior of individual elements, the IP theory is considered reliable for the near-neutral conditions present in LPS (Buggle et al., 2011; Sheldon and Tabor, 2009). In addition, adsorption to clay minerals is positively correlated with ionic radius (Fig. 2-9, Nesbitt et al., 1980). Based on this information, elements and element ratios used to examine weathering intensity, dust provenance and grain-size variability are reviewed.

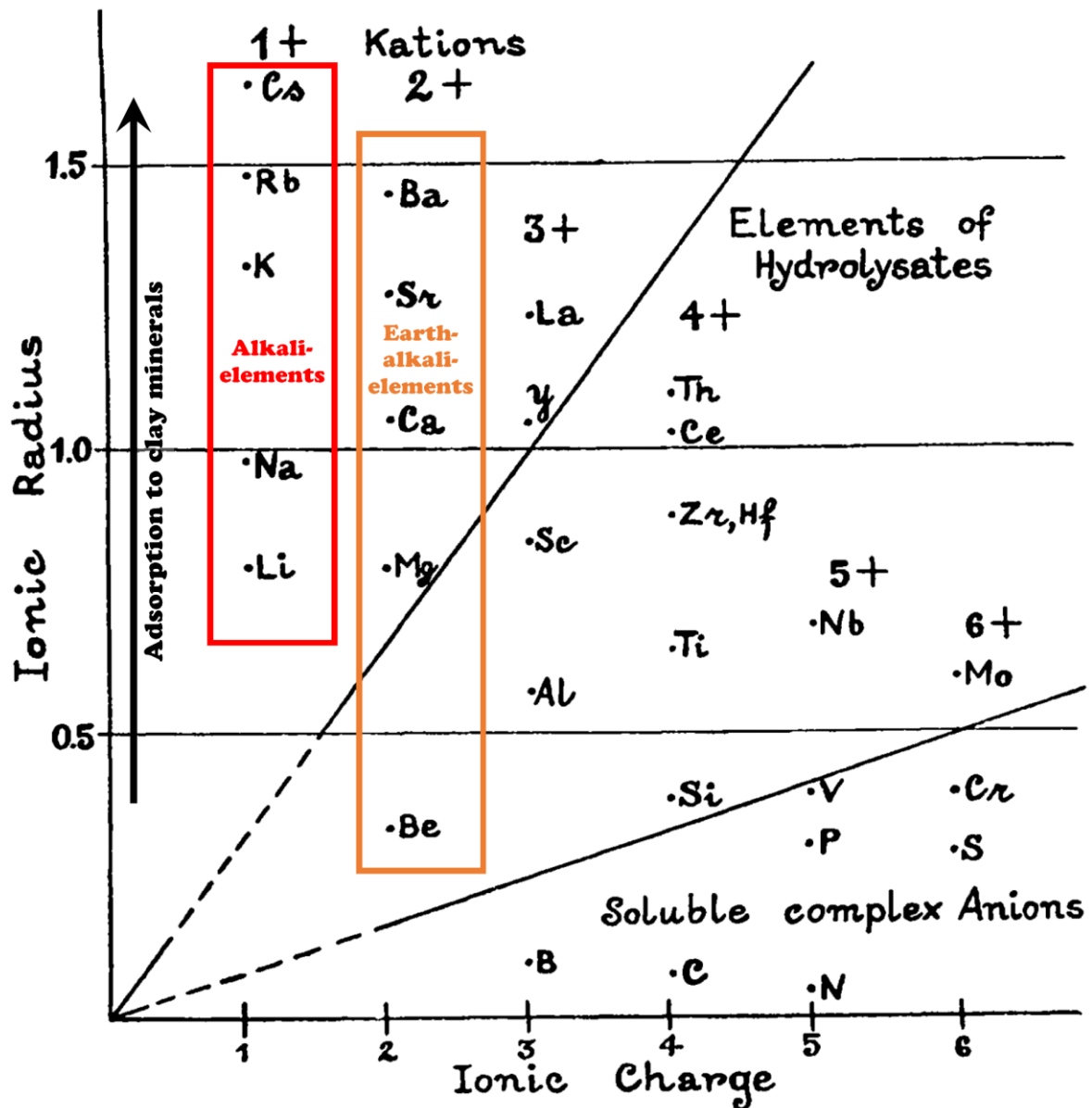


Fig. 2-9: Ionic potential of selected elements (modified after Goldschmidt, 1937: 665).

Investigating weathering intensity by chemical elements relies on ratios between immobile and mobile elements (Table 2-2). In general, alkali (Li, Na, K, Rb, Cs) and earth-alkali elements (Mg, Ca, Sr, Ba) except Be are soluble, though earth-alkali elements are more soluble than alkali elements due to their smaller ionic radii. Suggested ratios make use of different ionic radii either within the same element group (e.g. Rb/K) or different element groups (e.g. Rb/Sr, Ba/Sr, Ca/Ti). In addition, multi-element ratios, normalized to Al or Ti as weathering residuals (Schatz et al., 2015), are capable of documenting weathering of specific mineral groups, e.g. the Chemical Index of Alteration (CIA) reflects feldspar weathering (Nesbitt and Young, 1982). The weathering indices WI-1, WI-2 include Fe due to its pedogenesis-associated accumulation (Darmody et al., 2005) whereas the FENG index (Table 2-2) include Fe and Al due to their background concentrations in loess deposits related to the parent material (Feng, 1997). However, their susceptibility to changes in redox

conditions prevents Mn and Fe from being applied as reliable weathering indices (Bugge et al., 2011).

Table 2-2: Overview of element ratios used to investigate weathering intensity, dust provenance and grain-size variations (modified after: Schatz et al., 2015: 171; Sheldon and Tabor, 2009: 8).

Ratio		Molar ratio	Equation	Reference
Weathering index				
Multi-element	CIA Chemical Index of Alteration	X	$=[\text{Al} / (\text{Al} + \text{Na} + \text{Ca}^* + \text{K})] * 100$	Nesbitt and Young (1982)
	Index A	X	$=(\text{Si} + \text{Ca}^* + \text{K} + \text{Na}) / (\text{Al} + \text{Si} + \text{Ca}^* + \text{K} + \text{Na})$	Kronberg and Nesbitt (1981)
	Index B	X	$=(\text{Ca}^* + \text{Na} + \text{K}) / (\text{Al} + \text{Ca}^* + \text{Na} + \text{K})$	Kronberg and Nesbitt (1981)
	PWI Paleosol Weathering Index	X	$=[(4.20 * \text{Na}) + (1.66 * \text{Mg}) + (5.54 * \text{K}) + (2.05 * \text{Ca})] * 100$	Gallagher and Sheldon (2013)
	$\Sigma\text{bases}/\text{Al}$	X	$=(\text{Ca}^* + \text{Mg} + \text{Na} + \text{K}) / \text{Al}$	Retallack (2001)
K-free	CIW (CIA-K) Chemical Index of Weathering	X	$=[\text{Al} / (\text{Al} + \text{Na} + \text{Ca}^*)] * 100$	Harnois (1988) and Maynard (1992)
	PIA Plagioclase Index of Alteration	X	$=[(\text{Al} - \text{K}) / (\text{Al} + \text{Ca}^* + \text{Na} - \text{K})] * 100$	Fedo et al. (1995)
	YANG	X	$=(\text{Ca}^* + \text{Na} + \text{Mg}) / \text{Ti}$	Yang et al. (2006)
	WI-1 Weathering Index 1	X	$=(\text{Si} + \text{Ca}^*) / (\text{Fe} + \text{Ti})$	Darmody et al. (2005)
	WI-2 Weathering Index 2	X	$=(\text{Si} + \text{Ca}^*) / (\text{Fe} + \text{Ti} + \text{Al})$	Darmody et al. (2005)
Ca-free	CPA (CIW') Chemical Proxy of Alteration	X	$=[\text{Al} / (\text{Al} + \text{Na})] * 100$	Bugge et al. (2011) and Cullers (2000)
	FENG	X	$=(\text{Al} + \text{Fe}) / (\text{Na} + \text{K} + \text{Mg} + \text{P})$	Feng (1997)
Major elements	Si/Al	X		Ruxon (1968)
	Base/Ti	-		Sheldon and Tabor (2009)
	Ca/Sr	-		Bokhorst et al. (2009)
Trace elements	Rb/Sr	-		Nesbitt et al. (1980)
	Ba/Sr	-		Bokhorst et al. (2009)
	Rb/K	-		Nesbitt et al. (1980)
Provenance indices				
Major elements	Ti/Al	X		Chen et al. (2013)
	Si/Al	-		Klasen et al. (2015)
Trace elements	Ti/Zr	-		Muhs et al. (2003)
Grain-size indices				
Major elements	Si/Al	-		Liang et al. (2013)
	Ti/Al	-		Liang et al. (2013)
Trace elements	Zr/Rb	-		Chen et al. (2006)

Indices that contain Ca and Sr values are expected to be more sensitive to weak pedogenesis as Ca and Sr are leached during weathering as the first elements and substitute each other in minerals (Bugge et al., 2011; Gallet et al., 1996; Nesbitt et al., 1980). However, Ca and Sr dynamics are dominated by calcite and dolomite dynamics so that secondary carbonates in paleosols adversely affect Ca- and Sr-based weathering indices (Bugge et al., 2011). The presence of secondary carbonates would attenuate the recorded weathering intensity. Consequently, Bugge et al. (2011) suggest restricting the usage of “Sr-type” weathering indices to carbonate-free parent materials. The Chemical Proxy of Alteration is thus suggested as a Ca-free weathering index (Bugge et al., 2011). According to Bokhorst et al. (2009) leaching and secondary carbonate precipitation are led by Ca in comparison with Sr. Therefore, the simple ratio Ca/Sr may indicate the presence of secondary carbonates by a constant profile across loess and paleosols and thus may help to reliably apply “Sr-type” weathering indices to carbonate-bearing sediments.

K-feldspar weathering commences after the decay of Na- and Ca-bearing feldspars at advanced levels of weathering (Nesbitt and Young, 1984). Rb and Ba substitute for K in K-feldspars (Zech et al., 2008) and are released as a consequence of K-feldspar weathering together with K (Nesbitt et al., 1980). However due to their larger ionic radii, Rb and Ba adsorb more to clay minerals and thus become relatively enriched in paleosols (Bokhorst et al., 2009; Nesbitt et al., 1980; Zech et al., 2008). This qualifies Rb and Ba as immobile elements in weathering indices, though Ba dynamics in soils, in particular, are poorly understood (Sheldon and Tabor, 2009). Strong weathering conditions may cause leaching of Rb and Ba (Kronberg et al., 1979). K itself might be influenced by illitization (K-fixation), resulting in misleadingly low Rb/K values (Bugge et al., 2011; Nesbitt and Young, 1989). Inconsistent behaviors of K during weathering (Harnois, 1988; Nesbitt et al., 1980) may also indicate complex equilibria between K bound in mica as well as clay minerals and solute K (Fig. 2-10). This observation led to the development of K-free weathering indices (Table 2-2), whereupon the YANG index (Yang et al., 2006) was designed for LPS (Schatz et al., 2015).

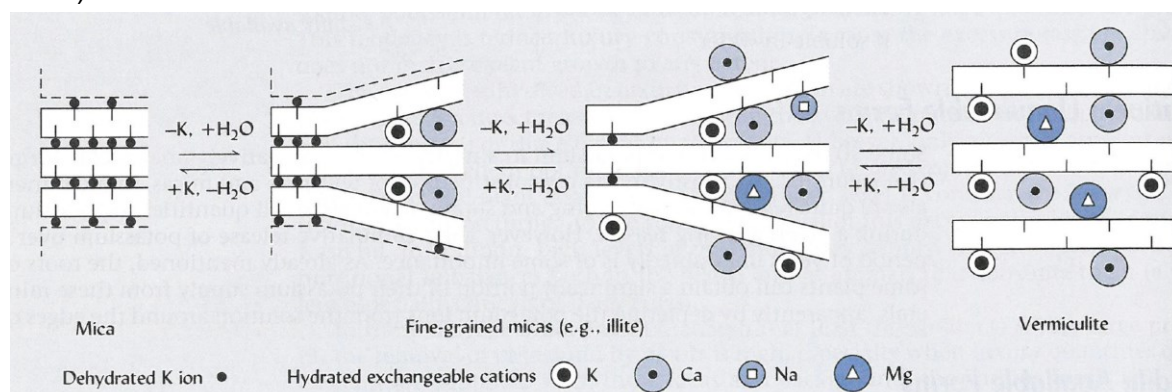


Fig. 2-10: Diagrammatic illustration of the release and fixation of potassium between primary micas, fine-grained mica (illite clay), and vermiculite. In the diagram, the release of K proceeds to the right, while the fixation process proceeds to the left. Note that the dehydrated K ion is much smaller than hydrated ions of Na^+ , Ca^{2+} , Mg^{2+} , etc. Thus, when K is added to a soil containing 2:1-type minerals such as vermiculite, the reaction may go to the left and K ions will be tightly held (fixed) in between layers within the crystal, producing a fine-grained mica structure (modified after: Brady and Weil, 2004: 452).

Although all multi-element weathering indices use weathering-inert elements (e.g. Al, Si, Ti, Zr) as immobile element instead of Rb or Ba, such use might be challenged by alternating dust sources and/or grain-size induced fractionation. Nonetheless, Ruxon (1968) introduced the molar ratio of Si/Al as a measure of pedogenesis due to enrichment of Al in clay minerals as a consequence of weathering (Sheldon and Tabor, 2009). Therefore, this ratio is also referred to as proxy for clayeyness (Sheldon and Tabor, 2009). Different dust sources may change the amount of the conservative elements independent of the minerals from which the soluble elements are released (Buggle et al., 2011). While Si and Zr predominantly occur in coarser grain-size fractions, Rb, Al and Ti are predominantly associated with fine particles (Buggle et al., 2011; Garcia et al., 1991; Hošek et al., 2015; Stiles et al., 2003). Grain-size-related sorting effects can be excluded for Al using the A-CN-K ternary diagram (Nesbitt and Young, 1984, 1989), a prerequisite for Al-based weathering indices (Buggle et al., 2011). Buggle et al. (2011) conclude that a Na- and Al-based weathering index is the best choice in a non-salt environment as both elements occur in the same host minerals and thus constitute a homogeneous mineralogical weathering system. However, since ITRAX XRF scanning provides qualitative data and is not able to measure Na and Mg, XRF scanning-derived weathering indices are limited to the “Sr-type” weathering indices and Rb/K.

Loess is generally considered to represent an average sample of the Upper Continental Crust (Gallet et al., 1996; Taylor et al., 1983). While this statement is valid for comparisons with oceanic crust, elemental compositions of loess may vary substantially with different rock compositions in respective dust source regions (Muhs, 2018). Scatter plots of major element ratios are linked to dominant mineralogy and its change according to weathering or dust source changes in comparison to the Upper Continental Crust (UCC) (Gallet et al., 1996; Gallet et al., 1998; Muhs, 2018). For example, K_2O/Al_2O_3 vs. Na_2O/Al_2O_3 identifies relative contributions of felsic versus mafic rocks (Muhs, 2018). Normalizing element concentrations of loess samples to element concentrations of the UCC reveals site-specific element dynamics often including Na, K and Sr depletion, Zr enrichment and slight Ti enrichment (Gallet et al., 1998; Újvári et al., 2008). Ca and Mg contents vary strongly from enrichment to depletion (Gallet et al., 1998). Depletion of weathering-susceptible elements indicate deposition of parent material that was affected by weathering in its source region while Ti and Zr enrichment points to heavy mineral enrichment (Újvári et al., 2008). The UCC composition consists of averaged element concentrations from many globally collected samples. Consequently, there is no sample available to actually measure the UCC composition. However, such measurements would be mandatory in order to compare qualitative XRF scanning results from loess samples with qualitative XRF scanning results from the UCC. Nonetheless, there are some element ratios that can be analyzed with the ITRAX XRF scanner.

Ti/Al may vary according to rock types of the parent material since Ti increases from felsic to mafic rocks while Al remains relatively constant (Sheldon and Tabor, 2009). Chen et al. (2013) suggest density-fractionation along the eolian transport pathway as an additional factor altering the initial Ti/Al ratio that is determined by the mineralogy of the parent rock. Si/Al is proposed to reflect dust source changes similar to Ti/Zr at the LPS Schwalbenberg II

in Germany (Klasen et al., 2015). Ti/Zr seems to fractionate differently between ultramafic and granitic rocks and e.g. was used successfully to separate Alaskan from mid-continental loess (Muhs et al., 2003; Muhs and Benedict, 2006). Zech et al. (2008) applied this ratio as proxy for dust provenance to Siberian LPS. However, Zr is solely present in the heavy-mineral zircon with a density ranging from 4.0 to 4.7 g/cm³ (Holland and Gottfried, 1955) and thus fractionates together with quartz towards sand (Garcia et al., 1991; Stiles et al., 2003), i.e. Zr might be also dependent on grain-size but opposite to the grain-size dependency of Ti and Al. Furthermore, sediment recycling leads to a relative accumulation of Zr (Caracciolo et al., 2011; Mongelli et al., 2006). The Al-Ti-Zr ternary plot unravels sediment recycling and sorting dynamics as these three elements inherit their relative abundances from their dust sources regardless of weathering (Caracciolo et al., 2011; Garcia et al., 1994; Mongelli et al., 2006). Interpretations deduced from this relationship include the establishment of a conceptual model for sediment recycling occurring at the beginning of MIS 2 at the LPS Schwalbenberg II. Additionally, the suggestion of tectonic uplift being an important driver for the observed sedimentation dynamics at the LPS Süttő in Hungary has been deduced from this relationship.

The grain-size dependent geochemical ratio that is most commonly applied is Zr/Rb with Zr representing coarse grains and Rb representing fine grains (Chen et al., 2006). Yang et al. (2006) systemically document grain-size-dependent element concentrations from Chinese and Tajik LPS. Results show Ti enrichment in the fine silt fraction, Al, Fe, Mn, Mg, K, P, Ba and Rb enrichment in the clay fraction and Si, Ca, Na and Sr in the coarse-silt and sand fractions. Therefore, they conclude that each commonly applied weathering index is adversely affected by grain-size dynamics, except for their suggested YANG index (Table 2-2). However, Zr/Rb may suffer from sediment recycling-induced Zr dynamics. In addition to Zr/Rb, Liang et al. (2013) suggest Ti/Al, Zr/Al and Si/Al as grain-size proxies with Si/Al corresponding best to grain-size variations. They interpret grain-size variations at the Jingyuan LPS (Chinese Loess Plateau) as rapid changes in the strength of winter monsoon that are linked to Dansgaard-Oeschger events during the last glacial period.

Further geochemical proxies not applied in this thesis involve rare earth elements (e.g. Liu, 1988; Muhs, 2018), radiogenic and stable isotope (e.g. Bayat et al., 2017; Koeniger et al., 2014; Prud'homme et al., 2018; Rousseau et al., 2014; Zöller, 2010) and biomarkers (e.g. Buggle and Zech, 2015; Liu and Huang, 2005; Zech et al., 2013a; Zhang et al., 2006).

3. X-ray fluorescence – theory and application

XRF core-scanning is a state-of-the-art technology that is routinely applied in marine and lacustrine geoscience. It is used to non-destructively as well as cost- and time-efficiently investigate relative changes in the composition of major elements with atomic numbers ≥ 13 and selected trace elements (commonly: Sr, Rb, Zr and Ba) along sediment profiles with an instrument dependent spatial resolution down to 100 μm (Davies et al., 2015; Rothwell and Croudace, 2015a, b). In contrast, loess-paleosol sequences (LPS) are sampled discretely and commonly analyzed time- and cost-intensively by conventional XRF and spectrometric methods to obtain quantitative element data from Na to U with a spatial resolution of 10 cm at best (Hošek et al., 2015; Mikulčić Pavlaković et al., 2011; Obreht et al., 2015; Peng et al., 2016). However, according to Weltje et al. (2015) it is only necessary to use quantified element data when fluxes or mass balances are of interest. Consequently, interpretations that rely on relative changes of element ratios, e.g. selected geochemical weathering and provenance indices along an LPS, are perfectly possible with qualitative data (e.g. Profe et al., 2016). In order to understand energy-dispersive (ED) XRF scanning-related limitations in comparison to conventional wavelength-dispersive (WD) XRF, both techniques are presented with an emphasis on their differences.

Both XRF techniques rely on the same principle: an initial polychromatic X-ray beam excites different atoms of different elements by ejecting an electron from one of their inner shells (Fig. 3-1). There are two ways for atoms to react to such a vacancy. A non-radiative transition occurs when the vacancy is filled by an electron from an outer shell and the transition energy causes another electron from an outer shell to be ejected (Auger effect) (Jenkins, 1988). Such an atom is then ionized twice. Lighter elements are more prone to Auger effects due to the vicinity of $K\alpha$ X-ray photon emission lines to the ionization energy of an L-shell electron (Potts, 1992). Furthermore, if the initial vacancy is in a higher shell than the K-shell, it is possible that the vacancy shifts to a higher subshell before being filled by another transition according to different angular-momentum quantum numbers within the main shell (Coster-Kronig transitions) (Bambynek et al., 1972). In contrast, a radiative transition occurs when the vacancy is filled by an electron from an outer shell while emitting an element-specific X-ray photon (photoelectric effect, Fig. 3-1) (Jenkins, 1988; Potts, 1992). The radiative transition predominates 95 % of all cases (Potts, 1992). Its wavelength is inversely coupled to the atomic number of an element (Z) by Moseley's law (Moseley, 1914). Being electromagnetic radiation, an X-ray photon can either be characterized by its wavelength (λ) or energy (E , eq. 2) "where h is the Planck constant = $6.626 \cdot 10^{-34}$ J/s, c is the velocity of light = $2.998 \cdot 10^8$ m/s" (Potts, 1992: 227).

$$E = \frac{hc}{\lambda} \quad (2)$$

The competing non-radiative and radiative transitions determine the fluorescence yield, the effectiveness of the radiative transitions of each element individually (Jenkins, 1988). This explains why highest count rates most often are observed for Ca and Fe, although often Si

and Al are most abundant in a sample. Jenkins (1988: 7) provides the example of pure Ba and pure Al with same concentrations resulting in 50-times more counts for Ba due to higher fluorescent yields.

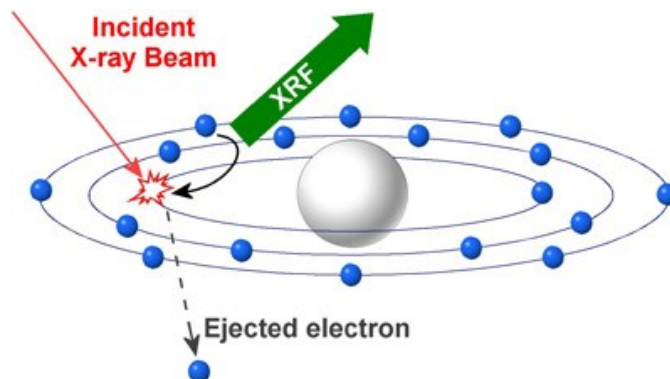


Fig. 3-1: Sketch showing the basic principle of X-ray fluorescence (XRF) (Horiba, 2017).

Sample matrix influences how element-specific X-rays are attenuated within the sediment by interaction with other atoms of the sediment or scattering. This relationship is formalized by the Beer-Lambert law (eq. 3) explaining the intensity of the incident X-ray beam (I_0) in a certain depth x (I) as a function of the mass attenuation coefficient ($\frac{\mu}{\rho}$) (Potts, 1992: 239).

$$I = I_0 \exp^{-\left(\frac{\mu}{\rho}\right)x} \quad (3)$$

Thus, the Beer-Lambert law determines the maximum depth of a sample from which fluorescence radiation of specific elements can be received. Results from powder pellets reveal a penetration depth of “~ 13 μm for Si, ~ 36 μm for Ca and ~ 900 μm for Rb” (Potts, 1992: 246). This arises the question how low Z elements (e.g. Al and Si) are reliably measurable when the maximum excitation depth may comprise a single grain from the analyzed sample only (Potts, 1992). Production of glass beads by fusing the rock material prior to analysis excludes grain-size-related matrix effects completely (Potts, 1992). Scattering of initial X-ray photons takes place either if the energy of an incident photon is not sufficient to excite an electron from an inner shell of an atom, or if an incident photon interacts with loosely bound electrons of an outer shell resulting in a photon with reduced energy. The former is called Rayleigh, elastic or coherent scatter while the latter is referred to as Compton, inelastic or incoherent scatter (Potts, 1992). Heavy elements are more prone to Rayleigh scatter due to high binding energies of inner-shell electrons whereas Compton scatter increases with decreasing atomic number due to decreasing binding energies of outer-shell electrons (Potts, 1992). Thomson et al. (2006) highlight this correlation for organic-rich sapropel units in a Mediterranean sediment core while Löwemark et al. (2011) outline how an organic matrix dilutes element counts compared to a clastic matrix along one sediment core. They opt for normalization to a common denominator in order to obtain environmentally meaningful results. Furthermore, Löwemark et al. (2011) refer this dilution to the closed-sum constrain, i.e. the measurement of elements plus scattering always equals to a constant sum (Rollinson, 1993). Accordingly, single elements do not vary independently but interdependently (Rollinson, 1993).

Grain-size, porosity, density and water content changes may lead to changes in XRF excitation due to varying amounts of air and water in pore spaces of a sample. This alters the amount of element-specific XRF radiation reaching the detector (Hennekam and de Lange, 2012; Jarvis et al., 2015; Tjallingii et al., 2007; Weltje and Tjallingii, 2008). Variations in sample geometry (surface roughness and orientation) modify the angle between sample surface and detector and thus contribute to XRF count alterations (Jarvis et al., 2015). Hence, the ideal sample is powdered, homogenized, dry and pressed to obtain homogeneous porosity and density as well as a smooth flat surface. In case of discrete sample measurements, these requirements are usually fulfilled whereas XRF scanning of sediment cores suffer from many of the aforementioned effects.

The key component of a WD-XRF device in contrast to ED-XRF analyzers is a diffracting crystal. WD-XRF devices consist of an X-ray tube and the so-called spectrometer vacuum chamber containing a diffracting crystal and a gas flow proportional counter which is coupled to a scintillation counter (Fig. 3-2A). A goniometer allows the measurement of different angles and guarantees correct angular alignment between components. The emitted fluorescence radiation is collimated and directed to a diffracting crystal (Fig. 3-2A) (Potts, 1992). Collimation narrows scatter angles of X-rays emitted from the sample (Fig. 3-2B, C) to allow constructive interference at the crystal according to Bragg's Law (eq. 4).

$$n\lambda = 2d \sin\theta \quad (4)$$

X-rays are strongly diffracted by crystals as long as their wavelengths (λ) and incident angles (θ) meet the lattice spacing of the crystal (d). Wavelengths being a multiple of the wavelength obeying Bragg's Law are diffracted as well and are represented by the integer n in eq. 4. Thus, the crystal cannot discriminate between such wavelengths (Fig. 3-2D, E). Wavelengths other than those obeying Bragg's Law lead to destructive interference (Potts, 1992). There are different crystals available depending on the elements of interest. The diffracted radiation might be collimated again before reaching the detector (Fig. 3-2A). Both gas proportional and scintillation counters characterize X-rays according to their energies. In contrast to ED-XRF devices, the detectors in a WD-XRF device are used to record quasi monochromatic radiation filtered by the diffracting crystal (Potts, 1992). Therefore, although both gas proportional and scintillation counters have lower energy resolutions compared to solid state detectors installed in ED-XRF devices, WD-XRF measurements reach a higher energy resolution because the latter is primarily determined by the diffracting crystal (Potts, 1992). Effects that are responsible for the specific energy resolution of a detector are outlined in the example of a silicon drift detector (SDD) installed in the ITRAX XRF core scanners that was used in this study.

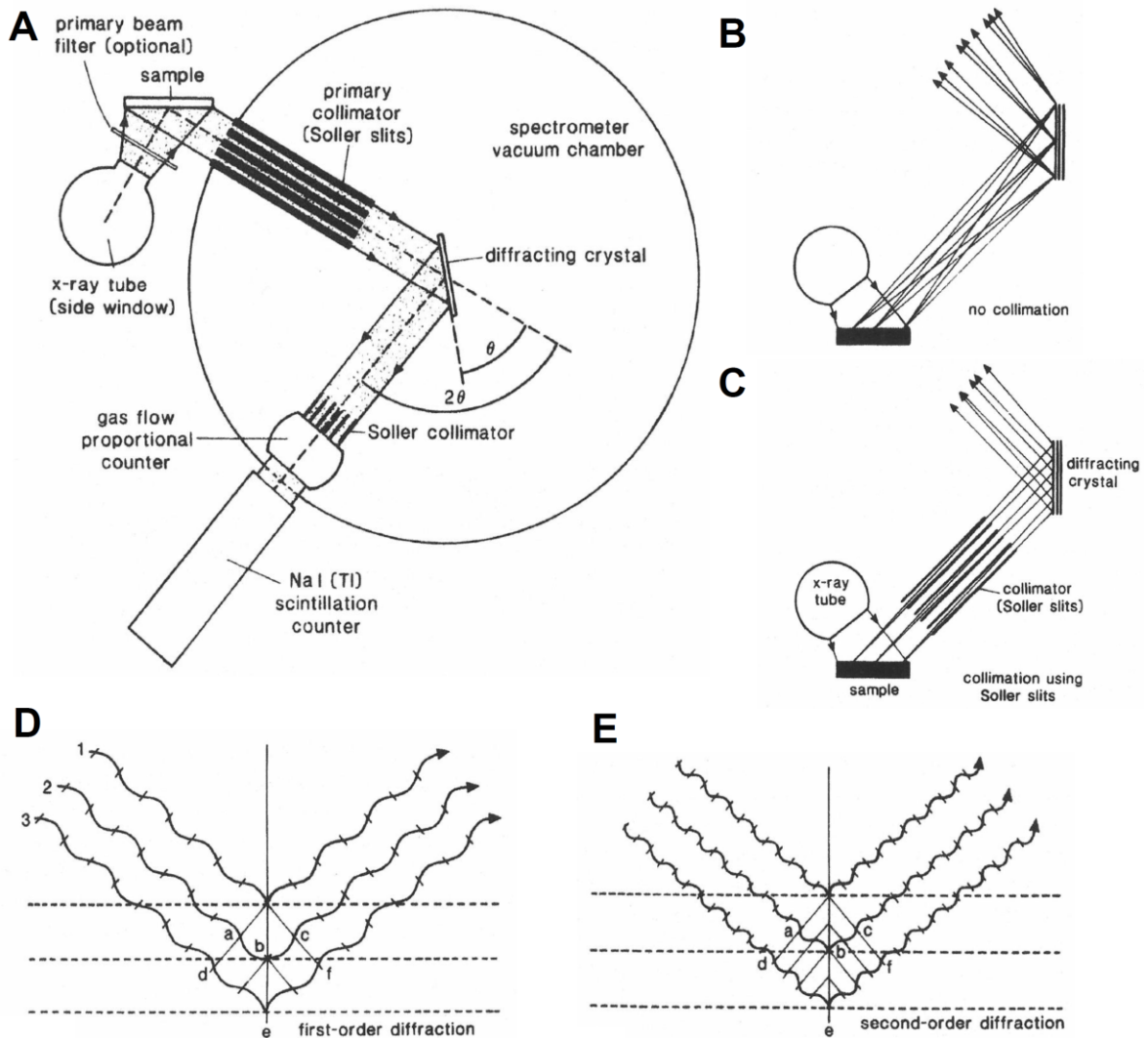


Fig. 3-2: Scheme illustrating a wavelength-dispersive XRF analyzer (A), the effect of collimation (B and C) and how diffraction occurs in a crystal lattice at fixed incident angles as a function of wavelength (D and E) (modified after Potts, 1992: 254ff.). D and E The path length difference between x-rays diffracted from adjacent atom layers corresponds to an integral number of wavelengths (1 for first-order (D) and 2 for second-order diffraction (E)). Nodes corresponding to $\lambda/2$ are marked (Potts, 1992: 256).

In contrast to WD-XRF, ED-XRF devices are designed to record the whole spectrum at once requiring robust deconvolution techniques in mathematical peak-fitting strategies to characterize single element counts (Potts, 1992; Van Espen, 2002). In a nutshell, XRF measurements rely on counting photons, i.e. random events that hit the detector, and thus obey Poisson statistics. Accordingly, element-specific measurement uncertainty can be approximated from the square root of counts as the standard deviation of counts (σ_N) equals the square root of mean counts (\sqrt{N} , eq. 5; Van Espen, 2002: 240). However, several factors (outlined below), which adversely influence the charge capturing process, challenge this relationship, hence impeding a straightforward application for data precision estimates in routine analyses (Jarvis et al., 2015).

$$\sigma_N = \sqrt{N} \quad (5)$$

ITRAX XRF core-scanners (Fig. 3-3) are equipped with a SDD and a multi-channel analyzer (MCA) with 1024 channels covering a range from 1 to 19 keV with a bin width of 18.5 eV (Croudace et al., 2006). SDD allow stable measurements and high count rates at room temperature (Lechner et al., 1996; Lechner et al., 2001). The detector installed at the ITRAX XRF core-scanner at the University of Bremen in the GEOPOLAR lab has an operational count rate of 30,000 counts per second. In addition, ITRAX XRF core-scanner can be equipped with different X-ray tubes to enable better excitation of the elements of interest. Commonly applied X-ray tubes are Cr for light elements (< Fe) and Mo for heavy elements (\geq Fe; Croudace et al., 2006).

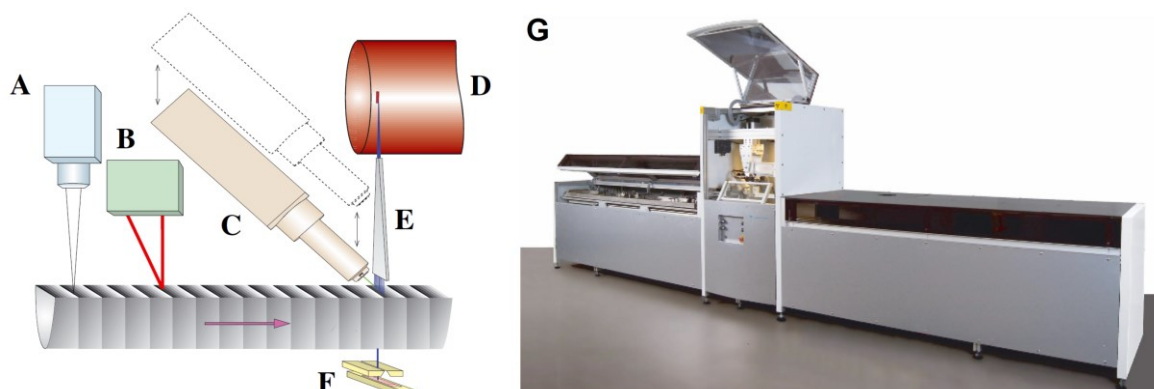


Fig. 3-3: Schematic of the ITRAX system showing the optical-line camera (A), laser triangulation system (B), necessary to measure the surface height of a sediment core in order to ensure a constant sample-detector-distance; motorized XRF Si-drift chamber detector (C), 3 kW X-ray tube (D), flat-beam X-ray waveguide (E), the X-ray line camera and slit system for the radiographic line camera (F) and a front view photograph (G). The horizontal arrow shows the incremental motion direction of a core and the vertical arrows the movement directions of the XRF detector (modified after Croudace et al., 2006: 53).

The processes from collecting an X-ray deposited charge on the detector to the final signal involves (1) charge collection in the detector, (2) transport and amplification of the collected charge and (3) processing of the amplified signal by the multi-channel analyzer (Knoll, 2010; Scholze and Procop, 2009). Especially, charge collection and the first amplification steps are most prone to errors due to small signal-to-noise ratios (Knoll, 2010). Regarding charge collection in the detector, three effects may deteriorate the signal: (1) incomplete charge collection, (2) escape peaks and (3) sum peaks (pile-up effects). The energy of an X-ray photon is not always completely collected by the detector resulting in incomplete charge collections and erroneous counts in channels of lower energies (Scholze and Procop, 2009). Escape peaks, i.e. additional peaks at energies reduced by XRF energies of the detector material, occur when an incoming X-ray photon excites an atom from the detector (Scholze and Procop, 2009; Schoonjans et al., 2012). If two or more X-ray photons hit the detector simultaneously, sum peaks occur because the detector cannot discriminate single events (Schoonjans et al., 2012). This often happens for elements with the highest count rates. Electronic noise summarizes effects of Brownian thermal motion, spontaneous current and voltage fluctuations due to quantum mechanics, and leakage currents, i.e., the flow of charge carriers when no X-ray photon bombardment takes place (Knoll, 2010: 650f.). That is why ED-XRF spectra show typical, nearly Gaussian shaped X-ray lines with widths of 140-250 eV instead of their theoretical linewidths of 5-10 eV (Van Espen, 2002). As a result of this peak broadening most counts are recorded by the multi-channel analyzer in

channels adjacent to the one that corresponds to the natural X-ray photon energy (Scholze and Procop, 2009). Moreover, each detector needs a specific time to process an X-ray photon hit before it can process the next one. Within this time, the so-called dead-time, the detector cannot record any X-ray photon hit. When another event happens during the detector's dead time, this event is not counted (Knoll, 2010).

ITRAX measurements are further affected by the air passage between sample and detector. Interactions with air molecules attenuate the XRF radiation emitted from the sample. This is especially true for light elements as their lower energy fluorescence radiation is strongly absorbed by oxygen atoms (Potts, 1992). Consequently, Al and Si suffer from low detectability (e.g. Huang et al., 2016) and Na and Mg are not detectable at all. Furthermore, XRF spectra contain Ar signals from air molecules (Liang et al., 2012).

Table 3-1: Comparing cost and time of WD-XRF and XRF scanning measurements according to reported preparation and processing fees. WD-XRF: Michigan State University, XRF Lab (MSU, 2017), XRF scanning: Stockholm University, Department of Geological Sciences (SU, 2017). Prices for WD-XRF measurements refer to the category "Major elements" for academic research. XRF scanning costs include two hours of charge for post-processing. Preparation time for preparing discrete samples for XRF measurement amounts to approximately 5 minutes per sample. Scanning time for 30 samples equals the chosen measurement time in minutes.

Test case Number of samples, analysis	Cost in given currency	Cost in €	Time	Measurement time
100 WD-XRF*	5150 US-\$	4367	ca. 1 week***	Unknown
1000 WD-XRF*	51500 US-\$	43672	ca. 10 weeks***	Unknown
100 Scanning*	9378 SEK	935	10.9 h	10 s
100 Scanning*	9535 SEK	951	12 h	30 s
100 Scanning*	10081 SEK	1006	15.9 h	100 s
100 Scanning**	1878 SEK	187	2.6 h	10 s
100 Scanning**	2035 SEK	203	3.7 h	30 s
100 Scanning**	2581 SEK	257	7.6 h	100 s
1000 Scanning*	77581 SEK	7738	90.9 h	10 s
1000 Scanning*	79144 SEK	7894	102.0 h	30 s
1000 Scanning*	84613 SEK	8440	140.9 h	100 s
1000 Scanning**	2581 SEK	257	7.6 h	10 s
1000 Scanning**	4144 SEK	413	18.7 h	30 s
1000 Scanning**	9613 SEK	959	57.6 h	100 s

* complete sample preparation done by the laboratory.

** complete sample preparation and measurement by the user.

*** time estimated according to experience in preparing glass beads for WD-XRF analysis.

WD-XRF outperforms ED-XRF with regard to chemical resolution and is well suited to calculate quantitative data while XRF scanning outperforms WD-XRF with regard to cost- and time-efficiency at the expense of providing qualitative data only. This is highlighted by using costing tables from XRF laboratories available on the internet. Cost and time are calculated for two test cases: 100 and 1000 samples with 100, 30 and 10 s measurement time for XRF scanning analyses (Table 3-1). Results highlight superior time- and cost-efficiency of XRF scanning of discrete samples in comparison to conventional WD-XRF analysis. XRF scanning costs including sample preparation are one quarter or less of the WD-XRF prices depending on the chosen measurement time. When sample preparation is

done by oneself, fees are reduced to a minimum, only including the required scanner time and about two hours of post-processing. Comparing the extremes (1000 samples with 10 s measurement time at the scanner and without preparation), XRF scanning of discrete samples outperforms WD-XRF analysis by a factor of 170 with regard to cost and by a factor of ca. 50 with regard to time. In this example WD-XRF time consumption (preparation + measurement) is calculated as eight hours per day, five days a week for ten weeks.

4. Study I – Schwalbenberg II

Geochemistry unravels MIS 3/2 paleoenvironmental dynamics at the loess-paleosol sequence Schwalbenberg II, Germany

Jörn **Profe**^{a*}, Bernd **Zolitschka**^a, Wolfgang **Schirmer**^{b,1}, Manfred **Frechen**^c,
Christian **Ohlendorf**^a

^a GEOPOLAR, Institute of Geography, University of Bremen, Celsiusstraße FVG, 28359 Bremen, Germany

^b former Department of Geology, Heinrich Heine University Düsseldorf, Moorenstraße 5, 40225 Düsseldorf, Germany

^c Department of Geochronology and Isotope Hydrology, Leibniz Institute for Applied Geophysics (LIAG), Stilleweg 2, 30655 Hannover, Germany

¹ Current Address: Wolkenstein 24, 91320 Ebermannstadt, Germany

* E-Mail: profe@uni-bremen.de, Phone: +49-421-218-67154

published

Palaeogeography, Palaeoclimatology, Palaeoecology 459 (2016) 537-551

doi: [10.1016/j.palaeo.2016.07.022](https://doi.org/10.1016/j.palaeo.2016.07.022)

The printed version equals the published version with editorial changes.

Contribution of authors

JP designed and conducted XRF data precision measurements and assisted in further sample analyses. In addition, JP interpreted and structured the results, recalibrated the ¹⁴C ages, drafted the manuscript and developed the figures. BZ is responsible for the study design and concept. He helped to improve the manuscript significantly. WS provided the samples, assisted in improving the chronology and helped to improve the manuscript. MF contributed to the chronology and the XRF data precision discussion, and helped to improve the manuscript. CO assisted in data analyses and structuring the manuscript.

Abstract

The Schwalbenberg II loess–paleosol sequence (LPS) denotes a key site for Marine Isotope Stage (MIS) 3 in Western Europe owing to eight succeeding cambisols, which primarily constitute the Ahrgau Subformation. Therefore, this LPS qualifies as a test candidate for the potential of temporal high-resolution geochemical data obtained by X-ray fluorescence (XRF) scanning of discrete samples providing a fast and non-destructive tool for determining the element composition. The geochemical data is first contextualized to existing proxy data such as magnetic susceptibility (MS) and organic carbon (C_{org}) and then aggregated to element log ratios characteristic for weathering intensity (Ca/Sr, Rb/Sr, Ba/Sr, Rb/K) and dust provenance (Ti/Zr, Ti/Al, Si/Al). Generally, an interpretation of rock magnetic particles is challenged in Western Europe, where not only magnetic enhancement but also depletion plays a role. Our data indicates leaching and top-soil erosion induced MS depletion at the Schwalbenberg II LPS. Besides weathering, Ca/Sr is susceptible for secondary calcification. Thus, also Rb/Sr and Ba/Sr are shown to be influenced by calcification dynamics. Consequently, Rb/K seems to be the most suitable weathering index identifying the Sinzig Soils S1 and S2 as the most pronounced paleosols for this site. Sinzig Soil S3 is enclosed by gelic gleysols and in contrast to S1 and S2 only initially weathered pointing to colder climate conditions. Also the Remagen Soils are characterized by subtle to moderate positive excursions in the weathering indices. Comparing the Schwalbenberg II LPS with the nearby Eifel Lake Sediment Archive (ELSA) and other more distant German, Austrian and Czech LPS while discussing time and climate as limiting factors for pedogenesis, we suggest that the lithologically determined paleosols are in-situ soil formations. The provenance indices document a Zr-enrichment at the transition from the Ahrgau to the Hesbaya Subformation. This is explained by a conceptual model incorporating multiple sediment recycling and sorting effects in eolian and fluvial domains.

Keywords

XRF-scanning of discrete samples
Paleoclimatology
Weathering index
Dust-provenance index
Middle Rhine valley

4.1. Introduction

Loess–paleosol sequences (LPS) on the one hand denote a valuable terrestrial paleoclimate archive, especially for the last glacial/interglacial cycle (Hošek et al., 2015; Tzedakis et al., 2006). On the other hand, their regionally patchy stratigraphies mirror the different oceanic or continental climate modes which complicate superregional correlations of LPS (Hošek et al., 2015). This impedes the reconstruction of superregional paleoclimate conditions such as the identification of the effects of millennial scale climate fluctuations related e.g. to Dansgaard–Oeschger events (Kadereit et al., 2013; Terhorst et al., 2015). In addition, chronologies often rely on luminescence ages with error margins of several thousand years, rarely supported by radiocarbon ages for the topmost 50 ka which reduce the temporal uncertainty (Frechen and Schirmer, 2011; Fuchs et al., 2013; Hošek et al., 2015; Kadereit et al., 2013; Kadereit and Wagner, 2014). Therefore, the correlations of proxies from LPS with Greenland ice cores and other global data sets should always be regarded with caution (Blaauw, 2012; Kadereit et al., 2013).

LPS are frequently investigated for their lithology, grain-size, rock magnetic properties, mineralogy, micromorphology, geochemistry, carbonate and organic carbon content as well as for pollen and other biomarkers (Antoine et al., 2009; Baumgart et al., 2013; Buggle et al., 2011; Gocke et al., 2014; Hošek et al., 2015; Kühn et al., 2013; Mikulčić Pavlaković et al., 2011; Schirmer, 2012; Schirmer et al., 2012; Zech et al., 2008; Zech et al., 2013b). However, high-resolution geochemical records with a spatial resolution of at least 2 cm, a standard for marine and lacustrine sediment records, in most cases are unavailable for LPS, although their need was highlighted recently (Liang et al., 2013; Liang et al., 2012; Obreht et al., 2015). Liang et al. (2012) evaluate the applicability of X-ray fluorescence (XRF) core scanning – a non-destructive, time- and cost-efficient method to track the chemical composition along a sediment profile qualitatively (Croudace et al., 2006) – using U-channels from the Chinese Loess Plateau and present a record with 0.5 cm resolution. In conclusion, they emphasize the benefits of high-resolution geochemical data to explain paleoclimate variations. As most LPS are usually discretely sampled with a resolution of > 10 to 2 cm (Liang et al., 2013; Novothny et al., 2009; Novothny et al., 2011; Sun et al., 2011; Wacha et al., 2011a; Wacha et al., 2011b), these samples provide an easily accessible but still unused potential to substantially increase the temporal geochemical resolution of many LPS.

In western central Europe the Schwalbenberg II LPS is reported to be a key site for Marine Isotope Stage (MIS) 3 due to its eight succeeding cambisols in the Ahrgau Subformation (Schirmer, 1995, 2012). Nevertheless, its chronology is still controversially debated. The lithophenomenological chronology assumes the Schwalbenberg II LPS to comprise the time span from the youngest MIS 5 up to MIS 2 whereas luminescence ages suggest a time span from MIS 4 to MIS 2 (Frechen and Schirmer, 2011; Schirmer, 2012). Due to the continuous sampling of the Schwalbenberg II LPS, this profile qualifies as a test site to investigate the potential of analyzing discrete samples with the XRF core-scanner technology to obtain temporal high-resolution geochemical data. This data enables the

reconstruction of paleoclimate conditions and sedimentation dynamics that were active during the late Pleistocene.

Hence, the objectives of this paper are: (1) investigating weathering and provenance indices derived from XRF-determined element data to deepen the knowledge about paleoenvironmental conditions and processes, and (2) testing the suitability of bromine counts as additional XRF-determined proxy for total organic carbon in LPS. The benefit of quasi-continuous qualitative element data of a discontinuous and potentially reworked LPS is finally discussed against the background of a chronologically-limited comparison with the Eifel Laminated Sediment Archive (ELSA, Sirocko et al., 2013; Sirocko et al., 2016).

4.2. Study site

The Schwalbenberg II LPS (50°34'N, 7°14'E, 92 m a.s.l., Fig. 4-1) is located in the northern part of the Middle Rhine valley south of the town of Remagen on the Lower Middle Terrace of the river Rhine. To the south, the river Ahr incises the Rhenish Shield and flows into the river Rhine (Schirmer, 2012).

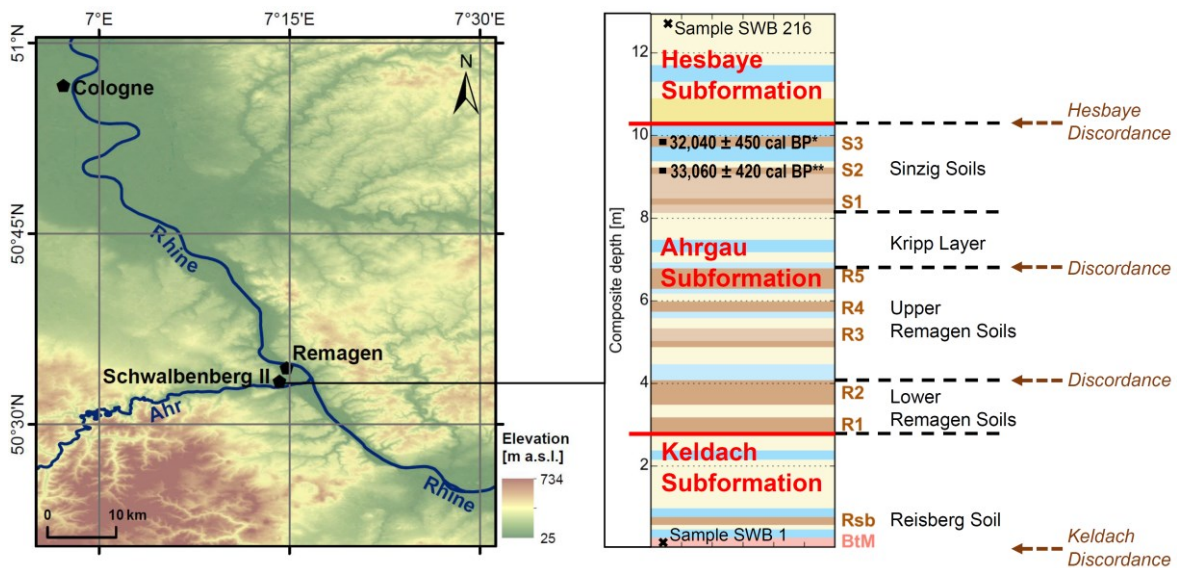


Fig. 4-1: Location, stratigraphy and chronological tie points of the Schwalbenberg II LPS. The Hesbaya Discordance also represents the transition from MIS 3 to MIS 2. *, **: ^{14}C ages (*KIA22209, **KIA22208) recalibrated with IntCal13 using OxCal v.4.2. Stratigraphy is modified after Schirmer (2012: 34). The numbering of the samples is in increasing order from bottom (SWB 1) to top (SWB 216) as documented in Schirmer (2012). Color scheme for stratigraphy: pale/strong yellow: loess/laminated, colluvial loess, dark/light brown: strong/weak cambisols, dark/light blue: grey/speckled gelic gleysols, pale red: BtM horizon - reworked material of a Bt horizon of a luvisol attributed to MIS 5 Schirmer (2012). Data sources of the map: OSM (2015) and SRTM data as provided by the US Geological Survey.

The Schwalbenberg II LPS comprises 13.05 m of loess with nine intercalated paleosols, subdivided into three stratigraphic subformations (Fig. 4-1). The stratigraphy presented by Schirmer (2012) is updated according to the German online encyclopedia on lithostratigraphy (Litholex, 2013) and Schirmer (2016). We are aware that – as usual – paleosols

or parts of paleosols might be parautochthonous, were subject to surface processes, bioturbation during and shortly after their formation as well as to diagenetic transformation and thus are considered as polygenetic formations (cf. Terhorst et al., 2015). The Keldach discordance cuts the luvisol on top of the Lower Middle Terrace at the base of the profile. The lowermost 2.8 m of solifluidal loess (Keldach Subformation) include reworked remains of a luvisol (BtM horizon at the bottom of the profile, Fig. 4-1) and one intercalated paleosol – the Reisberg Soil (Rsb, Fig. 4-1). The next 7.4 m (Ahrgau Subformation) encompass eight succeeding cambisols subdivided into the Lower Remagen Soils (R1 and R2), the Upper Remagen Soils (R3, R4 and R5), the Kripp Layer and the Sinzig Soils (S1, S2 and S3). The Lower Remagen Soils are in the outcrop separated from the Upper Remagen Soils by a discordance as well as the Upper Remagen Soils from the Kripp Layer (Fig. 4-1). The Kripp Layer itself describes a loess package of about 1 m thickness with two intercalated gelic gleysols. Above the Ahrgau Subformation, the uppermost 2.8 m of the Schwalbenberg II LPS consist of loess with a gelic gleysol and are considered as the lower part of the Hesbaya Subformation which is separated from the Ahrgau Subformation by the Hesbaya Discordance. The Hesbaya Discordance denotes a hiatus at the transition from MIS 3 to MIS 2. The lower Hesbaya Subformation is characterized by a laminated colluvial loess layer (Schirmer, 2012).

A robust and independent numerical chronology is the backbone for paleoenvironmental interpretations and correlations with various archives around the globe. At Schwalbenberg II, 44 luminescence (Frechen and Schirmer, 2011) and two radiocarbon samples (Schirmer, 2012) denote the chronological inventory. Infrared stimulated luminescence (IRSL) and thermoluminescence (TL) ages were determined on the same samples with analytical techniques of the 1990s (Frechen and Schirmer, 2011). The large 1σ error margins of up to ± 13 ka (Frechen and Schirmer, 2011) prevent a detailed chronology from being established. Re-evaluation of four samples with state-of-the-art single aliquot regenerative protocols yielded no further insights (Frechen and Schirmer, 2011) and thus confirmed both the old luminescence data and a recently elaborated quartz-luminescence chronology of a drill core (REM 1) 200 m northwest of Schwalbenberg II (Klasen et al., 2015). The luminescence ages point to a correlation of the Hesbaya Subformation with MIS 2 and of the Ahrgau Subformation with MIS 3. For the Keldach Subformation the results are ambiguous in terms of early MIS 3 or late MIS 4 when pushing error margins to their limits (Frechen and Schirmer, 2011). Furthermore, the luminescence ages contradict the litho-phenomenological chronology correlating paleosols with Greenland Interstadials (GIS) 17 to 5 – applying the GISP 2 chronology (Grootes and Stuiver, 1997) – on the basis of the number of soils, their vertical distances and their organic carbon contents (Frechen and Schirmer, 2011; Schirmer, 2012).

Gastropod shells from only two paleosols (S2 and S3) were analyzed for radiocarbon dating (Schirmer, 2012). Consequently, there is no robust age control for the litho-phenomenological chronology except for the two ^{14}C ages on gastropod shells from the soils S2 (KIA22208; at section scale: 8.95–9.25 m) and S3 (KIA22209; at section scale: 9.75–10.00 m) with error margins small enough to allow for an unambiguous correlation with the Greenland Ice Core Chronology (GICC05, Andersen et al., 2006; Svensson et al.,

2008; Svensson et al., 2006). Re-calibrating these ^{14}C ages using the IntCal13 calibration curve as implemented in OxCal v. 4.2 (Bronk Ramsey, 2009; Reimer et al., 2013) leads to a shift of up to 600 years towards younger ages for soil S3 from $32,650 \pm 380$ cal BP (Schirmer, 2012) to $32,040 \pm 450$ cal BP (Fig. 4-1) and for soil S2 from $33,350 \pm 430$ cal BP (Schirmer, 2012) to $33,060 \pm 420$ cal BP (Fig. 4-1). Applying the GICC05 chronology in the notation of Svensson et al. (2008: 50) and with consideration of the counting errors for the beginnings of the GIS, the S3 soil matches GIS 5 exclusively whereas the S2 soil either matches GIS 6 or GIS 5. This revises the correlations of S1 with GIS 8, S2 with GIS 7 and S3 with GIS 6 as suggested by Schirmer (2012), and indicates that the C_{org} peak appearing in the colluvial loess layer above the Hesbaya Discordance is likely related to reworked material from S3 as discussed in Schirmer (2012). Nonetheless, the re-calibrated ^{14}C -ages confirm the proposed correlations of one of the Sinzig Soils with the Lohne Soil in Nussloch (Kadereit et al., 2013; Kadereit and Wagner, 2014; Schirmer, 2012). The term Lohne Soil is commonly used to describe the uppermost of a sequence of cambisols attributed to the Ahrgau Subformation in Germany. Thus, it remains uncertain whether the Lohne Soil is always the same soil in different archives and whether it is comparable to the soil of the type locality at Lohne (Schirmer, 2010). In addition, ^{14}C ages from gastropod shells are possibly prone to reservoir effects if non-radiogenic carbon from carbonate rocks is incorporated into the gastropod shells (Goodfriend and Hood, 1983). This can lead to an age overestimation of up to 2 ka (Hatté et al., 2001), albeit the impact of such a reservoir effect for the Schwalbenberg II LPS has to remain open. Furthermore, reworking of older shell material is also possible due to the slope position of the Schwalbenberg II LPS.

4.3. Methods

4.3.1. Sampling

For this study, no field work was conducted. We use 216 archived samples from the outcrop Schwalbenberg II (Schirmer, 2012). These samples are stored at the Ruhr Museum, Essen (Germany) and were taken continuously by W. Schirmer in 1991 with lithology-dependent spatial resolutions (Schirmer, 2012) varying from 3 to 22 cm (mean: 6.0 cm, standard deviation: 3.3 cm).

4.3.2. XRF analyses

For XRF analyses, air-dried samples were homogenized by pestling. One cubic centimeter of these samples were filled into sample cups and compacted by hand. Subsequently, units of 30 sample cups were mounted on sample holders which allow easy measurement with the ITRAX XRF core-scanner (Cox Analytics) for elements from Al to U (Croudace et al., 2006). All samples are measured with a Mo- and a Cr-tube with a constant counting time of 100 s for each sample and tube-specific power settings of 30 kV, 30 mA for the Mo-tube and 30 kV, 40mA for the Cr-tube, to assure a constant count rate of approximately 30,000 counts per second (cps). The measured XRF spectra are translated into element counts by

mathematical peak fitting using the software Q-Spec (Croudace et al., 2006). In total, 12 elements (Al, Si, S, K, Ca, Ti, Fe, Br, Rb, Sr, Zr and Ba) that are indicative of organic matter, weathering and sediment provenance were selected for further investigation.

Data quality, in terms of statistical noise affecting XRF data precision, is investigated by tenfold measurements of a subset of 26 samples with both X-ray tubes. However, the samples were prepared again for quality control as well as for Cr-tube profile analysis due to interim removal. In addition, the Mo-tube was replaced between quality control and profile measurements. Accordingly, element ratios were calculated using raw element counts from the same tube with a precision-based tube selection. The acquired quality-control data was aggregated by calculating mean total counts as well as standard deviations of mean total counts for each sample and selected elements. To compare the precision of different elements exhibiting mean counts that differ by more than one order of magnitude, the standard deviation of mean total counts is also expressed as percent in relation to mean total counts. In addition, this procedure allows the evaluation of how normalization influences the precision of element counts derived from dried powdered homogenized samples by comparing the precision with and without applied normalization strategies. Normalization strategies, such as dividing element counts by coherent scattering counts when using a Mo-tube or by total counts per second when using a Cr-tube (Hahn et al., 2014; Ohlendorf et al., 2015), are commonly applied to minimize XRF signal influencing effects such as grain-size, porosity and water content (Croudace et al., 2006; Rothwell and Rack, 2006; Tjallingii et al., 2007). Zolitschka et al. (2014) assume that these effects are already minimized by using dried and powdered homogenized samples.

Another way to minimize the aforementioned effects is to use element ratios instead of raw counts of single elements for the interpretation of relative variations in the geochemical composition along a sediment profile. However, compositional data requires the expression as log ratios in order to avoid asymmetry against statistical analysis (Weltje et al., 2015; Weltje and Tjallingii, 2008). When using log ratios, it becomes non-relevant which element is the denominator or the numerator. Considering two arbitrary elements A and B, this relationship can be expressed as $\text{LOG}(A/B) = -\text{LOG}(B/A)$ whereas $A/B \neq B/A$. Although we are not aiming at quantifying XRF-scanning data, it has to be noted that the relationship between element raw counts and element concentrations is not always linear. However, linearity is met by relating element log-ratios of raw counts to element log-ratios of concentrations (Weltje and Tjallingii, 2008). Accordingly, the interpretation of element log ratios instead of element ratios appears more appropriate when comparing our data to element weathering indices based on element concentrations. Therefore, in this study XRF data is either presented as raw counts or as log ratios of raw counts.

4.3.3. Organic carbon

The organic carbon data presented in this study is taken from Schirmer (2012). Pulverized samples were combusted at 480 °C in a Dimatec laboratory furnace. In total, 459 analyses were performed for 216 samples (Schirmer, 2012).

4.3.4. Magnetic susceptibility

Magnetic susceptibility (MS) identifies the sum effect of magnetic minerals in a sample by applying a magnetic field. Iron oxides (and sulfides) are the most important ferromagnetic minerals in LPS contributing to MS (Baumgart et al., 2013 and references therein). Basically, higher MS values are either attributed to neoformation, to enrichment of ferromagnetic minerals during pedogenesis (e.g. Maher et al., 1994) or to enrichment of ferromagnetic minerals in unweathered loess due to high wind speeds (Begét et al., 1990). By measuring both low-field and high-field MS, the relative contribution of superparamagnetic minerals can be estimated as the frequency-dependent MS. Superparamagnetic minerals contribute more to MS under low-field frequencies because superparamagnetic minerals are stable under high-field frequencies (Heller et al., 1991; Maher, 2011), whereas coarser grained single- and multi-domain magnetic particles show no significant frequency-dependent changes (Baumgart et al., 2013). MS was determined for all 216 homogenized samples with a Bartington MS2B sensor for low-field (χ_{lf} , 0.465 kHz) and high-field (χ_{hf} , 4.65 kHz) MS at the 0.1 scale since the unpublished MS data of Cofflet (2005) is not available. First, all samples were analyzed at 0.465 kHz and subsequently at 4.65 kHz. The applied measurement strategy includes triple MS determination of each sample with MS determination of air before and after each single sample measurement. One sample container was measured threefold for MS but once for each frequency prior to sample measurement. Afterwards, each individual measurement is corrected for sensor drifting by subtracting half of the sum of the air measurements prior and after each sample measurement (Dearing, 1994), and for the sample container MS by subtracting this value as well (Bartington, 2016). MS is expressed as mass-normalized MS (χ) by multiplying the measured value by the quotient of calibration mass (10 g) and sample mass (Bartington, 2016) to provide comparability to other studies (e.g. Baumgart et al., 2013; Gocke et al., 2014). Frequency-dependent MS (χ_{fd}) is given in per cent and calculated as $100 * (\chi_{lf} - \chi_{hf}) / \chi_{lf}$ according to Dearing et al. (1996) and Maher (2011). Triple measurements allow calculation of means and standard deviations as estimates of data precision. Sample mass was weighed with an analytical scale. Tare weight of sample containers was analyzed for each sample container individually.

4.3.5. Grain-size

The grain-size data used in this study is taken from Schirmer (2012). He performed a conventional grain-size analysis by sieving and gravitational sedimentation of the fraction smaller than 2 mm resulting in seven grain-size fractions for each of the 216 samples (Schirmer, 2012). To investigate grain-size as a factor that influences the elemental composition, selected grain-size fractions are aggregated into the grain-size index “U-ratio” calculated as coarse silt (63-20 μm) divided by fine silt (6.3-2 μm) plus clay (< 2 μm) – in modification of Antoine et al. (2009). This U-ratio is well suited for correlation with elemental ratios since Zr and Si are enriched in coarse silt whereas Rb and Al are enriched in fine silt and clay (Chen et al., 2006; Liang et al., 2013).

4.3.6. Trend analysis

Boxplots allow simple data screening by visualizing the distribution of a dataset (Reese, 2005). Modifying the boxplot by normalizing and subsequent clustering of the data set results in normalized boxplots. First, the data of each parameter is normalized to values between 0 and 1 (eq. 6) to enable a comparison between data given in different dimensions, with x being the data value of the respective parameter to be normalized, x_{min} being the minimum data value of the respective parameter in the data set, x_{max} being the maximum data value of the respective parameter in the data set and x_{norm} being the normalized data value (Sorace and Zhan, 2003). Second, the data of each parameter (n: 216) is labeled according to stratigraphy in Schirmer (2012) (BtM horizon, n: 4; cambisol, n: 79; gelic gleysol, n: 51; and loess, n: 82). This results in four normalized boxplots per parameter, one for each group allowing the identification of trends within different lithologies. Boxes show data within the lower and the upper quartile with the median plotted as black line. Whiskers represent values above or below the lower and upper quartile of up to $0.5 * \text{inner quartile range}$ which is defined as upper quartile minus lower quartile (Reese, 2005).

$$x_{norm} = \frac{(x - x_{min})}{(x_{max} - x_{min})} \quad (6)$$

4.3.7. Correlation analysis

Testing the strength of relationships between random variables requires a correlation analysis (Zou et al., 2003). Due to skewed data, transferring element ratios into log space and comparing log-transformed and non-log-transformed variables, using the linear Pearson correlation coefficient (r) is inappropriate. Instead, we use the Spearman rank correlation coefficient (ρ , Spearman, 1904). According to the calculation of ranks prior to correlation, the correlation coefficient is insensitive to skewed data and to the form of relationship, i.e. linear or logarithmic (Zou et al., 2003). Because the Spearman ρ is uncommon in loess research, we present both correlation coefficients.

4.4. Results and discussion

4.4.1. XRF data quality

Element data acquired with the Mo-tube shows a mean precision of $\leq 2.2\%$ for Si, K, Ca, Ti, Fe, Rb, Sr and Zr exhibiting mean total counts well above 5000 (Fig. 4-2, supplementary material) for a measurement time of 100 s per sample. Similar results are obtained for the Cr-tube indicating a mean precision of 1.0% for K, Ca, Ti and Fe and decreasing mean precisions to 3.8% for Si, Zr, Sr and Rb (Fig. 4-2, supplementary material). Al and Ba exhibit a lower mean precision of 11.8% when measured with the Mo-tube (Fig. 4-2, supplementary material) compared to 2.5% (Al, Fig. 4-2) and 8.7% (Ba) when measured with the Cr-tube (supplementary material). Br shows similar low mean precisions for both

tubes (Br: > 100 %, Fig. 4-2) requiring a cautious interpretation. The commonly applied normalization strategies show either slight positive or no effects for the Mo-tube and slight negative effects for the Cr-tube. Therefore, we (1) confirm the assumption of Zolitschka et al. (2014) that most XRF signal influencing effects are already minimized by the usage of dried powdered and homogenized samples and (2) apply no normalization strategies to raw element counts in this study. Furthermore, counts determined by the Cr-tube are taken for element ratios including Al and Ba due to their higher precision.

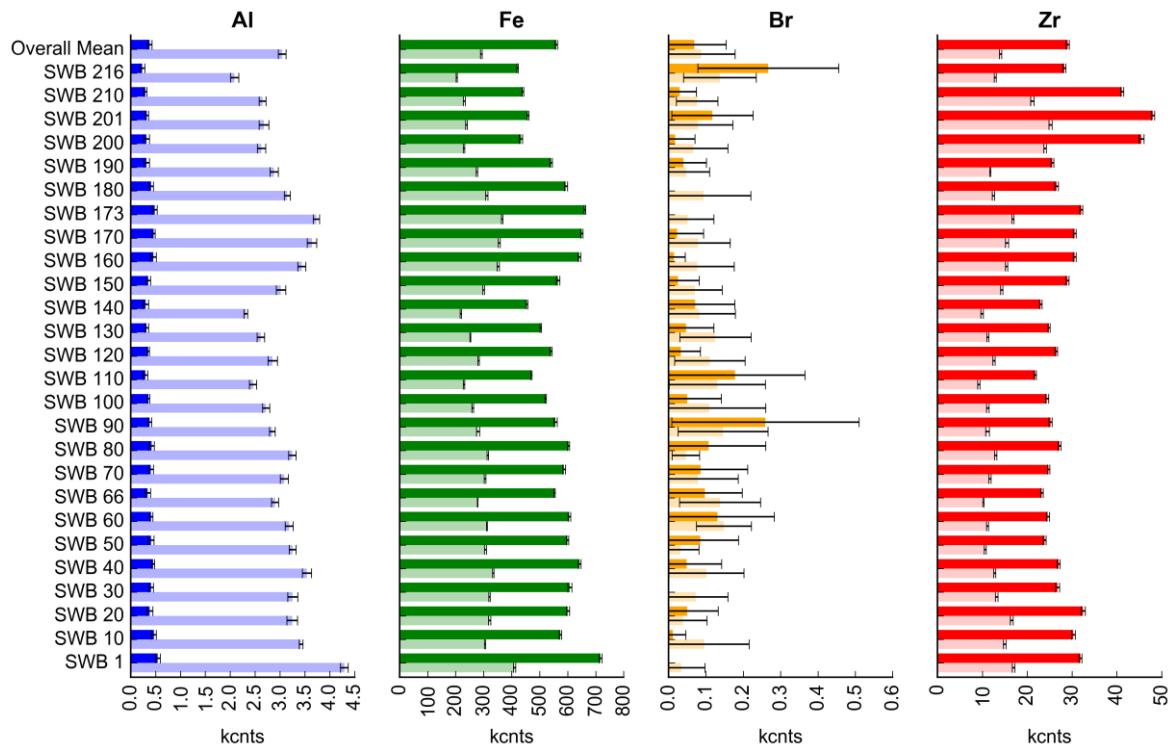


Fig. 4-2: Precision of Mo-tube (dark color) and Cr-tube (light color) determined Al, Fe, Br and Zr XRF element counts derived from tenfold measurement of every tenth sample (a subset of 26 samples). Additionally, the samples SWB 66 and SWB 216 are taken due to high Br values in the Mo-tube profile measurement; sample SWB 173 is due to a high Ba-value and SWB 201 is due to the highest Zr value in the Mo-tube profile. Error bars indicate $\pm 1\sigma$.

4.4.2. Rock magnetic properties

Compared to the MS values shown by Cofflet (2005), re-analyzed χ_{if} values presented in this study are one order of magnitude higher and range between 12 and $20.5 \times 10^{-8} \text{ m}^3 \text{ kg}^{-1}$ (Fig. 4-3) with a mean data precision of $\pm 0.1 \times 10^{-8} \text{ m}^3 \text{ kg}^{-1}$. This is similar to Nussloch (Gocke et al., 2014; Taylor et al., 2014) while considered Saxonian and Czech LPS show higher χ_{if} values up to $80 \times 10^{-8} \text{ m}^3 \text{ kg}^{-1}$, especially in paleosols (Baumgart et al., 2013; Fuchs et al., 2013; Hošek et al., 2015). Schwalbenberg II exhibits a bipartite structured MS record with a decreasing trend from 0 m to the overall minimum of $12.38 \times 10^{-8} \text{ m}^3 \text{ kg}^{-1}$ in the gelic gleysol at 7.38 m and rather constant values of approximately $14 \times 10^{-8} \text{ m}^3 \text{ kg}^{-1}$ between 7.38 m and 12.5 m. The uppermost part is in turn characterized by an increase to $17.41 \times 10^{-8} \text{ m}^3 \text{ kg}^{-1}$ in unweathered loess. We consider the highest χ_{if} value ($20.93 \times 10^{-8} \text{ m}^3 \text{ kg}^{-1}$, sample no. 96 at 5.45 m) located in a loess layer as an outlier because it is only one data point surrounded by data points showing much lower values of $14 \times 10^{-8} \text{ m}^3 \text{ kg}^{-1}$. In addition to the basic trend, local maxima with decreasing

intensity are identified in the Reisberg soil (Rsb), the BtM horizon and in the soils R1, R2, R3, R4, S1 and S2 (Fig. 4-3). This is comparable with Cofflet (2005) who argues that R1 and R2 reflect the most intensive pedogenesis according to the highest MS values found along the profile. However, Hošek et al. (2015) discuss leaching and erosion as MS depleting factors so that the observed MS signal also depends on the preserved paleosol horizon. In general, top soils show highest MS signals (Hošek et al., 2015). Therefore, R2 is confirmed as a top soil (Ah horizon, Schirmer, 2012) but not necessarily as the most intense paleosol of the profile. The upwards decreasing trend in χ_{if} including the described intercalated local maxima is also partly present in the Fe profile from 2.1 to 7.4 m (Fig. 4-3). Albeit, the paleosols S1 and S2 (8.1-10.20 m) are characterized by the highest Fe counts whereas the lowest Fe counts are present in the uppermost, loess dominated section (10.2-13.05 m, Fig. 4-3). The distinct maximum in Fe opposite to only subtle local maxima of χ_{if} in the soils S1 and S2 point to magnetic depletion, although χ_{fd} has to be taken into account to identify the likeliest driving forces.

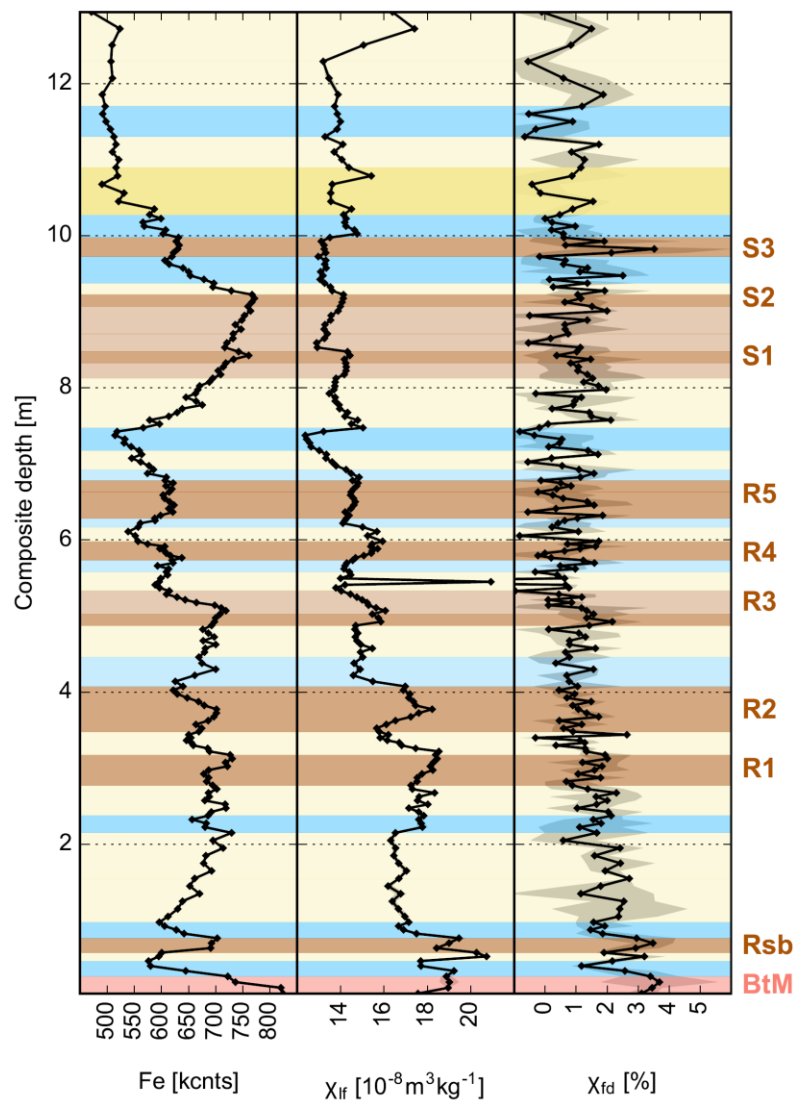


Fig. 4-3: Rock magnetic parameters. Profiles of iron (Fe), low-field mass-normalized magnetic susceptibility (χ_{if}) and frequency-dependent magnetic susceptibility (χ_{fd}) of the Schwalbenberg II loess–paleosol sequence. Grey shaded areas indicate $\pm 1\sigma$. Color scheme: pale/strong yellow: loess/laminated, colluvial loess, dark/light brown: strong/weak cambisols, dark/light blue: grey/speckled gelic gleysols, pale red: BtM-horizon - reworked material of a Bt-horizon of a luvisol attributed to MIS 5 (Schirmer, 2012).

χ_{hf} measurements necessary for χ_{fd} calculations show a data precision of $\pm 0.1 \times 10^{-8} \text{ m}^3 \text{ kg}^{-1}$. Limitations in data reproducibility of the Bartington MS2B sensor combined with low-field intensities < 20 contribute to χ_{fd} errors of $\pm 2 \%$ (Dearing et al., 1996). Our data precision is $\pm 0.89 \%$ with a mean χ_{fd} value of 1.03% . Negative χ_{fd} values caused by large error margins and by general low χ_{fd} values are considered as outliers but not removed from the data set. Especially sample 96 having the highest χ_{hf} value exhibits the lowest χ_{fd} value with -7.99% . Despite the large error margins, χ_{fd} also documents a bipartite structure with decreasing values from 0 m up to 4.5 m (the lower boundary of the R3 soil) and relatively constant values with fluctuations from 4.5 m towards the top (Fig. 4-3). Mostly, χ_{fd} is $< 2 \%$ and only a few samples (two from cambisols and three from the BtM-horizon) are $> 3 \%$ (Figs. 4-3 and 4-4) with maxima occurring in the BtM horizon and in the soils Rsb and S3. Therefore, frequency-independent magnetic grains seem to dominate the Schwalbenberg II LPS (Dearing et al., 1996). In spite of these low values, the scatterplot of χ_{hf} vs χ_{fd} from the Schwalbenberg II LPS (Fig. 4-4) is comparable to scatterplots from Ostrau, Gleina and Nussloch (Baumgart et al., 2013; Gocke et al., 2014), albeit Nussloch exhibits χ_{fd} values between 2% and 4% (Gocke et al., 2014) and the increase of χ_{fd} for low χ_{hf} at Schwalbenberg II is rather subtle.

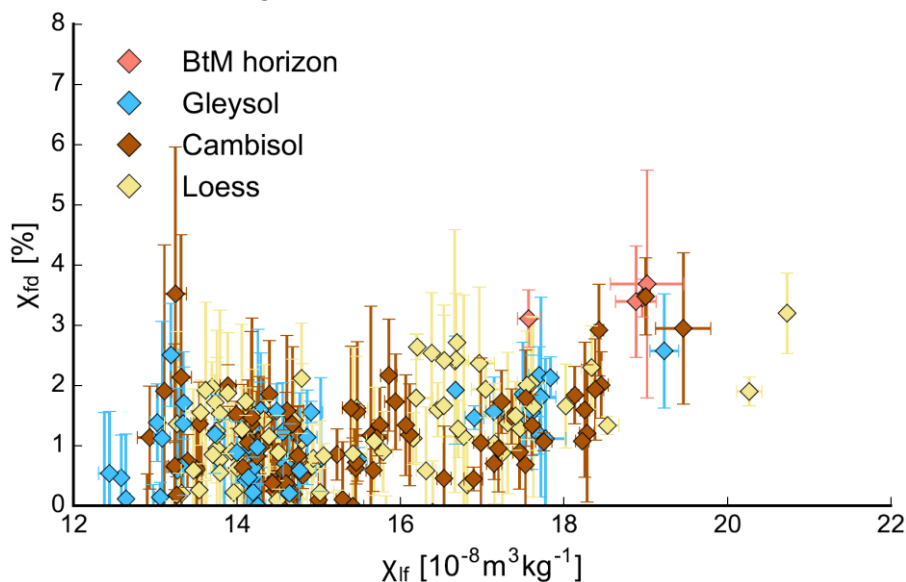


Fig. 4-4: Scatterplot χ_{hf} vs χ_{fd} .

Considering aggregated values of Fe, χ_{hf} and χ_{fd} (Fig. 4-5), it is obvious that the BtM horizon incorporates sediments of a soil that follows the pedogenic enhancement model (e.g. Maher et al., 1994) while the cambisols show no clear trend (Fig. 4-5). In contrast, gelic gleysols exhibit the lowest aggregated Fe values (Fig. 4-5) indicating anoxic conditions resulting from waterlogging and enabling the formation of water soluble Fe^{2+} . The dissolution of iron also leads to the dissolution of preferably small magnetic particles (Taylor et al., 2014). This causes an increase in magnetically weaker multi-domain magnetic particles and thus a drop in χ_{hf} (Taylor et al., 2014) as documented by low χ_{hf} values for the Schwalbenberg II LPS. Since χ_{fd} values remain at the same level as unweathered loess and cambisols and are predominantly too low to demonstrate the occurrence of superparamagnetic particles, the normalized boxplot (Fig. 4-5) confirms the theory-driven hypothesis according to Dearing et

al. (1996) that frequency-independent single- and multi-domain magnetic particles dominate the Schwalbenberg II LPS.

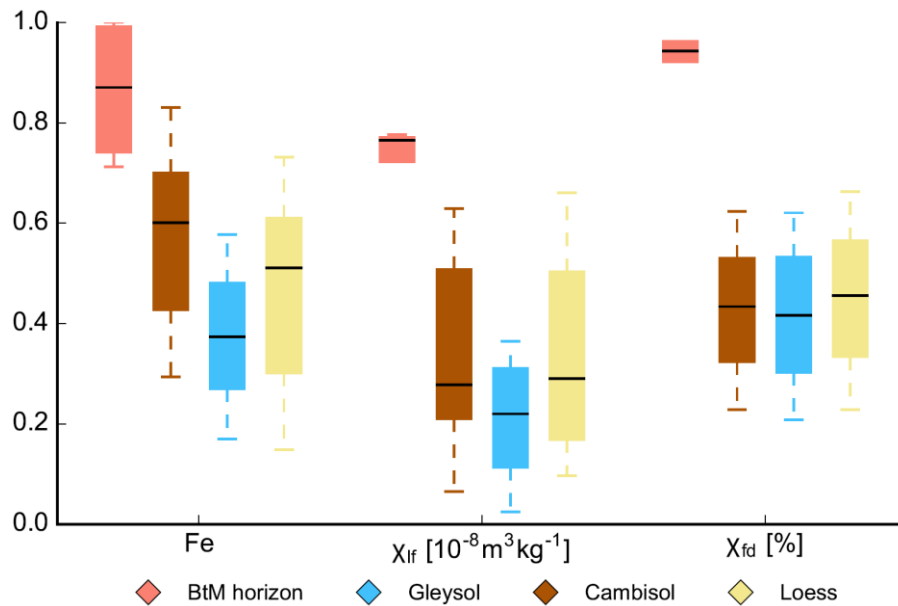


Fig. 4-5: Normalized boxplot of rock magnetic parameters Fe, χ_{f} and χ_{fd} .

However, the χ_{fd} maximum in S3 coinciding with a minimum in χ_{f} with increasing χ_{f} values in the overlying loess (Fig. 4-3) similar to the Lohne Soil at Nussloch (Gocke et al., 2014) may also indicate contrary to Taylor et al. (2014) depletion and destruction of primary magnetic particles relative to superparamagnetic particles as well as a decrease in grain-size of magnetic particles (Baumgart et al., 2013; Gocke et al., 2014). Seasonal waterlogging accompanying gleyification and dynamic reworking processes in combination with oxidation of magnetite at low temperatures are identified as dominant causes (Baumgart et al., 2013; Gocke et al., 2014). Therefore, these MS records (high χ_{fd} and low χ_{f}) point to more humid and cold permafrost-dominated periglacial climatic conditions (Baumgart et al., 2013). However, high Fe counts and subtle χ_{f} maxima in the Sinzig Soils S1 and S2 exclude waterlogging as a dominant cause for magnetic depletion so that leaching and erosion of the topsoil (Hošek et al., 2015) are considered as the most likely processes. Consequently, S1 and S2 seem – concerning rock magnetism – to be the most intense paleosols in contrast to R1 and R2 as suggested by Cofflet (2005).

4.4.3. Br counts as proxy for organic carbon

Br counts have been used as a proxy for C_{org} in marine (Ziegler et al., 2008), lacustrine (Biskaborn et al., 2013; Kalugin et al., 2007) and eolian–lacustrine sediments (Zolitschka et al., 2014). Applying this proxy to the Schwalbenberg II LPS shows that even though the highest Br counts coincide with paleosols (Fig. 4-6), the low precision of Br data (Fig. 4-2) prevents them from being identified as real signals. Their low precisions are also highlighted by $\rho = 0.16$ for the correlation of Mo-tube and Cr-tube determined Br counts (Table 4-1). Consequently, Br counts do not correlate with C_{org} (Table 4-1, $\rho \leq 0.31$). Two factors may

explain this finding: (1) the Br content is likely close to or below the detection limit of the XRF scanner (4/9 ppm for 100 s measurement time with Mo-/Cr-tubes, Rindby (2007)) as indicated by low precision and reported Br concentrations in soils typically ranging from 5 to 40 ppm (Leri and Myneni, 2012). In addition, a sound analysis requires a higher precision, i.e. a concentration ten times the detection limit (Rindby, 2007). (2) Dissolution of Br during translocation through the soil profile as a consequence of organic matter decay and higher pH values in subsoils compared to acidic and organic-rich topsoils favoring Br fixation (Yamada, 1968; Yuita et al., 1991).

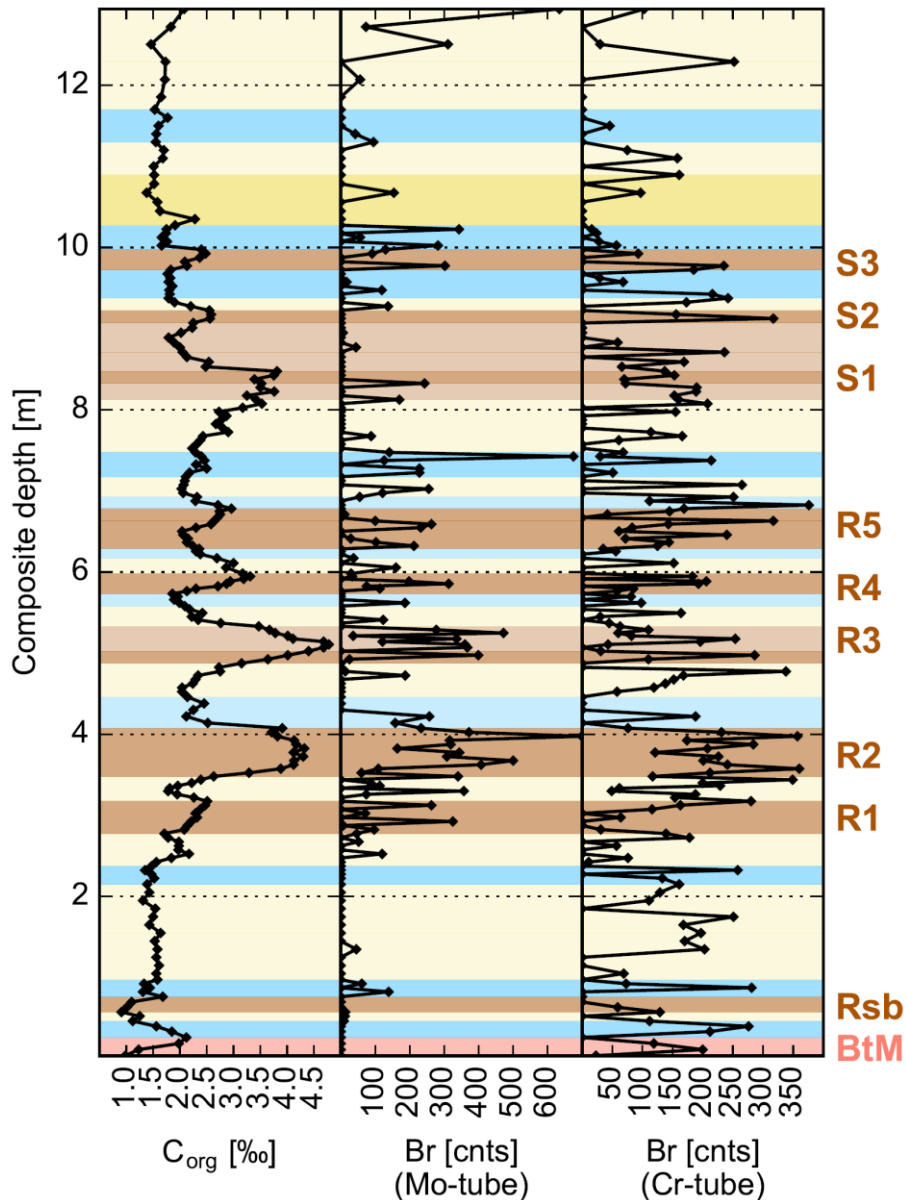


Fig. 4-6: Organic carbon (C_{org}) compared to Br counts derived from XRF analyses with Mo and Cr-tubes. Color scheme: pale/strong yellow: loess/laminated, colluvial loess, dark/light brown: strong/weak cambisols, dark/light blue: grey/speckled gelic gleysols, pale red: BtM-horizon – reworked material of a Bt-horizon of a luvisol attributed to MIS 5 (Schirmer, 2012). C_{org} data is from Schirmer (2012).

Table 4-1: Correlation matrix showing the Spearman rank correlation coefficient (ρ , numbers without brackets) and the Pearson correlation coefficient (r , numbers in brackets) of proxies characterizing the Schwalbenberg II LPS ($n = 216$).

	Fe	X _{if}	X _{id}	C _{org} [‰]	Br (Mo)	Br (Cr)	Ca (Mo)	Sr (Mo)	LOG (Ca/Sr)	LOG (Rb/Sr)	LOG (Ba/Sr)	LOG (Rb/K)	LOG (Ti/Zr)	LOG (Ti/Al)	LOG (Si/Al)	LOG (Zr/Rb)	U-ratio							
Fe	1	0.28 (0.30)	0.34 (0.32)	0.20 (0.22)	-0.11 (-0.10)	0.18 (0.17)	-0.80 (-0.76)	-0.64 (-0.63)	-0.75 (-0.64)	0.80 (0.76)	0.31 (0.29)	0.57 (0.54)	0.47 (0.61)	0.08 (-0.12)	-0.86 (-0.88)	-0.51 (-0.63)	-0.56 (-0.59)							
X _{if}		1	0.43 (0.31)	-0.10 (-0.09)	0.13 (0.08)	0.18 (0.13)	-0.11 (-0.15)	0.04 (0.07)	-0.36 (-0.33)	0.10 (0.05)	-0.34 (-0.31)	0.16 (0.19)	0.43 (0.33)	-0.10 (-0.09)	-0.37 (-0.38)	-0.49 (-0.40)	-0.48 (-0.40)							
X _{id}			1	-0.24 (-0.16)	-0.20 (-0.14)	0.00 (0.03)	-0.35 (-0.34)	-0.27 (-0.22)	-0.40 (-0.37)	0.33 (0.27)	0.06 (0.07)	0.24 (0.26)	0.15 (0.14)	0.14 (0.12)	-0.31 (-0.27)	-0.19 (-0.15)	-0.22 (-0.19)							
C _{org} [‰]				1	0.31 (0.42)	0.21 (0.26)	0.08 (0.01)	0.04 (-0.07)	0.20 (0.16)	0.01 (0.09)	-0.20 (-0.12)	0.06 (0.14)	0.32 (0.34)	-0.37 (-0.34)	-0.25 (-0.30)	-0.31 (-0.36)	-0.52 (-0.52)							
Br (Mo)					1	0.16 (0.18)	0.29 (0.25)	0.27 (0.18)	0.23 (0.21)	-0.24 (-0.18)	-0.30 (-0.23)	-0.11 (-0.07)	0.22 (0.14)	-0.20 (-0.19)	-0.04 (-0.05)	-0.25 (-0.19)	-0.15 (-0.17)							
Br (Cr)						1	-0.06 (-0.07)	-0.02 (-0.04)	-0.09 (-0.05)	0.09 (0.07)	-0.18 (-0.15)	0.12 (0.12)	0.20 (0.20)	-0.08 (-0.12)	-0.21 (-0.23)	-0.25 (-0.24)	-0.20 (-0.19)							
Ca (Mo)							1	0.91 (0.91)	0.83 (0.73)	-0.97 (-0.95)	-0.65 (-0.69)	-0.79 (-0.81)	-0.09 (-0.03)	-0.45 (-0.38)	0.58 (0.49)	0.12 (0.05)	0.25 (0.19)							
Sr (Mo)								1	0.55 (0.50)	-0.95 (-0.97)	-0.78 (-0.83)	-0.67 (-0.67)	0.13 (0.13)	-0.50 (-0.41)	0.37 (0.32)	-0.11 (-0.11)	0.12 (0.10)							
LOG									1	-0.71 (-0.63)	-0.33 (-0.32)	-0.72 (-0.66)	-0.33 (-0.16)	-0.30 (-0.13)	0.66 (0.47)	0.36 (0.22)	0.33 (0.22)							
(Ca/Sr)										1	0.67 (0.76)	0.78 (0.75)	0.08 (0.02)	0.44 (0.33)	-0.58 (-0.48)	-0.13 (-0.07)	-0.28 (-0.21)							
LOG											1	0.46 (0.48)	0.50 (0.49)	-0.04 (0.02)	0.37 (0.41)	0.20 (0.20)	0.20 (0.20)							
(Rb/Sr)												1	0.48 (0.48)	0.40 (-0.34)	-0.26 (-0.05)	-0.25 (-0.12)	-0.25 (-0.12)							
LOG													1	-0.32 (-0.32)	-0.65 (-0.83)	-0.56 (-0.66)	-0.56 (-0.66)							
(Rb/K)														1	-0.79 (-0.79)	-0.83 (-0.95)	-0.56 (-0.66)							
LOG															1	0.21 (0.21)	0.26 (0.26)							
(Ti/Zr)																1	0.26 (0.43)							
LOG																	1	0.67 (0.67)						
(Ti/Al)																		1	0.67 (0.67)					
LOG																			1	0.67 (0.67)				
(Si/Al)																				1	0.67 (0.67)			
LOG																					1	0.67 (0.67)		
(Zr/Rb)																						1	0.67 (0.67)	
U-ratio																							1	0.67 (0.67)

4.4.4. Inorganic geochemical parameters

Inorganic geochemical parameters in terms of element log ratios derived from XRF core-scanning are valuable tools to investigate paleosol genesis and changes in mineralogy which are associated with weathering intensity and dust provenance. Ca/Sr, Rb/Sr, Ba/Sr and Rb/K are linked to weathering (Buggle et al., 2011; Hošek et al., 2015), while Ti/Zr, Ti/Al, Si/Al are related to dust provenance (Klasen et al., 2015; Zech et al., 2008), although Si/Al is also influenced by grain-size variations (Liang et al., 2013). Due to different precisions of element counts acquired by different X-ray tubes (Mo vs. Cr tube), the ratios Ca/Sr, Rb/Sr and Rb/K are calculated from Mo-tube determined element counts whereas Ba/Sr, Ti/Zr, Ti/Al and Si/Al are estimated from Cr-tube derived element counts. Despite a higher Zr precision for the Mo-tube (0.6 % difference), the ratio Ti/Zr is based on Cr-tube determined counts because Ti and Zr counts are considered together with Al counts in a ternary plot. Although a reliable chronology only exists for the Sinzig Soils S2 and S3, the geochemical record of the whole profile is discussed.

4.4.4.1. Weathering indices

The underlying principle of weathering indices is to divide a relatively mobile element which is depleted during weathering (e.g. Ca, Sr, K) by a more immobile element (e.g. Rb, Ba) which remains either constant or becomes relatively enriched during weathering (Buggle et al., 2011).

4.4.4.1.1. Ca/Sr

Decalcification as an initial stage of weathering (Hošek et al., 2015) can be studied by Ca/Sr as both elements are leached while Sr is more adsorptive to clay minerals than Ca (Bokhorst et al., 2009). Thus, the ratio decreases with increasing weathering intensity (Bokhorst et al., 2009). However, in the case of secondary calcification dominated by Ca (Buggle et al., 2011), Sr and Ca neutralize each other resulting in a constant index and a high positive correlation (here: $\rho = 0.91$, cf. Table 4-1). In fact, the Ca/Sr ratio shows a constant trend with a negative excursion in the BtM horizon and subtle decreases in the soils Rsb, R1, R2, S1 and S2 (Fig. 4-7) indicating rather the intensity of secondary calcification than weathering intensity. This is consistent with micropedological analyses documenting extensive decalcification and subsequent secondary calcification in most paleosols (Schirmer et al., 2012). In addition, Ca and Sr exhibit the second lowest values along the profile in S1 and S2 soils supported by the second highest values in the Sr-type weathering indices Rb/Sr and Ba/Sr. This points to Ca and Sr leaching with reduced subsequent secondary calcification of S1 and S2. Presumably, permafrost dynamics as indicated by the two comparatively thick gelic gleysols enclosing S3 together with a trend towards drier climatic conditions during the overlying Hesbaye Subformation, prevented strong secondary calcification of S1 and S2.

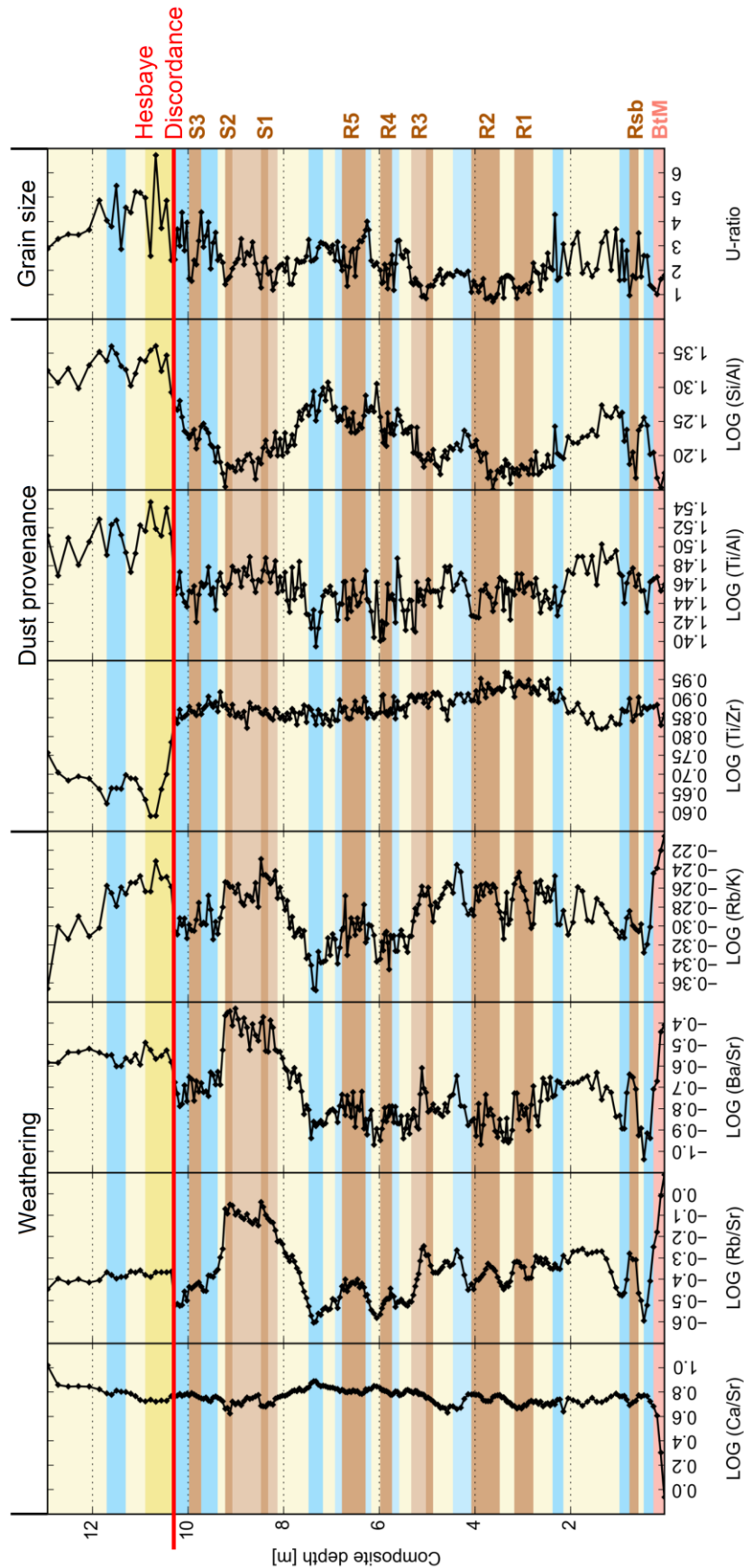


Fig. 4-7: Weathering, provenance and grain-size indices at Schwalbenberg II LPS as derived from XRF and grain-size data. Color scheme: pale/strong yellow: loess/laminated, colluvial loess, dark/light brown: strong/weak cambisols, dark/light blue: grey/speckled gelic gleysols, pale red: BtM horizon – reworked material of a Bt-horizon of a luvisol attributed to MIS 5 (Schirmer, 2012). Grain-size data used to calculate the U-ratio, i.e. coarse silt divided by fine silt plus clay, is from Schirmer (2012).

4.4.4.1.2. Rb/Sr, Ba/Sr, Rb/K

Weathering processes can be subdivided into “the early Ca, Sr removal stage, the intermediate K removal stage and at last the Si removal stage” (Hošek et al., 2015: 350). “Sr-type” weathering indices track the early stage of weathering but Ca and Sr dynamics distort them as shown for the Ca/Sr ratio (Buggle et al., 2011). Sr is a mobile element whereas Rb and Ba are more immobile due to their stronger adsorption to clay minerals (Buggle et al., 2011). Relative enrichment of Rb and Ba in paleosols results from weathering of K-bearing minerals and the loss of more mobile elements (Bokhorst et al., 2009; Hošek et al., 2015; Zech et al., 2008). Furthermore, sediment recycling and sorting effects can modify weathering indices by additionally increasing the amount of weathering resistant elements (Mongelli et al., 2006).

Rb/Sr and Ba/Sr records identify the BtM horizon (Fig. 4-1) together with S1 and S2 as the most intensively weathered paleosols followed by the soils R3, Rsb, R2, R1 and R5 (Fig. 4-7). This is partly consistent with previous publications addressing R2 as the thickest and R3 as the most intense paleosol among the Remagen Soils and S1 as the most intense among the Sinzig Soils (Schirmer, 2000a, b), whereas Cofflet (2005) identifies R1 and R2 as the most intense paleosols based on MS (Fig. 4-3). Schirmer (2012) identifies R3 as the most intense paleosol based on the global C_{org} maximum (Fig. 4-6) and Schirmer et al. (2012) based on an dissolved iron index. Finally, A. Iking in Schirmer et al. (2012) suggests R5 as the most intense paleosol based on micropedology. However, the differences between Rb/Sr, Ba/Sr and already published results derived from other proxies also indicate that secondary calcification, evidenced by micropedological investigations for all paleosols (Schirmer et al., 2012), mask the Sr signal resulting in misleadingly low Rb/Sr and Ba/Sr ratios (Buggle et al., 2011). Comparing Ba/Sr and Rb/Sr to Ca/Sr, the positive excursions of Rb/Sr and Ba/Sr at S1, S2, R3, R2, R1, Rsb and R5 accompany subtle negative excursions in Ca/Sr at S2, S1, Rsb, R2 and R1 (Fig. 4-7), both in decreasing order. With the knowledge that except for the BtM horizon the lowest counts of Ca and Sr occur at S1 and S2, Rb/Sr and Ba/Sr indicate reduced secondary calcification and enhanced weathering for S1 and S2.

The Rb/K ratio represents the intermediate stage of weathering as termed by Hošek et al. (2015) and defined by Nesbitt et al. (1980). It shows positive excursions for the BtM horizon, for the Sinzig Soils S1 and S2 and the Lower Remagen Soils (R1, R2 and R3) as well as in the basal part of the Hesbaye Subformation (Fig. 4-7). The latter might either be explained by reworked weathered material or by source and transport related changes in mineralogy (Muhs et al., 2003; Zech et al., 2008). In contrast, the Upper Remagen soils (R4 and R5) do not show distinct positive excursions (Fig. 4-7). Comparing the basic trends in the Rb/K ratio with the “Sr-type” indices, the former indicates stronger weathering of cambisols and of the reworked soil material (BtM horizon) than the latter (Fig. 4-8). This implies that, except for the Sinzig Soils (S1 and S2) the “Sr-type” indices are erroneously reduced by secondary calcification, and S1 and S2 as well as the Lower Remagen Soils (R1, R2 and R3) together with the BtM horizon are affected by the intermediate stage of weathering. This corroborates the MS based identification of soils S1 and S2 as the most intense paleosols at

Schwalbenberg II and points geochemically to in-situ soil formations, albeit R4 and S3 show very weak positive peaks only.

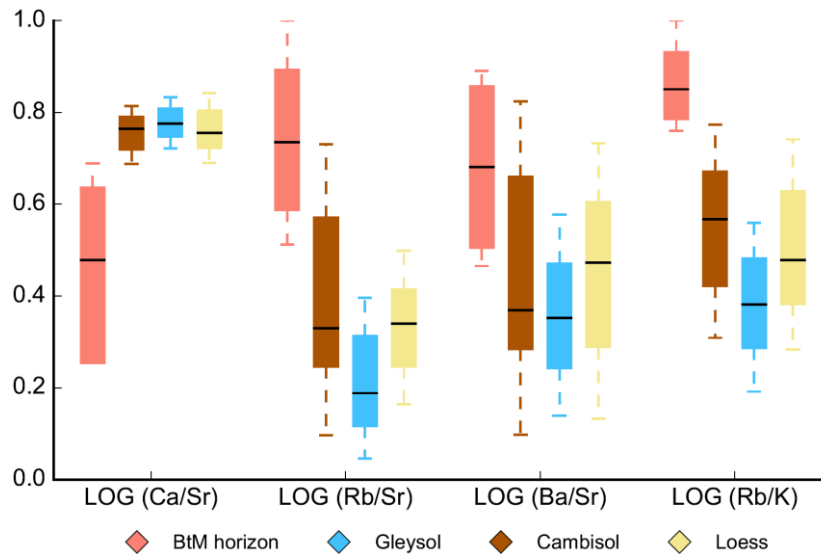


Fig. 4-8: Normalized boxplot highlighting the dynamics of weathering indices shown in Fig. 4-7 for the Schwalbenberg II LPS.

4.4.4.2. Provenance indices

4.4.4.2.1. Ti/Zr, Ti/Al

The elements Ti and Zr occur in weathering resistant minerals while Al is found in weathering residuals. Therefore, they are best suited to examine changes in sedimentation processes, such as dust source changes or the incorporation of reworked material which is accompanied by sediment recycling and sorting (Garcia et al., 1991; Mongelli et al., 2006; Muhs et al., 2003; Zech et al., 2008). Accordingly, these elements disqualify as an immobile part for weathering indices (Bugge et al., 2011).

One dominant transition to lower Ti/Zr and higher Ti/Al values is found at the Hesbaye Discordance separating two sections of fairly constant values (Fig. 4-7). Also the core REM 1 shows a similar but more gradual transition towards lower Ti/Zr values (Klasen et al., 2015). This suggests erosion of ca. 1.6 m (5.4 m–3.8 m at REM 1) at the Schwalbenberg II LPS which is represented by the Hesbaye Discordance. Furthermore, the Eltville Tephra present in REM 1 and characterized by a positive Ti/Zr excursion (Klasen et al., 2015) is not present in the Schwalbenberg II LPS.

The abrupt shifts in the Ti/Zr and Ti/Al profiles indicate changing sedimentation dynamics such as different wind directions and thus different dust sources or sediment recycling due to local, proximal or distal reworking processes active during the Hesbaye Subformation (MIS 2, Klasen et al., 2015). Especially reworking processes comprising (1) production of sediment transported into rivers by large-scale soil erosion, (2) fluvial transport and overprinting of sediments produced by process (1) in rivers and (3) deflation of sediments reworked by processes (1) and (2) have the potential to alter the mineralogical composition of re-deposited eolian sediments substantially (Fig. 4-9). It seems likely that such processes

were active at pronounced climatic transitions such as at the MIS 3/MIS 2 transition. This transition is detected at different European sites and always associated with erosion (Gocke et al., 2014; Kadereit and Wagner, 2014; Terhorst et al., 2015). Therefore, Klasen et al. (2015) assume that the shift in the Ti/Zr ratio documents the MIS 3/MIS 2 transition which is confirmed by this study. Since the MIS 2 climate is reported to be cold, arid and extremely windy (Antoine et al., 2009), the eroded material transported by rivers is deflated as soon as the runoff is sufficiently reduced. Dependent on the dominant wind direction, the eroded material might be deposited close to the locations where it was previously eroded from. This hypothesis is contrary to Klasen et al. (2015) who assume a transition from local (Ahrgau Subformation) to distal (Hesbaye Subformation) sediment sources. But it is in agreement with Antoine et al. (2009) and Taylor et al. (2014) who suggest a new local dust source rich in magnetic particles such as the braided bed of the river Rhine due to enhanced MS in loess deposits of the Hesbaye Subformation at Nussloch. The Ti/Zr peak in the Hesbaye Subformation at Schwalbenberg II (10.8 m) also coincides with a subtle peak in χ_{lf} .

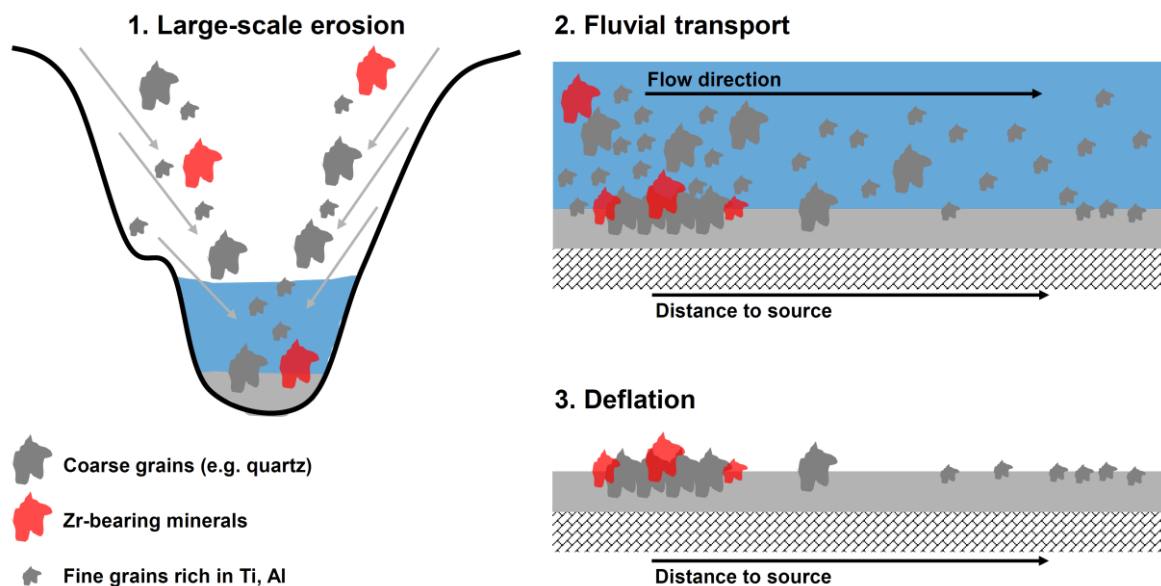


Fig. 4-9: Illustration of a conceptual model of sediment recycling and sorting processes active at the MIS 3/MIS 2-transition that explains the Zr-enrichment.

There are three options to explain the observed Ti/Zr and Ti/Al shifts at Schwalbenberg II:

- (1) Colluvial redistribution of sediment with incorporation of local bedrock (Muhs et al., 2003);
- (2) Other dust sources such as the Ahr floodplains and the Eastern slopes of the Rhine floodplains gained importance in combination with more frequent easterly winds during the period 32-24 ka BP and during the Last Glacial Maximum (LGM, 21-18 ka BP, Dietrich and Seelos, 2010). However, it is unknown which wind directions are most favorable for loess deposition at Schwalbenberg due to its location at the western-side of the river Rhine north of the river Ahr (Schirmer, 2012), in contrast to the Nussloch LPS which is located at the eastern-side of the river Rhine (Kadereit et al., 2013). Thus, northwesterly winds as suggested for Nussloch (Rousseau et al., 2014) seem unlikely as a dominant dust source for Schwalbenberg;

(3) Assuming the aforementioned reworking processes (Fig. 4-9) affecting eolian sediments at Schwalbenberg, it is likely to observe a distinct increase in Zr compared to other conservative elements such as Ti and Al. Conservative elements associated with clay or fine-grained fractions are presumably transported in suspension unless they are too heavy and sink to the riverbed. Consequently, the larger the grain-size and the higher the grain density, the faster the sedimentation. Thus, Zr-bearing minerals accumulate in the riverbed first and become enriched proximal in relation to their point of erosion (Fig. 4-9). If the river runoff is reduced and the wind strength is increased substantially, dust deflated from these locations is enriched in Zr-bearing minerals. Due to its higher density, Zr-bearing material is transported over shorter distances compared to other sediment particles and deposited first (Fig. 4-9). This hypothesis explains the enrichment of Zr relative to other conservative elements at Schwalbenberg due to its vicinity to the floodplains of the rivers Rhine and Ahr. Both of these rivers are assumed to have a higher Zr content, because degrading vegetation at the transition from MIS 3 to MIS 2 causes slopes of the floodplains to become more and more prone to erosion. Hence, weathered material is eroded and transported into the rivers Ahr and Rhine where it is additionally fractionated by grain-size and grain density and thus is becoming enriched in Zr.

Considering transportation and deposition of suspended matter, recycling and mechanical sorting become important processes (Garcia et al., 1991; Mongelli et al., 2006). Mechanical sorting separates clay minerals from feldspars and quartz, and thus Al and Ti from Si and Zr (Mongelli et al., 2006; Perri et al., 2013). Consequently, weathering and provenance proxies are influenced by mechanical sorting (Caracciolo et al., 2011). Recycling includes the mobilization and redeposition of already transported, deposited and weathered material. Therefore, recycled material may contain higher amounts of elements that are contained in heavy minerals, especially Zr (Ahmad and Chandra, 2013), due to cumulative effects of weathering of its parent source material (Mongelli et al., 2006). Hence, both effects influence weathering and provenance proxies that rely on these elements (Caracciolo et al., 2011; Mongelli et al., 2006).

Sorting can be identified by mixing trends on a ternary Al-Ti-Zr diagram (Fig. 4-10) as weathering effects are eliminated by considering weathering-inert elements only (Garcia et al., 1991). The diagram shows possible sorting with a mixing trend towards higher Zr values at the expense of Al and Ti values. Accordingly, this pattern reflects a recycling-affected sorting effect, i.e. the increase in Zr-bearing minerals due to sediment recycling involves sorting in fluvial and eolian domains. Sorting is presumed to be density rather than grain-size dominated since Zr/Rb as well as Si/Al ratios show moderate correlations with the U-ratio ($\rho = 0.56, 0.67$, Table 4-1). Zr/Rb and Si/Al are often associated with grain-size variations owing to predominant abundances of Zr and Si in coarse and Rb and Al in fine grains (Chen et al., 2006; Liang et al., 2013). Furthermore, Fig. 4-10 indicates a clustering into two groups of samples with Group 2 (samples 197-216) corresponding to the Hesbaye Subformation. Although the first 1.6 m of the Hesbaye Subformation are assumed to be lacking at the Schwalbenberg II LPS, the ternary plot indicates the sedimentation of recycled and sorted material during MIS 2 at the Schwalbenberg II LPS. This requires large scale

erosion prior to deposition as described above and thus climatic conditions that are unfavorable for a stabilizing vegetation and soil cover.

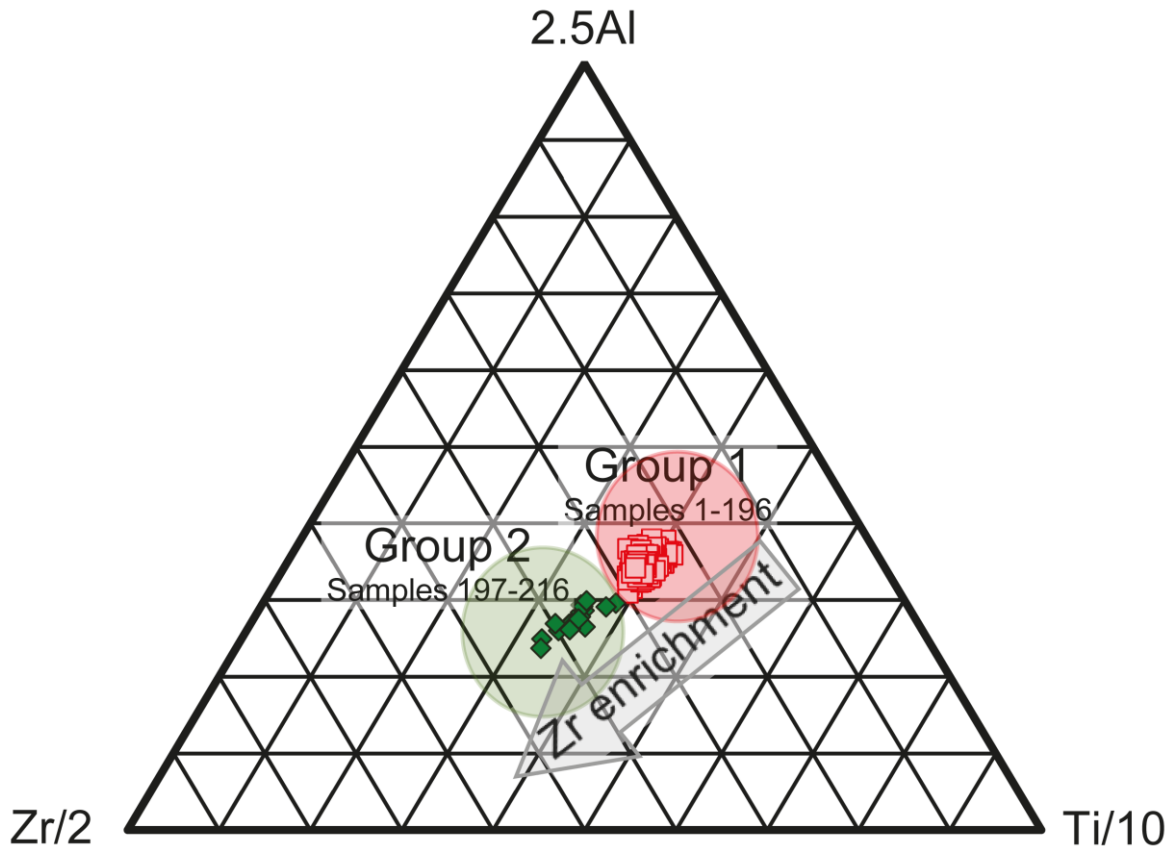


Fig. 4-10: Ternary 2.5Al-Ti/10-Zr/2 diagram showing possible sorting effects. Data is centered according to Garcia et al. (1994) and the plot is created using the Excel spreadsheet TernPlot from Marshall (1996).

4.4.4.2.2. Si/Al

Klasen et al. (2015) present Si/Al as an additional proxy for changes in mineralogy interpreted as dust source alterations. This is in contrast to (Liang et al., 2013) suggesting Si/Al as a grain-size proxy unaffected by provenance or transportation induced heavy mineral alterations. Comparing the results of (Klasen et al., 2015) to ours highlights the similar pattern of both records with a more gradual shift towards higher Si/Al values at the REM 1 record. This underlines the assumed erosion of 1.6 m at the Schwalbenberg II LPS. The negative Si/Al excursion corresponding to the Sinzig Soils at Schwalbenberg II as well as the subtle negative Si/Al excursions corresponding to the uppermost three reworked calcaric cambisols at REM 1 point to a correlation of these stratigraphic horizons. However, this proxy-based correlation is challenged by numerical age control as the Sinzig Soil S2 is radiocarbon-dated to $33,060 \pm 420$ cal BP and the corresponding second uppermost reworked calcaric cambisol at REM 1 dates to 27.3 ± 2.9 ka, an age obtained by optical stimulated luminescence (OSL) on quartz (Klasen et al., 2015). Both ages are not in agreement within their 1σ standard deviations. Another open aspect is the grain-size dependency of Si/Al. The U-ratio shows a positive correlation of $\rho = 0.67$ (Table 4-1) with Si/Al indicating that also a grain-size related sorting effect influences the Si/Al signal.

Therefore, the Si/Al ratio is neither influenced exclusively by mineralogy (Klasen et al., 2015) nor by grain-size (Liang et al., 2013).

4.4.5. Paleoenvironmental implications and relations to other regional climate archives

The Schwalbenberg II LPS is compared with other European climate archives to determine the climatic conditions during the time of the Ahrgau Subformation. Going from proximal to distal archives, Schwalbenberg II is related to the comprehensive ELSA stacks (Brunck et al., 2016; Förster and Sirocko, 2016; Sirocko et al., 2013; Sirocko et al., 2016), to Nussloch (e.g. Antoine et al., 2009), to Saxonian (Baumgart et al., 2013; Meszner et al., 2013) as well as to Austrian and to three Czech LPS at the transition zone from a dominant oceanic to a continental climate mode (Bábek et al., 2011; Hošek et al., 2015; Terhorst et al., 2002; Terhorst et al., 2015). In particular, the discussion of the Czech LPS Dolní Věstonice, Dobšice and Zeměchy is reasonable as they are the closest LPS providing a comparable geochemical record.

The recently established ELSA vegetation stack documents a spruce forest vegetation for the early MIS 3 (Fig. 4-11, Landscape Evolution Zones 8 and 9, GIS 17-13 (GICC 05), Sirocko et al., 2016) with a transition to a more open landscape with boreal forest during the middle MIS 3 (Fig. 4-11, Landscape Evolution Zone 7), albeit July temperatures between 15 and 18 °C are still reported for the ending GIS 12 (GICC 05, Sirocko et al., 2016). Consequently, cambisol genesis in terms of temperate to boreal and humid climatic conditions (Meszner et al., 2013; Terhorst et al., 2015) seems likely during this period. It corresponds to the Remagen Soils (Fig. 4-11) according to the litho-phenomenological chronology suggested by Schirmer (2012). However, luminescence ages, which we understand as sediment ages at the time of deposition and not at the time of soil formation (Zander, 2000), indicate 35-50 ka (Frechen and Schirmer, 2011) and thus Landscape Evolution Zone 7 (Fig. 4-11) as the likeliest time window for the formation of the Remagen Soils. Based on the duration of GIS 16, 14, 12, 11, 10 and 8 as well as based on the fact that millennial time scales might be enough time for cambisol development under boreal climatic conditions (Targulian and Krasilnikov, 2007), the formation of six cambisols appears likely.

Landscape Evolution Zone 6 (36.5-28.0 ka b2k, encompassing GIS 7-5, GICC 05) is characterized by a steppe climate still allowing the growth of birch and pine trees (Sirocko et al., 2016). Due to the lack of charcoal, Sirocko et al. (2016) presume climatic conditions moist enough to prevent the grassland from burning. In addition, sediment laminae with orange-brown silt layers are interpreted as indicators for soil formation (Sirocko et al., 2016). Therefore, soil formation appears likely and corresponds to the time frame of the Sinzig Soils at Schwalbenberg II (black arrows in Fig. 4-11). Although the climate for cambisol genesis seems not as favorable as in Landscape Evolution Zone 7, the geochemical weathering indices identify the Sinzig Soils S1 and S2 as the most intense paleosols, whereas the Sinzig Soil S3 corresponding to GIS 5 shows only subtle chemical weathering.

This points to an initial pedogenesis opposed to S1 and S2, albeit GIS 5 lasts approximately as long as GIS 6. Since unfavorable climatic conditions impede pedogenic processes (Targulian and Krasilnikov, 2007), S3 may document a trend towards colder climatic conditions at the margin of climatic conditions that allow cambisols to be formed.

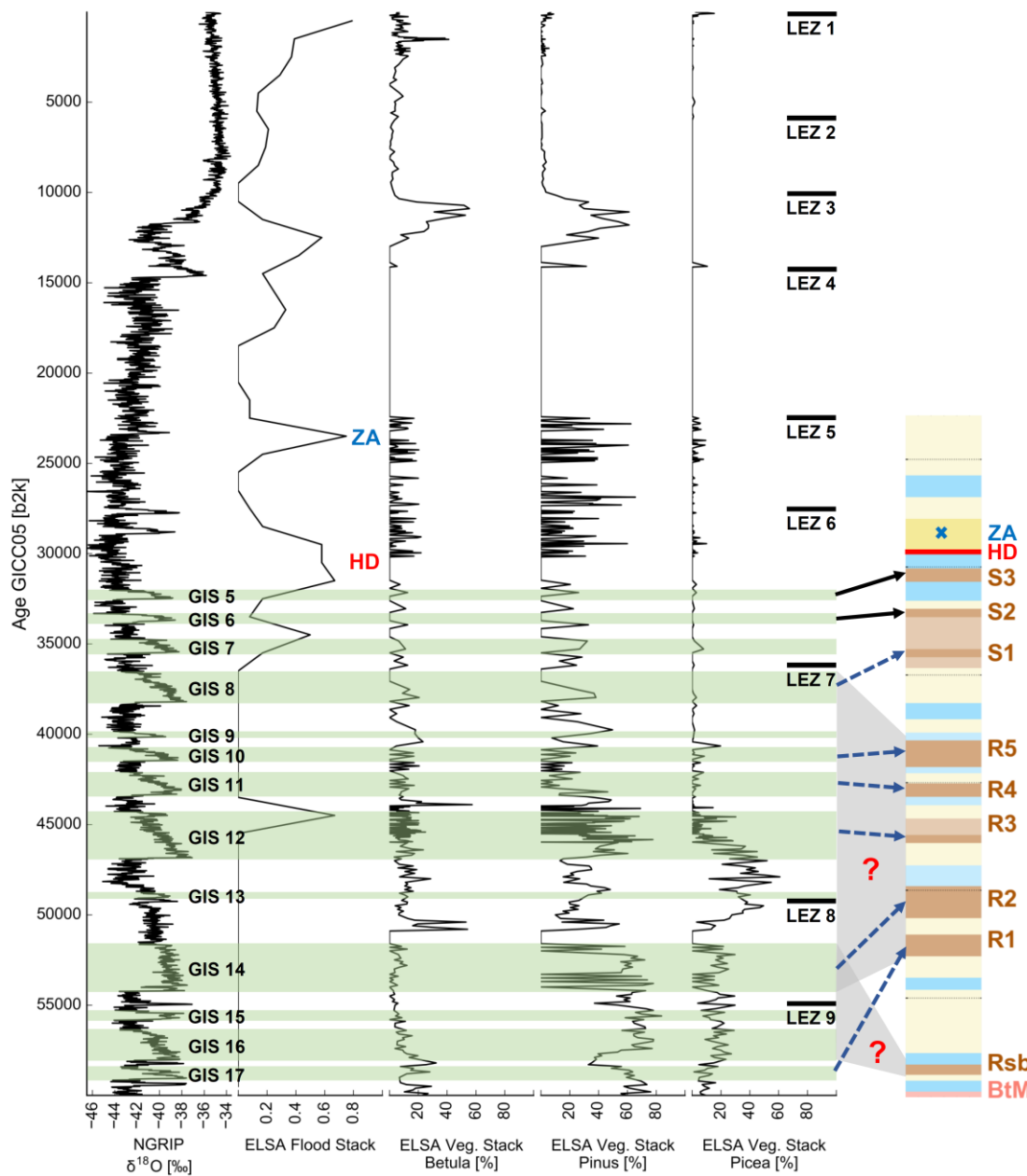


Fig. 4-11: Comparison of the NGRIP oxygen isotope record, the ELSA flood and vegetation stack with the Schwalbenberg II LPS stratigraphy. The Greenland interstadials (GIS) are highlighted according to the GICC05 chronology on the NGRIP oxygen isotope record (Andersen et al., 2006; Rasmussen et al., 2006; Svensson et al., 2008; Svensson et al., 2006; Vinther et al., 2006). The ELSA flood stack is recalculated according to the data published in Brunck et al. (2016). The ELSA vegetation stack data is from two Eifel maar lake sediment cores (Holzmaar 1, HM1, and Dehner Maar 3, DE3) and published in Sirocko et al. (2016). LEZ indicates the Landscape Evolution Zones as introduced by Sirocko et al. (2016). The grey boxes with the red question marks highlight the general possibility of soil genesis during LEZ 9–7 corresponding to the Reisberg Soil and the Remagen Soils as indicated by luminescence ages (Frechen and Schirmer, 2011). The dark blue and dashed arrows show the correlation of the Remagen Soils and the Sinzig Soil S1 with GIS as suggested by (Schirmer, 2012: 43). However, a precise correlation of single soils to single GIS is prevented by an ambiguous chronology. The black arrows highlight the most likely timing of the Sinzig Soils S2 and S3 as evidenced by two radiocarbon ages. HD: Hesbaye Discordance indicated by the red line in the Schwalbenberg profile. The positive excursion in the ELSA flood stack is presumed to trigger the HD. ZA: zircon-anomaly, i.e. Zr-enrichment in the laminated colluvial loess layer above the HD. ZA in the ELSA flood stack indicates the potential trigger for colluvial re-deposition.

Major flood events observed between GIS 5 and GIS 4 (GICC 05, Brunck et al., 2016; Sirocko et al., 2016) coincide with the expected timing of the Hesbaye Discordance (HD in Fig. 4-11). Subsequently, there is a phase of reduced flood activity, maybe pointing to drier climatic conditions enabling the deflation of eroded and fluvially transported material as suggested by our conceptual model. Deposition of Zr-enriched material is the consequence and thus supports the explanation of the Zr-anomaly as multiple recycling-affected sorting of sediments in eolian and fluvial domains (ZA in Fig. 4-11). Afterwards, the flood activity raises again and may provoke reworking resulting in the preserved laminated colluvial loess layer above the Hesbaye Discordance as described by Schirmer (2012) which exhibits the Zr-anomaly (ZA in Fig. 4-11). Considering the timing of these events, they are in agreement with the established luminescence chronology by Frechen and Schirmer (2011) as the loess above this laminated colluvial loess layer is supposed to be younger than 20 ka for IRSL or approximately 25 ka with error margins of up to ± 5.4 ka for TL ages. However, the ELSA chronology relies on ice-core tuning and tephra ages and is partly in contradiction with other independent numerical age controls such as radiocarbon and luminescence ages (Sirocko et al., 2016). Hence, the ELSA record also suffers from an ambiguous chronology like the Schwalbenberg II LPS (cf. Frechen and Schirmer, 2011; Klasen et al., 2015) and thus the correlations made have to be considered with caution as they may suggest correlations which are supposed to be in phase but are actually out of phase (Blaauw, 2012).

Comparing Schwalbenberg II with other LPS covering MIS 3, the eight cambisols at Schwalbenberg II compare to commonly only up to two preserved at other European LPS. The older preserved cambisol is often termed as Böckingen Soil in Southern Germany and Austria and dated by TL- and IRSL luminescence techniques to ~40 ka at Böckingen (Frechen, 1999) and to 46.5 ka at Trindorf close to Linz in Austria (Terhorst et al., 2002). Therefore, a correlation of one of the Remagen Soils with the Böckingen Soil appears likely as already noted by Schirmer (2000a), albeit a more explicit relation is still prevented by the Schwalbenberg chronology and by missing high-resolution geochemical records from other LPS.

Meszner et al. (2013) report erosion and reworking for the time period 60–30 ka in Saxonian LPS. Only reworked soil sediments called the Gleina Complex are preserved together with up to two in-situ gelic gleysols (Meszner et al., 2013). This is comparable to the Stillfried B LPS in Lower Austria, albeit a Lohne Soil equivalent is suggested (Terhorst et al., 2015). In contrast, at a similar longitudinal position to Saxonian LPS, the LPS Krems-Wachtberg does not show any cambisol formation. However, the archaeological findings at the time of the Lohne Soil formation at other locations (~30 ka) are interpreted as a period of ameliorating climatic conditions (Terhorst et al., 2015). As suggested in other studies (Kadereit et al., 2013; Kadereit and Wagner, 2014; Schirmer, 2012) and confirmed by this study, the Lohne Soil at Nussloch corresponds to one of the Sinzig Soils at Schwalbenberg II.

The comparison with the geochemical records of Czech LPS allows identifying patterns of MS, Rb/Sr and Rb/K representative for mainly interstadial paleosols. The weak brown soil in approximately 7 m depth at Dolní Věstonice (PK I) is attributed to MIS 3 for its slightly positive shifts in MS, Rb/K and Rb/Sr (Bábek et al., 2011). These are compared to more

pronounced excursions in chernozems (PK II, MIS 5a–5c, Bábek et al., 2011) and a Bt-horizon (PK III, MIS 5e, Frechen et al., 1999). This is consistent with the Sinzig Soils S1 and S2 (MIS 3) and the BtM horizon denoting reworked soil material from a luvisol formed during MIS 5 at Schwalbenberg II (Schirmer, 2012). Relating the PK I soil complex from the Central European key site Dolní Věstonice to the Sinzig Soils at Schwalbenberg II according to their geochemical patterns agrees with TL, IRSL and OSL ages (45.0 ± 1.9 ka, Fuchs et al. (2013); 36.7 ± 4.1 ka – 56.3 ± 8.0 ka, Zander (2000)) indicating sediment deposition (Zander, 2000) and radiocarbon ages (28-30 ka, Frechen et al. (1999) and 31.64-33.36 ka cal BP, Fuchs et al. (2013)) indicating soil formation. Fuchs et al. (2013) stress the incompleteness of PK I due to an erosion prone slope position of Dolní Věstonice.

At Zeměchy, the weathering index pattern is comparable to the pattern of the Sinzig Soils S1 and S2 at Schwalbenberg II with moderate positive excursions for PK I which are not followed by the MS record (Hošek et al., 2015). In contrast, PK I at Dobšice is subdivided into a younger initial pseudogley and an older pararendzina. The latter is characterized by a moderate positive excursion in the Rb/K profile (Hošek et al., 2015) which is in agreement with the Sinzig Soils S1 and S2 and to a lesser extent with R2. The soil R2 shows features of a calcified regosol but (Schirmer et al., 2012) classifies R2 as an eroded cambisol due to no indication of humus in the investigated thin sections. Numerical age control is only available for Zeměchy. Although Zander (2000) and Zander et al. (2000) did not recognize the initial soil development below the gravel layer attributed to PK I by Hošek et al. (2015), Zander (2000) and Zander et al. (2000) identified a hiatus between 45 ka and 20 ka for sediments below and above the gravel layer. Thus, the sedimentation age of the loess in which the PK I developed at Zeměchy accords with the ages provided for Dolní Věstonice (Frechen et al., 1999; Fuchs et al., 2013). Hošek et al. (2015) interpret the gravel layer at Zeměchy as an indicator for erosion occurring during MIS 3. This agrees with Saxonian LPS characterized by a hiatus between 60 ka and 30 ka (Meszner et al., 2013). Loess accumulation recommenced around 25 ka (Zander, 2000) pointing to a potential soil development at a similar time as for Dolní Věstonice. Therefore, also a relation of PK I at Zeměchy to the Sinzig Soils S1 and S2 at Schwalbenberg II seems feasible. Based on stratigraphy Hošek et al. (2015) correlate PK I at Zeměchy with the PK I complex at Dobšice. Consequently, there is no age control available for the potential geochemical correlation of the soils S1, S2 and R2 at Schwalbenberg II with PK I at Dobšice.

Climatically, the Bohemian LPS Zeměchy is located at the eastern margin of oceanic climate conditions whereas the Moravian LPS Dobšice belongs to an area of a dry continental climate. Therefore, the stronger excursion of Rb/Sr and Rb/K at Zeměchy are attributed to more humid conditions favoring leaching (Hošek et al., 2015). Accordingly, the Sinzig Soils S1 and S2 reflect a humid climate sufficient for soil development whereas soil forming conditions deteriorated with waterlogging and permafrost towards the Hesbaye Discordance agreeing with Sirocko et al. (2016) who observed indications for moist and cold climatic conditions in the Eifel region during the late MIS 3 (corresponding to Landscape Evolution Zone 6). This relation stresses the suitability of geochemical data as a linking tool and underlines the need for temporal high-resolution geochemical data for LPS in general, but for key sites such as Nussloch in particular.

These findings corroborate the cooling trend during the Ahrgau Subformation as deduced from MS at Schwalbenberg II, although MS depletion is not only linked to unfavorable conditions for soil development but also to leaching and erosion (Hošek et al., 2015). In addition, the changing weathering intensities of paleosols mirror these climatic fluctuations by more intense pedogenesis of the Lower Remagen (R1 and R2) and Sinzig Soils (S1 and S2) compared to the Upper Remagen Soils (R3, R4 and R5). With regard to the Sinzig Soils attributed to GIS 5–7 (GICC 05), S3 seems to represent an example of decelerated pedogenesis by unfavorable climatic conditions. Gelic gleysols enclosing S3 support this hypothesis as they may form in decades (Targulian and Krasilnikov, 2007) and indicate a frost-dominated climate (Terhorst et al., 2015). This additionally strengthens the idea of enhanced permafrost conditions for S3 preventing secondary calcification of S1 and S2. Although ELSA and Schwalbenberg II chronologies are questionable, the geochemical record of Schwalbenberg II together with the new ELSA vegetation stack highlights the possibility of pedogenesis, especially cambisols, throughout the MIS 3. Hence, based on the findings of this study and supported by previous studies (e.g. Schirmer, 2012; Schirmer et al., 2012), it tends to be likely that the lithologically determined paleosols at Schwalbenberg II are indeed in-situ soil formations. However, we cannot completely exclude that reworking processes were active during the Ahrgau Subformation.

4.5. Conclusion

Element dynamics of the Schwalbenberg II LPS in comparison with published proxy data provide new insights regarding the paleoenvironmental conditions during the Ahrgau Subformation (MIS 3) and the early Hesbaye Subformation (MIS 2). Taking into account that leaching and erosion can cause MS depletion, the intensity of pedogenesis should be evaluated by both MS and element data. Based on Fe, MS as well as Rb/Sr, Ba/Sr and Rb/K S1 and S2 are identified as the most intense paleosols, albeit Ca/Sr indicates the “Sr-type” indices to be influenced by calcification dynamics. Thus, Rb/K is regarded as the most reliable weathering index which corroborates S1 and S2 as strong paleosols but also documents weathering for the Lower Remagen Soils (R1, R2 and R3). Discussing the time required for cambisol formation as a function of existing climatic conditions, points to the possibility of cambisol formation in many of the GIS attributed to MIS 3 and corresponding to the Ahrgau Subformation. Gelic gleysols enclose S3 which shows only subtle chemical weathering. This might indicate a trend to cold frost dominated climatic conditions and explains why S1 and S2 are hardly affected by secondary calcification. Presumably, these cold excursions and the subsequent climate of the LGM accompany permafrost conditions that prevent water from percolating through S1 and S2.

The transition from the Ahrgau to the Hesbaye Subformation is characterized by dust source changes as suggested by Klasen et al. (2015) and evidenced in this study by the Ti/Zr and Ti/Al ratios. Moreover, this transition coincides with the MIS 3/MIS 2 transition. It separates the more humid and warmer MIS 3 climate from the cold, arid and extremely windy LGM climate. Based on the dynamics of Al, Ti and Zr, a conceptual model explaining the Zr-

enrichment at Schwalbenberg II during MIS 2 is developed. It indicates more local dust sources during MIS 2 due to multiple recycling-affected sorting of sediments in eolian and fluvial domains.

Acknowledgements

Financial support of the German Research Foundation (DFG, ZO 102/ 22-1) is gratefully acknowledged. We thank Lena Neumann and Sabine Stahl for sample preparation and executing XRF analyses. Furthermore, we are much obliged to Udo Scheer from the Ruhr Museum in Essen for sample maintenance and to Rik Tjallingii for a detailed explanation of log ratios. We also thank Astrid Techmer (LIAG, Hannover) for improving an earlier version of this manuscript and four anonymous referees for their detailed and constructive suggestions.

4.6. Supplementary material

Proxy data is available at Pangaea. <https://doi.pangaea.de/10.1594/PANGAEA.855547>.
Supplementary data associated with this article can be found in the online version, at <http://dx.doi.org/10.1016/j.palaeo.2016.07.022>.

5. Study II – Susak

XRF scanning of discrete samples – a chemostratigraphic approach for loess-paleosol sequences exemplified on the Island of Susak, Croatia

Jörn **Profe**^{1,*}, Lara **Wacha**², Manfred **Frechen**³, Christian **Ohlendorf**¹, Bernd **Zolitschka**¹

¹ University of Bremen, Department of Social Sciences, Institute of Geography, GEOPOLAR, Celsiusstraße 2 FVG-M, D-28359 Bremen, Germany

² Croatian Geological Survey, Department of Geology, Sachsova 2, HR-10 000 Zagreb, Croatia

³ Leibniz Institute for Applied Geophysics (LIAG), Geochronology and Isotope Hydrology, Stilleweg 2, D-30655 Hannover, Germany

Corresponding author: Jörn Profe, Email: profe@uni-bremen.de

under review

Quaternary International – Special Issue “Quaternary of Croatia”

A modified version of the printed version has been published in Quaternary International.

Profe, J., Wacha, L., Frechen, M., Ohlendorf, C., Zolitschka, B., 2018. XRF scanning of discrete samples – A chemostratigraphic approach exemplified for loess-paleosol sequences from the Island of Susak, Croatia. Quaternary International, <https://doi.org/10.1016/j.quaint.2018.05.006>.

Contribution of authors

JP and LW did the field work. JP performed XRF scanning and TOC analyses, analyzed the XRF, TOC and grain-size data, established the chemostratigraphy, compared them with other available proxy data, drafted all figures as well as the manuscript and contributed to the study design. LW and MF provided grain-size data and helped to improve the manuscript. CO assisted in XRF data precision, compaction and standard addition experiments as well as in structuring the manuscript. BZ is responsible for the study design and improved the manuscript.

Abstract

X-ray fluorescence (XRF) scanning of discrete samples provides a time- and cost-efficient alternative to conventional geochemical analyses of discretely sampled paleoenvironmental archives. Loess-paleosol sequences (LPS) as complex terrestrial archives are thus predestinated for benchmarking this new application of the well-established XRF scanning technology. Stratigraphically incomplete outcrops often exposed as cliffs to the sea and prone to reworking on the Island of Susak (Croatia) are unique paleoenvironmental archives at least for the penultimate and last interglacial-/glacial cycles, and thus providing an ideal test site. Available proxy data from previous investigations on Susak ensure validation of conclusions drawn on XRF scanning-derived data.

Three representative profiles were studied to examine the potential of XRF scanning-derived element ratios as proxy for certain environmental processes: (1) Ca/Sr for the strength of ubiquitously present secondary calcification; (2) Rb/K for the intensity of weathering; (3) Ti/Al and Ti/Zr for changes in wind speed with Zr being additionally indicative for sediment recycling; (4) Si/Al mainly represents changes in grain-size; (5) Br and Cl as proxies for sea spray. Furthermore, we established multivariate statistics-based chemostratigraphy to facilitate profile correlation and to improve lithostratigraphic considerations as exemplified on the paleosol O-P1. In conclusion, this study demonstrates that XRF scanning of discrete samples is a valuable tool for LPS. High-resolution qualitative geochemical data successfully provided knowledge to improve the characterization and correlation of different LPS and allowed paleoenvironmental reconstructions.

Keywords

Geochemistry,
multivariate statistics,
paleoclimate,
sediment archive,
bromine,
loess

5.1. Introduction and regional setting

XRF scanning of discrete samples (Ohlendorf, 2018) provides a cost- and time-efficient geochemical screening tool for discontinuous terrestrial archives such as loess-paleosol sequences (LPS) to acquire geochemical data with high spatial resolution (Profe et al., 2016). Furthermore, recording Cl and Br without any additional preparation step is unique and outperforms standard analytical techniques such as conventional glass-bead XRF or inductively-coupled plasma mass-spectrometry (ICP-MS). Therefore, this study benchmarks XRF scanning-derived element ratios as proxies for weathering intensity or dust provenance and thus paleoenvironmental reconstruction in a very complex and polygenetic environment such as the Island of Susak in Croatia (Fig. 5-1). Strong secondary calcification, often in the form of rhizoconcretions (Durn et al., 2017b), and potential sea-water spray entrapment in soils challenge commonly applied element ratios. Br and Cl are accordingly tested as potential proxies for sea-water spray entrapment as well as for paleo-transgressions of the Adriatic Sea. In addition, multivariate statistics are applied to establish a chemostratigraphy in 2 cm spatial resolution facilitating correlation of different profiles or identifying both very thin horizons (< 10 cm) and particularities that require e.g. detailed grain-size, mineralogical or micromorphological investigations.

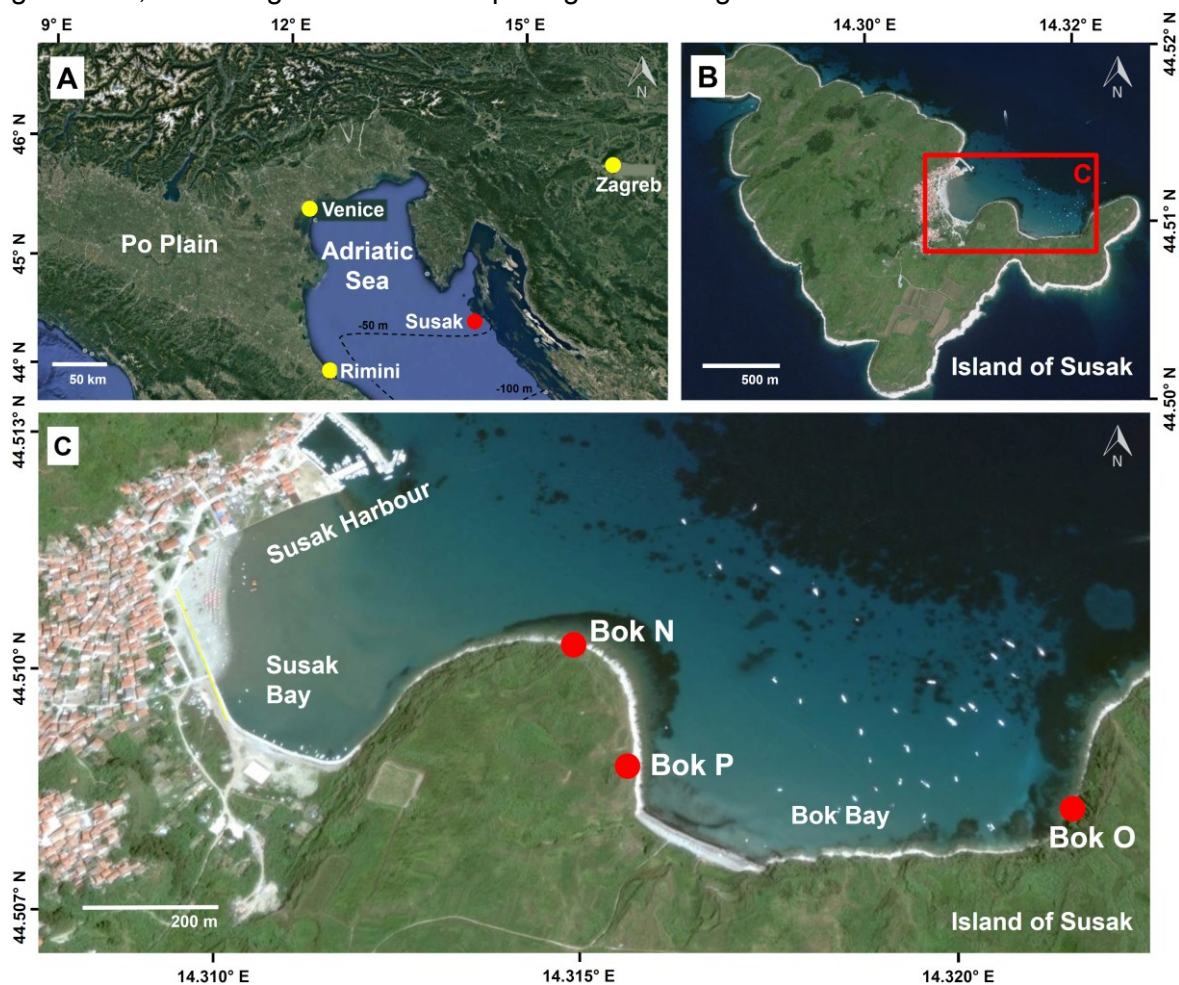


Fig. 5-1: Satellite images of the study site (modified after: Google-Earth, 2017). A) Overview of the Po plain and the northern Adriatic Sea. Bathymetry is adapted from Babić et al. (2013). B) The Island of Susak. C) North-eastern coast of the Island of Susak with indicated profile locations (red dots). Bok N (44.5102°N, 14.3145°E, WGS 84), Bok O (44.5078°N, 14.3176°E, WGS 84) and Bok P (44.5088°N, 14.3155°E, WGS 84) denote the three profiles analyzed in this study.

The Island of Susak (3.8 km², Fig. 5-1) is an exceptional location in the northeastern Adriatic Sea (Kvarner Archipelago) to study paleoenvironmental dynamics from LPS during the last two interglacial-/glacial cycles (Bognar et al., 2003; Cremaschi, 1990; Durn et al., 2017a; Durn et al., 2017b; Mikulčić Pavlaković et al., 2011; Wacha et al., 2011a; Wacha et al., 2011b; Wacha et al., 2017). More than 30 m thick and plateau-like Quaternary deposits overlay the Cretaceous limestone characterized by karst and abrasion dynamics (Durn et al., 2017a; Durn et al., 2017b; Wacha et al., 2017). However, due to the intensively dissected geomorphology caused by human activity (Bognar et al., 2003), a continuous sediment sequence has not yet been recognized on Susak. Accessible outcrops are only available as stratigraphically incomplete loess-paleosol cliffs close to the shore and in a slope position requiring correlation by marker horizons (e.g. three tephra layers, Mikulčić Pavlaković et al., 2011) or representative soil horizons (e.g. Durn et al., 2017b). These locations are prone to relocation processes and erosion that further complicate the establishment of a comprehensive composite profile (Bognar et al., 2003; Mikulčić Pavlaković et al., 2011; Wacha et al., 2011a; Wacha et al., 2017). Nonetheless, many adjacent individual LPS on Susak were studied by luminescence dating, granulometry, geochemistry and mineralogical analyses during the last decade (Durn et al., 2017a; Durn et al., 2017b; Mikulčić Pavlaković et al., 2011; Wacha et al., 2011a; Wacha et al., 2011b; Wacha et al., 2017). Results that we use to evaluate our XRF scanning results.

Dust deposition on Susak is driven by paleoenvironmental dynamics of the deltaic system of the paleo river Po as evidenced by heavy mineral analyses (Cremaschi, 1990; Mikulčić Pavlaković et al., 2011). Mikulčić Pavlaković et al. (2011) determined Alpine material and thus the paleo Po floodplain area as the primary dust source with minor contributions from the northern Apennines. The Pleistocene is characterized by several transgressive-regressive cycles due to changes in the global ice volume. The mean relative sea-level was about 90 m lower than today during MIS 6 and 120 m lower during MIS 2 as inferred from a planktonic foraminiferal $\delta^{18}\text{O}$ stack situated at the Strait of Gibraltar (Rohling et al., 2017). This caused the paleo Po delta to expand towards south-east and to completely cover today's northern part of the Adriatic Sea including the location of the Island of Susak (Fig. 5-1, Maselli et al., 2011; Zecchin et al., 2017). During interglacial periods the paleo Po delta varied its position (Zecchin et al., 2017), changing dust source distances over time. The MIS 4 and MIS 3 mean relative sea-levels were between 100 m and 50 m lower than today (Rohling et al., 2017).

Three profiles (Bok N, Bok O, Bok P, Figs. 5-1 and 5-2) serve as an example representative for the oldest stratigraphic units so far recognized on Susak covering the time period from Marine Isotope Stage (MIS) 7 to MIS 4 (Durn et al., 2017b; Wacha et al., 2011a). We refer to MIS according to the notation of Lisiecki and Raymo (2005). We evaluate our results with grain-size, total organic carbon (TOC) and CaCO₃ data as well as with results reported by Mikulčić Pavlaković et al. (2011) and Durn et al. (2017b).

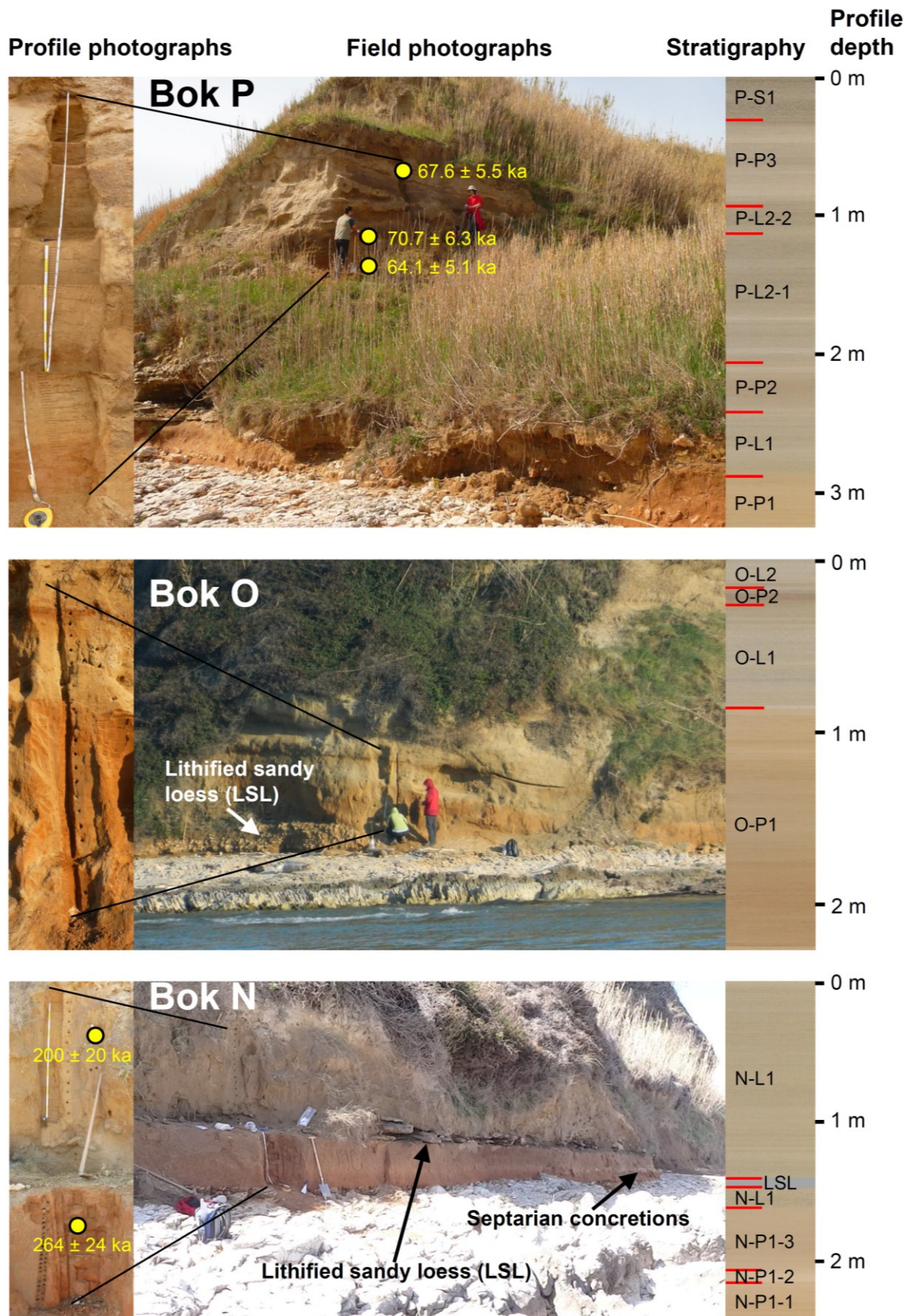


Fig. 5-2: Profile (left) and field photographs (middle) as well as RGB images from the samples prepared for XRF scanning (right) of the profiles Bok N (bottom), Bok O (middle) and Bok P (top) sampled in 2015. Yellow dots indicate the positions of luminescence ages taken at this exact locations for dating: Bok P fading corrected infrared stimulated luminescence ages are reported in Wacha et al. (2011a) while Bok N fading corrected post-infrared infrared stimulated luminescence ages at 225 °C (pIRIR₂₂₅) are reported in Durn et al. (2017b).

5.2. Material and methods

5.2.1. Sampling and stratigraphic description

In April 2015, three profiles were sampled in 2 cm resolution, situated in the Bok Bay: Bok N, Bok O and Bok P (Figs. 5-1 and 5-2). These outcrops, most accessible and most representative for research, correspond to the stratigraphically oldest parts of the composite profiles described in previous studies by Mikulčić Pavlaković et al. (2011), Wacha et al. (2011a) and Wacha et al. (2011b) and in more recent studies by Durn et al. (2017b). In total, we took 396 samples for XRF scanning and granulometry. To avoid misunderstandings with regard to composite profiles (Wacha et al., 2011a), we use individual profile depths and labels (Fig. 5-2). Furthermore, specific sample depths are always given as top of sample.

The profile Bok N represents the stratigraphically oldest known deposits from Susak with a total thickness of 242 cm where altogether 119 samples were collected (Fig. 5-2). The sequence consists of a red paleosol (N-P1, 242-160 cm) with a tripartite structure directly covering the Cretaceous basement (Durn et al., 2017b). The middle part of the N-P1 paleosol (N-P1-2, 214-208 cm) is characterized by a lighter color and corresponds to the position of septarian concretions as described by Mikulčić Pavlaković et al. (2011) and observed laterally some meters apart (Fig. 5-2). The N-P1 paleosol is covered by a 1.6 m thick loess layer (N-L1, 160-0 cm) intercalated by an up to 10 cm thick lithified sandy loess layer (LSL, 148-142cm, not sampled). Mikulčić Pavlaković et al. (2011) characterize this LSL (sandstone bench sensu Bognar et al. (2003)) as discontinuous with thicknesses up to 70 cm caused by re-precipitation of CaCO₃ leached from the overlying loess. The same location was investigated in detail from a paleopedologic perspective by Durn et al. (2017b). Fading corrected post-infrared infrared stimulated luminescence ages at 225°C (pIRIR₂₂₅) determined by Durn et al. (2017b) allow correlation of the N-P1 soil formation to MIS 7 and the subsequent loess deposition to the transition from MIS 7 to MIS 6.

The profile Bok O comprises 114 samples for 226 cm (Fig. 5-2). An orange-brown paleosol (O-P1, 226-86 cm) is exposed in the lower part of the sequence covered by loess (O-L1, O-L2) which in its upper part is intercalated by a thin brown paleosol (O-P2, 26-16 cm). O-P1 dips towards the west – north-west and laterally inclines, likely following the paleorelief. Fig. 5-2 shows that O-P1 covers both the LSL and the Cretaceous basement at this position while at other not shown nearby locations O-P1 covers loess and the red paleosol (likely N-P1). Therefore, we assume that Bok O is stratigraphically younger compared to Bok N. Same stratigraphic assumptions were made by Wacha et al. (2011a), Wacha et al. (2011b) and Mikulčić Pavlaković et al. (2011), albeit no detailed investigations were performed on Bok O before.

At the Bok P profile (162 samples, 324 cm, Fig. 5-2) an orange-brown paleosol (P-P1, 324-288 cm) is also exposed and covered by loess (P-L1, 286-242 cm). The upper part of P-L1 is overprinted by a brown paleosol (P-P2, 240-206 cm). The overlying loess (P-L2, 204-94 cm) coarsens in the topmost 20 cm (P-L2-2, 114-94 cm) and is superimposed by another

brown paleosol with slight color modulations (P-P3, 92-30 cm). The topmost part (P-S1, 28-0 cm) represents a sand layer that is coarser and more homogeneous than the coarse loess (P-L2-2) below P-P3. The identical location was previously investigated by Mikulčić Pavlaković et al. (2011), Wacha et al. (2011a) and Wacha et al. (2011b). They provide infrared stimulated luminescence ages ranging from 64.1 ± 5.1 ka to 70.7 ± 6.3 ka thus suggesting a correlation of Bok P with MIS 4.

5.2.2. XRF scanning of discrete samples

Sample preparation (Fig. 5-3) comprised freeze drying of field samples (Fig. 5-3A) and subsequent homogenization by pestle and mortar (Fig. 5-3B). Approximately 1.2 g of sample material was used to fill a 0.88 cm³ sample cup (Fig. 5-3C, D). To assure homogeneity and a smooth flat surface (Fig. 5-3D), a plunger (Fig. 5-3C) was used to compact the sample material by hand. Up to 30 sample cups were then mounted on one sample carrier (Fig. 5-3E). The design of the sample cups and carriers allow continuous measurement in 5 mm steps resulting in an alternating sequence of sample and sample carrier spectra (Ohlendorf, 2018). Further data processing required removal of sample carrier spectra, data copying and sumspectra calculation. We automated these processing steps using the free and open-source programming language Python v. 2.7 (Fig. 5-3G).

Measurements were performed with an ITRAX XRF core-scanner at the University of Bremen (GEOPOLAR). Prior to XRF measurements, a surface scan was done to assure a constant sample-detector-distance (Croudace et al., 2006). Together with this step, a RGB color image was acquired with a resolution of 250 dpi (Croudace et al., 2006). After cropping, we use RGB color images of the samples to illustrate the lithostratigraphy (Fig. 5-2). For XRF scanning, we set the measurement time to 100 s, which is the longest possible measurement time for 5 mm in continuous scanning mode due to the slowest possible motor speed of the ITRAX carrying system. All samples were scanned with a Mo X-ray tube and afterwards with a Cr X-ray tube. The Cr-tube was particularly used to assure reliable count rates for light elements (Al, Si). Tube settings were adjusted to obtain 30,000 counts per second (Mo-tube: 30 kV, 30 mA; Cr-tube: 30 kV, 40 mA). After measurement, the XRF spectra were transformed into element counts by fitting a mathematical model to the actual recorded XRF spectra (e.g. Hahn et al., 2014). We used the proprietary software Q-Spec (version 8.6.0) for this peak fitting step. It is important to fit the calculated sumspectra manually to account for specific sediment matrices.

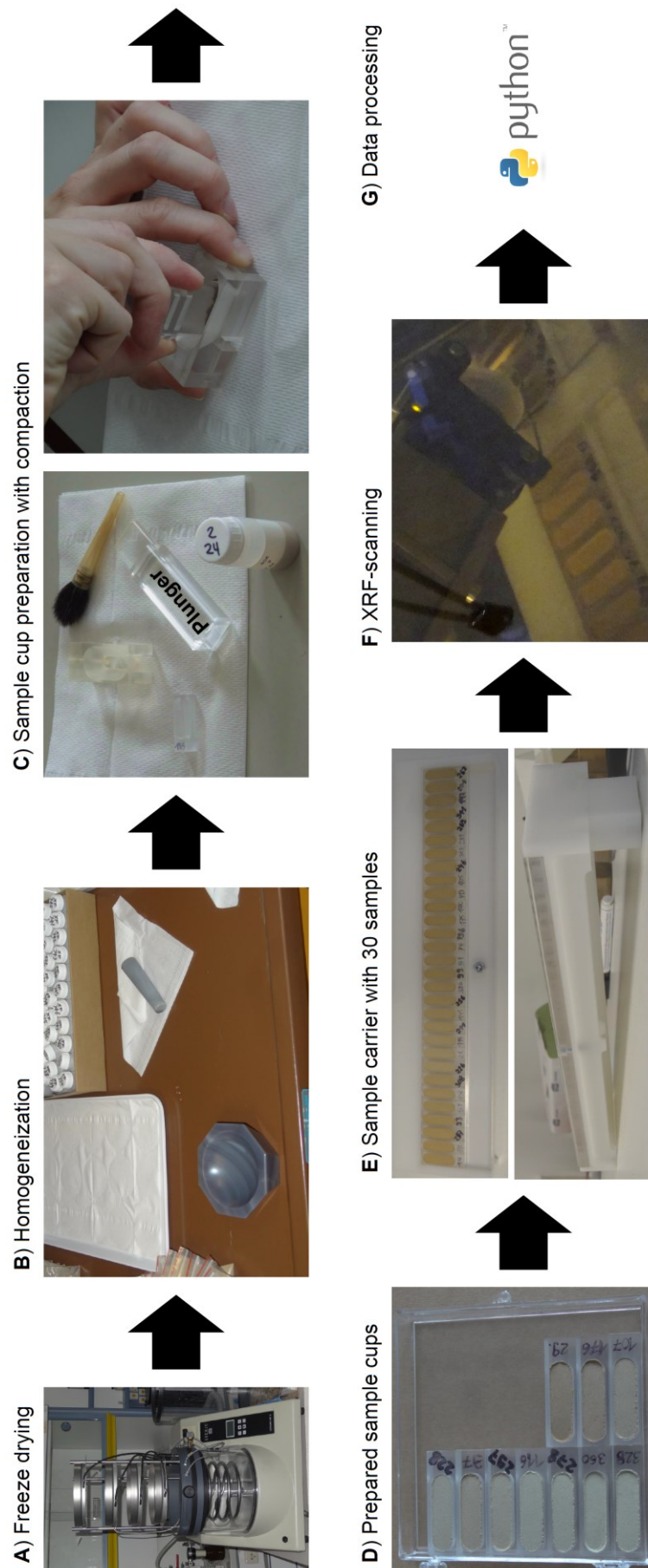


Fig. 5-3: Workflow illustrating sample preparation and measurement procedure for XRF scanning of discrete samples.

Data quality in terms of data precision was analyzed by triplicate measurements of 84 samples (Bok N: 0-44 cm, 170-242 cm; Bok P: 278-324 cm). In addition, we checked data precision against compaction for Mo-tube measurements. Due to aging of the Mo-tube between measurements of the LPS and standard addition samples, we analyzed the compaction test samples at 30 kV and 31 mA. Compaction is a critical step in XRF measurements as porosity changes and irregular surfaces may adversely influence the recorded XRF signal (cf. Jarvis et al., 2015; Tjallingii et al., 2007). Since we used a plunger to compact samples by hand, we estimated the effects of sample preparation by different persons including one test run without compaction. For the compaction test three different well-homogenized mixed loess samples from the LPS Süttő in Hungary (Novothy et al., 2011; Profe et al., under review) were each prepared by four different persons in duplicates. In addition, we included non-compacted samples in duplicates for comparison. To highlight differences between persons and non-compacted samples, we (1) calculated mean relative standard deviations per element and person and (2) estimated differences between a selected reference person and the other persons and non-compacted samples to unravel compaction-induced data precision effects.

We investigated a variety of element ratios. Ca/Sr indicates decalcification due to leaching by a negative excursion since Ca is leached more intensively compared to Sr. On the other hand it also indicates strong secondary calcification by a positive excursion since Ca dominates this enrichment process of secondary calcification (Bokhorst et al., 2009; Profe et al., 2016). Rb/Sr and Ba/Sr are often used as weathering indices, with Sr becoming leached and Rb and Ba relatively enriched during weathering. However, calcite dynamics in the profiles may superimpose their ability to record the weathering signal (Buggle et al., 2011). Rb/K relies on relative Rb enrichment due to K-feldspar weathering (Buggle et al., 2011) and indicates the intermediate stage of weathering (Hošek et al., 2015). Dust provenance can be best investigated by weathering inert elements such as Si, Al, Ti and Zr. For this purpose we use ratios of Si/Al, Ti/Al and Ti/Zr (Klasen et al., 2015; Profe et al., 2016; Sheldon, 2006; Sheldon and Tabor, 2009; Zech et al., 2008). Chen et al. (2006) and Liang et al. (2013) document that most elements are also influenced by grain-size differences. Zr/Rb and Si/Al ratios are suggested as grain-size proxies due to relative enrichment of Rb and Al in fine particles, Zr in coarser particles with irregular trends and Si in coarse particles as weathering-resistant quartz. Particularly, Si/Al records grain-size sorting effects related to winter monsoon strength on the Chinese Loess Plateau (Liang et al., 2013). Therefore, we apply Zr/Rb and Si/Al to test for grain-size induced changes in the geochemical record. In addition, we consider Fe/Mn as a redox-sensitive element ratio (Rothwell and Croudace, 2015b). We express XRF scanning-derived element ratios as log ratios to avoid statistical asymmetry and to account for matrix effects (Profe et al., 2016; Weltje et al., 2015; Weltje and Tjallingii, 2008).

5.2.3. Chemostratigraphy

Multivariate statistics allow investigation of several parameters at once and thus enable the establishment of a chemostratigraphy to support the lithostratigraphy on the basis of

hierarchical clustering of selected XRF scanning-derived elements (e.g. Bloemsma, 2015; Martin-Puertas et al., 2017). However, XRF scanning-derived element intensities represent compositional data that suffer from the closed sum constrain (Von Eynatten et al., 2003) and sediment matrix as well as surface roughness effects (Jarvis et al., 2015; Tjallingii et al., 2007), and thus prevent multivariate statistics from being applied (Aitchison, 1986). Therefore, we performed a centered log-ratio (clr) transformation (e.g. Aitchison, 1986) prior to clustering in order to overcome these adverse effects. Since we used different X-ray tubes for data acquisition, clr-transformation was done for each tube separately. Subsequently, we standardized (z-scored) each element data to zero mean and unit variance to give each element equal importance. Based on data precision we took Al, Si, K, Ca, Ti (measured with Cr-tube) and Mn, Fe, Rb, Sr, Zr (measured with Mo-tube) into account for hierarchical clustering using the Ward algorithm (Ward, 1963). We implemented this workflow in Python v. 2.7 adapting the required functionality available in the R package “composition” (van den Boogaart and Tolosana-Delgado, 2008). The number of clusters was preset to five according to the number of different described lithologies and the relative linkage distance between clusters.

5.2.4. Standard addition calibration

Identification of sea-water spray entrapment in paleosols requires quantification of Br and Cl intensities that in turn enables comparison of Br and Cl concentrations with published data (e.g. Leri and Myneni, 2012; Öberg, 2003; Yamada, 1968). For quantification, we adopted the standard addition approach (de Vries and Vreboos, 2002; Miller, 1991; Pind, 1984) to estimate Br and Cl concentrations in LPS. We took a mixed sample of the Schwalbenberg II LPS (Profe et al., 2016 and references therein) which has no reliably measurable Br and Cl concentrations to avoid sediment matrix effects. However, we cannot exclude background concentrations smaller than detection limits of the ITRAX XRF core scanner. To assure homogeneous spiked samples with either Br or Cl, we applied aqueous NaBr and NaCl solutions and dried as well as homogenized the spiked samples after application. The resulting calibration curves provide linear equations with $R^2 > 0.99$ (supplementary material, Fig. 5-11). Due to aging of the Mo-tube between measurements of the LPS and standard addition samples, we analyzed the standard addition samples at 30 kV and 31 mA in ten replicate measurements. Uncertainty of data quantification in the established calibration curves was investigated by leave-one-out cross-validation and reported as confidence limits at the 95 % confidence level according to Miller (1991). Uncertainties of quantified concentrations along the studied subprofiles are also provided at the 95 % confidence level.

5.2.5. Total organic carbon and calcium carbonate content

Total organic carbon (TOC) and CaCO_3 were measured with 10 cm resolution. TOC was determined by a CNS element analyzer (Euro EA, Eurovector) at the GEOPOLAR laboratory, University of Bremen, following the protocol outlined in Hahn et al. (2013). In addition, CaCO_3 was estimated from total inorganic carbon (TIC) and TOC. Therefore, two

aliquots of the same sample were prepared. One was analyzed for total carbon (TC) and the other was analyzed for TOC. Based on the molar ratio between C and CaCO₃, multiplying the calculated TIC (TIC = TC – TOC) with the constant factor 8.33 results in CaCO₃ in per cent.

5.2.6. Grain-size analysis

Grain-size analyses were carried out for each of the 395 samples at the Leibniz Institute for Applied Geophysics (LIAG) in Hannover using a Beckman-Coulter LS 13320 PIDS laser diffractometer. Samples were not pretreated in terms of organic matter or carbonate removal because previous studies showed that it has negligible effects (e.g. Schulte et al., 2016; Wacha et al., 2017). Each sample was measured in triplicate and the mean value is reported. According to the underestimation of clay minerals in laser diffractometry, we selected the value of 5.5 µm instead of 2 µm as the threshold between silt and clay fractions (Beuselinck et al., 1998; Vandenberghe, 2013; Vandenberghe et al., 1985). The measurement protocol is presented in detail by Wacha et al. (2017).

5.3. Results

XRF scanning provides geochemical data for LPS with high spatial resolution (Profe et al., 2016). We present data from the Susak LPS to understand whether element ratios are a useful tool as proxies for weathering intensity or dust provenance under such polygenetic environmental conditions. Furthermore, we evaluate the combined potential of the chemostratigraphy and the element ratios to correlate the three investigated profiles. Results are reported for every profile separately and grouped into the following order: First, we show similarities between the Ca/Sr ratio and CaCO₃. Subsequently, we compare weathering indices (Rb/Sr, Ba/Sr, Rb/K) with TOC, Br and Cl concentrations as well as with the redox-sensitive Fe/Mn ratio. In addition, we discuss dust provenance indices (Ti/Al, Ti/Zr, Si/Al) as well as the grain-size index (Zr/Rb) and relate them to actual grain-size data. Finally, we compare the observed trends in the element ratios with the derived chemostratigraphy.

5.3.1. Data quality

Most elements reveal mean relative standard deviations ≤ 2.6 %, except for Ba, Br and Cl when measured with both tubes as well as Al when measured with a Mo-tube and Rb when measured with a Cr-tube (Table 5-1). This is in agreement with data precision tests carried out on samples from the LPS Schwalbenberg II (Profe et al., 2016). Accordingly, we used Cr-tube data for log-ratio calculation involving the elements Al and Si.

Table 5-1: Data precision of XRF scanning-derived element data. Due to high concentration ranges of e.g. Br and Cl, both mean and median are reported in relative standard deviations (RSD).

	Al	Si	Cl	K	Ca	Ti	Mn	Fe	Br	Rb	Sr	Zr	Ba
X-ray tube	Cr	Cr	Cr	Cr	Cr	Cr	Cr	Cr	Cr	Cr	Cr	Cr	Cr
Mean RSD (%)	2.63	1.02	9.20	0.92	0.88	0.94	2.54	0.90	47.92	3.24	2.41	1.82	13.48
Median RSD (%)	2.61	0.86	2.28	0.81	0.76	0.82	2.57	0.81	25.89	3.20	2.33	1.61	13.23
X-ray tube	Mo	Mo	Mo	Mo	Mo	Mo	Mo	Mo	Mo	Mo	Mo	Mo	Mo
Mean RSD (%)	9.01	1.60	26.58	0.98	0.85	1.18	1.42	0.76	33.05	1.62	1.37	1.72	9.19
Median RSD (%)	8.10	1.43	5.69	0.88	0.77	1.08	1.33	0.63	18.46	1.63	1.32	1.58	8.02

Compaction tests document negligible changes in mean relative standard deviations between persons with differences ranging from one-tenth to one-sixth of the original mean relative standard deviations (Table 5-2). In addition, there is hardly any difference between compacted and non-compacted (loose) samples. XRF scanning results are thus considered as insensitive to sample preparation conducted by different persons underlining the robustness of the method.

Table 5-2: Compaction-induced changes of mean relative standard deviations. P1-P4: four different persons. Loose: sample preparation without compaction. Left: mean relative standard deviations derived from three different samples each measured in duplicate. Right: differences between the arbitrary chosen reference person (P1) and the other persons and the non-compacted samples. Differences represent absolute changes in mean relative standard deviations.

Element	P1	P2	P3	P4	Loose	P1-P2	P1-P3	P1-P4	P1-Loose
Al	15.83	13.80	13.26	12.81	15.22	2.03	2.57	3.02	0.61
Si	1.37	1.77	1.45	1.51	1.70	-0.40	-0.08	-0.14	-0.33
K	1.09	1.29	1.17	0.97	1.28	-0.20	-0.08	0.12	-0.19
Ca	0.81	1.22	0.96	0.95	1.10	-0.41	-0.16	-0.14	-0.30
Ti	1.16	1.44	1.05	1.34	1.18	-0.28	0.11	-0.18	-0.03
Mn	1.52	1.47	1.33	1.47	1.52	0.06	0.19	0.05	0.00
Fe	0.77	1.11	0.80	0.75	0.98	-0.33	-0.02	0.02	-0.21
Rb	2.31	2.44	2.23	2.56	2.44	-0.13	0.09	-0.25	-0.12
Sr	1.68	1.74	1.37	1.44	1.50	-0.07	0.31	0.23	0.18
Zr	1.70	1.59	1.61	1.68	1.74	0.11	0.10	0.03	-0.04
Ba	14.22	11.40	14.81	12.85	12.32	2.82	-0.59	1.36	1.90

5.3.2. Bok N

Ca/Sr shows a very similar behavior to CaCO₃ ($\rho = 0.65$, Figs. 5-4 and 5-5). N-P1 is characterized by a tripartite structure with 15 % CaCO₃ in the lower (N-P1-1), 25 % CaCO₃ in the central (N-P1-2) and a gradual decrease to 5 % CaCO₃ in the upper part (N-P1-3). In N-P1-3 there is again a gradual increase of CaCO₃ to 30 % towards the bottom of the overlying loess N-L1. This loess is intercalated by the LSL. N-L1 above the LSL exhibits homogeneous CaCO₃ values of about 20 %. Ca/Sr records the same pattern with much better spatial resolution underlining the result of the one high data point in the CaCO₃ record at 212 cm depth (Fig. 5-4).

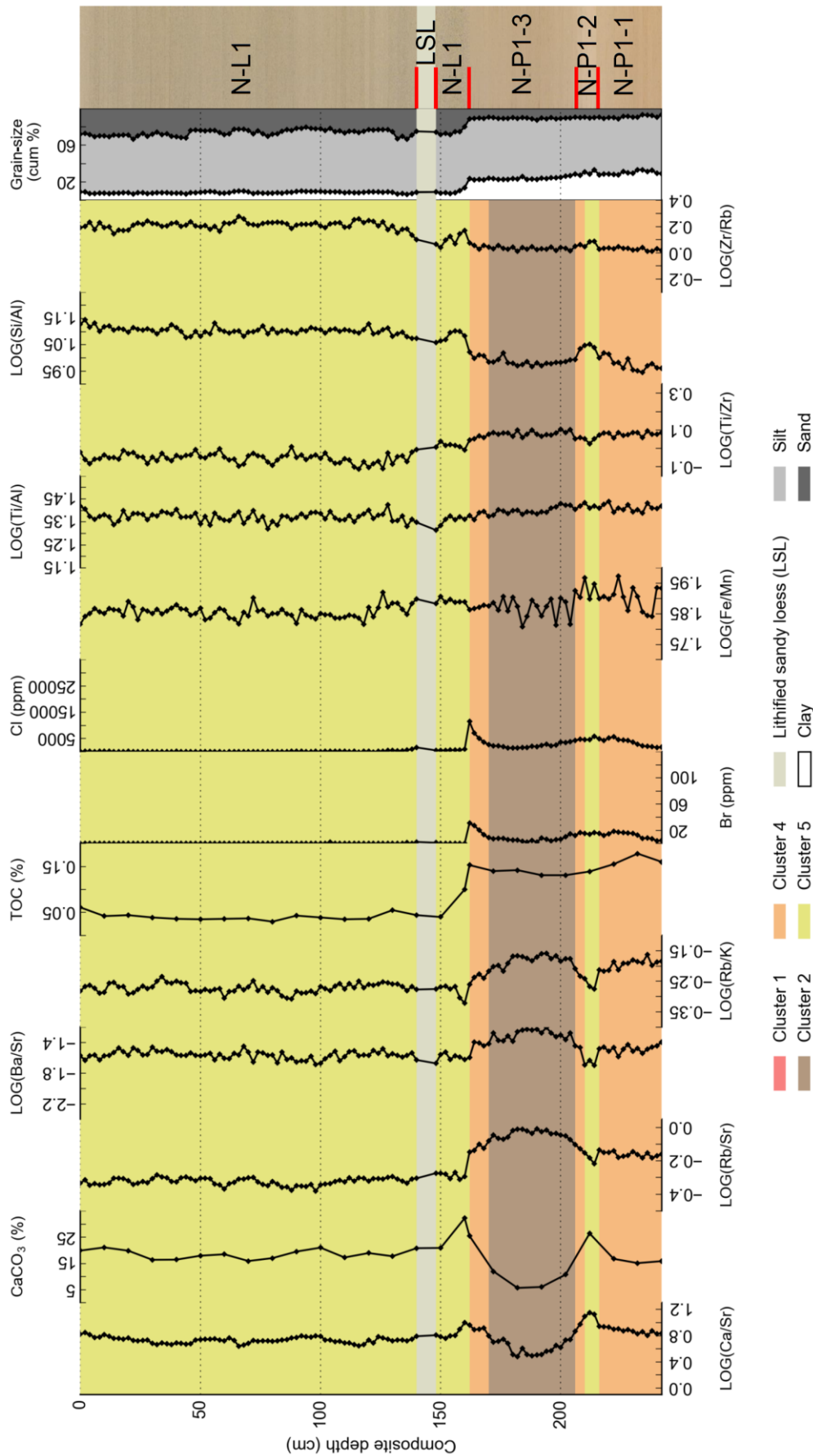


Fig. 5-4: Geochemical record of the Bok N profile together with grain-size data. Color shading indicates chemostratigraphy. The legend displays all elements present in Figs. 5-4, 5-6 and 5-8 for better comparability. X-axes limits are the same in Figs. 5-4, 5-6 and 5-8 for better comparability (cum %: cumulative %).

The weathering indices (Rb/Sr, Ba/Sr, Rb/K) mirror the patterns of Ca/Sr and CaCO₃ and are negatively correlated with these two parameters (Figs. 5-4 and 5-5). TOC only changes between loess and paleosol with values between 0.12-0.18 % in the red paleosol and below 0.06 % in the loess (Fig. 5-4). Br and Cl are well-correlated ($\rho = 0.86$, Figs. 5-4 and 5-5) and also correlated to TOC with $0.78 \leq \rho \leq 0.84$. Both are enriched in N-P1 with N-P1-1 being more enriched ($\leq 19 \pm 5$ ppm Br and $< 5,800 \pm 360$ ppm Cl) than N-P1-3 ($\leq 8 \pm 5$ ppm Br and $< 3,000 \pm 315$ ppm Cl) apart from their absolute maxima (31 ± 5 ppm Br and $11,443 \pm 776$ ppm Cl) at the top of N-P1-3. Br and Cl drop to $\leq 8 \pm 5$ ppm Br and $< 2,500 \pm 315$ ppm Cl within the upper 10 cm of N-P1-3 while the central calcite-enriched horizon N-P1-2 is not reflected in their profiles (Fig. 5-4). Fe/Mn represents a constant profile with an increased variability in N-P1 (Fig. 5-4).

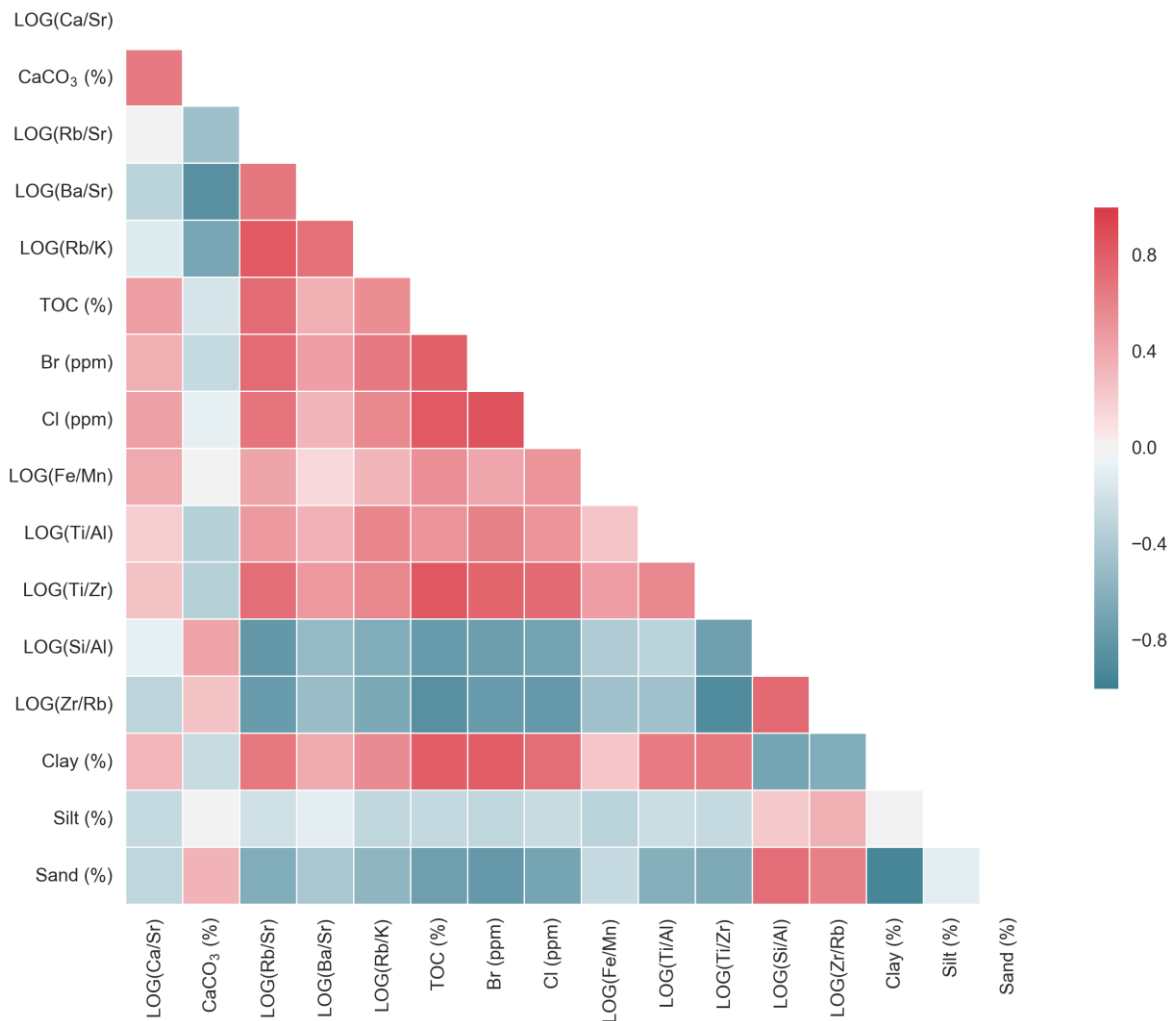


Fig. 5-5: Correlation matrix between geochemical and grain-size proxies for Bok N. Correlation is indicated by the Spearman rank correlation coefficient (ρ). Due to 10 cm sampling resolution of total organic carbon (TOC) and CaCO₃, ρ is calculated on the basis of 26 samples for these two parameters at Bok N.

While Ti/Al and Ti/Zr depict a constant profile ($\rho = 0.58$, Fig. 5-4) with a slight decline at the transition from the red paleosol to the loess, Si/Al shows the opposite trend with a sharp increase towards the loess (Figs. 5-4 and 5-5). In addition, Si/Al gradually increases in N-P1-1 with a local maximum in N-P1-2. The grain-size index Zr/Rb is very similar to Si/Al

($\rho = 0.74$, Figs. 5-4 and 5-5). Si/Al and Zr/Rb particularly reflect changes in the sand fraction while the clay fraction is negatively correlated to both ratios (Figs. 5-4 and 5-5). The red paleosol exhibits 20-35 % clay and ≤ 10 % sand whereas the loess contains approximately 10 % clay and approximately 25 % sand (Fig. 5-4).

Hierarchical clustering reveals that three of five clusters are present in Bok N (Fig. 5-4). The tripartite structure of N-P1 is also reflected by the clusters as N-P1-1 is assigned to cluster 4 whereas N-P1-2 is mainly attributed to cluster 5 and N-P1-3 is related to cluster 2. In contrast to N-P1, N-L1 completely correlates with cluster 5.

5.3.3. Bok O

Ca/Sr and CaCO₃ are positively correlated ($\rho = 0.96$, Figs. 5-6 and 5-7). Below 150 cm CaCO₃ exhibits the lowest values ranging from 0.2 to 2 %. Within the upper 70 cm of O-P1 CaCO₃ gradually increases up to 18 % CaCO₃. In contrast, Ca/Sr gradually increases from bottom to top throughout O-P1. The loess (O-L1, O-L2) shows fairly constant values of CaCO₃ and Ca/Sr with the absolute maximum of 28 % CaCO₃ at 10 cm depth. The CaCO₃ sample within O-P2 reveals a depletion of at least 10 % compared to the O-L1. Ca/Sr is also characterized by a slight negative excursion in O-P2.

Rb/Sr, Ba/Sr and Rb/K are negatively correlated with Ca/Sr and CaCO₃ ($-0.98 \leq \rho \leq -0.92$, Figs. 5-6 and 5-7) and exhibit a decreasing trend from their absolute maxima at the bottom of O-P1 towards the top of O-P1, relative constant values in the loess (O-L1, O-L2) and a minor positive excursion in O-P2 (Fig. 5-6). Furthermore, especially Rb/Sr and Rb/K are strongly correlated with silt ($\rho = 0.85$) and sand ($\rho \leq -0.82$, Fig. 5-7). In contrast, TOC is characterized by three peaks in O-P1 at 210 cm (0.18 %), 130 cm (0.17 %) and 90 cm (0.19 %), one peak in O-P2 at 20 cm (0.18 %) and one peak in O-L2 at 10 cm (0.17 %). However, O-P1 and O-L2 are both represented by only one TOC sample due to the different sampling resolution.

Br and Cl are positively correlated ($\rho = 0.98$, Figs. 5-6 and 5-7) but show a weaker correlation with TOC ($\rho = 0.69$) and are not correlated with the other weathering indices ($-0.20 \leq \rho \leq 0.00$, Fig. 5-7). The absolute maxima with a Br concentration of 122 ± 5 ppm and a Cl concentration of $30,725 \pm 2,139$ ppm occur in the topmost 20 cm of O-P1 with a sharp transition to low values in the overlying loess (O-L1) and a more gradual transition to low values with minor positive fluctuations within O-P1 (Fig. 5-7). Minimum concentrations exist for the lowest 30 cm of the profile and between 40 and 80 cm in O-L1. The uppermost 40 cm of the Bok O profile are characterized by a moderate positive excursion with concentrations up to 66 ± 5 ppm Br and $20,032 \pm 1,372$ ppm Cl in both O-P2 and O-L2. Fe/Mn reflects a constant line with a positive excursion in the lowest part of O-P1 from 230-190 cm and a negative excursion around 166 cm (Fig. 5-6). In addition, a subtle negative excursion occurs at 20 cm in O-P2 (Fig. 5-6).

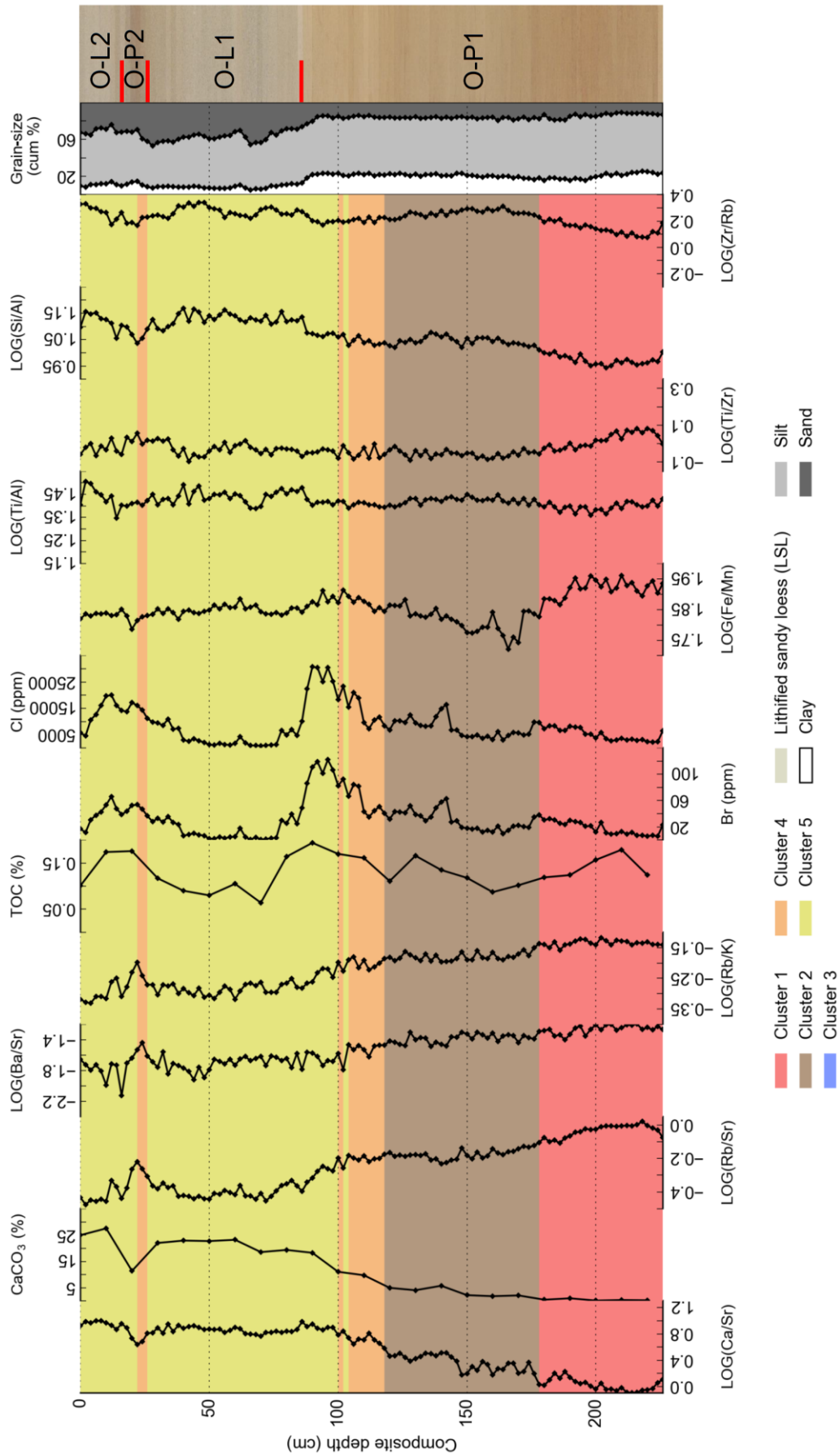


Fig. 5-6: Geochemical record of the Bok O profile together with grain-size data. Color shading indicates chemostratigraphy. The legend displays all elements present in Figs. 5-4, 5-6 and 5-8 for better comparability. X-axes limits are the same in Figs. 5-4, 5-6 and 5-8 for better comparability (cum %: cumulative %).

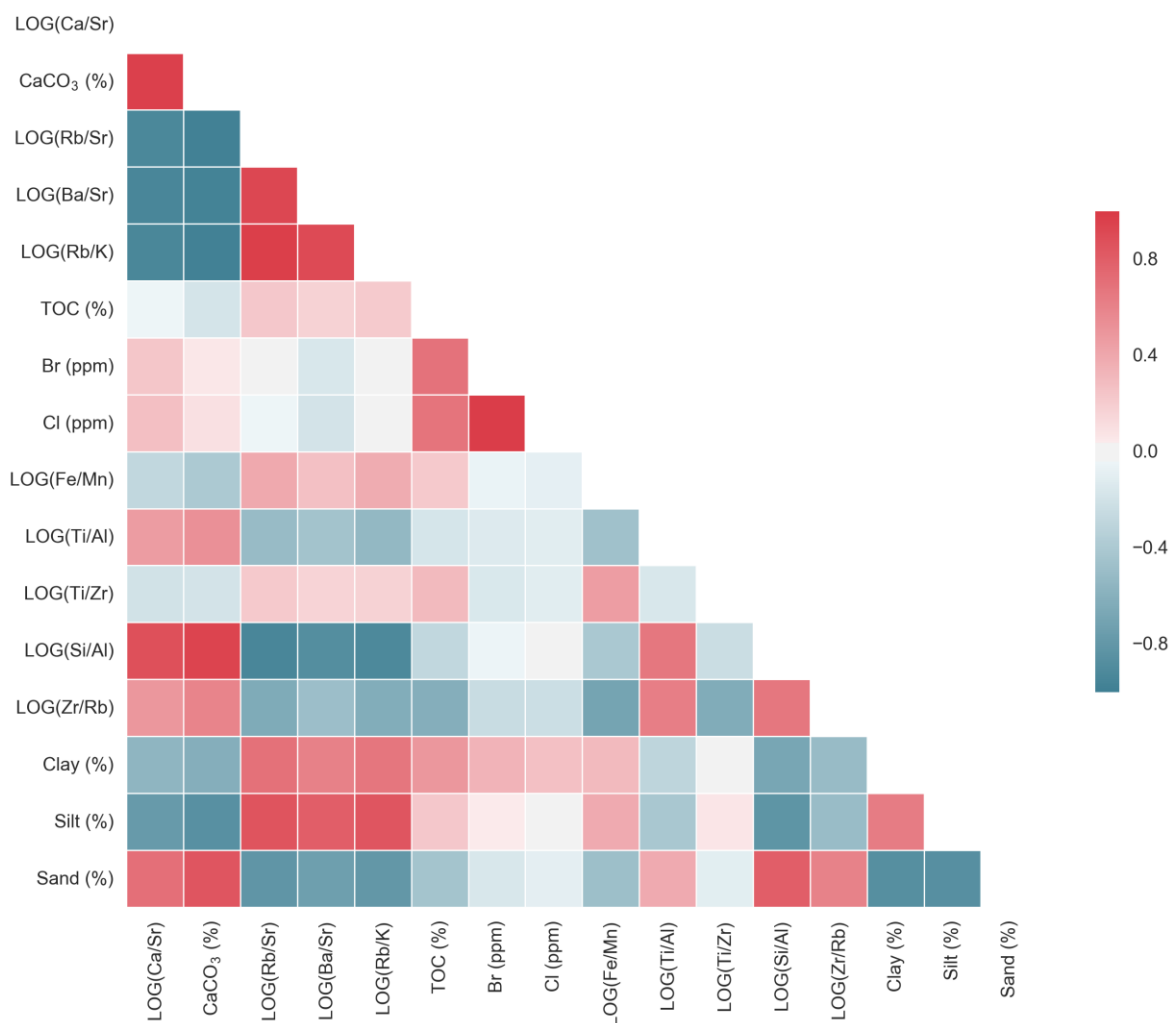


Fig. 5-7: Correlation matrix between geochemical and grain-size proxies for Bok O. Correlation is indicated by the Spearman rank correlation coefficient (ρ). Due to 10 cm sampling resolution of total organic carbon (TOC) and CaCO₃, ρ is calculated on the basis of 23 samples for these two parameters at Bok O.

The provenance index Ti/Al shows a constant profile with subtle variations along Bok O whereas Ti/Zr shows a slight gradual decrease in the lowest 50 cm of O-P1 and rather stable values for the rest of Bok O (Fig. 5-6). Si/Al demonstrates another pattern with a gradual increase within O-P1, a sharp increase at the transition to O-L1 and constant values in O-L1 and O-L2 with a subtle negative excursion in O-P2. Si/Al is positively correlated with Ti/Al ($\rho = 0.67$) and with sand ($\rho = 0.80$) but negative with silt ($\rho = -0.83$, Fig. 5-7). Zr/Rb follows the basic trend of Ti/Zr but in opposite direction ($\rho = -0.63$, Figs. 5-6 and 5-7). Comparing Zr/Rb and Si/Al ($\rho = 0.67$) with grain-size data (Fig. 5-6), the sharp grain-size transition between O-P1 and O-L1 for clay and sand contents seems to be better recorded by Si/Al. The best correlation between grain-size and element ratios is found in O-P2 where clay increases by 5 % and accompanies slight negative excursions of Si/Al and Zr/Rb (Fig. 5-6).

Bok O is represented by four different clusters (Fig. 5-6). In contrast to the stratigraphic description, the hierarchical clustering subdivides O-P1 into four parts. The lowest 48 cm of

O-P1 are related to cluster 1 while the middle part (178-118 cm) is assigned to cluster 2. The upper part of O-P1 is split into cluster 4 (116-100 cm) and cluster 5 (98-86 cm). O-L1 and O-L2 are assigned to cluster 5. The lower part of O-P2 is attributed to cluster 4 whereas the upper part is attributed to cluster 5.

5.3.4. Bok P

The calcium carbonate content is lowest in P-P1 with < 5 % while it increases to 13 % in P-P2 and peaks at 30 % in P-P3. Instead, P-L1, P-L2 and P-S1 show similar values of 15 to 25 % for CaCO₃ (Fig. 5-8). These changes are reflected by Ca/Sr ($\rho = 0.83$), although the magnitude of changes appears to be smaller for the element ratio (Fig. 5-8). There are very subtle negative excursions in P-P1 and P-P2 while there is one homogeneous positive excursion in P-P3 (Fig. 5-8).

The weathering indices (Rb/Sr, Ba/Sr, Rb/K) exhibit individual patterns that are only partly coupled (Figs. 5-8 and 5-9). Ba/Sr represents a constant but noisy profile with slightly increased values in P-P1. Rb/Sr is characterized by a homogeneous maximum in P-P1, intermediate values in P-L1 and a minor positive excursion in P-P2. The next change occurs approximately 20 cm above P-P2 with first the absolute minima along the profile and fairly constant values afterwards up to the top of P-P3. There is neither a change at the transition between P-L2-1 and P-L2-2 as well as between P-L2-2 and P-P3 nor within P-P3. Rb/Sr sharply declines to low constant values at the transition to P-S1 (Fig. 5-8). In contrast, Rb/K can be summarized in three main parts. The highest values are recorded in P-P1 with a gradual decrease to average values in the lower half of P-L1. Such average values remain constant up to the lowermost part of P-P3 with no alterations in P-P2. After a sharp decline in the lowermost part of P-P3, Rb/K gradually increases towards the top of Bok P (Fig. 5-8).

TOC reflects paleosols with values > 0.15 % and has the best correlation with Rb/Sr ($\rho = 0.72$) among the weathering indices (Figs. 5-8 and 5-9). P-P3 is of particular interest as there is no double structure visible in the weathering indices but tentatively in the TOC profile with two maxima separated by a local minimum. However, this minimum is represented by a single sample only according to the lower sampling resolution of 10 cm for TOC (Fig. 5-8). Br and Cl concentrations are very low ($< 16 \pm 5$ ppm Br and $\leq 5,240 \pm 404$ ppm Cl) along Bok P but with subtle positive excursions in P-P1 and P-P2. On the contrary, P-P3 does not show any increased Br and Cl concentrations. Nevertheless, Br and Cl correlate moderately with Rb/Sr ($0.41 \leq \rho \leq 0.63$) and TOC ($0.36 \leq \rho \leq 0.70$, Fig. 5-9). Fe/Mn is almost constant along Bok P except for P-L2-2 and the lower two thirds of P-P3 exhibiting low values (Fig. 5-8).

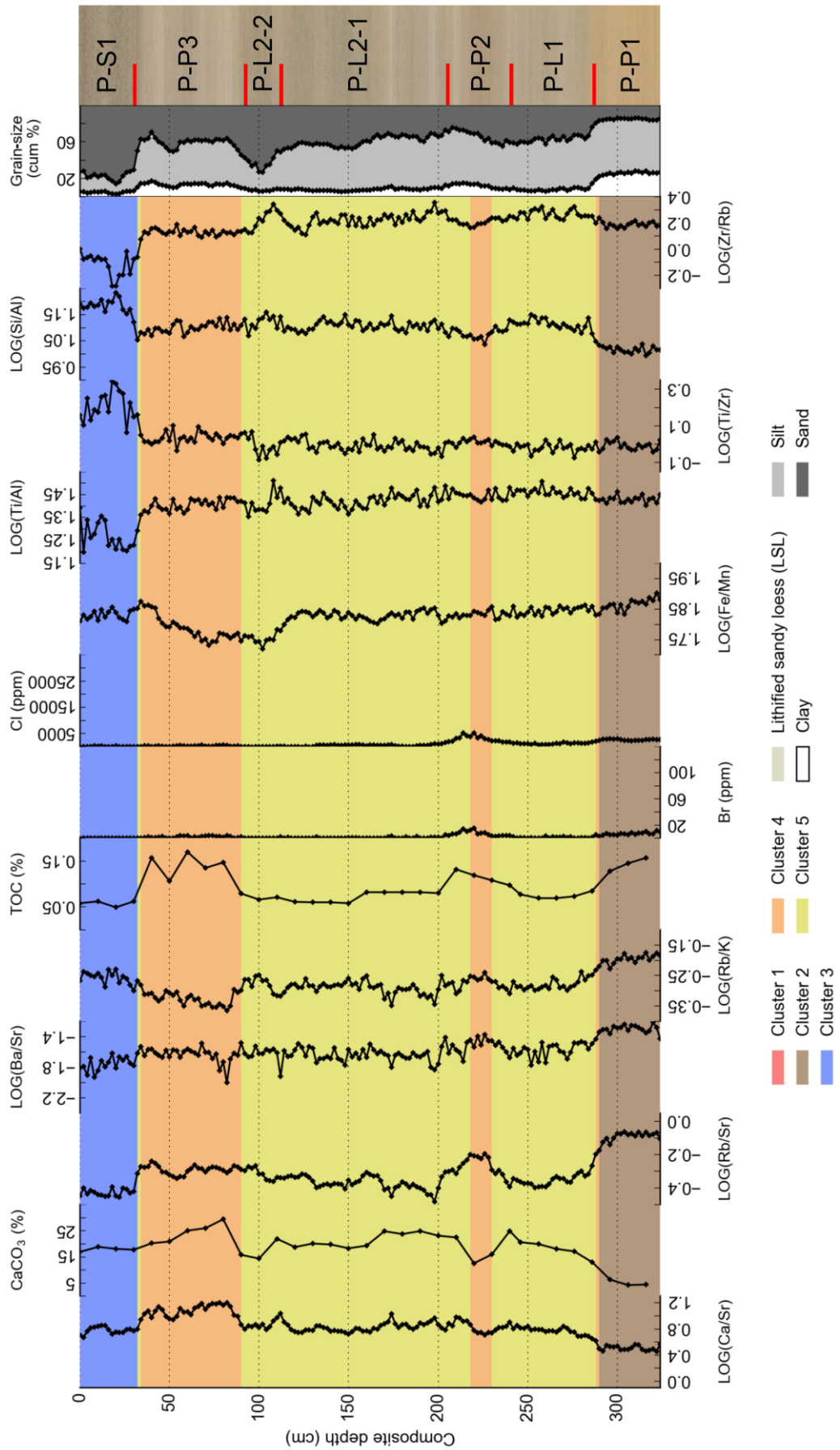


Fig. 5-8: Geochemical record of the Bok P profile together with grain-size data. Color shading indicates chemostratigraphy. The legend displays all elements present in Figs. 5-4, 5-6 and 5-8 for better comparability. X-axes limits are the same in Figs. 5-4, 5-6 and 5-8 for better comparability (cum %: cumulative %).

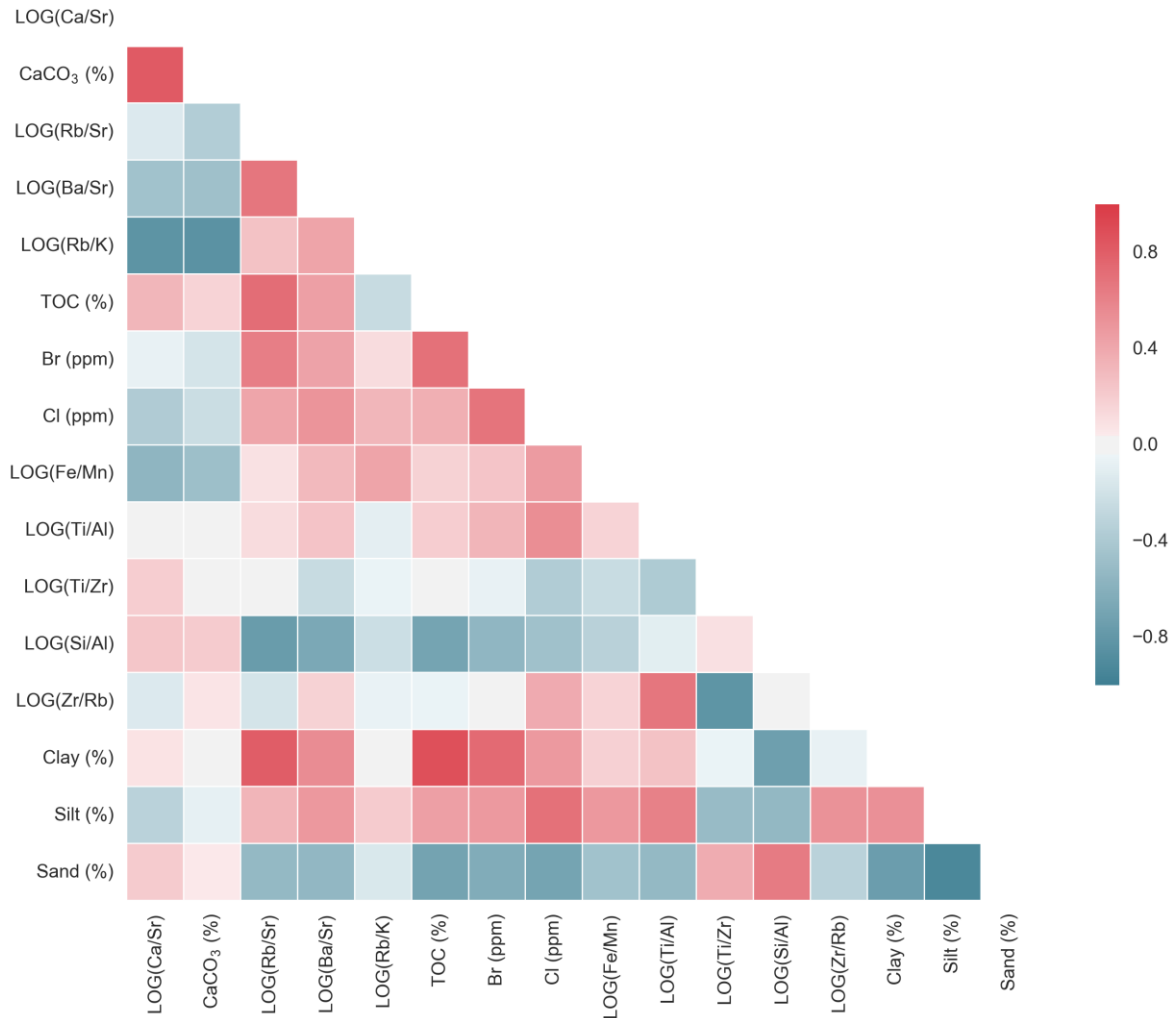


Fig. 5-9: Correlation matrix between geochemical and grain-size proxies for Bok P. Correlation is indicated by the Spearman rank correlation coefficient (ρ). Due to 10 cm sampling resolution of total organic carbon (TOC) and CaCO₃, ρ is calculated on the basis of 33 samples for these two parameters at Bok P.

The provenance indices are alike each other except for P-S1 where Ti/Al decreases while Ti/Zr and Si/Al increase (Fig. 5-8). Opposed to Ti/Al and Si/Al, Ti/Zr additionally reveals a tiny increase in the upper third of P-L2-2 and within P-P3. Compared to Ti/Al and Ti/Zr, Si/Al additionally shows minimum values in P-P1. Zr/Rb is similar to Ti/Al (Fig. 5-8) and is only moderately coupled with silt (Fig. 5-9, $\rho = 0.52$). Along Bok P, there are large grain-size variations between P-P1 and the rest of the profile. P-P1 exhibits 25-30 % clay and 15 % sand whereas loess and P-S1 consist of < 15 % clay and 30-70 % sand (Fig. 5-8). These large variations are, however, not sufficiently recorded in the Zr/Rb profile. Instead, Si/Al corresponds mostly to changes in clay ($\rho = -0.74$) and sand (Fig. 5-9, $\rho = 0.65$).

Hierarchical clustering refers to P-P1 as cluster 2 while P-P2 partly and P-P3 completely correlate with cluster 4. P-L1 and P-L2 are related to cluster 5 whereas P-S1 is assigned to cluster 3. In total, Bok P is reflected by four different clusters (Fig. 5-8).

5.4. Discussion

5.4.1. Reliability of XRF scanning-derived element ratios

We presented XRF scanning-derived element ratios and compared them with TOC, CaCO₃ and grain-size data. In this section we check the reliability of element ratios against mineralogical, micromorphological and additional geochemical studies carried out either at the same profiles or at the same stratigraphic positions. This section is structured in the same way as the results and considers each profile individually. We start with the discussion of Ca/Sr as proxy for secondary calcification followed by discussions of Rb/Sr, Ba/Sr and Rb/K as weathering indices, Fe/Mn as indicator for redox conditions, Ti/Al, Ti/Zr and Si/Al as dust provenance indices as well as Si/Al and Zr/Rb as grain-size indices. Br and Cl are discussed separately in section 5.4.2.

5.4.1.1. Bok N

The decrease of Ca/Sr in N-P1-3 (Fig. 5-4) indicates that decalcification during pedogenesis was stronger than post-pedogenetic secondary calcification. CaCO₃ content, rhizoconcretions and micromorphological investigations confirm post-pedogenetic secondary calcification in N-P1 (Durn et al., 2017b). According to calcified roots of modern grass found in NP-1, secondary calcification is considered as an ongoing process (Durn et al., 2017b). Furthermore, Ca/Sr as well as Rb/Sr, Ba/Sr and Rb/K document the same tripartite structure of N-P1 as reported by Durn et al. (2017b). They classify N-P1, which they term as the red paleosol, based on soil properties as preserved B-horizon of a Hypereutric Chromic Cambisol (Episiltic, Endoloamic) according to the soil classification system of the World Reference Base for Soil Resources (WRB, 2015). Although clay mineralogical and micromorphological investigations suggest a polygenetic soil formation in terms of incorporating old soil material in the very likely antepenultimate loess from which the red paleosol (N-P1) formed, Durn et al. (2017b) propose top-down in-situ weathering for the red paleosol (N-P1) due to poorly sorted coarse material and a gradual decrease in the clay/silt ratio from bottom to top. Consequently, a polygenetic pedogenesis as supposed for the pedocomplexes P7 and P2 at Paudorf (Austria), being the result of several cycles of pedogenesis, erosion, reworking and dust accumulation (Sprafke et al., 2014), appears unlikely for N-P1. Since secondary calcification is present, it is likely that Rb/Sr and Ba/Sr underestimate weathering intensity, especially for the stronger re-calcified N-P1-1 horizon (Fig. 5-4). This explanation is underlined by Rb/K showing the same positive values in N-P1-1 and N-P1-3 separated by lower values in N-P1-2 (Fig. 5-4). However, illitization, i.e. K-fixation, may adversely affect Rb/K (Bugge et al., 2011), albeit Nesbitt et al. (1980) report slightly increased Rb/K values for samples affected by increased illite contents. Since smectite followed by illitic material predominate the clay fraction in N-P1 (Durn et al., 2017b), we cannot completely rule out illitization as a factor influencing Rb/K. Nonetheless, we consider Rb/K as the most reliable weathering index.

Although Fe/Mn varies more in N-P1 than in N-L1 (Fig. 5-4), there is no evidence of changing redox conditions in terms of Mn depletion. However, fine Fe/Mn nodules and

concretions are inferred from thin sections indicating pseudogleyization in N-P1 (Durn et al., 2017b). Given the facts that (1) Fe/Mn nodules may have large variations in their Fe/Mn ratios with a tendency towards lower ratios in smaller concretions (Zhang and Karathanasis, 1997) combined with (2) the occurrence of anaerobic microenvironments favoring mobilization of Fe and Mn due to the respiration of plants and microorganisms in well-aerated soils (Keiluweit et al., 2016) and (3) that calcite fixates Mn in soils (Fujimoto and Sherman, 1948), the higher variability of the XRF scanning-derived Fe/Mn ratio in N-P1 likely reflects the results of interactions between all these processes.

Higher TOC values (> 0.12 %) throughout N-P1 increase with pedogenesis (Fig. 5-4). However, Durn et al. (2017b) describe a decreasing trend of organic carbon with depth from 0.6 to 0.0 %. As the samples investigated by Durn et al. (2017b) were taken at the same profile, this difference might be attributed to the different methods used for organic carbon estimation: direct measurement (our study) vs. calculation from total carbon also determined by an element analyzer and CaCO₃ determined gas-volumetrically (Durn et al., 2017b). Comparing our CaCO₃ values with the gas-volumetrically measurements of Durn et al. (2017b) at the same profile and the acid treatment-based estimation of Mikulčić Pavlaković et al. (2011) on different samples from a nearby subprofile, points to an underestimation of approximately 5 % of our method except for N-P1-2. N-P1-2 (214-208 cm) corresponding to the Bwb 2 horizon in Durn et al. (2017b) reveals 26.5 % CaCO₃ (our estimate) compared to 14.7 % CaCO₃ reported by Durn et al. (2017b). Tentatively, sample homogenization might be responsible for such a difference. Apart from this difference, N-P1-2 with maxima in Ca/Sr and minima in Rb/Sr, Ba/Sr and Rb/K in a 6 cm thick horizon (Fig. 5-4) emphasizes the importance of high-resolution data. Such a thin zone of variability might be overseen or only represented by one sample with a sampling resolution of more than 4 cm.

The constant profiles of Ti/Al and Ti/Zr (Fig. 5-4) confirm that the parent material of N-P1 is the same as the overlying loess and thus no dust source changes occurred. This corroborates the findings of Durn et al. (2017b) who used ICP emission spectrometry determined Ti/Al as a provenance indicator. Furthermore, the mineralogy of bulk, clay, heavy and light mineral fractions underline strong similarities between N-P1 and the overlying loess N-L1 (Durn et al., 2017b). Variations in Si/Al are predominated by grain-size dynamics (Figs. 5-4 and 5-5) rather than dust source changes as suggested by Liang et al. (2013) and thus approves its applicability as indirect weathering index representing clayeyness (Sheldon and Tabor, 2009). Our results show the same trend like the Al/Si ratio considered by Durn et al. (2017b) in terms of a weathering index according to Sheldon and Tabor (2009). Comparing Si/Al with Zr/Rb (Figs. 5-4 and 5-5), Si/Al better reflects grain-size changes at the Bok N profile. Based on the rather coarse loess material (Wacha et al., 2017) with a sand content of approximately 30 % along Bok N, this may point to a stronger enrichment of Si compared to Zr in the sand fraction. While DiLabio (1989) report grain-size related Zr fractionation in Canadian tills but with low Zr concentrations in fine to medium sand and high concentrations in other grain-size fractions, Muhs and Benedict (2006) document no grain-size but provenance related Zr fractionation in Alaskan loess. Therefore, incorporation of recycled material (e.g. Újvári et al., 2008) together with the distance to

source (Muhs and Bettis III, 2000) seem to influence Zr dynamics. Increasing Zr concentrations are positively correlated to sediment recycling and negatively correlated to distance to source rather than grain-size fractionation. In conclusion, the observed trends in elemental compositions along the Bok N profile agree with Mikulčić Pavlaković et al. (2011) who analyzed three samples from the stratigraphic units present in Bok N (B1-5/6/2, loess; B1-5/5, red paleosol – upper part; B1-5/3, red paleosol – lower part) using ICP techniques.

5.4.1.2. Bok O

Ca/Sr and CaCO₃ values indicate strong decalcification for the lower half of O-P1. The gradual calcification trend towards the top of O-P1 (150-86 cm, Fig. 5-6) points to post-pedogenetic secondary calcification due to decalcification of the overlying loess (O-L1). A further slight decalcification occurs in O-P2. Accordingly, Rb/Sr and Ba/Sr might underestimate weathering intensity in the upper half of O-P1 due to calcite dynamics (Buggle et al., 2011). However, as Rb/K strongly correlates with Rb/Sr and Ba/Sr ($\rho \geq 0.90$, Figs. 5-6 and 5-7), all indices are assumed to provide reliable information about weathering intensity for the whole Bok O profile. The TOC maxima neither support nor challenge the XRF scanning-derived weathering indices but may indicate a polygenetic pedogenesis including slope-induced reworking processes as the maximum of organic carbon is expected to occur in the topsoil. Because highest Rb/K values in the lower third of O-P1 (226-178 cm) coincide with high TOC values (Fig. 5-6), this either suggests in-situ paleosol formation in loess or, similar to N-P1, to in-situ paleosol formation in a mixture of loess and old soil material. The middle part of O-P1 up to the next TOC maximum at 130 cm (Fig. 5-6) may represent another in-situ soil formation in reworked colluvial soil material deposited on top of the previous paleosol (lower third of O-P1). The top part of O-P1 (128-86 cm) may be related to another phase of colluvial activity with subsequent time-limited pedogenesis due to a TOC maximum at 90 cm. The absolute minimum in the Fe/Mn ratio (172-164 cm, Fig. 5-6) may reflect a horizon of preferred re-oxidization of Mn, albeit the question, why this horizon occurs at this specific position, has to remain open and requires detailed micromorphological investigations. The same holds true for the second minimum in O-P2, tentatively indicating the initial formation of small Fe/Mn-nodules characterized by higher Mn concentrations (Zhang and Karathanasis, 1997).

Dust source changes are unlikely owing to the constant profiles of Ti/Al and Ti/Zr (Maynard, 1992; Sheldon, 2006; Zech et al., 2008). Si/Al is strongly coupled to grain-size changes (Figs. 5-6 and 5-7) and thus disqualifies as a dust provenance indicator. In contrast, Zr/Rb is only moderately correlated with grain-size changes (Fig. 5-7) owing to elevated Zr counts between 190 and 120 cm opposed to gradually increasing Rb counts with depth throughout O-P1 (supplementary material). The decrease of Zr below 190 cm also explains the slight increase in Ti/Zr as Ti remains constant. This Zr dynamic may point to a dust source change or the incorporation of recycled sediment (cf. Profe et al., 2016) in terms of reworked soil material between 190 and 120 cm. Moreover, the clay/silt ratio used to identify top-down pedogenesis at N-P1 by a decreasing trend from bottom to top (Durn et al., 2017b), shows

the same trend at O-P1 from 226 to 190 cm but an opposed trend above supporting the idea of polygenetic pedogenesis, especially in the upper part of O-P1 (190-86 cm). Consequently, O-P1 might be considered as a paleosol complex similar to the paleosol complexes P7 and P2 at Paudorf in Austria characterized by multiple phases of pedogenesis, reworking, erosion and dust accumulation (Sprafke et al., 2014).

Mikulčić Pavlaković et al. (2011) provide quantitative element data to verify the element dynamics identified by the XRF data. However, even under the presumption that O-P1 stratigraphically equals the orange-brown paleosol, the comparison is limited to one sample from the orange-brown paleosol (B1-5/7/2) and a loess sample from a slightly humified horizon above the orange-brown paleosol (B1-5/8/1) that were taken at a nearby location. Ca and Sr are depleted whereas Rb, Ba, Al, Ti, Fe and Zr are enriched in the orange-brown paleosol consistent with our observations at O-P1. Contrary to our XRF scanning data, also K is enriched by 0.4 % from 1.95 to 2.38 % (numbers referring to K₂O weight %) in the orange-brown paleosol (Mikulčić Pavlaković et al., 2011). Although this is likely attributed to the different sample locations it may also indicate that the XRF scanning-derived Rb/K index might overestimate weathering due to not taking the increase in K into account. The latter is supported by both weak correlations between quantitative and XRF scanning-derived K measurements (Huang et al., 2016; Sun et al., 2016) and mineralogical investigations showing illite and chlorite as dominant clay minerals (Mikulčić Pavlaković et al., 2011).

5.4.1.3. Bok P

Ca/Sr suggests strong secondary calcification in P-P3 with highest values and subtle decalcification or initial decalcification overprinted by subsequent secondary calcification for P-P1 and P-P2 (Fig. 5-8). This hypothesis is confirmed by absolute CaCO₃ values, albeit P-P1 seems to be least affected by secondary calcification with CaCO₃ values < 10 % (Fig. 5-8). In addition, calcified roots were present throughout the profile with the most secondary carbonates present in P-P3.

Despite the observed calcite dynamics, Rb/Sr indicates weathering in P-P1 and P-P2 whereas it indicates no weathering in P-P3. Ba/Sr shows a constant but noisy profile while Rb/K is high in P-P1 but low in P-P3 (Fig. 5-8). This indicates that secondary calcification negatively affects Sr-based weathering indices (Buggle et al., 2011) and that the differences in Ba and maybe Sr are too small to be reliably detected by XRF scanning. However, a comparison of Ba and Sr concentrations along the Bok 1 composite profile (cf. Mikulčić Pavlaković et al., 2011) shows an enrichment of 40-60 ppm Ba and a depletion of 30-60 ppm Sr in the paleosols (not shown). Considering the raw counts of Rb and K reveals that in P-P3 the Rb counts remain on the loess level while K counts are slightly increased (supplementary material). This is in line with samples B1-5/9/3, B1-5/10/1 and B1-5/10/3 from Mikulčić Pavlaković et al. (2011) documenting an increase of K₂O by 0.3 % from 1.72 to 2.02 % K₂O and a subtle increase of Rb by 20 ppm from 68 to 88 ppm in the brown double paleosol (P-P3). In P-P1, K counts remain constant whereas Rb counts are distinctly

increased (supplementary material). This may indicate either illitization, which might be in concordance with an increased clay content (Fig. 5-8), or an increased K-feldspar content for P-P3. However, due to missing clay mineralogy of P-P3, this question has to remain open. In contrast to the weathering indices, TOC clearly indicates pedogenesis by elevated values in P-P3. Fe/Mn also exhibits higher Mn values for P-P3. This might be explained by the Mn fixating effect of calcite (Fujimoto and Sherman, 1948) or preferential forming of small Fe/Mn nodules (Zhang and Karathanasis, 1997).

Ti/Al and Ti/Zr seem to identify a dust source change for P-S1 due to low Ti/Al and high Ti/Zr values (Fig. 5-8). Si/Al and Zr/Rb also notice this change, even though Si/Al is unambiguously related to grain-size (Fig. 5-9). It reflects the tripartite structure of the sand content best (Fig. 5-8). Taking the variations of the raw counts of Ti, Al, Zr and Si between P-S1 and the rest of the profile into account, P-S1 is characterized by low Ti, rather constant Al, very low Zr and high Si counts (supplementary material). This fully agrees with the geochemical data presented for the samples B1-5/10/1, B1-5/10/3 and B1-5/11 in Mikulčić Pavlaković et al. (2011). Consequently, Ti/Al and Ti/Zr do not necessarily reflect dust source changes here but wind strength-induced changes in mineralogy. This is supported by coarse material being enriched in micaceous minerals and depleted in ultrastable minerals such as zircon, tourmaline and rutile (Mikulčić Pavlaković et al., 2011) tentatively explaining low Zr and high Al counts in P-S1. Another line of evidence are ultradense minerals that are suggested as proxies for both distance-to-source and wind strength with frequent occurrences in Northern Italy (proximal to source, Ferraro, 2009) and rare occurrences on Susak (distal to source, Mikulčić Pavlaković et al., 2011). In addition, Chen et al. (2013) demonstrate that long distance transport of eolian dust exemplified on Asian dust storm events accompanies gravity fractionation of heavy minerals and reduced Ti/Al ratios. Hence, there is no dust source but wind speed change responsible for the transport of different minerals that are not coercively linked to the observed changes in grain-size. This dismantles Zr/Rb as reliable grain-size proxy on Susak (Fig. 5-8). On the contrary, due to pronounced alterations in Si according to fluctuations in the sand content (Fig. 5-9, supplementary material), Si/Al competes with Zr/Rb as reliable grain-size proxy on Susak.

5.4.2. Bromine and chlorine

The elements Br and Cl are ubiquitously present in soils at low ppm levels and preferably related to organic matter (Leri and Myneni, 2012; Öberg, 2003). Br concentrations typically range from 5 to 40 ppm and Br fixation occurs enzymatically-catalyzed to organohalogene compounds (Leri and Myneni, 2012). Higher Br concentrations correlate with proximity to the sea shore (Leri and Ravel, 2015). Yuita (1983) provides an average Cl concentration of 126 ppm in Japanese soils while Cl concentrations vary between 37-130 ppm in Swedish soils (Öberg, 2003). Ziegler et al. (2008) report a strong correlation between Br and TOC ($R^2 > 0.78$) in marine sediments. Leri et al. (2014) explain this relationship by preferential preservation of brominated aromatic organic compounds in marine sediments. This is consistent with Cl/Br ratios of 288 for sea water, 300 for rain water and around 10 for soils in Western Australia (Gerritse and George, 1988). Consequently, in case Br and Cl are

suitable as proxies for transgressions of the Adriatic Sea, their ratio is expected to be smaller than 300 and Br is expected to be strongly correlated with TOC.

However, Cl/Br ratios between 250 and 375 (Table 5-3) suggest rainwater or sea spray as source and in addition no direct link to organic matter. This is especially true against the background of maximum TOC concentrations of 0.19 % but contradictory to a moderate correlation between TOC and both Br ($R^2 = 0.61$) and Cl ($R^2 = 0.71$) at Bok N. Since Br and Cl are typically bound to organic matter in the topsoil impeding further biodegradation, halogenated organic matter might be more stable. However, deeper in the soil, there are several pathways available for dehalogenation under both aerobic and anaerobic conditions (Leri and Myneni, 2010, 2012). Thus, our results indicate that the observed Br and Cl dynamics are not only controlled by the availability of TOC but also influenced by other processes. Presumably, Mediterranean climate conditions play a dominant role in Br and Cl entrapment by evaporation and temporal fixation in soil pore-water or in the form of micro salt crystals in soil pores. Frequent wet-dry cycles as deduced from micromorphological investigations of Fe/Mn-nodules in N-P1 (Durn et al., 2017b) support this hypothesis. Hence, the sharp decline of Br and Cl with depth in the uppermost 10 cm of N-P1-3 (Fig. 5-4) might be related to a combination of increased water retention due to increased clay content and vicinity to the sediment surface favoring frequent desiccation of the uppermost 10 cm during dry phases. Besides proximity to the sediment surface (N-P1-3, O-L2 and O-P2), proximity to the present water surface and thus to sea-water spray produced by waves (N-P1-1, O-P1) might be responsible for the observed Br and Cl maxima (Table 5-3). Consequently, our current knowledge prevents Br and Cl from being used as a proxy for transgressions of the Adriatic Sea. Br and Cl may rather serve as a proxy for modern Na input due to modern sea-water spray thus identify a challenge for using Na as the mobile element in weathering indices. Mikulčić Pavlaković et al. (2011) suggested a potential sea-water spray influence on weathering proxies if Na is used.

Table 5-3: Br and Cl concentration maxima together with Cl/Br ratios for the profiles Bok N, Bok O and Bok P. Concentration uncertainties are given at the 95 % confidence level.

Location	Profile depth (cm)	Max. Br (ppm)	Max. Cl (ppm)	Cl/Br
Bok P – P-2	214	14 ± 5	5,239 ± 406	374
Bok P – P-2	220	15 ± 5	5,209 ± 404	347
Bok O – O-L2 and O-P2	12	66 ± 5	20,032 ± 1,372	304
Bok O – O-P1	90	111 ± 5	30,725 ± 2,139	277
Bok O – O-P1	96	122 ± 5	30,498 ± 2,122	250
Bok N – N-P1-3	162	31 ± 5	11,443 ± 776	369
Bok N – N-P1-1	52	17 ± 5	5,787 ± 432	340
Bok N – N-P1-1	60	19 ± 5	5,679 ± 427	299

5.4.3. Chemostratigraphy vs. lithostratigraphy

In general, the lithostratigraphy is well reflected in the established chemostratigraphy with a preset number of five clusters. The chemostratigraphy reliably separates loess from paleosols albeit sometimes attributing paleosols such as O-P1 to more than one cluster (Fig. 5-6). Starting with clusters that are unambiguously related to lithostratigraphic units, all loess samples from all investigated profiles are assigned to cluster 5. Therefore, loess can be considered as geochemically homogeneous and thus confirming previous mineralogical investigations (Cremaschi, 1990; Mikulčić Pavlaković et al., 2011) that suggest one dominant dust source for loess on Susak – the paleo Po floodplain. However, the sand layer at the top of Bok P (P-S1) differs strongly from all other chemostratigraphic units as only P-S1 is attributed to cluster 3 (Figs. 5-4, 5-6, 5-8). As deduced from weathering-inert element ratios (Ti/Al, Ti/Zr), this does not necessarily reflect a dust source change but wind strength-induced changes in mineralogical composition.

Paleosols are assigned to three different clusters (cluster 1, 2, 4; Figs. 5-4, 5-6, 5-8). Based on N-P1 where most data are available for its characterization, we can understand which elements may influence the established chemostratigraphy most. From a paleopedological perspective N-P1 reflects a tripartite B-horizon (Durn et al., 2017b) and N-P1-1 and N-P1-3 predominantly vary in the strength of secondary calcification with N-P1-1 being stronger recalcified than N-P1-3. N-P1-1 and transitional parts of N-P1-3 are characterized by higher CaCO_3 values and attributed to cluster 4 while most parts of the stronger decalcified horizon N-P1-3 are assigned to cluster 2 (Fig. 5-4). Consequently, cluster 4 can be interpreted as indicative for weak or secondary calcification superimposed on pedogenesis whereas cluster 2 represents intermediate to strong pedogenesis. Applying these characteristics to O-P1 (Fig. 5-6) represented by clusters 1, 2, 3, 5, secondary calcification seems to be the dominant driver of paleosol-related cluster discrimination. Accordingly, cluster 1 covering the lowest 48 cm of O-P1 reflects the strongest pedogenesis among the studied profiles characterized by complete decalcification, highest values of Sr-based weathering indices as well as of Rb/K and Fe/Mn. The middle part of O-P1 (176-118 cm) is assigned to cluster 2 and differs most in Ca/Sr, Fe/Mn and Ti/Zr compared to cluster 1. The upper part from 116-86 cm is reflected by cluster 4 and 5, likely due to a transition to loess-like Ca/Sr and Rb/Sr values in the uppermost 15 cm. This chemostratigraphic subdivision of O-P1 generally agrees with conclusions drawn on possible multiple phases of pedogenesis preserved in O-P1 based on element ratios in comparison with TOC maxima and grain-size (cf. section 5.4.1.2). Hence, we have to update the lithologically-derived O-P1 to O-P1-1 (226-178 cm), O-P1-2 (176-118 cm) and O-P1-3 (116-86 cm) and consider O-P1 as a pedocomplex with at least three different phases of paleosol formation (Fig. 5-10). The attribution of O-P2 to cluster 4 complies with weak pedogenesis characteristic for cluster 4 (Fig. 5-6). The same holds true for the paleosols P-P2 and P-P3 while P-P1 correlates with cluster 2 (Fig. 5-8).

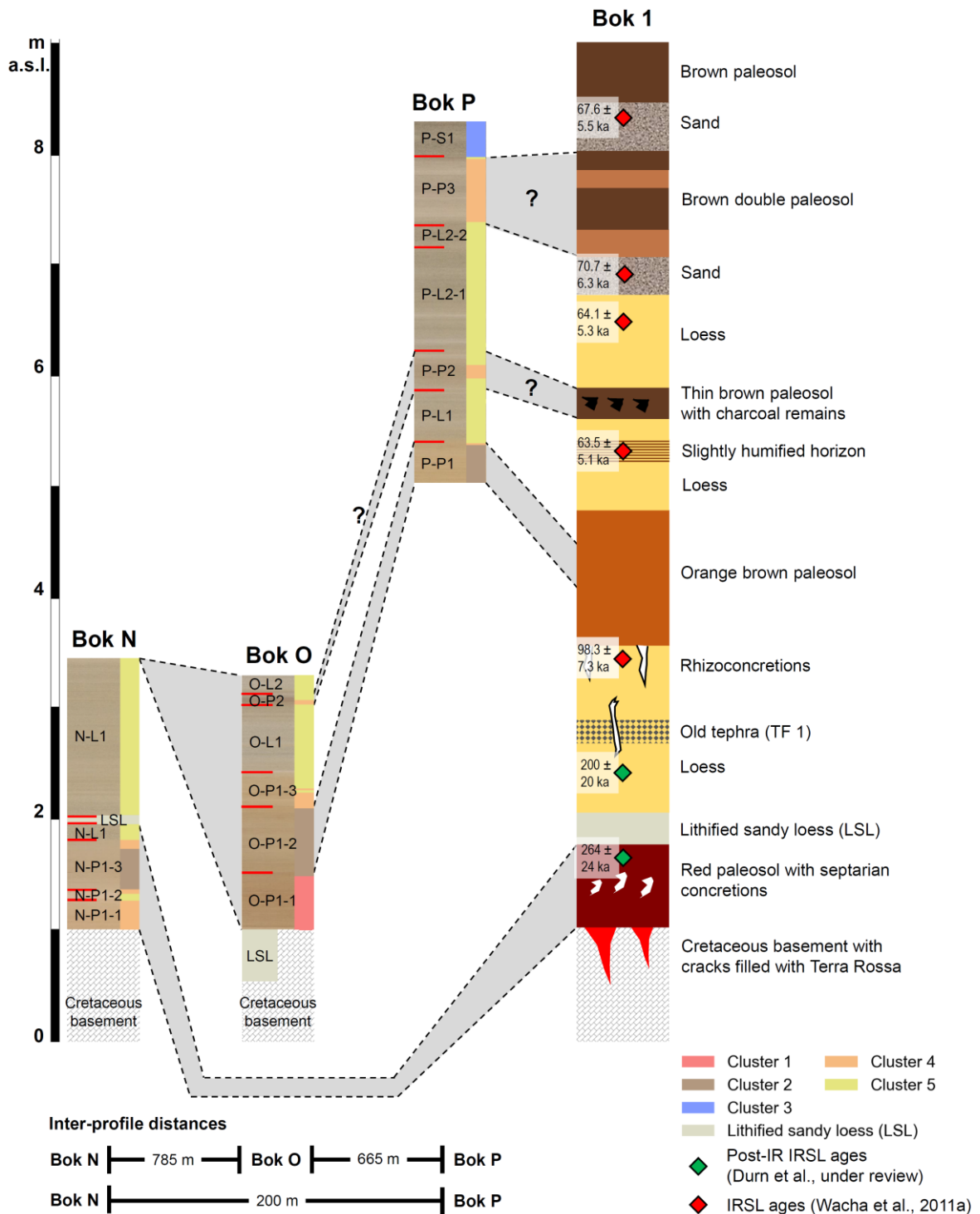


Fig. 5-10: Profile correlation including the previously compiled composite profile Bok 1 by Mikulčić Pavlaković et al. (2011) and Wacha et al. (2011a). In addition, luminescence ages discussed in text are displayed. Question marks indicate tentative correlations.

Based on field observations a correlation is presumed between P-P1 and O-P1. According to the established chemostratigraphy such a correlation seems to be possible only for O-P1-2 as this part of Bok O is attributed to the same cluster as P-P1 (Fig. 5-10). In addition, there might be another correlation between O-P1-2 and N-P1-3 as N-P1-3 also correlates with cluster 2 (Fig. 5-10). In case O-P1 corresponds to the orange-brown paleosol described

in Wacha et al. (2011a) and N-P1 corresponds to the red paleosol described in Wacha et al. (2011a) and Durn et al. (2017b) combined with the assumption that O-P1 might be stratigraphically younger than N-P1 (e.g. Wacha et al., 2011a), a correlation of O-P1 and N-P1 appears unlikely and indicates that a pure cluster-based correlation can be misleading and must be considered with caution. However, investigating the element ratios in detail (Figs. 5-4, 5-6, 5-8), there are slight but unambiguous differences in Ti/Zr and Zr/Rb between N-P1 on the one hand and O-P1-2 as well as P-P1 on the other hand. This suggests a correlation in favor of O-P1-2 and P-P1 (Fig. 5-10). Correlating O-P1-2 with P-P1 implies either an undulated paleorelief or slice-sliding-like reworking processes as proposed by Bognar et al. (2003) due to the elevation difference of approximately 3 m between the same stratigraphic horizon in the profiles Bok O and Bok P (Fig. 5-10).

From a geochemical point of view, we cannot exclude a correlation between P-P2 and O-P2 as both are attributed to cluster 4. However, Bok P coincides with one of the locations investigated by Mikulčić Pavlaković et al. (2011) to compile the composite profile Bok 1 and in contrast to the thin brown paleosol above the orange-brown paleosol at Bok 1 no charcoal remains were found in both O-P2 and P-P2. This may challenge a correlation of O-P2 and/or P-P2 with each other and Bok 1. The same holds true for P-P3 and the brown double paleosol at Bok 1 since XRF scanning-derived element ratios as well as CaCO_3 neither identify a paleosol nor a double structure (Fig. 5-10). Only TOC exhibits elevated values in P-P3 and may point to a double structure. Although not consistent with the TOC maxima, another hint might be the RGB color information showing lighter hues in the upper and lower parts compared to the middle part of P-P3 (Fig. 5-10). Luminescence age control supports this idea by indicating early MIS 4 for the development of P-P3 (Fig. 5-2). If we accept the double structure, the idea of pedogenesis being a consequence of two competing, contemporaneously active processes (dust sedimentation vs. soil development) during MIS 4 (Ferraro, 2009) may explain the observed proxy behavior in P-P3.

5.4.4. Paleoenvironmental implications

As indicated by Ti/Al and Ti/Zr, N-P1 and O-P1 likely developed from material which is similar to material deposited during the last glacial cycle. Thus, we act on the assumption that there is one dominant dust source (the paleo Po floodplain) throughout the considered time period in agreement with previous mineralogical investigations (Cremaschi, 1990; Mikulčić Pavlaković et al., 2011). Durn et al. (2017b) suggest a polygenetic development of N-P1 in partly colluvial material of older soils. Luminescence ages propose their developments during MIS 7 (N-P1, Durn et al., 2017b) and MIS 5 (O-P1, Wacha et al., 2011a). Adjacent paleosols preserved from MIS 7 are sparse, thus limiting a comparison to dated and more distant sites like Šarengrad II in Eastern Croatia (Wacha et al., 2013) and Paks in Hungary (Thiel et al., 2014). Following the comparison of paleosols attributed to MIS 5 with other LPS from adjacent regions (Northern Italy, Istria, Hungary) by Wacha et al. (2011a), MIS 5 paleosols are described as rubified clayey paleosol in Val Sorda (Northern Italy, Ferraro, 2009), as red paleosol in Savudrija, Istria (Durn, 2003; Zhang et al., under review) and as chernozem-like paleosol underlain by a reddish-brown paleosol in

Süttő (Hungary, Novothny et al., 2011). In Süttő, the reddish-brown paleosol is attributed to MIS 5e and the chernozem-like paleosol to MIS 5c.

From the chemostratigraphic point of view, the tripartite structure of O-P1 may mirror a pedocomplex alike Paudorf P2 (Sprafke et al., 2014) as proposed earlier. O-P1-1 as the most weathered paleosol thus may have developed during the last interglacial (MIS 5e) followed by MIS 5d characterized by erosion and/or colluvial reworking. The incorporation of already weathered material in O-P1-2 is documented by Zr enrichment indicating sediment recycling. Therefore, paleosol formation of O-P1-2 may have required less time and/or less favorable climatic conditions as O-P1-1 and thus might be attributed to MIS 5c. MIS 5b is assumed to be another phase of erosion and/or colluvial reworking. During MIS 5a processes similar to that of MIS 5c might have been active during the formation of O-P1-3. According to a warm MIS 5a characterized by forest development and marine transgression into the Po plain (Amorosi et al., 2004), a formation of O-P1-3 appears likely during MIS 5a. The transition from MIS 5 to MIS 4 accompanies aridification together with colder and more stable climatic conditions with steppe or shrub-steppe vegetation in the Po plain (Cremaschi et al., 2015; Ferraro, 2009; Zerboni et al., 2014). During this time a Pleistocene alluvial plain environment developed in the Po plain (Amorosi et al., 2004). Dust sedimentation started at several Northern Italian LPS (Cremaschi et al., 2015; Ferraro, 2009; Zerboni et al., 2014) and a coarsening trend is observed in sediments deposited in the Po Plain (Amorosi et al., 2004). This may explain the attribution of O-P1-3 to cluster 4 and 5 and may refer to a syn-pedogenetic dust deposition during late MIS 5a. Concluding this discussion, Susak may provide a very detailed record of MIS 5. However, until now Bok O is not constraint by numerical ages assessing the conclusions drawn as preliminary. Accepting a correlation of O-P1 with the orange-brown paleosol in the Susak composite profile Bok 1 (Fig. 5-10), there are two IRSL ages bracketing the orange-brown paleosol (O-P1, P-P1) to 98.3 ± 7.3 ka in the loess below the orange-brown paleosol and 63.5 ± 5.1 ka in the loess above the orange-brown paleosol (Wacha et al., 2011a). These luminescence ages suggest a formation of O-P1 during the time period MIS 5c to MIS 5a, albeit new luminescence ages are required for Bok O to confirm our conclusions.

Ferraro (2009) reports chernozems formed during MIS 4 and 3 at Val Sorda in Northern Italy. This is consistent with IRSL ages (Wacha et al., 2011a) indicating early MIS 4 as the most likely time for the development of P-P2 and P-P3 (Fig. 5-2). The sand layer (P-S1) at Bok P represents the stratigraphically youngest material of the investigated profiles and corresponds to an IRSL age of 67.6 ± 5.5 ka at Bok 1 that can be attributed to MIS 4 (Wacha et al., 2011a). According to mineralogical considerations (cf. section 5.4.1.3), Ti/Al serves as proxy for wind speed instead of dust source changes. Since coarse material transported by high wind speeds is poor in ultrastable and ultradense minerals (Ferraro, 2009; Mikulčić Pavlaković et al., 2011) and thus poor in Zr, Ti/Zr also becomes unsuitable as a reliable proxy for dust provenance. Observed low Ti/Al, high Ti/Zr values together with low Ti, rather constant Al and very low Zr counts in PS-1, indicate transport distance-superimposed wind-speed changes rather than dust-source changes.

Zr solely occurs in considerable amounts in zircon (Muhs, 2018) with densities ranging from 4.0 to 4.7 g/cm³ (Holland and Gottfried, 1955) while Al and Ti occur in various heavy and light minerals. In addition, the mineral zircon is related to quartz and thus Zr often occurs together with quartz in coarse material due to its weathering resistance (Mongelli et al., 2006). Muhs and Bettis III (2000) show that Zr concentration decreases with distance to floodplain in Peoria loess at the Missouri river. With regard to European LPS, Profe et al. (2016) document sorting-induced sediment recycling for the Schwalbenberg II LPS close to the river Rhine due to density-related fractionation in both fluvial and eolian domains. Accordingly, (1) weathered material, which is eroded from the floodplain slopes is transported into the river Rhine, (2) fluvial transport fractionates smaller and lighter particles from larger and heavier particles so that large and heavy particles remain on the floodplains close to the position where the material was previously eroded from. (3) Zr enriched floodplain material is lifted by strong winds and transported over short distances back to the floodplain slopes where the material was previously eroded from, accompanied by another phase of Zr enrichment in the eolian domain since the heavy Zr-minerals deposit first. This conceptual model exactly meets the criteria of the event sequence suggested for LPS formation by John Hardcastle (Smalley and Fagg, 2015). Adapting this concept to the situation on Susak during MIS 4 leaving behind the sand layer P-S1, helps to explain the observed pattern in weathering-inert elements.

During glacial times west winds prevailed south of the Alps, in the regions of the paleo Po and of Susak, as evidenced for the Last Glacial Maximum (Wang et al., 2018). This favors deposition of dust originating from the Alps on Susak. Consequently, material ground by glaciers together with eroded material from floodplain slopes in Northern Italy enters the paleo Po especially during transition periods characterized by large-scale erosion. Subsequently, the material is affected by fluvial transportation fractionating large and heavy particles from small and light particles on their way to the paleo-delta of the river Po, i.e. fractionating Zr- from Al- and Ti-bearing minerals. This delta was located up to 100 km south of Susak during MIS 4 due to a 50 – 100 m lower mean relative sea-level (Fig. 5-1, Rohling et al., 2017). Hence, floodplain sediments in the vicinity of the Island of Susak are relatively depleted in Zr whereas floodplain sediments in Northern Italy are relatively enriched in Zr. This idea is supported by finding the same pattern for ultrastable and ultradense minerals (e.g. zircon and rutile) in sediments from Northern Italy and Susak (Ferraro, 2009; Mikulčić Pavlaković et al., 2011). Assuming that the sand forming P-S1 originates from adjacent floodplains, the coarse material deflated from these floodplains is already depleted in Zr and to a lesser extent depleted in Ti due to density fractionation. Although this hypothesis explains the observed patterns, it only holds true for negligible input of weathered and Zr enriched material from nearby locations compared to the dominant input of material affected by long distance fluvial transport and thus depletion in Zr. This in turn appears likely since the Po drains most parts of the Southern Alps providing large amounts of sediments for fluvial transport. Tentatively, P-S1 might be the result of a sand storm event as hypothesized for the sand layer attributed to MIS 4 loess at Süttő (Novothy et al., 2011). Apart from that, another unknown factor is how regression of the Adriatic Sea, in accordance with glacial isostatic adjustment at the position of Susak, on the way to full glacial conditions provided a temporally exposed shelf area as proximal dust source influencing Ti/Al and Ti/Zr ratios

because of possible intermittent deflation of marine sediments with presumably different mineral compositions.

5.5. Conclusions

This study benchmarks high-resolution XRF scanning of discrete samples from LPS in a complex and polygenetic environment – the Island of Susak in Croatia. To estimate the reliability of paleoenvironmental conclusions drawn on XRF scanning derived element intensities, we tested data precision. Triplicate control measurements of 84 samples reveal a mean relative standard deviation of $< 3\%$ for most elements. This is in good agreement with other studies (e.g. Profe et al., 2016). In addition, we checked data precision against compaction and document a negligible contribution of compaction-induced interferences when samples are prepared by different persons highlighting the robustness of this technique.

High-resolution XRF scanning of discrete samples yielded a detailed geochemical record of three profiles attributed to the time period from MIS 7 to MIS 4. Comparison with micromorphological, mineralogical, calcium carbonate, organic carbon and grain-size data demonstrate that the XRF scanning-derived element ratios provide valuable information about calcification dynamics (Ca/Sr), weathering intensity (Rb/Sr, Ba/Sr, Rb/K), redox conditions (Fe/Mn), dust transport and sediment recycling (Ti/Al, Ti/Zr) and grain-size (Si/Al). Furthermore, multivariate statistics enable the establishment of a chemostratigraphy facilitating profile correlations and identification of potential pedocomplexes as exemplified on the paleosols O-P1 and P-P1. Especially O-P1 is re-considered as a pedocomplex, tentatively representing a complete record of all MIS 5 substages. The preset number of five clusters show meaningful correlations with lithological units: sand (cluster 3), loess (cluster 5), weak or secondary calcification-superimposed pedogenesis (cluster 4), intermediate pedogenesis (cluster 2) and strong pedogenesis (cluster 1). Critical and individual discussion of each element index against other proxies reveal that Rb/Sr and Ba/Sr tend to underestimate weathering intensity due to strong post-pedogenetic secondary calcification in the form of rhizoconcretions. Based on the example of O-P1, Rb/K may suffer from the XRF scanner performance to reliably detect small changes in K. Due to the complex processes influencing Fe and Mn within soils, Fe/Mn is not a straightforward proxy for redox conditions but may serve as a proxy for combined effects of Mn fixation due to CaCO_3 (Fujimoto and Sherman, 1948) and the size of Fe/Mn nodules with small nodules often being enriched in Mn (Zhang and Karathanasis, 1997). Careful assessment of weathering-inert element dynamics further unravels transport and sediment recycling dynamics. On Susak, Ti/Al and Ti/Zr are related to wind strength-induced changes in mineralogy rather than attributed to dust source changes. Suggesting Zr depletion of coarse material in the floodplain adjacent to Susak, density fractionation during fluvial transport in the paleo Po explains low Ti/Al and high Ti/Zr values in the sand layer P-S1. At the same time this process dismantles Zr/Rb from being a reliable grain-size proxy. In contrast Si/Al predominantly varies with grain-size changes as exemplified for Bok P. Br and Cl were

evaluated as proxies for transgressions of the Adriatic Sea and potential sea-water spray entrapment in the sediment. While the latter is confirmed and explained as a combination of preferred preservation of organohalogene compounds and frequent desiccation leading to micro salt crystals in sediment pores, the former hypothesis is dismissed according to these reasons.

The importance of spatially distributed and high-resolution data is emphasized by the example of the tripartite structure of N-P1 and O-P2. Sampling resolutions >4 cm would have missed considerable variation of mainly Ca/Sr and weathering indices. Furthermore, geochemical similarity supports the correlation of O-P1-2 with P-P1 and thus with the orange-brown paleosol at the Bok 1 composite profile. In conclusion, this study highlights the benefits of using XRF scanning of discrete samples as a geochemical screening tool for LPS providing versatile and valuable qualitative information about calcification dynamics, weathering intensity, sediment recycling, dust source or wind activity changes and grain-size alterations as characteristic element ratios.

Acknowledgements

Financial support of the German Research Foundation [DFG, ZO 102/22-1] is gratefully acknowledged. In addition, LW appreciates financial support by the Croatian Science Foundation [HRZZ-UIP-11-2013-4425]. We thank Mihovil Brlek for assistance in the field and Sabine Stahl as well as Sonja Riemenschneider for assistance in the laboratory. Junqiang Xu is thanked for sample preparation for the compaction test.

5.6. Supplementary material

XRF-scanning, TOC and CaCO₃ data are available on Pangaea:
<https://doi.pangaea.de/10.1594/PANGAEA.879353>.

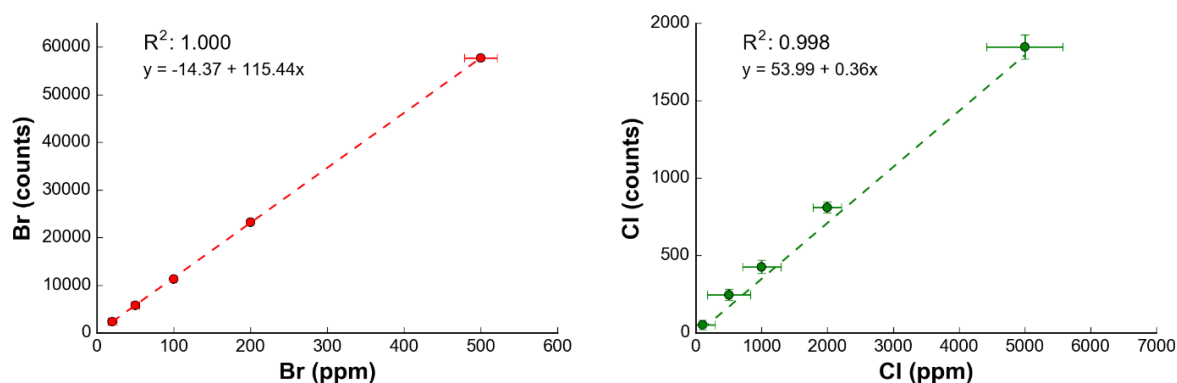


Fig. 5-11: Standard addition curves for Br (left) and Cl (right). X-error bars indicate confidence limits at the 95 % confidence level as derived from leave-one-out cross-validation. Y-error bars indicate standard deviation (1σ) of mean counts.

6. Study III – Süttő

Persistent arid climatic conditions during the last glacial- /interglacial cycle deduced from geochemical data of the loess-paleosol sequence at Süttő (Hungary)

Jörn Profe^{a,*}, Lena Neumann^{a,b}, Ágnes Novothny^c, Gabriella Barta^c, Christian Rolf^d,
Manfred Frechen^d, Christian Ohlendorf^a, Bernd Zolitschka^a

^a University of Bremen, Institute of Geography, GEOPOLAR, Germany

^b University of Education Heidelberg, Department of Geography, Research Group for Earth Observation (rgeo),
Germany

^c Eötvös Loránd University Budapest, Department of Physical Geography, Hungary

^d Leibniz Institute for Applied Geophysics (LIAG), Geochronology and Isotope Hydrology, Hannover, Germany

Corresponding author: Jörn Profe, profe@uni-bremen.de

under review

Quaternary Science Reviews

A modified version of the printed version is currently under review in
Quaternary Science Reviews.

Profe, J., Neumann, L., Novothny, Á., Barta, G., Rolf, C., Frechen, M., Ohlendorf, C., Zolitschka, B., under review. Paleoenvironmental conditions and sedimentation dynamics in Central Europe inferred from geochemical data of the loess-paleosol sequence at Süttő (Hungary). *Quaternary Science Reviews*.

Contribution of authors

JP did laboratory work, analyzed the data, established the chemostratigraphy and subsequent PCA and biplot analyses, conceptualized and drafted all figures and the manuscript. LN wrote her Bachelor thesis about the geochemistry at Süttő. AN, GB, CR and MF provided the samples as well as grain-size and magnetic susceptibility data. As field experts they contributed site particularities to the discussion. CO helped to structure data analysis and the manuscript. BZ and JP designed the study. All authors contributed to draft the manuscript.

Abstract

This study provides a detailed geochemical record of the well-studied and complete key loess-paleosol sequence (LPS) Süttő covering the time period from Marine Isotope Stage (MIS) 6 to MIS 2. It is situated in the northwestern Carpathian Basin at the transition between oceanic and continental climate. We investigate weathering intensity, dust source changes and sediment recycling by high-resolution X-ray fluorescence (XRF) scanning of discrete samples in comparison with quantitative XRF and other already published proxy data such as grain-size, magnetic susceptibility (MS) and micromorphology. Based on eleven elements, we establish a high-resolution chemostratigraphy of a Hungarian LPS for the first time. Chemostratigraphy together with principal component and biplot analyses reveal pedogenesis and grain-size as main drivers influencing the elemental composition. However, there is no indication of K-weathering pointing to arid continental paleoenvironmental conditions throughout the last glacial-/interglacial cycle. The weathering-inert elements Al, Ti and Zr indicate Zr addition and thus sediment recycling being strongest during MIS 6. Since correlation analysis rules out grain-size as predominant factor affecting Zr dynamics and since no evidence exists for a dominant input from dust sources other than the adjacent Danube floodplain, the distance to floodplain controls Zr addition. In contrast to a change in horizontal distance, we suggest an increase in vertical distance. We hypothesize that the decrease of Zr addition towards the top of the sequence is a result of tectonic uplift by approximately 70 m of the LPS Süttő since MIS 6. Hence, the vertical rather than the horizontal distance to the floodplain is archived in the LPS Süttő. In conclusion, our study highlights how high-resolution qualitative geochemical data contributes to a better understanding of paleoenvironmental and sedimentation dynamics at LPS in general.

Keywords

Pleistocene
Paleoclimatology
Central Europe
Inorganic geochemistry
Sedimentology, loess
XRF scanning of discrete samples
Cluster analysis
Chemostratigraphy

6.1. Introduction

Loess, a silt-sized, calcic material, often associated with periglacial environments during cold climatic periods, covers more than 10 % of the Earth's surface (Pécsi, 1990; Sprafke and Obreht, 2016) and serves as parent material for the development of loess-paleosol sequences (LPS). LPS are important terrestrial paleoenvironmental archives characterized by an alternation between dust deposition and paleosol formation. Chemical weathering, dust source and dust availability changes, grain-size dynamics, as well as sediment sorting and recycling on their transport paths leave behind specific signals in elemental composition (Ahmad and Chandra, 2013; Buggle et al., 2011; Buggle et al., 2008; Chen et al., 2013; Chen et al., 2006; Liang et al., 2013; Profe et al., 2016; Újvári et al., 2008; Újvári et al., 2014). Consequently, geochemical variations characterize sedimentological variations of LPS associated with changing paleoenvironmental conditions (e.g. Buggle et al., 2011; Buggle et al., 2008; Profe et al., 2016; Újvári et al., 2008).

In the last decade, the LPS in the Carpathian Basin in particular attracted researchers because the Danube was a preferred pathway for humans on their way to Central Europe (Fitzsimmons et al., 2012; Marković et al., 2016; Marković et al., 2015). Moreover, the unique geological setting caused the development of numerous LPS that cover several glacial-/interglacial cycles (e.g. Paks: 800 ka, Újvári et al., 2014). Thus, the LPS in the Danube basin provide excellent archives to reconstruct paleoenvironmental conditions which may have thrived on human evolution (Black et al., 2015; Fitzsimmons et al., 2013; Fitzsimmons et al., 2012; Marković et al., 2016; Zeeden et al., 2016). The LPS Süttő (Fig. 6-1) located in the northwestern Carpathian Basin at the western foothill of the Geresce Mountains (Novothy et al., 2011) is regarded as a key site due to its location in the transition zone between the western European LPS, dominated by oceanic climate, the central European LPS, dominated by continental climate, and the south-eastern European LPS, dominated by Mediterranean climate. Sprafke et al. (2014), Terhorst et al. (2015) and Hošek et al. (2015) describe transitions from North Atlantic-dominated to continental climate for Austrian and Czech LPS whereas Obreht et al. (2017) highlight the confluence of all three climatic modes in south-eastern Europe, especially during Marine Isotope Stage (MIS) 3. We refer to MIS in the notation of Lisiecki and Raymo (2005). Although Süttő covers the time window from MIS 6 to MIS 2 (Novothy et al., 2010; Novothy et al., 2011), most LPS in the northern Carpathian Basin, including the type localities of Basaharc and Mende, suffer from considerably hiatuses during the last glacial-/interglacial cycle, and in particular during MIS 5 (Frechen et al., 1997; Gábris et al., 2012; Marković et al., 2016; Novothy et al., 2009).

Although Süttő is among the best studied LPS in Hungary (Horváth and Bradák, 2014), a detailed geochemical record is still missing for a better understanding of paleoenvironmental conditions and dust origin (cf. Újvári et al., 2008; Újvári et al., 2014). Hence, we acquire qualitative element data via XRF scanning of discrete samples (Ohlendorf, 2018) due to its time- and cost-efficiency compared with analytical methods providing quantitative geochemical data, and apply for the first time a multivariate statistical approach (e.g. Martin-Puertas et al., 2017) to LPS from Hungary aiming at establishing a

high-resolution chemostratigraphy (e.g. Raczky et al., 2015; Sial et al., 2015). Furthermore, we investigate and evaluate the suitability of qualitative geochemical data to track weathering intensity, grain-size dynamics, dust source changes, sediment sorting and recycling along this LPS by contextualizing them with existing proxy data as well as total organic carbon (TOC), quantitative XRF and X-ray diffraction (XRD) measurements.

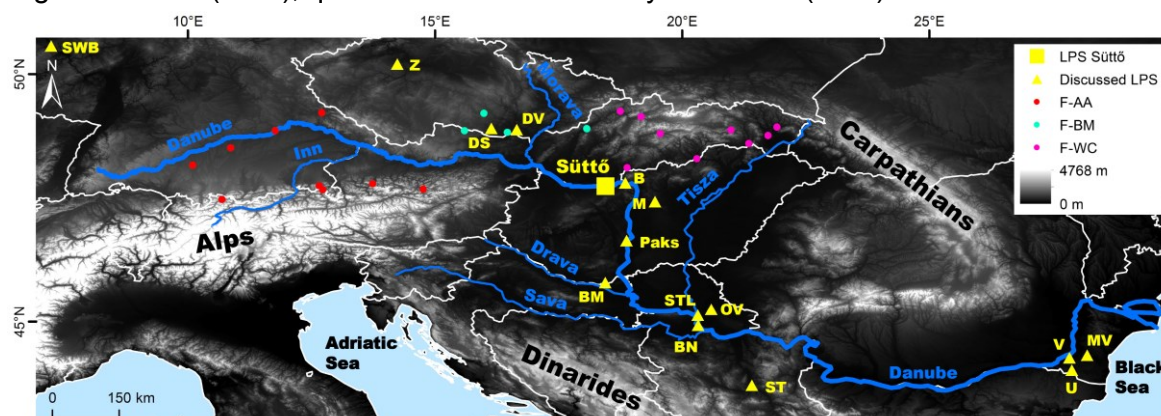


Fig. 6-1: Map of Central Europe showing the discussed loess-paleosol sequences (LPS) and the river Danube and its major tributaries. In addition, dust provenance at the LPS Süttő is inferred from floodplain sediments (F-AA: Austroalpine cover nappes area, F-BM: Bohemian Massif, F-WC: Western Carpathians). B: Basaharc, BM: Beremend, Majs, Nagynyárád, Töttös, BN: Batajnica, DS: Dobšice, DV: Dolní Věstonice, M: Mende, MV: Mircea Voda, OV: Orlovat, ST: Stalač, STL: Stari Slankamen, SWB: Schwalbenberg II, U: Urluia, V: Vlasca, Z: Zeměchy. GCS ERTS 1989. Data base: Shuttle Radar Topographic Mission (USGS, 2003), administrative boundaries (GADM, 2015), rivers (WISE, 2012).

6.2. Regional setting and previous work

The Carpathian Basin is a continental basin in central Europe, enclosed by the Alps in the northwest the Dinarides in the southwest and the Carpathian Arc in the north, east and south. Neotectonic uplift of pre-Neogene rocks forms the Hungarian mountain range which subdivides the Carpathian Basin into the Little Hungarian Plain in the northwest and the Great Hungarian Plain in the southeast (Ruszkiczay-Rüdiger et al., 2005; Török et al., 2017). This basin represents a unique climatically favored region in central-eastern Europe (Marković et al., 2016) as it was not part of the continuous permafrost zone during the last glacial period (Ruszkiczay-Rüdiger and Kern, 2016). The present-day soil assemblage is dominated by Chernozems on loess in plains and Luvisols, as well as Cambisols in mountainous regions (Ibáñez et al., 2013). In addition, the western forelands of the Transdanubian Mountains, the so-called D3 region, rank among the most complex regions along the Danube with regard to dust origin (Smalley and Leach, 1978). Glacial material from the Alps and Moravia, as well as weathered flysch from the West Carpathians, denote the three main dust sources (Smalley and Leach, 1978). Tributaries such as Inn, Morava and Tisza transport material prior to final eolian deposition through the Danube into the Carpathian Basin, resulting in an LPS whose parent material has already undergone multiple cycles of transport and deposition (Smalley et al., 2009; Smalley and Leach, 1978; Wright, 2001a). This idea goes back to John Hardcastle in 1889, explaining the formation of LPS in New Zealand by this event-sequence model (Smalley and Fagg, 2015).

The up to 20 m thick LPS Süttő (Fig. 6-2, 47.738°N, 18.448°E) exposed in the Hegyháti quarry is subdivided into 16 lithological units (Novothy et al., 2011). It covers the time period MIS 6 to MIS 2 (Novothy et al., 2009; Novothy et al., 2010; Novothy et al., 2011; Rolf et al., 2014) and is underlain by a meteo-gene travertine complex formed on a paleo-terrace of the river Danube during MIS 9 to MIS 7 (Sierralta et al., 2010). This travertine complex developed on a Danube terrace and has been uplifted by more than 100 m since its formation (Novothy et al., 2009; Török et al., 2017).

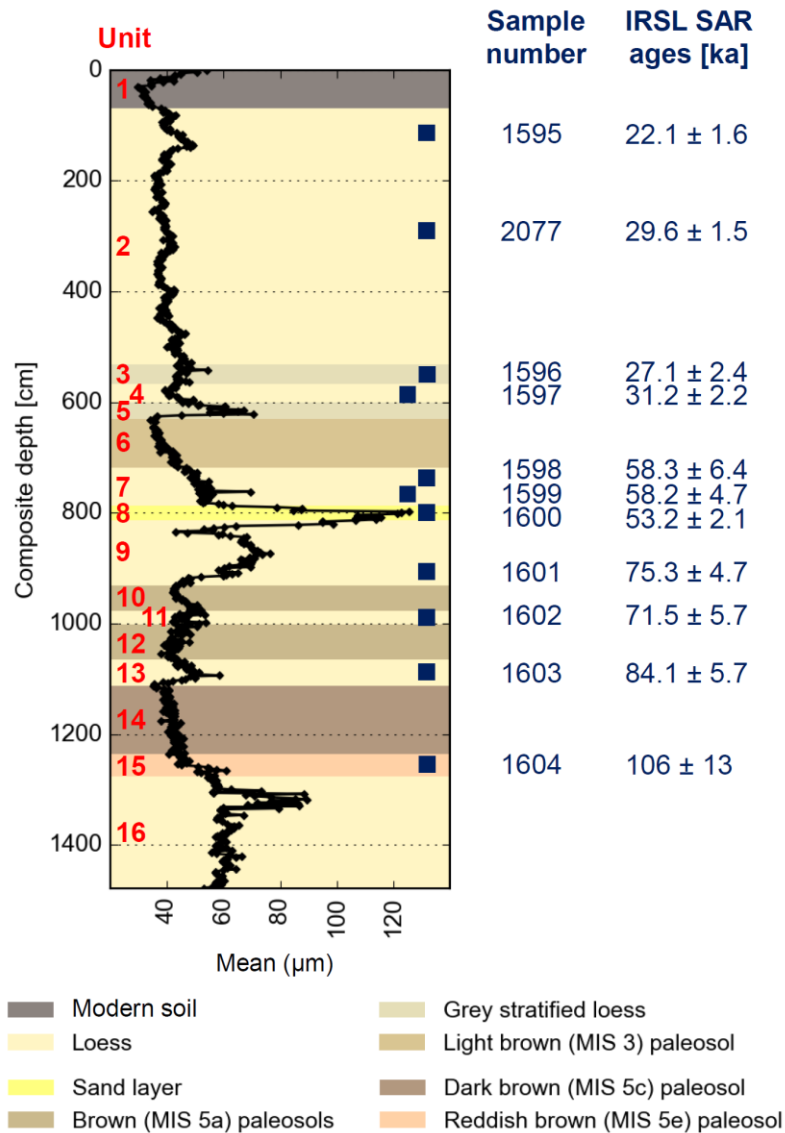


Fig. 6-2: Stratigraphic overview of the loess-paleosol sequence Süttő, modified after Novothy et al. (2011). The red labels illustrate the lithological units defined in Novothy et al. (2011) and the displayed grain-size data, the sample numbers, as well as the fading-corrected infrared-stimulated luminescence single aliquot regenerative dose protocol (IRSL SAR) ages correspond to the data presented by Novothy et al. (2011).

Previous work at the LPS Süttő comprises grain-size (Novothy et al., 2011), magnetic susceptibility (MS), paleomagnetic properties (Novothy et al., 2011; Rolf et al., 2014), secondary carbonate morphology (Barta, 2014), stable carbon and oxygen isotope analyses (Koeniger et al., 2014), and malaco-thermometer (Sümegei and Krolopp, 2002) based July temperature reconstructions for MIS 3 and MIS 2 (Novothy et al., 2011).

Luminescence ages (Novothy et al., 2010; Novothy et al., 2011), together with amino-acid racemization (Novothy et al., 2009) and relative paleo-intensity of magnetic remanence (Rolf et al., 2014) provide robust time control. In contrast to many other LPS, especially to those of Western Europe, the deposited loess material is very coarse. There is a decreasing trend in grain-size from MIS 6 to MIS 2 with a considerable high sand content in the well-developed paleosols attributed to MIS 5e and MIS 5c. Novothy et al. (2011) attribute the high sand content to the vicinity of the Danube and the Bicol Creek. High CaCO₃ contents in Unit 16 either indicate strong leaching of Unit 14 and 15, or a stronger contribution of the Bicol Creek as dust source area (Barta, 2014). Opposed to MIS 6 and MIS 4 loess being characterized by lower sedimentation rates owing to erosional or less favorable environmental conditions, MIS 2 loess shows the lowest sand content but the highest sedimentation rates along the LPS, pointing to alterations either in paleo-wind intensity and direction or a different contribution of the Bicol Creek as local dust source (Novothy et al., 2011). Secondary carbonates and grain-size analyses identify different phases of dust deposition during MIS 2 (Barta, 2014; Novothy et al., 2011). The sand layer (Unit 8) reflects a dust storm event which is dated to 53.2 ± 2.1 ka by optically stimulated luminescence of coarse quartz grains using the single aliquot regeneration protocol. The overlying loess layer (Unit 7) reveals a fading-corrected infrared stimulated luminescence age of 58.2 ± 4.6 ka (Novothy et al., 2011).

The last interglacial period reveals colder and more arid climate conditions during MIS 5. Preliminary micromorphological results indicate development of Unit 15 under wetter conditions in comparison with the steppe-like vegetation at the time of Unit 14 (Novothy et al., 2011). Although frost deformation is recognized micromorphologically in Unit 12, the absence of secondary carbonates documents strong leaching and more humid conditions compared to Unit 10. In Unit 10 low clay content indicates strong but rapid soil formation (Barta, 2014; Novothy et al., 2011). Unit 6 reflects the most intense paleosol during MIS 3 and is characterized by abundance of hypocoatings which may represent evaporation-based CaCO₃ impregnations and thus arid, steppe conditions (Barta, 2014). Mollusc fauna supports this interpretation by July temperatures (20.9°C, Novothy et al., 2011) comparable to today (21.6°C, Szalai et al., 2005). Units 5 and 3 are attributed to simultaneous dust deposition, bioturbation and weak pedogenesis (Barta, 2014) during late MIS 3 (Novothy et al., 2011).

6.3. Materials and methods

6.3.1. Material

In this study, we analyzed the samples previously taken for grain-size measurements by Novothy et al. (2011) with 2 cm spatial resolution. We considered 735 samples that correspond to the composite profile introduced in Novothy et al. (2011) down to a depth of 1478 cm. We provide depth-related information as top of sample in the remainder of this study. Furthermore, measurements of eight mixed samples (SU08: 0-300 cm, SU08A: 304-

560 cm, SU08B: 562-636 cm, SU08C: 644-756 cm, SU08D: 758-832 cm, SU08E: 834-1108 cm, SU08F: 1110-1266 cm, SU08G: 1268-1478 cm) that cover all lithologies yielded quality control. For the following depths no sample material was available: 280 cm, 302 cm, 638 cm, 640 cm and 642 cm. In addition, we removed several data points due to extremely low Al counts (Table 6-1) from further analyses. Such low Al values represent outliers and would affect multivariate statistics adversely by exaggerating the content of all other considered elements.

Table 6-1: Removed outliers based on Al counts.

Top of sample (cm)	42	48	54	64	68	198	1360	1446
Al (counts)	6	12	21	34	35	4	30	24

6.3.2. Methods

6.3.2.1. Laboratory analyses

6.3.2.1.1. XRF scanning of discrete samples

Prior to measurement, the 735 samples were air-dried and then homogenized by pestle and mortar. Special sample cups and carriers designed for the continuous XRF scanning of discrete samples with an ITRAX XRF core scanner (Ohlendorf, 2018; Profe et al., 2018; Profe et al., 2016) were used to measure up to 60 samples in a row. Measurements were carried out with a Mo-tube, 30 kV, 31 mA and 100 s measurement time to assure optimal data quality (Ohlendorf, 2018). Discrete sample analysis causes an alternating sequence of sample and sample cup material XRF-spectra. The sample cup material spectra were removed automatically by a Python script. We calculated element intensities by fitting a mathematical model to the recorded XRF-spectra using the proprietary software Q-Spec (v. 8.6.0). Ten replicate measurements of eight mixed samples (SU08 - SU08G), covering all lithologies, provided quality control on counting statistics in terms of data precision of XRF scanning measurements. Data reliability was documented by a correlation analysis between XRF scanning-derived element intensities and wavelength-dispersive (WD) XRF-derived element concentrations according to Sun et al. (2016).

6.3.2.1.2. Quantitative XRF measurements

WD-XRF measurements were carried out for 33 discrete samples and for the eight mixed samples (SU08-SU08G) covering all lithological units (supplementary material Table 6-2) at the laboratory of the Institute for Chemistry and Biology of the Marine Environment (ICBM) in Oldenburg, Germany, according to the protocol reported in Beck et al. (2013). In-house standards account for data precision < 5 % for major and < 10 % for trace elements (Beck et al., 2013; Schnetger et al., 2000).

6.3.2.1.3. Bulk powder X-ray diffraction (XRD)

Four unweathered loess samples from the LPS Süttő were analyzed by XRD at depths of 342 cm (MIS 2), 864 cm (MIS 4), 1308 cm (MIS 6) and 1420 cm (MIS 6). These four samples served as validation for hypothesized dust provenance changes between MIS 6 and younger loess observed by other proxies (Novothny et al., 2011). The XRD measurements were carried out at the University of Bremen, Central Laboratory for Crystallography and Applied Material Sciences, ZEKAM, Department of Geosciences using a Philips X'Pert Pro diffractometer equipped with a Cu-tube ($k\lambda$ 1.541, 45 kV, 40 mA). Angles between $3 - 85^\circ 2\theta$ were measured in 0.016° steps with a measurement time of 100 s per step. Minerals were identified and percentages were calculated semi-quantitatively by the proprietary software X'Pert HighScore.

6.3.2.1.4. Total organic carbon and calcium carbonate determination

We densified the total organic carbon (TOC) record presented in Koeniger et al. (2014) to a spatial resolution of 10 cm at the same sampling depths used for CaCO_3 determination. For this purpose, we used an EuroEA Eurovector CNS analyzer and followed the procedure that was outlined before in Hahn et al. (2013).

6.3.2.2. Data analyses

6.3.2.2.1. Multivariate statistics

Chemostratigraphy is similar to the approaches of bio- and lithostratigraphy but based on geochemical data. In the 1980s, it was originally developed in the marine realm based on stable carbon and oxygen isotope studies (Ramkumar, 2015; Sial et al., 2015). Since then, among other locations and archives, this approach was applied to LPS (Hill, 2005; Raczky et al., 2015). Chemostratigraphy identifies homogeneous units along an LPS while highlighting their differences at the same time. However, considering several parameters at once requires robust multivariate statistical approaches such as hierarchical cluster analysis (e.g. Martin-Puertas et al., 2017). Log-transformation of XRF element intensity data is consistent with quantitative geochemical data and the statistical theory of compositional data (Weltje et al., 2015). Therefore, chemo-stratigraphic intervals were determined using hierarchical cluster analysis (Wards) after log-transformation of the XRF element intensity data (Martin-Puertas et al., 2017; Weltje et al., 2015). Based on the precision of the XRF scanning analyses, the statistical analyses included the elements Al, Si, K, Ca, Ti, Mn, Fe, Rb, Sr, Zr, and Ba. To account for either low data precision and/or noisy profiles, we smoothed the Al, Ti, Mn, Zr and Ba data by using a 5-pt running mean. In addition, we standardized each log-transformed element data to zero mean and unit variance to give each element equal importance. The number of clusters was determined by a dendrogram according to their relative linkage distances and expert knowledge about the number of expected lithological units. Further evaluation was carried out by principal component analysis (PCA) and biplot analysis (Martin-Puertas et al., 2017) to provide information about element correlations. We implemented this workflow using the free programming language Python.

6.3.2.2.2. Element ratios

Commonly applied element ratios are Ca/Sr to identify the degree of decalcification or secondary calcification (Bokhorst et al., 2009; Profe et al., 2016), Rb/Sr, Ba/Sr and Rb/K to characterize weathering intensity (Buggle et al., 2011), Ti/Al, Ti/Zr and Si/Al to detect dust source changes (Klasen et al., 2015; Muhs and Benedict, 2006; Zech et al., 2008) or sediment sorting and recycling (Chen et al., 2013; Garcia et al., 1991; Profe et al., 2016), and Si/Al and Zr/Rb to track grain-size variations (Chen et al., 2006; Liang et al., 2013). Instead of interpreting XRF scanning-derived profiles of commonly applied element ratios, we used biplots to identify element ratios that are most representative for the processes that dominate the first two principal components. To avoid statistical asymmetry, we express element ratios as log ratios (Profe et al., 2016; Weltje and Tjallingii, 2008). Single elements are reported as centered log-ratio (clr)-transformed data (Martin-Puertas et al., 2017).

Ternary plots, such as the A-CN-K or the Al-Ti-Zr plots, are well known for the characterization of weathering trends (Nesbitt and Young, 1989) or sediment sorting and recycling (Garcia et al., 1991; Garcia et al., 1994). Evaluation of XRF scanning data is done by comparison with quantitative WD-XRF data. On the one hand, the A-CN-K plot demands WD-XRF data as it relies on Na as well as apatite- and carbonate-corrected Ca data (Nesbitt and Young, 1989). On the other hand, WD-XRF data allow calculation of the chemical index of alteration (CIA, Nesbitt and Young, 1982), comparison with the UCC, and the identification of Zr addition and dust source homogeneity by Zr/metal and Th/metal ratios (e.g. Újvári et al., 2008). CaO is corrected for apatite by using the measured P₂O₅ values according to Buggle et al. (2008). CaO is further corrected for the non-silicate Ca fraction according to the procedure presented in McLennan (1993): if CaO > NaO, CaO* = NaO, else CaO* = CaO. Since XRF-scanning does not provide Na data (Croudace et al., 2006), we suggest a Sr-K-Rb instead of an A-CN-K ternary plot to address the first two stages of weathering: decalcification and K-removal (Hošek et al., 2015; Nesbitt et al., 1980). Sr-K-Rb plots are expected to yield reliable information unless secondary calcification dynamics influence Sr.

6.3.2.2.3. Correlation analysis

Contextualization of XRF scanning-derived element data with other proxy data allows us to examine the potential of qualitative geochemical data to mirror variations in other proxy data. For this purpose, the clr-transformed values of the 11 elements used for the multivariate statistical analysis are compared with grain-size (clay, silt and sand fractions as well as mean grain-size), TOC, CaCO₃ content and MS data via a correlation analysis. We followed the approach outlined in Yu et al. (2016) using the Spearman rank correlation coefficient ρ .

6.3.2.3. Geochemical reference

For a detailed geochemical characterization of the LPS Süttő, we take into account literature values for the UCC, average loess composition and composition of potential dust source

areas, as represented by floodplain sediments from different tributaries of the river Danube. UCC data are taken from the map model of Condie (1993). According to topographic setting and assumed prevailing west winds (Sebe et al., 2011), the Danube floodplains in the west of Süttő are the most likely dust sources (Novothy et al., 2011; Smalley and Leach, 1978). Hence, floodplain sediments of different tributaries along the Danube were considered as representatives for the geochemical composition of potential dust source areas (Smalley and Leach, 1978), as they provide an average signal of the catchment area (Buggle et al., 2008). We used the same data as Buggle et al. (2008) from the FOREGS (Forum of European Geological Surveys) data base (Fig. 6-1) to distinguish between contributions from the glaciofluvial Austroalpine cover nappes area not including the Inn (F-AA), the crystalline and metamorphic Bohemian Massif area (F-BM), and the lithologically very diverse Western Carpathian area (F-WC). The river Inn is not included in F-AA due to its catchment covering parts of the crystalline Central Alps. F-WC data serve as a negative control for prevailing east winds due to the contribution of F-WC material via the river Tisza flowing into the Danube east of Süttő. Comparing the average loess composition (AVL³), based on more than 150 unweathered loess samples from around the world, with unweathered loess samples from the LPS under study, reveals either differences caused by regional specifics of the parent material, or sediment recycling (Újvári et al., 2008).

6.4. Results and discussion

6.4.1. Data quality control

Major elements exhibit mean relative standard deviation $\leq 1.5\%$, except for Al with 14.3% (Fig. 6-3). Trace elements reveal similar results with mean relative standard deviations $\leq 2.0\%$, except for Ba with 14.9% (Fig. 6-3). Low detectability explains the lower precision of Al while peak overlaps with Ti explain the lower precision of Ba. Moreover, X-ray fluorescence of Ba is recorded by its L-lines ($L\alpha$: 4.47 keV, Bearden, 1967) resulting in a weaker signal compared to the overlapping Ti K-lines ($K\alpha$: 4.51 keV, Bearden, 1967). The smallest mean relative standard deviations ($\leq 0.7\%$) are observed for elements with the highest fluorescence yields (Ca, Fe, Jenkins, 1988).

Fig. 6-4 documents strong correlations between element intensities and element concentrations with $R^2 \geq 0.80$, except for Al, Si, K and Ba, with $0.52 \leq R^2 \leq 0.67$. Accordingly, changes in element intensities reflect changes in element concentrations and confirm a high data quality of XRF scanning-derived element intensities. Weaker correlations of Al and Ba are related to their lower data precisions. In contrast, weaker correlations of Si and K element intensities with their corresponding concentrations might be attributed to sediment matrix effects caused by a quartz-rich loess matrix together with large changes in Ca and Fe contents between loess and paleosols (cf. Potts, 1992).

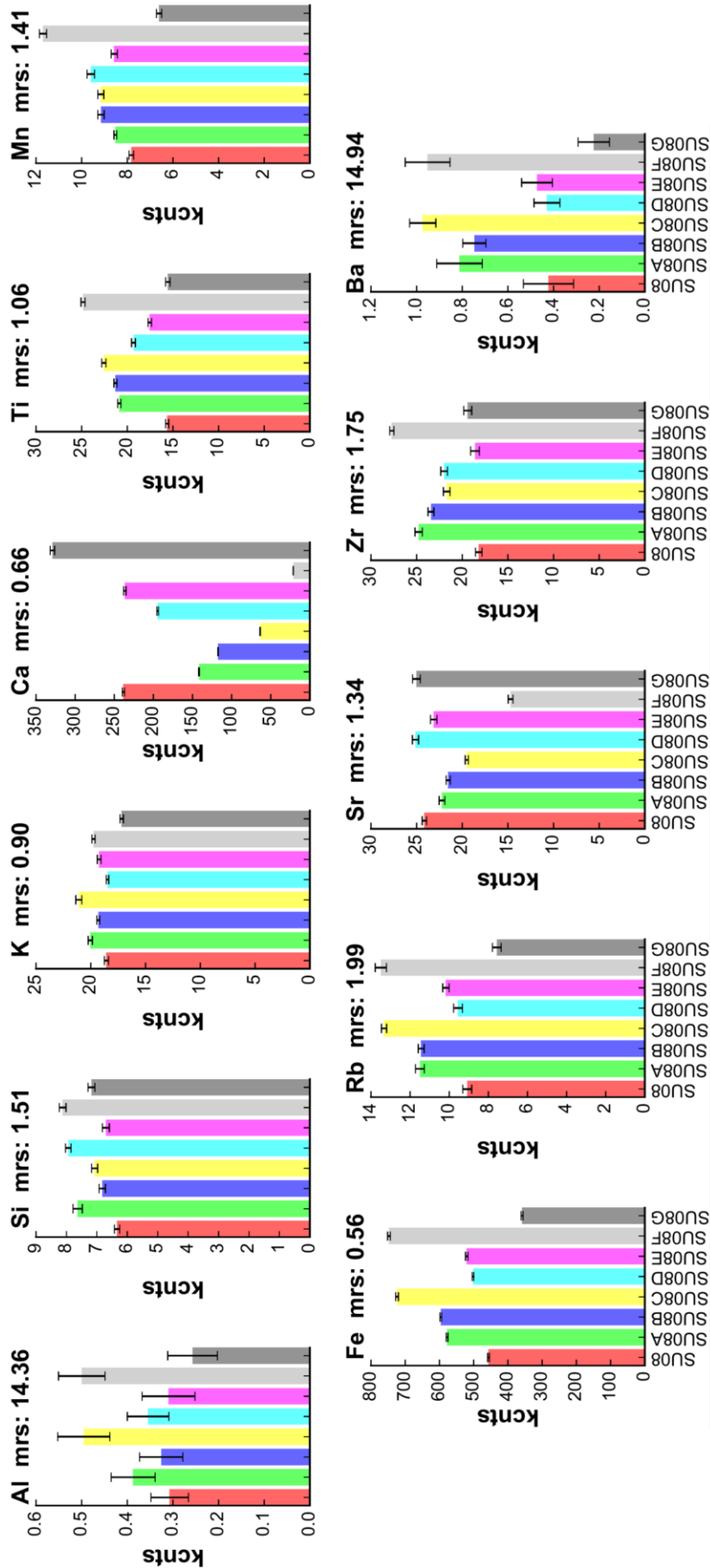


Fig. 6-3: Mixed sample (SU08-SU08G) based data precision of analyzed elements. Raw element intensities are reported in counts. mrs: mean relative standard deviation in %.

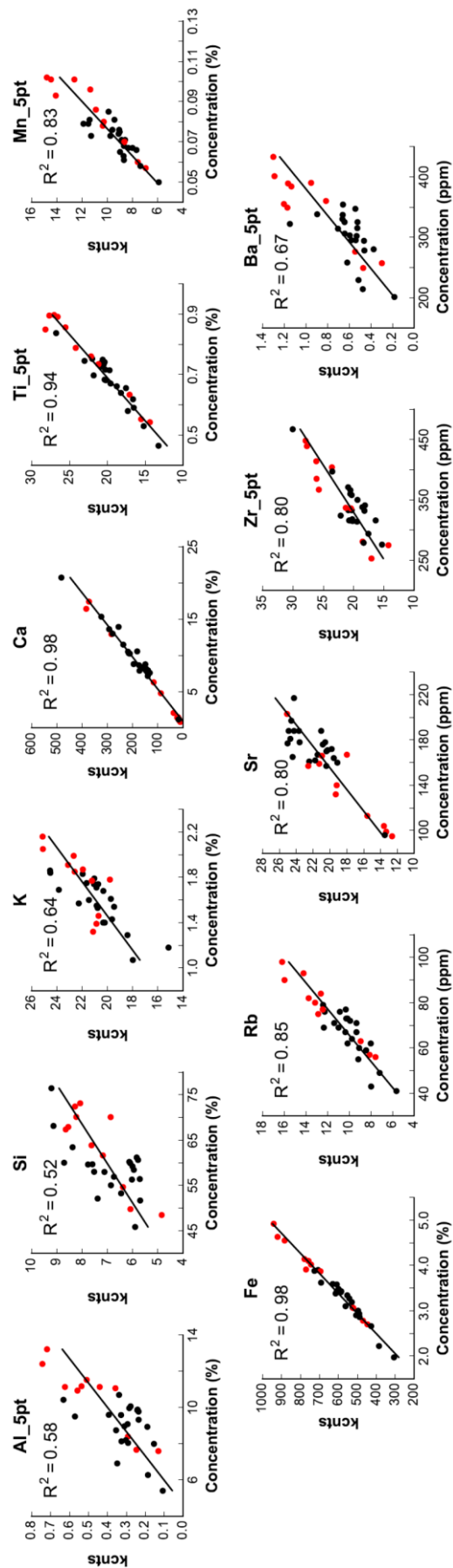


Fig. 6-4: Scatter plots of WD-XRF-derived element concentrations vs. XRF scanning-derived element intensities. Black dots: loess, red dots: paleosols and the modern soil. 5pt indicates element counts after smoothing with a 5-pt running mean.

The highest correlation between results derived from quantitative XRF and XRF scanning analyses of U-channels from the Chinese LPS Gulang exist for Ca with $R^2 = 0.72$. Whereas K shows the worst correlation with $R^2 = 0.29$, based on 751 samples (Sun et al., 2016). The low concentration range of approximately 0.5 % together with an applied measurement time of 15 s may explain this weak correlation. However, they apply a Cr-tube which is better suited to measure lighter elements such as K. Liang et al. (2012) investigate the same LPS and use the same settings as Sun et al. (2016) but they report an even worse correlation with $R^2 = 0.20$ ($n = 54$) for K. However, such a weak correlation may also point to difficulties in reliably measuring small concentration changes of K with an ITRAX XRF scanner. Liang et al. (2012) evaluate only the five elements Si, Ca, Fe, Sr and Zr with $R^2 > 0.60$ as robustly measurable. Comparing this categorization with our results, we can robustly measure K, Ca, Ti, Mn, Fe, Rb, Sr, Zr and Ba, however with a Mo-tube and 100 s measurement time. Nonetheless, the differences to our study highlight the advantage of XRF scanning of discrete samples using dry and homogenized samples instead of U-channels that are adversely affected by water content and surface roughness alterations (cf. Jarvis et al., 2015). However, even the usage of dry powdered geochemical reference standards does not prevent K from results that indicate intermediate measurability ($0.60 \leq R^2 < 0.90$) with an ITRAX XRF scanner, irrespective of measurement time and applied X-ray tube Huang et al. (2016).

6.4.2. Chemostratigraphy

In consideration of the lithologically-defined units (Fig. 6-5D), seven clusters are selected according to the dendrogram (Fig. 6-5A), with paleosol and loess clusters being geochemically the most different. Among the loess clusters, cluster 3, representing the oldest loess (MIS 6), differs most from younger loess (MIS 4 and MIS 2) suggesting a potential dust source change. In contrast, clusters 4 and 5 as well as 6 and 7 are similar (Fig. 6-5A) indicating either comparable climatic conditions or the same dust sources. Especially the occurrence of cluster 7 in MIS 5b, MIS 5a and later MIS 2, favors a rather homogenous dust source for the last glacial period. PCA and biplot analyses (Fig. 6-5B) corroborate this finding with loess and paleosol clusters being separated along the first principal component (PC) and explaining 63.5 % of total variance. The biplot indicates that Ca and Sr dominate loess clusters while Al, Ti, Mn, Fe, Rb, Zr and Ba dominate paleosol clusters (Fig. 6-5B). This is in accordance with the element ratios Rb/Sr and Ba/Sr which are usually applied to characterize weathering intensity. Therefore, PC1 represents pedogenesis. PC2 explains 14.9 % of total variance, and reflects grain-size dynamics, because the sand layer plots along PC2 as a tiny band and the biplot points to a dominance of Si (Fig. 6-5B). In total, the first two PCs are driven by pedogenesis and grain-size dynamics and account for 78.4 % of total variance.

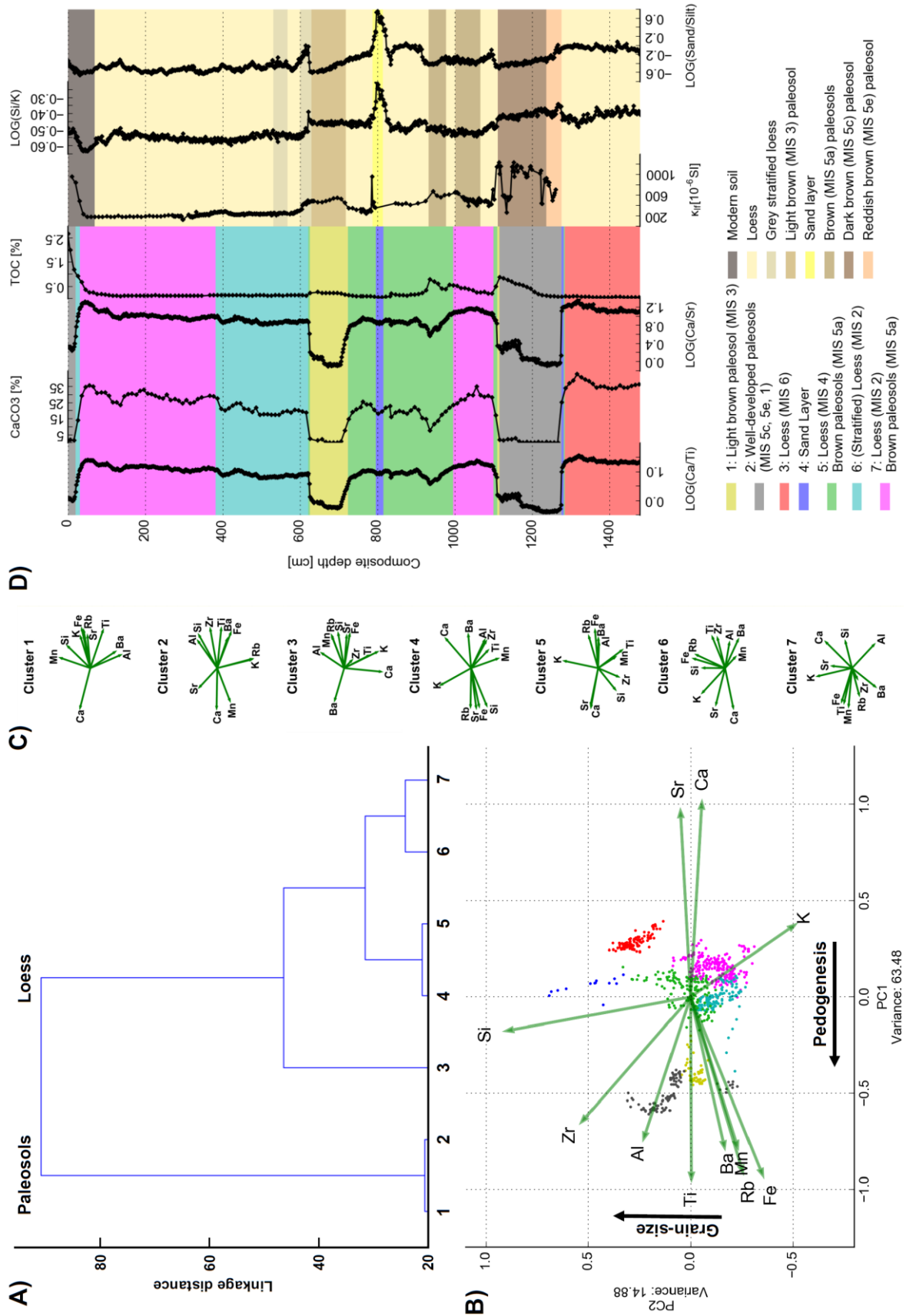


Fig. 6-5: Chemostratigraphy of the LPS Süttő. A) dendrogram, B) PCA and biplot with color coded data points according to the established chemostratigraphy, C) Biplots of individual clusters, D) biplot-based selected XRF scanning-derived element ratios in comparison with CaCO₃, total organic carbon (TOC), low-field volume-specific k_{lf} and the log-ratio of the grain-size fractions sand and silt. Background colors highlight similarities and differences between chemo- and lithostratigraphy. Grain-size and k_{lf} data are taken from Novothny et al. (2011). For detailed explanation, see text.

Based on PCA and biplot analyses, Ca/Ti and Si/K denote proxies for weathering intensity (Ca/Ti) and grain-size variability (Si/K) along the LPS Süttő (Fig. 6-5). Low Ca/Ti values indicate decalcification and thus paleosols. However, Ca/Ti exhibits slightly increased values in the upper parts of Unit 14 (1168-1110 cm) and Unit 6 (660-626 cm). This pattern either indicates syn-depositional pedogenesis or secondary calcification. According to micromorphological investigations of Barta (2014), the pedocomplex (Units 14-15) is well-leached with calcified root cells as secondary carbonate features present in the uppermost part of Unit 14 and in the lowermost part of Unit 15. In addition, Unit 6 is characterized by calcified root cells and the development of hypocoatings. Consequently, the observed increases in Ca/Ti are related to secondary calcification. This is further supported by the Ca/Sr ratio revealing contribution of secondary carbonate features by slightly increased values (e.g. Unit 14: 1168-1110 cm) compared to fully-leached conditions (e.g. Unit 14: 1234-1168 cm), while clearly indicating pedogenesis by low values (Fig. 6-5D). Furthermore, the small excursions to lower values along the Ca/Ti profile, at around 950 cm and around 400 cm, may point to initial pedogenesis, which is not recognized by the established chemostratigraphy. The lower excursion coincides with the upper boundary of Unit 10 and local maxima in TOC and κ_{if} , while the upper excursion accompanies a subtle positive excursion of κ_{if} . Hence, Ca/Ti is a reliable proxy for pedogenesis, even for paleosols which are not chemostratigraphically recognized as a specific cluster. However, secondary calcification needs to be taken into account as an important factor adversely influencing Ca- or Sr-based weathering indices (Bugge et al., 2011).

Si/K (Fig. 6-5D) shows a tripartite structure with high values from 1478 cm to 1110 cm, intermediate values from 1108 cm to 626 cm interrupted by a coarse sand layer from 810 cm to 784 cm, and low values from 624 cm to the top (Fig. 6-5D). This reflects the general upward fining trend in grain-size characteristic for Süttő (Fig. 6-5D). Attributing the parts of similar Si/K values to certain time periods, results in high values for MIS 6 loess (Unit 16) and for the depositional age of the material in which the mature MIS 5 paleosols (Units 14-15) developed. The same holds true for the intermediate values related to late MIS 5, MIS 4 and the parent material of the light brown paleosol (MIS 3) (Units 6-13). Low values correspond to late MIS 3 and MIS 2 loess (Units 2-5). Correspondingly, constant paleoclimatic conditions prevailed during the penultimate glacial period, the period between MIS 5b and MIS 3 and the Last Glacial Maximum (MIS 2), with a trend towards finer material.

Performing PCA and biplot analyses for each cluster separately, removes the dominant drivers pedogenesis and grain-size from the element dynamics between clusters. Since the LPS Süttő solely consists of eolian sediments (Novothy et al., 2009; Novothy et al., 2010; Novothy et al., 2011), the interpretation of cluster-specific biplots will be different to those of lacustrine sediments in which inner-cluster variability may either represent organic or minerogenic terrigenous input (cf. Martin-Puertas et al., 2017). We identify single elements that dominate clusters because of inner-cluster variability or transitions at the cluster's boundaries. The paleosol clusters 1 ($n = 49$) and 2 ($n = 90$) are characterized by strong correlations of Rb and K, while cluster 1 is additionally dominated by Ca. A strong positive correlation of Rb and K points to the same host minerals, which excludes illitization as a

dominant process for these clusters. In case of illitization, K and Rb would be rather anti-correlated due to K-entrapment. In contrast, Rb and K are not correlated in the loess clusters 3 ($n = 96$), 4 ($n = 13$), 5 ($n = 134$), 6 ($n = 126$) and 7 ($n = 219$). Clusters 4, 6 and 7 are not dominated by variabilities of certain elements while there is a high Ba variability in cluster 3 that is not linked to another element. Since the lowest Ba counts occur in cluster 3 along the LPS, such a low Ba content may question reliable Ba measurements. Cluster 5 mirrors the biplot for the whole dataset, with Ca and Sr being anti-correlated to Rb, Ba, Fe, Al indicating weathering, and Si being anti-correlated to K indicating grain-size variability. This is in line with the negative excursion in Ca/Ti at around 900 cm suggesting initial pedogenesis that is not represented by the established chemostratigraphy. The weathering-inert elements show positive correlations in clusters 1, 2, 4 and 6 whereas Ti and Zr are clearly negatively correlated with Al in cluster 3. Clusters 5 and 7 reveal no correlation between Zr and Al, but positive correlations of Ti with both Al and Zr. Leaching of weathering-susceptible elements may lead to relative enrichment of weathering-inert elements (Mongelli et al., 2006), and thus causes positive correlations between Al, Ti and Zr. In contrast, sediment sorting and recycling provoke negative correlations. While recycling leads to Zr enrichment at the expense of Al, and partly Ti, sorting primarily leads to Al enrichment (Caracciolo et al., 2011; Garcia et al., 1994; Mongelli et al., 2006; Perri et al., 2013). However, the leading processes affecting weathering-inert elements cannot be identified from PCA and biplot analyses alone.

6.4.3. Weathering trends

WD-XRF measurements allow the investigation of feldspar weathering by relating molar ratios of removable elements Na, Ca, and K to the molar ratio of the residual element Al (Nesbitt and Young, 1982). The CIA ranges from 0 to 100, whereupon 50 indicates unweathered Na-, Ca- and K-bearing feldspars, 75-85 reflects micas as well as clay minerals such as illite, and 100 represents Al-rich clay minerals (Nesbitt and Young, 1982, 1984, 1989). The UCC shows a CIA value of 51, whereas the AVL³ shows a value of 59. This points to slight weathering of the parent material at many loess sites (Gallet et al., 1998). Süttő reveals CIA values of 54-62, with a mean of 60 for unweathered loess, and 60-69 with a mean of 63 for paleosols. The lowest CIA values (54 and 56) correspond to the sand layer. Similar values are reported for the adjacent LPS Paks (Loess: 60-66, Paleosol: 61-72, Újvári et al., 2014) and the southern Hungarian LPS Nagynyárád, Majs and Töttös, with values between 58-69 (Újvári et al., 2008). These Hungarian LPS cover parts of the Young Loess Series (YLS, 16-280 ka, MIS 8 to MIS 2, Újvári et al., 2008). Obrecht et al. (2015) document for the Orlovat section in Serbia (MIS 6 to MIS 2) CIA values confined to the range between 64-69 for both loess and paleosols. Higher values, comparable to the post-Archean Australian average shale (PAAS, Taylor and McLennan, 1985), which is often used as a reference to weathering-altered sediments (CIA: 70), occur at the Hungarian Beremend LPS (likely MIS 17 to MIS 2) (Loess: 67-77, Paleosol: 70-78, Varga et al., 2011), whereas the Czech LPS Zeměchy and Dobšice (likely MIS 5 to MIS 2) show larger variabilities, with CIA values ranging from 45 in loess to 75 in paleosols (Hošek et al., 2015).

The A-CN-K diagram (Fig. 6-6A) reveals the typical line of weathering of Ca- and Na-bearing feldspars parallel to the A-CN join (Buggle et al., 2008; Nesbitt and Young, 1984; Újvári et al., 2014). Loess samples cluster around the AVL³ composition and indicate already weathered material when compared to the UCC (Fig. 6-6A). The loess samples closest to the UCC are referred to the sand layer, and thus, to the least weathered material at Süttő. Since the weathering trend can be traced back to the UCC, the loess parent material reflects a felsic rock composition comparable to the UCC and like the igneous rock type granodiorite (Újvári et al., 2008). According to the expected weathering trend, paleosol samples plot closer to the K-A join than loess samples. In contrast, floodplain sediments selected as representatives of unaltered parent material from potential source areas plot closely together and close to the mostly weathered paleosol samples (Fig. 6-6A), suggesting that floodplain sediments have already been affected by weathering. Nonetheless, their composition is characterized as UCC-like as well, because they are connected to the UCC linearly parallel to the A-CN join (Buggle et al., 2008). We deduce from the plotting pattern that neither K-enrichment nor weathering of K-bearing minerals, such as micas or illite, took place at Süttő. K-enrichment would direct the line of weathering more to the K-A join (Fedo et al., 1995) while K-removal would direct the line of weathering more to the A-CN apex (Nesbitt and Young, 1989). Furthermore, we can exclude grain-size-related sorting trends at Süttő, as there are no samples plotting on a line perpendicular to the CN-K join. Coarse grains carry more feldspar minerals, and are thus poor in Al, whereas fine grains tend to be rich in Al (Buggle et al., 2008; Nesbitt et al., 1996).

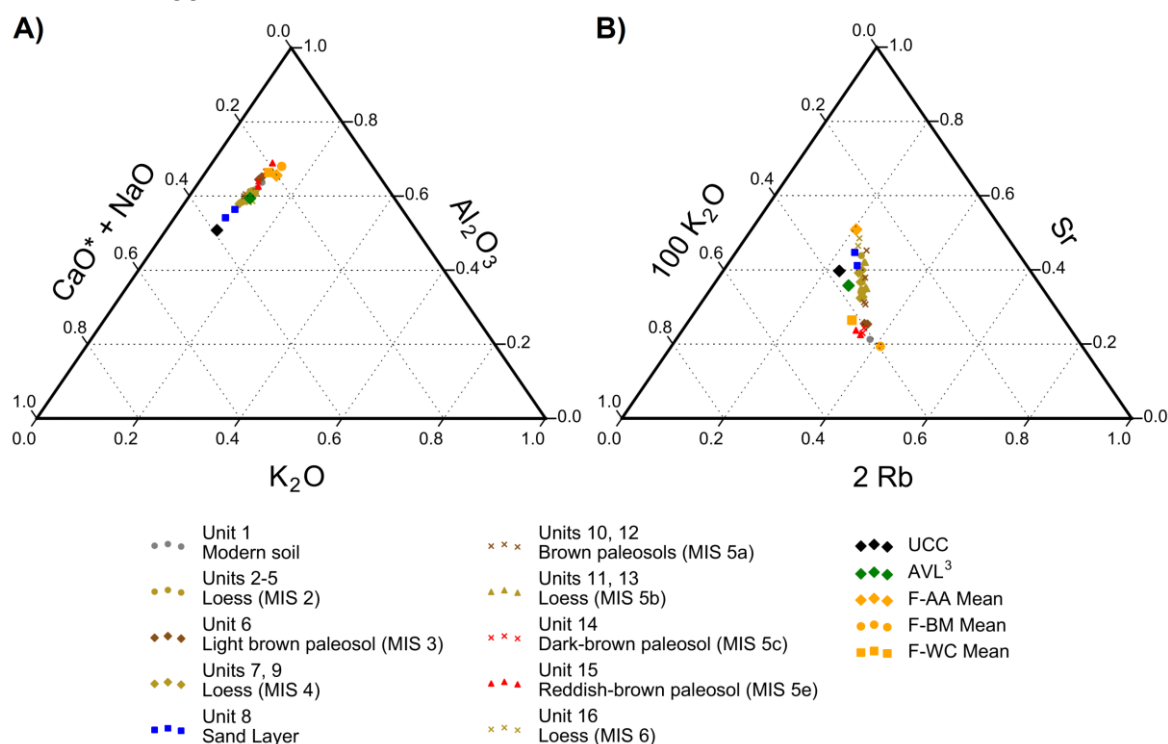


Fig. 6-6: Weathering-related ternary plots based on WD-XRF data. A) A-CN-K plot, B) Sr-K-Rb plot. UCC: Upper continental crust after the map model in Condie (1993), AVL³: Average loess composition after Újvári et al. (2008), F-AA Mean: Mean of the floodplain sediments from the Austroalpine cover nappes area, F-BM Mean: Mean of the floodplain sediments from the Bohemian Massif, F-WC Mean: Mean of the floodplain sediments from the Western Carpathians (Buggle et al., 2008).

At the Sr-K-Rb plot (Fig. 6-6B), loess and paleosol samples plot on a straight line directed to the Sr-K apex, with a slight deviation towards the K-Rb apex for paleosol samples. Loess samples from Unit 16 are located at the upper end towards the Sr-apex corresponding to the highest CaCO₃ values along Süttő. Micromorphological investigations (Barta, 2014), together with low CaCO₃ values in paleosols, document minor importance of secondary calcification dynamics. Nonetheless, extensive leaching of the overlying paleosols may have contributed to the high CaCO₃ content in Unit 16 (Barta, 2014). Compared to the UCC and the AVL³, loess samples are poorer in K but richer in Rb (Fig. 6-6B). Relative Rb-enrichment occurs as a consequence of substitution of K in K-feldspars (Buggle et al., 2011; Nesbitt et al., 1980). Consequently, K depletion, together with Rb enrichment, may point to already weathered material that formed the loess at Süttő. Paleosol samples show enrichment in both K and Rb with a slight tendency towards the Rb apex (Fig. 6-6B). There are three possible explanations for this behavior: (1) Sr depletion causes a relative enrichment in both K and Rb without an actual increase of K and Rb concentrations, (2) grain-size dynamics with coarse particles being rich in Sr and fine particles being rich in Rb and K superimpose weathering trends, or (3) illitization and K-feldspar weathering are competitive processes that are active at the same time, with a slight dominance of K-feldspar weathering. Taking into account the findings deduced from the A-CN-K plot (Fig. 6-6A), there are no hints for the last two explanations. Floodplain sediments denote end-members in the Sr-K-Rb plot, with the F-AA samples plotting towards the Sr apex, and the F-BM as well as F-WC samples plotting towards the K-Rb join (Fig. 6-6B). This favors a dust source dominated by F-AA material, with minor contributions of F-BM and F-WC material, presumably dependent on the prevailing wind directions and the actual position of the river Danube in the Little Hungarian Plain through time.

In contrast to the WD-XRF-derived Sr-K-Rb plot, the XRF scanning-derived Sr-K-Rb plot (Fig. 6-7) indicates Sr depletion combined with Rb enrichment, while K remains constant. The complete data set clusters along the Sr-Rb join with MIS 6 loess closest to the Sr-K join and the MIS 5e and MIS 5c related paleosols closest to the K-Rb join (Fig. 6-7). Consequently, this plot reflects the decalcification trend correctly, but then fails to represent the simultaneous but relative K and Rb enrichment. Constant K values in combination with increasing Rb values may support the idea that illitization and K-feldspar weathering are competitive processes active at the same time. However, the used ITRAX XRF core-scanner tends to have difficulties reliably recording small concentration changes in K (Huang et al., 2016; Profe et al., 2018; Sun et al., 2016). This might be explained by inter-element effects between Ca and K (Potts, 1992) which might be not compensated for by the XRF processing software. High Ca concentrations in loess enhance K counts as K atoms partly absorb Ca XRF radiation. In contrast, low Ca concentrations in paleosols prevent Ca XRF radiation-related excitation of additional K atoms. Consequently, K counts may successfully compensate for the lower Ca contribution but fail to represent slightly increased K concentrations (up to 1 % at Süttő) in paleosols. A correlation between WD-XRF-derived K₂O and Rb concentrations corroborates this hypothesis by $R^2 = 0.96$. Although only 33 samples were measured by WD-XRF, this result sounds a note of caution to XRF scanning-derived K-bearing weathering indices.

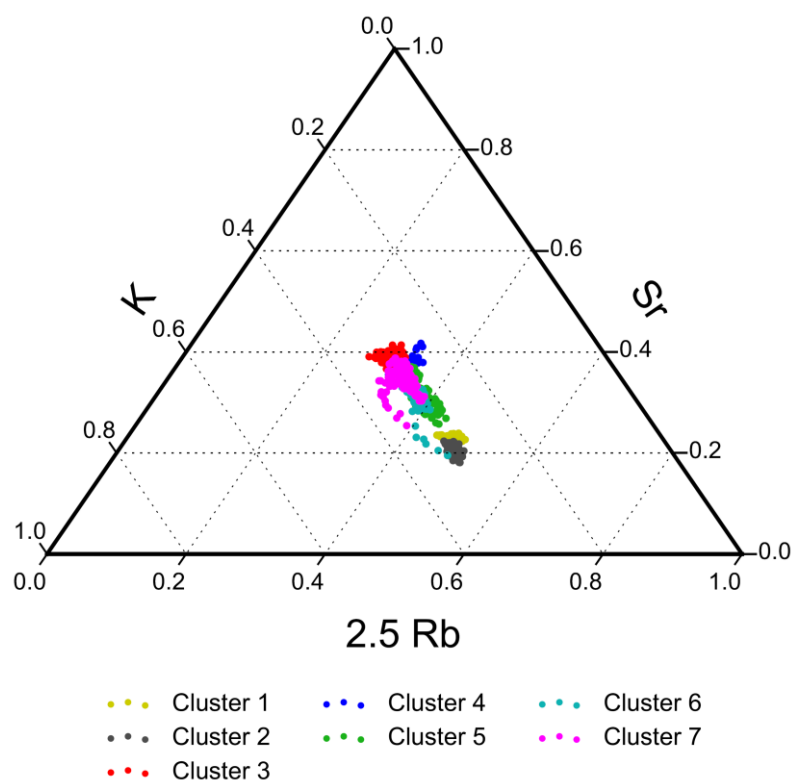


Fig. 6-7: XRF scanning-derived Sr-K-Rb ternary diagram. Clusters are explained in Fig. 6-5.

6.4.4. UCC, sediment recycling and dust provenance

The geochemical composition of the LPS Süttő is similar to that of the UCC except for Ca and Mg enrichment in loess and depletion in paleosols (Fig. 6-8). This points to a dolomite-rich mineral composition (Újvári et al., 2008). Buggle et al. (2008) attribute Ca and Mg enrichment in loess to leaching from paleosols into the underlying loess units. Loess samples scatter around AVL³, whereupon the oldest loess shows the largest deviations from AVL³. Ti, P, Nb, U and Zr are enriched whereas Al, Fe, Na, K, Ba, Ni, Sr and V are depleted in loess samples (Fig. 6-8). The weathering scheme of terrestrial sediments is mirrored with removal of water soluble elements such as Na, Ca and Sr (Buggle et al., 2011; Nesbitt et al., 1980).

Depletion of K and Ba indicate the intermediate stage of weathering with K-removal and accompanying relative Rb and Ba enrichment. Since retention of ions in soils is controlled by their ionic potential in relation to their atomic radius, large ions such as Rb and Ba preferentially adsorb to clay minerals as a consequence of weathering releasing Rb and Ba from K-bearing minerals (Buggle et al., 2011). In case of secondary clay mineral formation due to strong chemical weathering, atoms with a large ion radius are also leached (Buggle et al., 2011; Nesbitt et al., 1980). This explains the general differences between Rb and Ba when compared with the UCC (Fig. 6-8). Ba is more depleted than Rb under the same weathering conditions, according to its comparatively smaller ion radius. However, leaching of Ba and Rb as a consequence of strong chemical weathering appears unlikely, due to the

small differences in the sample/UCC ratios between unweathered loess and paleosols at Süttő. Instead, this signal points to an inherited weathering signal of parent material from the source areas.

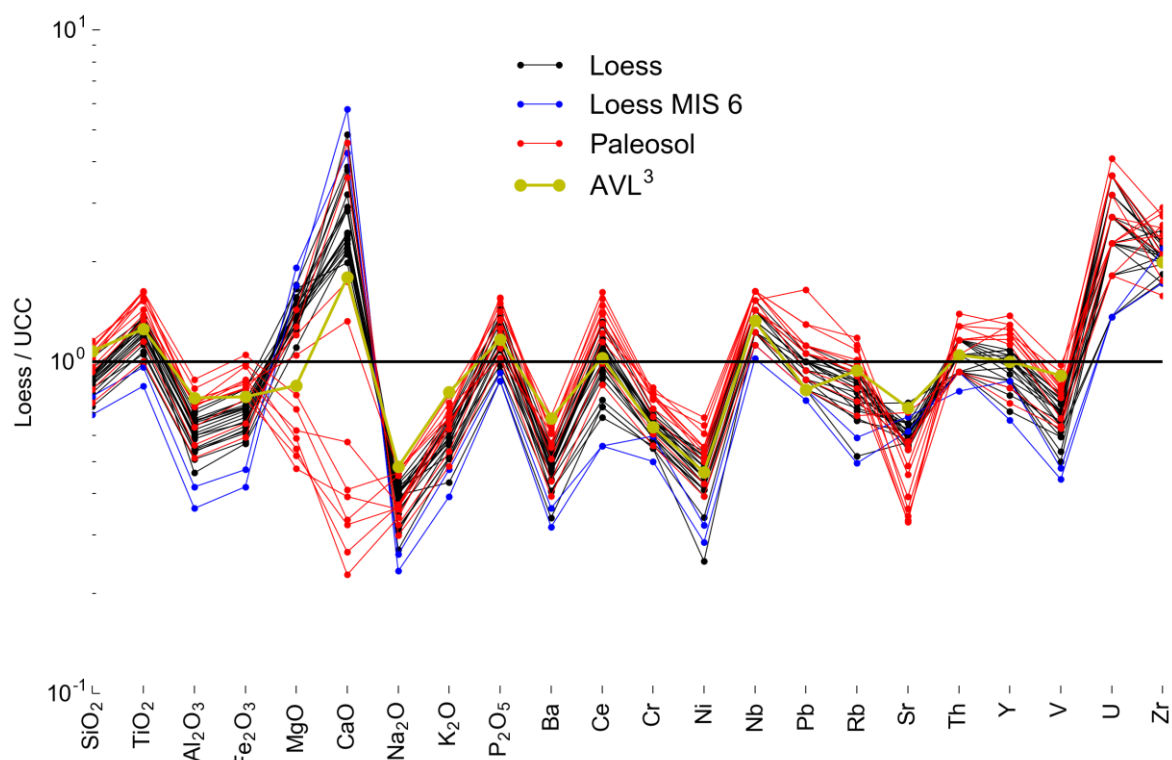


Fig. 6-8: UCC-normalized element patterns at the LPS Süttő. AVL³ (Újvári et al., 2008) is plotted for comparison. Loess: Units 2-5, 7-9, 11, 13. Loess MIS 6: Unit 16. Paleosol: Units 1, 6, 10, 12, 14, 15.

Depletion of compatible elements (Ni, Cr, V, Fig. 6-8) with regard to magmatic melts documents an insignificant contribution of mafic or ultramafic rocks in the source areas (Floyd et al., 1989; McLennan et al., 1993; Tripathi and Rajamani, 1999; Újvári et al., 2008). This is further supported by depletion of Al and Fe, and enrichment of the weathering-inert elements Ti and Zr (Fig. 6-8) that are predominantly associated with felsic rocks (Taylor et al., 1983). In addition, Ti and Zr indicate transport-induced mineral sorting that accumulates heavy minerals in clastic sediments (Buggle et al., 2008; Gallet et al., 1996; Újvári et al., 2008). Wind preferentially lifts particles with a size in the order of 80 μm (Smalley and Markovic, 2017). This leads to Zr enrichment, as Zr predominantly occurs in heavy minerals that are associated with coarse grains. In contrast, Ti may occur in coarse and fine particles dependent on their incorporation in heavy or clay minerals (Garcia et al., 1994; Mongelli et al., 2006).

The Al-Ti-Zr ternary plot (Fig. 6-9) contributes to a better understanding of sediment sorting and recycling dynamics at Süttő. Compared to the UCC, all considered samples plot along the A-Zr join with the end-members F-AA floodplain sediment (most Al) and MIS 6 loess (least Al). In addition, MIS 6 loess plots slightly directed to the Zr apex (Fig. 6-9A). This pattern represents sediment recycling, i.e. Zr addition, typical for clastic sediments that experienced multiple erosion-deposition cycles (Caracciolo et al., 2011; Újvári et al., 2008). The floodplain sediments, as well as the AVL³, show Zr addition relative to the UCC inferring

loess as dust depositions where the source material may have undergone several weathering cycles before. Süttő is more strongly affected by sediment recycling than the AVL³, independent of paleosol development. Since paleosol samples scatter between loess samples, chemical weathering is successfully eliminated by considering weathering-inert elements only. The XRF scanning results (Fig. 6-9B) reveal a more differentiated pattern with Al depletion at the expense of both Ti and Zr. This is particularly true for younger loess clusters while paleosol clusters scatter rather towards the Al apex. MIS 6 loess is slightly more directed towards the Zr apex, comparable to the WD-XRF data. However, samples of the sand layer plot towards the Al-Zr join (Fig. 6-9B), indicating that coarse grains are depleted in Ti and predominantly enriched in Zr. Despite this clear hint for sediment sorting, i.e. fractionation of Ti (fine) from Zr (coarse) (Mongelli et al., 2006), this trend cannot be confirmed by the sand samples in the WD-XRF plot (Fig. 6-9A). Therefore, both Al-Ti-Zr ternary plots reveal sediment recycling, especially for the oldest loess, but show ambiguous results with respect to sediment sorting.

Considering Zr/V and Zr/Ni ratios in relation to Th/Ni and Th/V ratios provides additional information about Zr addition. Th and Zr are incompatible in igneous melts, and thus enriched in felsic rocks, whereas Ni and V are compatible in igneous melts and preserve a provenance signal (Újvári et al., 2008; Újvári et al., 2014). Fig. 6-10 highlights Zr addition, as our data is directed to the right of the compositional trend line (dashed line) (Újvári et al., 2008). Such Zr derivation from the compositional trend line reflects sediment recycling (Caracciolo et al., 2011; Mongelli et al., 2006; Újvári et al., 2008). When compared with UCC and PAAS concentrations, samples from the LPS Süttő plot above them and shift to the right, highlighting Zr and Th enrichment. This is characteristic for felsic rocks, and confirms that mafic rocks contributed negligibly to parent material of the LPS Süttő (Újvári et al., 2008; Újvári et al., 2014). Furthermore, the samples plot in a very confined region with regard to the Th/metal ratios (Újvári et al., 2008; Újvári et al., 2014). This indicates one major dust source region throughout the depositional history of Süttő. Accordingly, our results are in line with other central European LPS such as Paks (Újvári et al., 2008; Újvári et al., 2014).

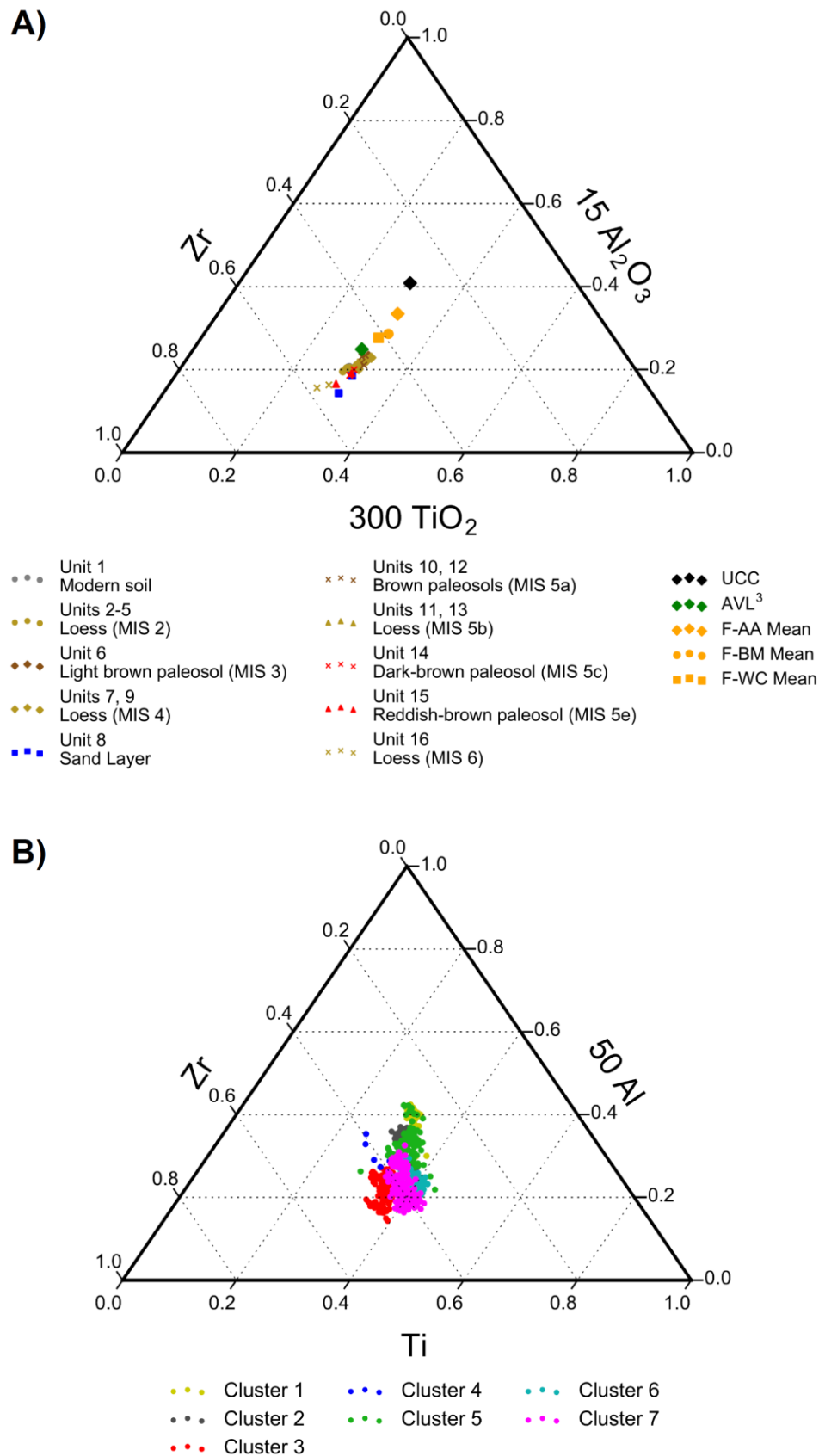


Fig. 6-9: Al-Ti-Zr ternary plots for the LPS Süttő. A) WD-XRF data, B) XRF scanning data. Data is centered according to Garcia et al. (1994). UCC: Upper continental crust after the map model in Condie (1993), AVL³: Average loess composition after Újvári et al. (2008), F-AA Mean: Mean of the floodplain sediments from the Austroalpine cover nappes area, F-BM Mean: Mean of the floodplain sediments from the Bohemian Massif, F-WC Mean: Mean of the floodplain sediments from the Western Carpathians (Bugge et al., 2008).

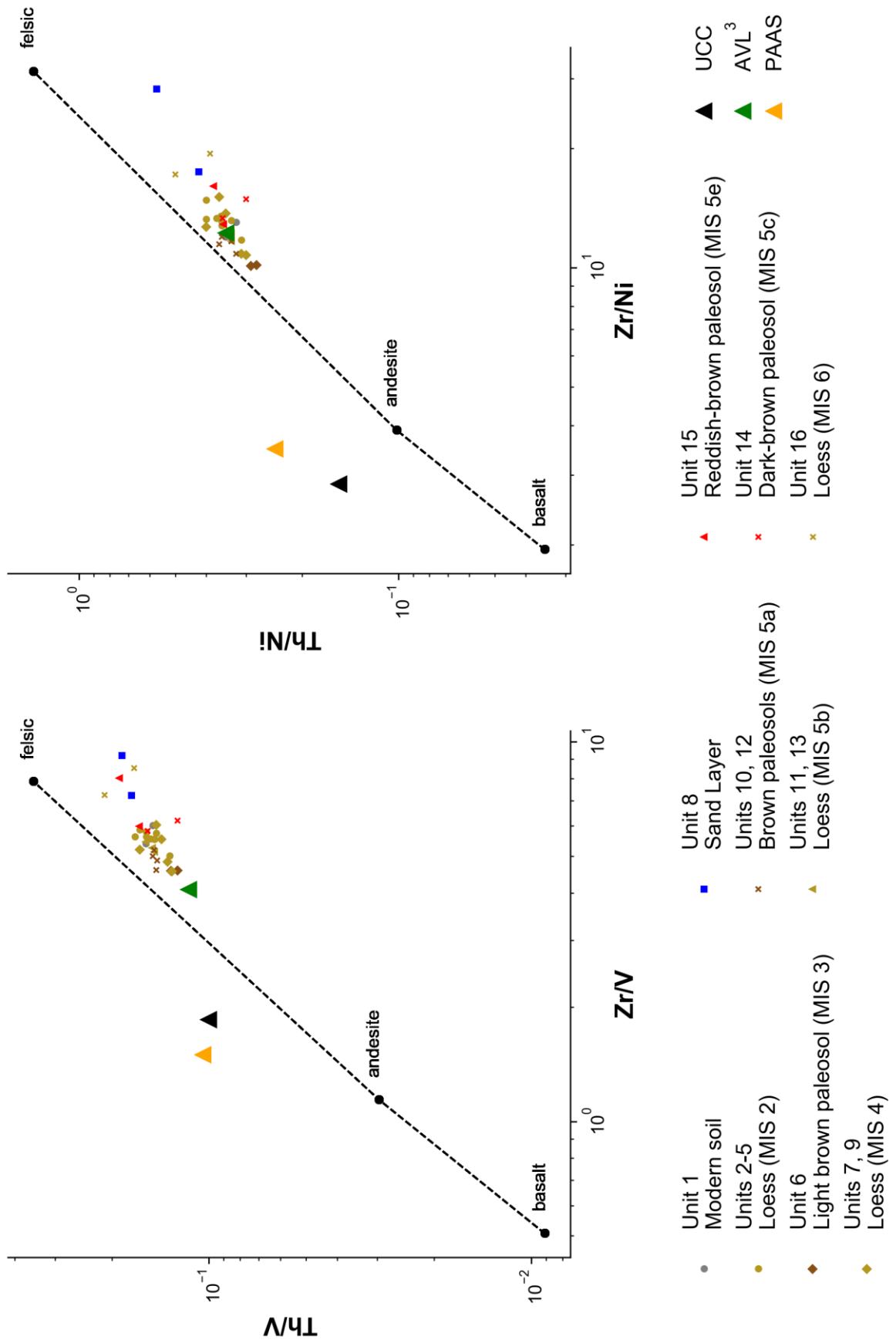


Fig. 6-10: Zr/V vs. Th/V and Zr/Ni vs. Th/Ni scatter plots. UCC: Upper continental crust after the map model in Condie (1993), AVL³: Average loess composition after Újvári et al. (2008), PAAS: Post-Archean Australian average shale (McLennan, 2001).

6.4.5. Proxy correlation analysis

We correlated the XRF scanning-derived and clr-transformed element data with grain-size, TOC, CaCO₃ content and MS (Fig. 6-11) to determine dominant processes that control element dynamics. Ca, Sr and, to a lesser extent, K, are positively correlated to each other while they are negatively correlated to Al, Ti, Mn, Fe, Rb, Zr and Ba. Si followed by K are least correlated to any other element. This pattern resembles the biplot for the complete data set as shown in Fig. 6-5B. Weak correlations between K and both Rb ($\rho = -0.23$) and Ba ($\rho = -0.50$) suggest that there is no dominant process linking K with Rb and/or Ba dynamics along the LPS Süttő. However, the weak correlation between XRF scanning-derived and clr-transformed K and Rb counts contradicts the strong correlation between WD-XRF-derived K and Rb concentrations ($R^2 = 0.96$), and thus confirm difficulties of the ITRAX XRF scanner in reliably detecting small concentration changes of K. Consequently, only the A-CN-K plot provides reliable information about K dynamics at Süttő.

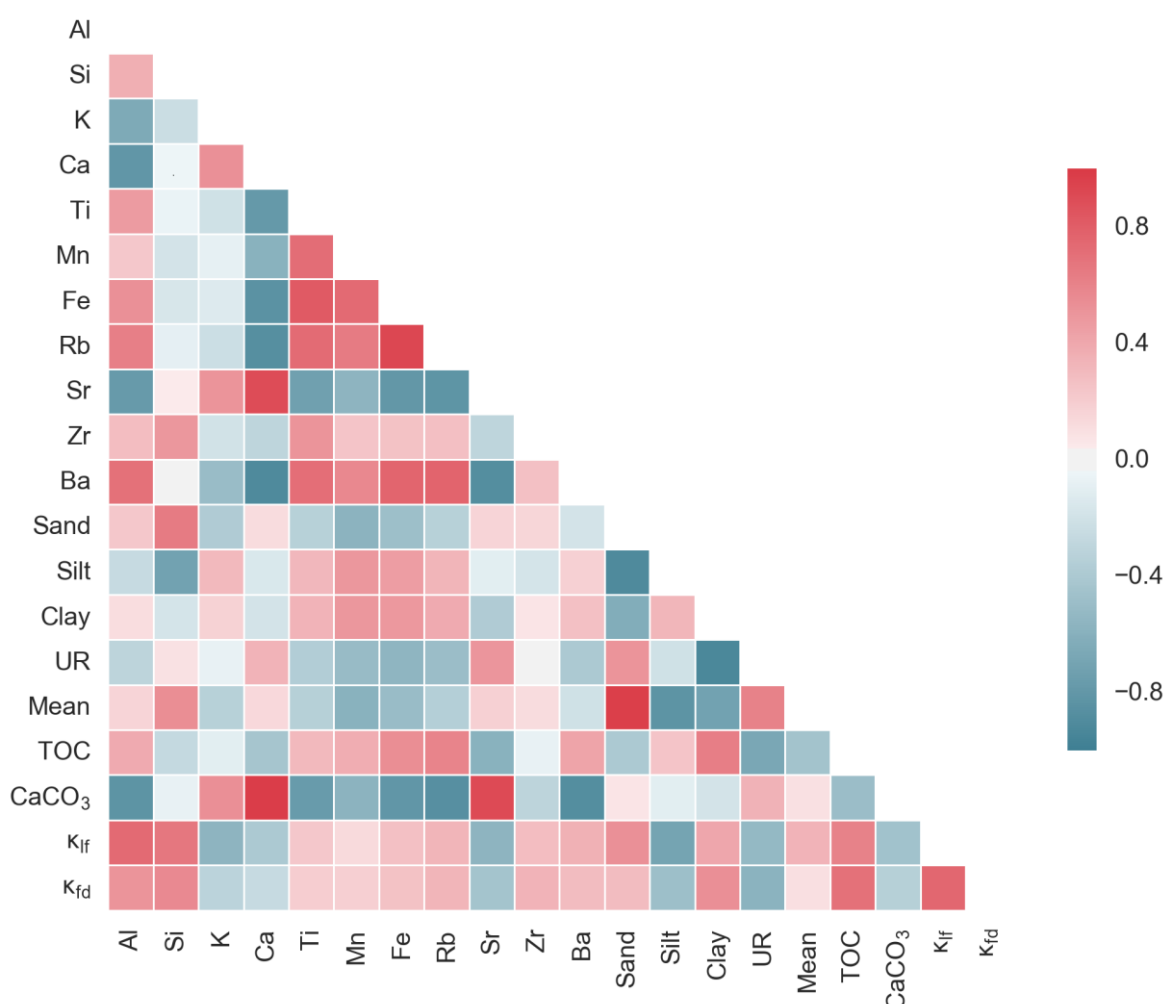


Fig. 6-11: Correlation matrix between XRF scanning-derived and clr-transformed element data and other proxy data. The Spearman rank correlation coefficient (ρ) is displayed. UR = U-ratio (16-44 μm / 5.5-16 μm ; Novothny et al., 2011). TOC = total organic carbon. κ_{lf} = low-field volumetric magnetic susceptibility (Rolf et al., 2014). κ_{fd} = frequency-dependent magnetic susceptibility (Rolf et al., 2014). Grain-size data is taken from Novothny et al. (2011). Due to different spatial resolutions of TOC, CaCO₃, κ_{lf} and κ_{fd} , the number of data points used for the calculation of ρ differs for these parameters. TOC and CaCO₃: $n = 148$, κ_{lf} : $n = 315$, κ_{fd} : $n = 294$.

In contrast, Si is the only element showing significant correlations to the grain-size fractions sand ($\rho = 0.64$) and silt ($\rho = -0.72$). Clay is best correlated with Fe ($\rho = 0.49$) and Mn ($\rho =$

0.50). This implies that none of the commonly applied element ratios work as grain-size proxy at Süttő. Given the fact that K shows a rather constant profile, Si/K is the best suited element ratio to represent grain-size dynamics (Figs. 6-5D and 6-11). However, the opposite direction of their arrows in the biplot might be rather attributed to their non-correlation with other elements than to an actual anti-correlation (Fig. 6-5B). This is in line with the identified weak measurement capabilities of the ITRAX XRF scanner as to K. However, the observed anti-correlation might be true in the PC1 and PC2 space, since the first two PCs account for 78.4 % of total variance (Fig. 6-5B). Hence, we can exclude grain-size dynamics from influencing element-based weathering and dust provenance indices.

While Ca and Sr are best correlated to CaCO_3 ($\rho \geq 0.91$) indicating that Ca and Sr are predominantly contained in CaCO_3 , only Rb, Fe and Sr show correlations ($|\rho| \geq 0.54$) with TOC (Fig. 6-11). TOC, in turn, is linked to grain-size (U-ratio, $\rho = -0.68$ and clay, $\rho = 0.63$) and volume-specific MS (κ_{if} , $\rho = 0.61$), as well as frequency-dependent MS (κ_{fd} , $\rho = 0.70$). Therefore, Units 10 and 12, representing initial pedogenesis, are characterized by positive excursions of TOC and MS, but are not reflected by the element record.

MS is predominantly correlated to Al, Si, sand, clay and TOC and anti-correlated to silt (Fig. 6-11). This points to magnetic minerals with a predominant grain-size in the range of sand or clay. In addition, Si and Al are usually not related to magnetic minerals. Si, especially quartz, is characterized by diamagnetism instead (Rochette, 1987). According to Rolf et al. (2014), coarse magnetic multi-domain grains are responsible for high κ_{if} values in the sand layer, while fine super-paramagnetic grains contribute most to high κ_{if} values in paleosols. The latter is mostly accompanied by high κ_{fd} values, and thus behaves in accordance with the in-situ formation of super-paramagnetic minerals during pedogenesis (Heller et al., 1991). On the contrary, high κ_{if} values in the sand layer may suggest the wind-vigor model to be active at times of enhanced wind activity and dust supply, e.g. during Heinrich events (Evans et al., 2003). The wind-vigor model was first described for Alaskan loess, which is characterized by low κ_{if} values in paleosols, and high κ_{if} values in loess. Strong winds are able to transport dense magnetic minerals and deposit them downwind (Begét and Hawkins, 1989). The wind-vigor model may also explain correlations between Si and MS due to grain-size variability. Correlations between both Al and Si and MS may imply availability, transport and deposition of different magnetic minerals, dependent on the dominant dust supply from the Danube floodplains. Since mica-rich sediments may reach $\kappa_{\text{if}} > 500 \cdot 10^{-6}$ SI (Rochette, 1987), the mineralogical composition may influence MS data. In addition, some paleosol samples exhibit high κ_{if} and low κ_{fd} values (Rolf et al., 2014) indicating magnetic depletion as a consequence of low-temperature oxidization or water logging (Baumgart et al., 2013). However, water logging appears unlikely in a continental, non-permafrost dominated climatic region, while low-temperature oxidization may occur particularly during cold seasons. Usual proxies for MS such as Fe and Ti reveal no correlation with $|\rho| \leq 0.27$.

6.4.6. Bulk loess mineralogy

Bulk loess mineralogy (Fig. 6-12) reveals a dominance of quartz in MIS 6 loess (> 43 %, 1420 cm, 1308 cm). In contrast, MIS 4 loess is characterized by micas with more than 50 % whereas MIS 2 loess is dominated by both quartz and micas with each 35 %. Carbonates are rather constant in MIS 2 (342 cm) and MIS 4 (864 cm) loess (ca. 14 %) but most abundant in MIS 6 loess (22 %). Feldspars play a subordinate role in loess at the LPS Süttő with 4 to 19 %. Due to the dominance of micas during MIS 4, increased MS during MIS 4 compared to MIS 2 (Fig. 6-5) might be attributed to changes in mica content.

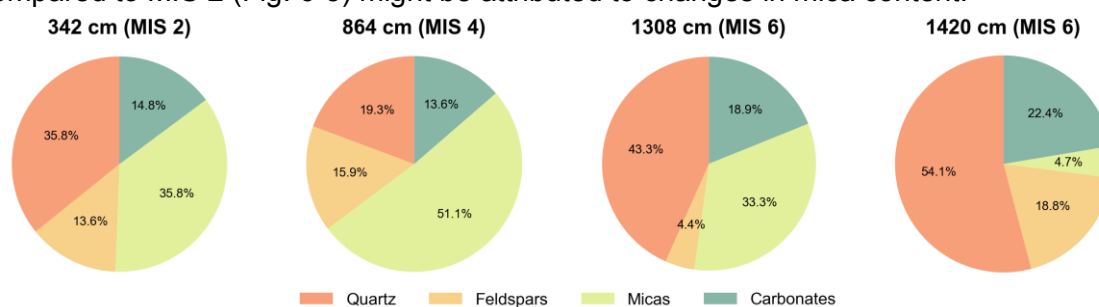


Fig. 6-12: Bulk mineralogical composition of four representative loess samples.

6.4.7. Paleoenvironmental implications

6.4.7.1. Weathering

Geochemistry tracks in-situ weathering for all mature paleosols (Units 6, 14, 15), including the modern soil (Unit 1). The chemostratigraphy distinguishes between Units 1, 14, 15 and Unit 6 while biplots, A-CN-K and Sr-K-Rb ternary plots as well as the comparison with the UCC document decalcification for all of the abovementioned four lithological units. There is no clear evidence for K-removal or K-fixation as a consequence of the intermediate stage of weathering. This is in agreement with A-CN-K plots from Batajnica / Stari Slankamen (Vojvodina, Serbia), Mircea Voda (Dobrudja, Romania) that also show no hints for K-feldspar weathering (Bugge et al., 2008). The YLS at the Beremend LPS in south-western Hungary is characterized by Sr depletion, whereas Rb and K show rather constant profiles (Varga et al., 2011). Mineralogical investigations reveal smectite production in paleosols, while illite remains rather constant. Consequently, K is neither removed due to K-feldspar weathering nor enriched due to illitization (Varga et al., 2011). At Paks a similar trend is observed towards a slight Rb enrichment in paleosols (Újvári et al., 2014), although there are no paleosols exposed that are attributed to MIS 5 (Thiel et al., 2014). The comparison between paleosols of the Old Loess Series (OLS, 280-900 ka, MIS 9-24, Újvári et al., 2008) and the YLS at Paks indicates higher illite contents and lower CIA values in YLS paleosols (Újvári et al., 2014). This is often referred to as aridization of paleoenvironmental conditions since MIS 10 (Újvári et al., 2014). However, interpreting illite as a proxy for physical weathering (Liu et al., 2005), higher illite contents point to chemically less weathered material, together with a higher sedimentation rate as a consequence of increased dust supply (Újvári et al., 2014; Varga et al., 2011). Therefore, lower CIA values do not necessarily reflect aridization, but increased sedimentation of chemically less weathered

material (Újvári et al., 2014). Obreht et al. (2016) document this long-term paleoclimate change from Mediterranean to continental climate, favoring Chernozem instead of rubified Cambisol development during interglacials for the Middle Danube basin (Batajnica / Stari Slankamen, Fig. 6-1) and the Central Balkans (Stalać, Serbia) for the last 350 ka. Comparing Batajnica / Stari Slankamen with Stalać reveals Mediterranean climate at the southern LPS Stalać (Fig. 6-1) until 110 ka, suggesting stronger and earlier aridization in the north (Obreht et al., 2016).

For Süttő, this implies arid climatic conditions that prevented K-feldspar weathering from being active throughout the last glacial-/interglacial cycle. Decreasing CIA values from 69 (Unit 15) to 64 (Unit 14) confirm degrading climatic conditions from MIS 5e to MIS 5c as previously deduced from micromorphology (Novothy et al., 2011). In addition, Unit 14 is stratigraphically classified as a Chernozem-like paleosol, pointing to its formation under a steppe-like climate (Novothy et al., 2011). In contrast, Unit 15 is lithologically determined as a reddish-brown paleosol indicating wetter climatic conditions. The chemostratigraphic similarity between Units 1, 14 and 15 suggests comparable paleoenvironmental conditions for MIS 5e, MIS 5c and MIS 1. This is in line with present-day Chernozem-dominated soil assemblages in the Carpathian Basin (Ibáñez et al., 2013), and supports rather arid continental climatic conditions. Although secondary carbonate formation is likely responsible for the increase of Ca/Ti in the upper part of Unit 14, the decrease of κ_{if} may indicate syn-pedogenic dust deposition lowering the CIA from 67 to 64.

The sequence of a reddish-brown paleosol (Cambisol) attributed to MIS 5e, followed by the development of a Chernozem related to MIS 5c, is also suggested for the polygenetic formation of the pedocomplex P2 at Paudorf in Lower Austria (Sprafke et al., 2014). In contrast, Dolní Věstonice in Moravia is characterized by a truncated Luvisol with formation of a Bt-horizon (MIS 5e) followed by a tripartite Chernozem complex (MIS 5c to MIS 5a, Antoine et al., 2013). The Czech LPS Zeměchy and Dobšice reveal the same stratigraphy, with CIA values >70 in the truncated Luvisols (Hošek et al., 2015) indicating wetter climatic conditions than for the Carpathian Basin. However, reddish-brown and brown forest paleosols at the LPS Beremend also exhibit CIA values > 70 (Varga et al., 2011). This may point to a reduced input of physically weathered material, due to a larger distance to source when compared with Süttő. Further west, LPS in Upper Austria and northern France also show Luvisols as interglacial paleosols (Antoine et al., 2016; Terhorst et al., 2002) representing a climate driven by the influence of the North Atlantic. Towards the east, this influence diminishes in favor of a continental climate in Lower Austria, strengthening towards the Carpathian Basin as exemplified on the LPS Süttő.

From a geochemical perspective, Units 12 and 10 exhibit a weak pedogenesis with local TOC maxima (Fig. 6-5D), and are attributed to MIS 5a (Novothy et al., 2011). The latter also accompanies a slight increase in κ_{if} , and a decrease in Ca/Ti (Fig. 6-5D) as well as Rb (supplementary material Table 6-2). They are not recognized as paleosols in the chemostratigraphy due to their geochemical similarity to unweathered loess. However, from a lithological perspective, Units 12 and 10 seem to represent a stronger pedogenesis than Unit 6. Although Unit 12 lacks secondary carbonates compared to Unit 10 (Barta, 2014),

Unit 10 exhibits less CaCO_3 than Unit 12. While specific secondary carbonates indicate frost deformation, and thus more humid climatic conditions during Unit 12 (Barta, 2014), higher clay content points to strong but rapid soil formation under arid climatic conditions in Unit 10 (Novothy et al., 2011). According to Targulian and Krasilnikov (2007), initial pedogenesis might be possible within several hundred years, depending on the specific climatic conditions. Both paleosols are more characterized by organic matter accumulation than chemical weathering, as deduced from the correlation analysis, and thus likely developed under cool-arid steppe-like conditions. The high TOC values, together with the positive κ_{if} excursion, suggest preservation of the topsoil as κ_{if} is expected to be highest in topsoils (Hošek et al., 2015). Consequently, κ_{if} is more sensitive to pedogenesis compared to chemical proxies at Süttő and underlines the completeness of the LPS Süttő for MIS 5.

Unit 6 reveals a CIA of 65, similar to that of Unit 14 and 15, while Units 5 and 3 show CIA values of 60 and are thus not considered as paleosols (supplementary material Table 6-2). However, secondary carbonates in the form of hypocoatings, carbonate coatings and calcified root cells indicate weak pedogenesis, while dust deposition prevails in the stratified loess of Units 5 and 3 (Barta, 2014). Since Units 5 to 3 are attributed to late MIS 3 (Novothy et al., 2011), a sharp transition in paleoclimatic conditions between middle and late MIS 3 appears likely. The chemostratigraphy does not separate among Units 5, 4 and 3, but between Unit 6 and the other identified paleosols. This is related to slightly increased Ca and Sr values that are either related to the presence of secondary carbonates or syn-pedogenic dust deposition. Grain-size dynamics support this interpretation due to a sand peak in Unit 5. Furthermore, hypocoatings represent evaporation-based CaCO_3 impregnation of the matrix and thus arid, steppe-favoring conditions during MIS 3 (Barta, 2014). Malacothermometry reveals July temperatures (20.9°C) comparable to today (Novothy et al., 2011). The LPS Vlasca and Urluia (Romania) record the same trend at the Danube delta, emphasizing a large-scale change in atmospheric circulation patterns towards drier and windier conditions during late MIS 3 (Obrecht et al., 2017).

6.4.7.2. Dust provenance and tectonics

Th/metal ratios together with the similarity of samples in comparison with the UCC confirm that the LPS Süttő is most likely fed by one dominant dust source – the adjacent Danube floodplains (Novothy et al., 2011). According to the geomorphodynamic concept of Smalley and Leach (1978), material from the Danube and its tributaries denotes the main dust source. Different tributaries either transport material from the Alps, Moravia or the West Carpathians, contributing to a specific, identifiable geochemical fingerprint (Buggle et al., 2008). Additional dust sources might be the Bikol Creek (Novothy et al., 2011) as well as Tertiary rocks from which paleo-yardangs have intermittently formed for the last 1.5 Ma (Sebe et al., 2011). Comparison of loess samples with different floodplain sediments identifies glaciofluvial sediments from the Austroalpine cover nappes (F-AA) area as the dominant dust source, according to their highest Sr content in the Sr-K-Rb ternary plot (Fig. 6-6). Although minor contributions of the Bikol Creek or Tertiary rocks cannot be completely excluded, F-AA sediments indicate prevailing northwest to west winds

throughout the last glacial-/interglacial cycle. Topographic obstacles such as the Carpathian Arc or the Dinarides hamper surface winds from other directions than northwest to west (Sebe et al., 2011). These circumstances led to the intermittent formation of paleo-yardangs, predominantly in northwest-southeast direction during periods of enhanced wind activity, until the termination of the last glacial period (Sebe et al., 2011). This is consistent with numeric model results for MIS 5b and 4, indicating only small changes in world atmospheric circulation patterns compared to interglacial conditions (Löfverström et al., 2014). However, more sophisticated regional climate models may provide better reconstructions of regional atmospheric circulation patterns (Ludwig et al., 2017). Results of atmospheric general circulation model (AGCM)-runs for MIS 3 Greenland stadials, interstadials and Heinrich events also demonstrate prevailing west to northwest winds at 850 hPa (Rousseau et al., 2011) for the Little Hungarian Plain. Sebe et al. (2015) suggest northwest wind directions in Eastern Austria during millennial-scale wind erosion periods, attributed to MIS 2 based on ventifacts and eolian sand deposits. Another factor is the position of the Paleo-Danube. As the position of the Danube along the Transdanubian Mountains and the Little Hungarian Plain was stable throughout the considered time period (Gábris and Nádor, 2007), dry floodplains during cold and arid climate phases likely supplied large amounts of silt-sized sediments that were prone to deflation.

Weathering-inert elements provide information about sediment recycling and sorting. Al-Ti-Zr ternary diagrams reveal Zr addition being essential for the oldest loess (Unit 16, MIS 6) followed by younger loess predominantly at the expense of Al. Checking Al, Ti and Zr against their correlations with grain-size ($|\rho| \leq 0.34$) rules out sediment sorting as the main reason for Zr addition. In particular, Zr exhibits the least correlation to any grain-size fraction, with ($|\rho| \leq 0.18$). Zr/metal ratios provide further evidence for Zr addition, and thus sediment recycling, at Süttő. This is a typical pattern for clastic sediments that underwent multiple cycles of weathering prior to final deposition (Caracciolo et al., 2011; Újvári et al., 2008). Smalley and Leach (1978) and Smalley et al. (2009) explain loess deposition in the Carpathian Basin as a kind of cascade process, involving multiple cycles of transport and deposition prior to its final eolian deposition. Profe et al. (2016) suggest the same process for the Schwalbenberg II LPS in Germany at the transition from MIS 3 to MIS 2. As a consequence of dry and windy climatic conditions during MIS 2, floodplain sediments of the river Rhine, likely consisting of already weathered and eroded material, became available for eolian transport. This results in Zr enrichment due to fractionation processes active in fluvial and eolian domains. Hence, both Süttő and Schwalbenberg II resemble the so-called event-sequence approach first introduced by John Hardcastle (Smalley and Fagg, 2015) and finally applied to Chinese LPS in its most developed form by Smalley et al. (2014).

Despite grain-size is not linked to Zr, Zr addition partly follows the observed grain-size trend, i.e., that the oldest loess is most enriched in Zr while younger loess is less enriched in Zr. Muhs and Bettis III (2000) outline decreasing Zr concentrations as a function of distance to source; in their case, the distance to the river Missouri. Accordingly, dust source alterations or changing distances to the Danube floodplains might be an explanation. However, these explanations are unlikely because of the stable position of the Paleo-Danube (Gábris and Nádor, 2007) and only one dust source. Therefore, changes in wind intensity between MIS 6

and subsequent MIS related to glacial periods might be the reason for degrading Zr enrichment. Investigations of ice sheet extensions in Montenegro and Greece show larger ice extents for MIS 6 than for younger MIS (Hughes et al., 2006; Hughes et al., 2011). Against this background, together with finer grain-size during the last glacial period, Obrecht et al. (2016) claim generally milder conditions since MIS 5, despite a general aridization trend in the Vojvodina region since 350 ka ago. Following this idea, it is likely that the Danube transported more physically-weathered and already recycled material during MIS 6, in consequence of a more pronounced glacial climate accompanying enhanced erosion, runoff and more intense permafrost conditions in the Danube catchment area. Increased wind intensity facilitated short-distance eolian transport of ultradense minerals such as zircon ($4.0\text{-}4.7\text{ g/cm}^3$, Holland and Gottfried, 1955). Another important factor is tectonic uplift. Accelerated tectonic uplift since 350 ka, with an estimated uplift rate of 0.46 mm/a in the region of the Geresce mountains (Ruszkiczay-Rüdiger et al., 2005), suggests an uplift of about 70 m during the last 150 ka. This is in line with the suggested uplift of 100 m for the travertine complex underlying the LPS (Novothy et al., 2009). During MIS 6, the difference in elevation between the Danube floodplain and the basement of the LPS are smallest, so that heavy and coarser grains can be transported to this location, tentatively even by saltation. Reduced wind speeds in the Carpathian Basin during MIS 4 to MIS 2, as hypothesized by Stevens et al. (2011), together with an increased vertical distance between the Danube and the top of the LPS Süttő, complicate eolian transport and deposition of ultradense minerals. In addition, sporadic permafrost conditions, together with colder and drier climatic conditions during MIS 2 (Barta, 2014; Novothy et al., 2011; Ruszkiczay-Rüdiger and Kern, 2016), may have reduced surface runoff and provided a braided river system that periodically fell dry. This explains higher sedimentation rates with finer particles and less Zr enrichment during the last glacial-/interglacial cycle. Furthermore, bulk mineralogy of four exemplary loess samples indicates quartz and thus zircon-rich material during MIS 6, while other minerals predominate MIS 4 and MIS 2.

6.4.8. XRF scanning vs. WD-XRF

LPS are commonly investigated by quantitative techniques such as WD-XRF and inductively-coupled plasma mass spectrometry (ICP-MS). This study demonstrates XRF scanning of discrete samples as being a reliable tool to track relative changes along LPS and to identify homogeneous units geochemically. This is consistent with Liang et al. (2012) and Profe et al. (2016), as the former applies XRF scanning with a spatial resolution of $500\text{ }\mu\text{m}$ to a U-channel taken from a Chinese LPS and evaluates the XRF scanning capabilities by comparison with conventional XRF measurements, while the latter demonstrates that XRF scanning of discrete samples (Ohlendorf, 2018) is a cost- and time-efficient screening tool for the geochemical characterization of LPS. The established chemostratigraphy unravels dominant drivers that are responsible for individual geochemical fingerprints observed at Süttő: pedogenesis and grain-size. Ternary plots derived from XRF scanning data show similar trends to those derived from WD-XRF data except for K. Since Na and P data are not available with analyses of the ITRAX XRF scanner, we suggest the Sr-K-Rb plot as an alternative to the commonly applied A-CN-K plot. The Sr-K-Rb plot reliably

detects decalcification under the presumption that there is no secondary calcification, while conclusions drawn on K dynamics are ambiguous due to difficulties of the scanner in detecting small changes in K concentrations reliably. Such difficulties are also reported for loess U-channel analyses (Sun et al., 2016) and geochemical reference standards (Huang et al., 2016) when measured with an ITRAX XRF scanner. The basic trend in the Al-Ti-Zr plot derived from WD-XRF data (Fig. 6-9A) is mirrored by the Al-Ti-Zr plot derived from XRF scanning data (Fig. 6-9B), albeit the twenty-times higher amount of data points in the latter plot blurs clear trends visible in the WD-XRF data. Presumably, low detectability of Al (Huang et al., 2016), as illustrated in Fig. 6-4, also contributes to the differences between WD-XRF and XRF scanner-derived Al-Ti-Zr plots (Fig. 6-9).

Even though XRF scanning of discrete samples is shown to be a cost- and time-efficient geochemical screening tool for LPS, it has limitations. Commonly, dust source provenance, together with sediment sorting and recycling, is investigated by normalizing element concentrations to the respective element concentrations of the UCC. In case of LPS AVL³ is often used as a reference for an average loess composition. However, such data reflect synthetic data calculated as an average of many individual samples. Since neither of these individual samples nor the averaged samples are available as real rock samples, a measurement with the ITRAX XRF scanner is impossible in order to compare element intensities of the UCC or AVL³ with individual loess samples. The same holds true for elements such as V and Th that are very difficult to detect with the ITRAX XRF scanner due to their low concentrations usually present in LPS. Therefore, XRF scanning of discrete samples provides fast data that allows identification of major paleoenvironmental factors influencing geochemistry. Due to the high achievable spatial resolution, in the case of a sediment core down to 200 μm , this technique helps to identify important transitional or homogeneous units, and thus facilitates planning of further sampling and selection of additional analysis techniques.

6.5. Conclusions

The established high-resolution chemostratigraphy identifies seven clusters representing geochemically homogeneous units. These units correlate well with lithologically identified units along the studied LPS Süttő covering the last 150 ka. However, weak pedogenesis attributed to MIS 5a and characterized by humus and k_{if} enrichment are not reflected in the chemostratigraphy. This points to a cold continental-steppe climate that prevented pedogenesis from leaving behind a characteristic geochemical fingerprint. PCA and biplot analyses identify pedogenesis and grain-size dynamics as dominant factors influencing the geochemical record at Süttő. Together with WD-XRF-derived A-CN-K and Sr-K-Rb ternary plots, biplots reveal only decalcification, even in mature interglacial paleosols that are attributed to MIS 5e and MIS 5c. Consequently, K-feldspar weathering is likely inhibited by arid continental climatic conditions throughout the last 150 ka. UCC comparisons, in combination with Al-Ti-Zr as well as Th/metal and Zr/metal ratios, document a polygenetic origin of the LPS Süttő. Th/metal ratios indicate one dominant dust source, while the

comparison of loess samples with floodplain sediments of potential dust source areas confined the dominant dust source to the F-AA-related Danube floodplain sediments in the west of Süttő. Furthermore, Al-Ti-Zr plots and Zr/metal ratios point to sediment recycling in terms of Zr addition. Grain-size related Zr addition is ruled out by correlation analysis of Zr with grain-size. Zr addition decreases with time, resembling the fining trend from MIS 6 to MIS 2. Thus, the strongest sediment recycling occurs concomitantly with deposition of coarse grains. Although minor contributions from local dust sources such as the Bicol Creek cannot be excluded, the dominant dust source is the Danube floodplain in the immediate vicinity of the LPS. Upward fining in grain-size is related to more ameliorated climatic conditions compared to MIS 6. This may also limit the capacity of wind to uplift and transport ultradense particles leading to upward reduction of Zr addition. In addition, tectonics uplifted the LPS Süttő by about 70 m since MIS 6, increasing vertical transport distances and further exaggerating transport and deposition of ultradense particles and reducing Zr addition. In conclusion, this study documents rather stable and arid continental climatic conditions throughout the last 150 ka, with milder conditions throughout the last glacial-/interglacial cycle. XRF scanning of discrete samples is proven as a time- and cost-efficient geochemical screening tool for LPS, although specific geochemical fingerprinting in comparison with the UCC or the AVL requires quantitative element data.

Acknowledgements

Financial support of the German Research Foundation [DFG, ZO 102/22-1] is gratefully acknowledged. In addition, AN and GB wish to thank the Hungarian National Research, Development and Innovation Office [NKFIH, project K119366] for financial support. We are much obliged to Rik Tjallingii (GFZ Potsdam) for his advice in the establishment and interpretation of cluster and further PCA and biplot analyses. We thank Sabine Stahl (University of Bremen) and Carola Lehnert (ICBM, University of Oldenburg) for technical support. Jonathan von Schröder is thanked for his mathematical support in data preprocessing for the cluster analysis. Finally, JP thanks the Science Chat Group of PhD students at the University of Bremen for helpful discussions.

6.6. Supplementary material

XRF-scanning, carbon and CaCO₃ data are available on Pangaea:
<https://doi.pangaea.de/10.1594/PANGAEA.884092>.

Table 6-2: WD-XRF-determined concentrations of major and trace elements and estimated CIA values at the loess-paleosol sequence Süttő (n = 33). CaO* values correspond to the corrected CaO values after McLennan (1993).

Composite depth (cm)	Type	Unit	SiO ₂ (%wt)	TiO ₂ (%wt)	Al ₂ O ₃ (%wt)	Fe ₂ O ₃ (%wt)	MnO (%wt)	MgO (%wt)	CaO (%wt)	CaO* (%wt)	Na ₂ O (%wt)	K ₂ O (%wt)	P ₂ O ₅ (%wt)	Ba (ppm)	Ce (ppm)	Cr (ppm)	Ni (ppm)	Nb (ppm)	Pb (ppm)	Rb (ppm)	Sr (ppm)	Th (ppm)	Y (ppm)	V (ppm)	U (ppm)	Zn (ppm)	Zr (ppm)	CIA
10	Paleosol	1	70.08	0.788	11.06	3.91	0.102	1.15	1.41	1.26	1.26	1.99	0.122	389	75	83	31	15	28	93	104	10	29	67	6	57	404	63.7
52	Loess	2	48.47	0.542	7.59	2.70	0.057	3.03	17.41	0.95	0.95	1.39	0.112	257	39	58	23	12	14	56	167	8	17	51	5	37	275	62.1
200	Loess	2	51.67	0.590	7.99	2.93	0.071	4.13	13.93	1.07	1.07	1.54	0.117	294	56	61	24	12	15	62	217	8	23	55	5	39	316	60.6
300	Loess	2	56.41	0.639	8.93	3.19	0.076	3.79	10.55	1.22	1.22	1.68	0.130	303	65	64	25	13	17	71	188	10	25	59	4	43	332	60.5
400	Loess	2	58.44	0.716	9.85	3.59	0.081	3.44	8.77	1.29	1.29	1.83	0.131	347	74	72	29	14	17	77	176	9	26	68	5	49	341	61.3
540	Loess	3	60.62	0.733	9.96	3.43	0.061	3.24	7.59	1.41	1.41	1.74	0.144	330	68	68	25	14	18	73	160	10	26	64	6	47	371	60.4
554	Loess	3	60.20	0.736	9.88	3.48	0.065	3.44	7.94	1.40	1.40	1.74	0.149	325	61	71	27	14	18	72	164	10	24	64	8	49	360	60.4
566	Loess	4	59.21	0.726	9.77	3.43	0.085	3.58	8.39	1.39	1.39	1.75	0.149	325	62	68	28	14	16	73	170	10	23	61	7	48	358	60.2
582	Loess	4	59.92	0.749	10.06	3.58	0.063	3.38	8.15	1.32	1.32	1.79	0.143	337	76	75	28	15	18	76	172	10	25	66	7	50	366	61.6
608	Loess	5	61.17	0.714	9.32	3.34	0.075	3.17	8.44	1.40	1.40	1.61	0.138	306	67	70	25	14	17	67	171	9	21	61	8	44	338	59.5
660	Paleosol	6	67.90	0.895	13.21	4.92	0.101	1.92	1.48	1.48	1.62	2.16	0.170	433	93	84	38	16	22	98	140	11	33	84	5	68	385	64.4
700	Paleosol	6	67.35	0.849	12.4	4.63	0.086	1.74	1.20	1.20	1.59	2.05	0.160	401	85	80	36	16	22	90	132	10	29	80	8	63	367	65.1
730	Loess	7	60.01	0.745	10.42	3.88	0.081	4.01	7.15	1.42	1.42	1.84	0.156	338	57	68	30	14	17	76	161	9	24	67	6	52	324	61.0
770	Loess	7	58.01	0.681	8.74	3.10	0.073	3.74	10.24	1.34	1.34	1.57	0.140	295	51	62	23	13	15	62	181	8	19	57	8	41	316	58.9
792	Sand	8	63.43	0.683	8.13	2.90	0.068	3.29	8.80	1.44	1.44	1.43	0.134	258	42	57	19	12	15	55	177	8	21	46	5	34	333	56.4
802	Sand	8	68.13	0.741	6.91	2.66	0.071	2.67	7.88	1.39	1.39	1.18	0.105	214	42	57	14	12	14	43	165	8	21	43	5	30	397	54.2
834	Loess	9	59.67	0.752	10.69	3.90	0.079	3.39	7.88	1.52	1.52	1.86	0.165	354	65	69	29	14	19	79	167	9	25	69	6	54	315	60.4
838	Loess	9	59.62	0.697	9.59	3.38	0.073	3.45	8.63	1.50	1.50	1.69	0.150	314	61	65	25	13	17	69	178	10	22	61	8	45	318	58.6
902	Loess	9	57.98	0.661	8.96	3.07	0.067	3.48	10.51	1.47	1.47	1.55	0.152	295	54	61	22	12	16	64	188	8	25	55	6	40	333	57.9
938	Paleosol	10	63.85	0.760	11.52	4.02	0.096	2.53	4.77	1.66	1.66	1.91	0.186	390	81	75	31	14	19	84	159	10	29	69	6	55	337	60.5
958	Paleosol	10	61.62	0.734	11.13	3.87	0.080	2.91	6.28	1.65	1.65	1.85	0.187	360	75	71	28	14	18	80	157	10	28	67	8	54	336	60.0
982	Loess	11	56.91	0.670	9.58	3.41	0.076	3.12	10.30	1.32	1.32	1.60	0.174	315	64	67	27	13	17	71	162	9	24	60	6	47	316	61.2
992	Loess	11	56.29	0.655	9.08	3.27	0.074	3.00	11.48	1.25	1.25	1.53	0.165	302	63	70	26	13	15	67	157	9	26	61	4	44	314	61.1
1026	Paleosol	12	54.63	0.633	8.39	3.06	0.070	3.08	12.93	1.13	1.13	1.46	0.151	276	57	63	24	12	15	63	166	8	18	54	7	40	281	61.3
1056	Paleosol	12	49.77	0.552	7.66	2.78	0.060	3.47	16.42	1.05	1.05	1.32	0.123	249	49	58	22	11	14	57	203	8	20	55	4	38	253	61.1
1076	Loess	13	53.25	0.618	8.19	3.00	0.066	3.42	13.61	1.10	1.10	1.40	0.131	280	53	66	24	12	14	60	188	8	20	53	3	40	294	61.5
1096	Loess	13	55.04	0.579	8.04	2.86	0.067	3.54	12.99	1.11	1.11	1.40	0.123	278	44	59	23	12	17	59	188	8	21	51	3	39	279	60.9
1136	Paleosol	14	70.12	0.856	11.17	4.14	0.101	1.50	2.06	1.30	1.30	1.87	0.180	384	89	82	31	16	19	82	113	11	30	71	4	55	414	63.9
1206	Paleosol	14	73.13	0.897	10.93	4.10	0.093	1.32	0.96	0.96	1.29	1.78	0.132	355	80	81	30	16	18	77	99	9	31	72	5	54	448	66.6
1246	Paleosol	15	72.42	0.891	11.13	4.55	0.078	1.42	0.82	0.82	1.19	1.77	0.145	349	70	87	34	16	19	75	95	12	31	73	9	53	439	68.9
1274	Paleosol	15	76.45	0.837	9.50	3.62	0.079	1.26	1.16	1.16	1.27	1.71	0.161	322	66	81	29	15	16	69	96	11	27	58	5	41	467	62.6
1320	Loess6	16	45.83	0.464	5.40	1.97	0.050	4.10	20.73	0.82	0.82	1.07	0.105	201	32	52	16	10	13	41	178	8	16	38	3	26	276	58.3
1466	Loess6	16	52.10	0.529	6.27	2.22	0.058	4.65	15.33	0.92	0.92	1.29	0.111	229	32	62	18	11	14	49	197	7	21	41	3	29	350	58.6
SU08	Mix	-	53.27	0.598	8.25	2.94	0.067	3.66	13.47	1.12	1.12	1.57	0.119	287	60	62	23	13	15	62	192	8	22	54	3	39	308	-
SU08A	Mix	-	60.74	0.729	9.81	3.43	0.070	3.37	7.98	1.44	1.44	1.74	0.144	329	71	70	26	14	18	73	164	10	27	64	4	48	382	-
SU08B	Mix	-	61.25	0.769	10.25	3.71	0.082	3.16	7.29	1.44	1.44	1.77	0.146	343	55	72	29	14	19	76	167	10	27	67	4	49	363	-
SU08C	Mix	-	65.42	0.835	12.05	4.49	0.086	2.64	3.47	1.50	1.50	2.01	0.165	394	80	77	36	15	20	88	147	10	30	79	4	62	355	-
SU08D	Mix	-	61.20	0.681	8.24	2.97	0.076	3.47	9.38	1.41	1.41	1.47	0.133	271	47	63	20	12	14	56	177	7	22	54	2	37	341	-
SU08E	Mix	-	55.68	0.647	9.04	3.24	0.071	3.20	11.71	1.27	1.27	1.56	0.149	300	49	67	26	14	16	68	178	9	23	59	3	44	308	-
SU08F	Mix	-	72.51	0.881	11.19	4.24	0.096	1.44	1.32	1.30	1.30	1.84	0.160	364	76	83	32	17	19	79	107	10	31	69	3	53	419	-
SU08G	Mix	-	52.00	0.515	6.17	2.20	0.057	4.41	15.29	0.97	0.97	1.29	0.111	212	30	56	18	10	13	49	188	8	15	39	4	30	294	-

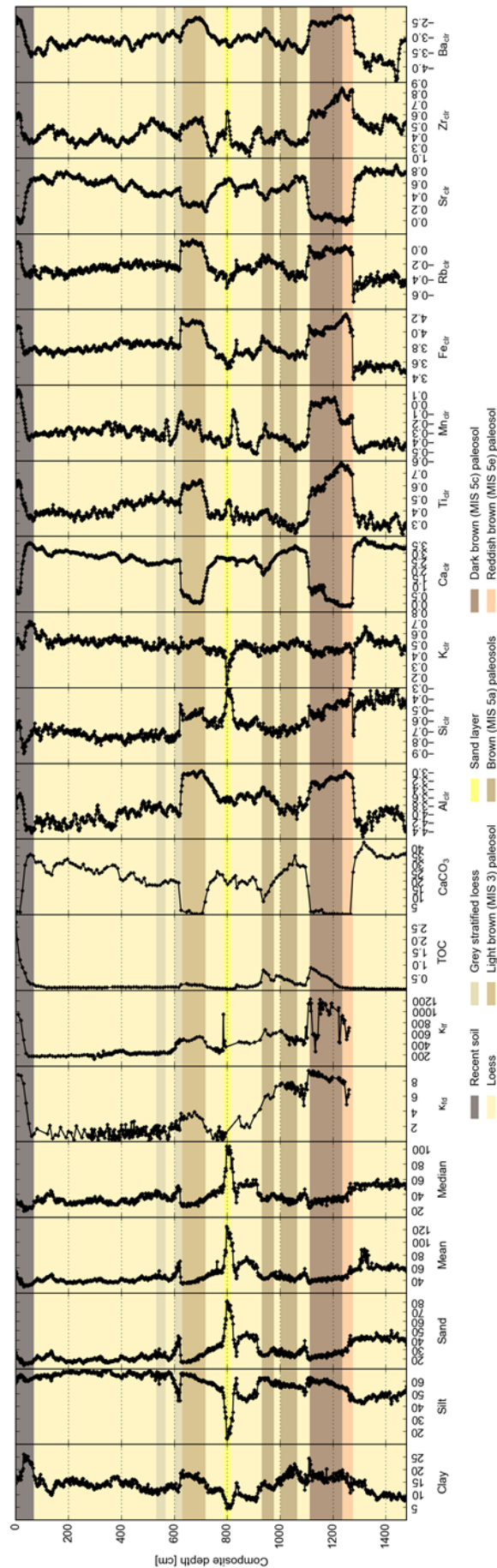


Fig. 6-13: Profile view of clr-transformed element data in comparison with other proxy data. Labels according to lithology. Grain-size data from Novothny et al. (2011), magnetic susceptibility data from Rolf et al. (2014).

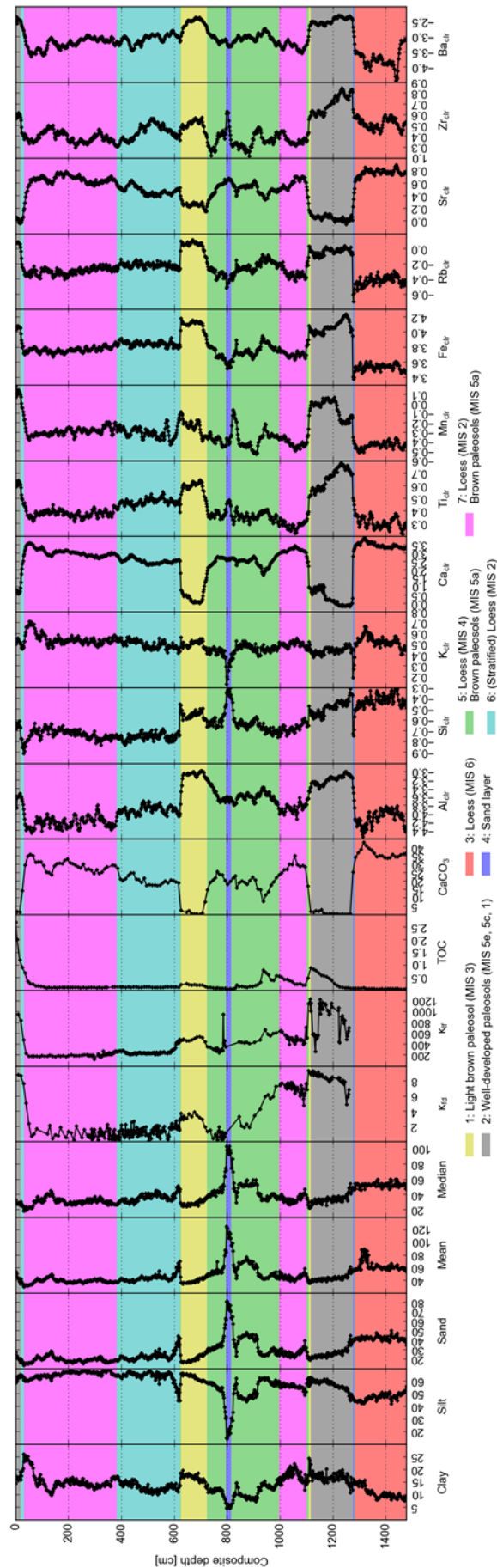


Fig. 6-14: Profile view of clr-transformed element data in comparison with other proxy data. Labels according to clusters. Grain-size data from Novothny et al. (2011), magnetic susceptibility data from Rolf et al. (2014).

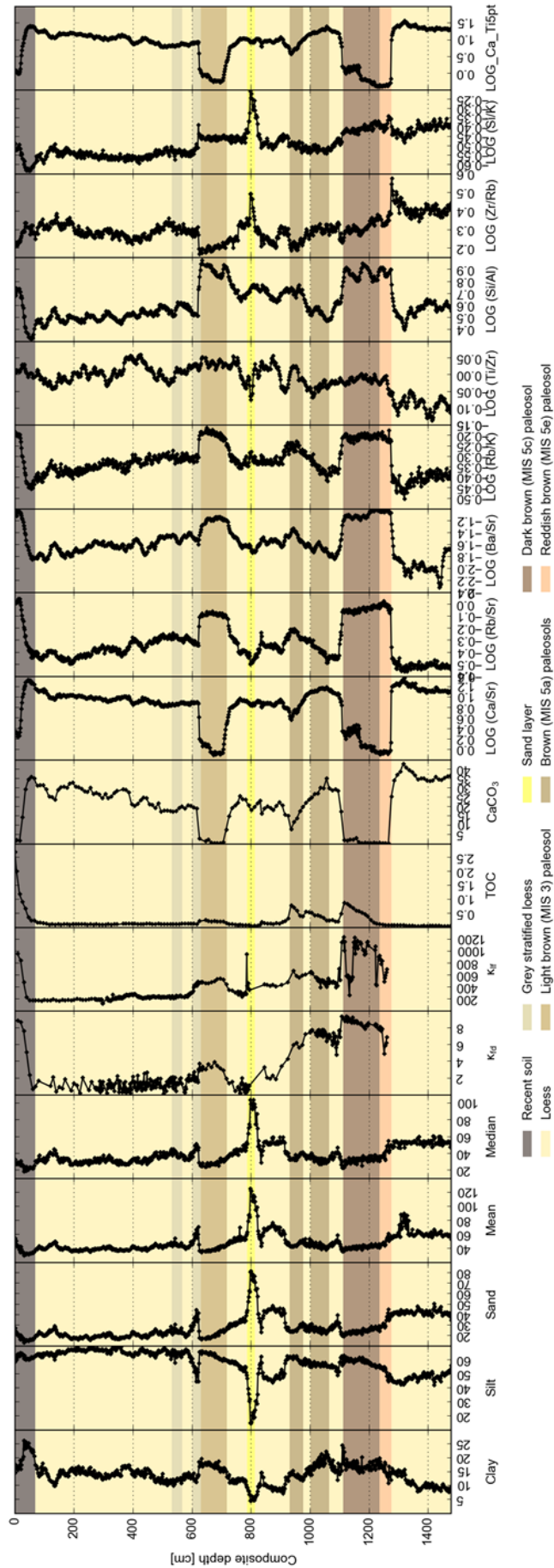


Fig. 6-15: Profile view of usually applied element ratios in comparison with other proxy data. Labels according to lithology. Grain-size data from Novothny et al. (2011), magnetic susceptibility data from Rolf et al. (2014).

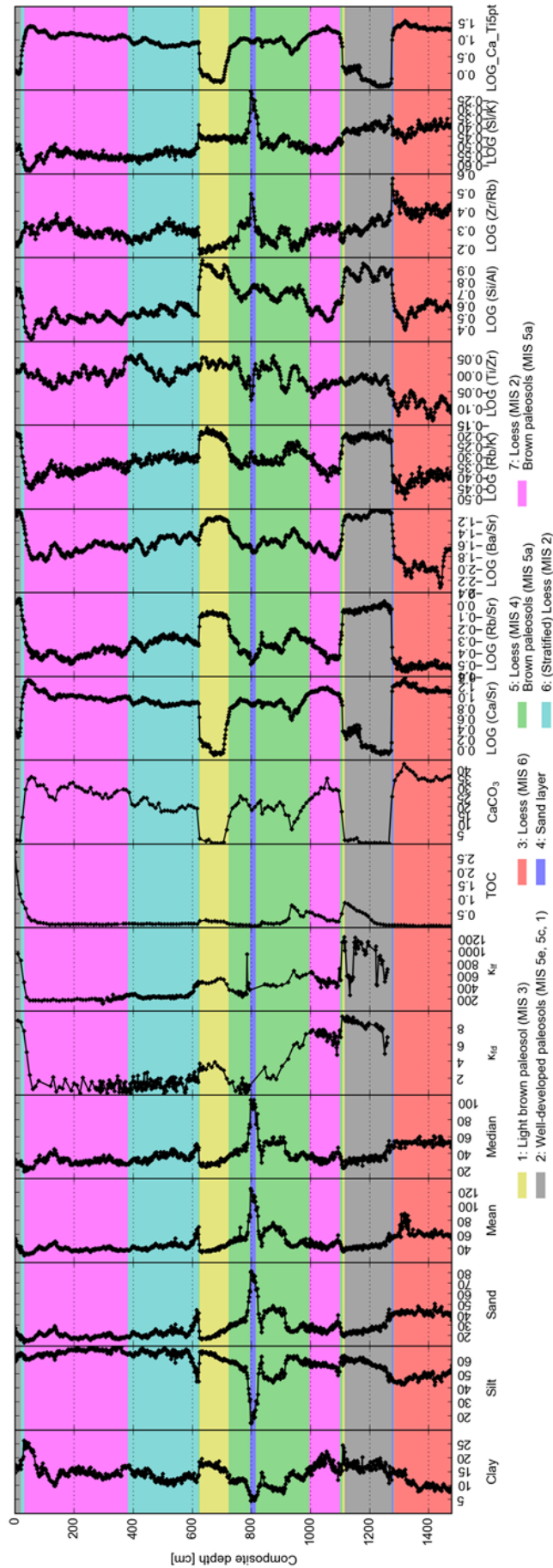


Fig. 6-16: Profile view of usually applied element ratios in comparison with other proxy data. Labels according to clusters. Grain-size data from Novothny et al. (2011), magnetic susceptibility data from Rolf et al. (2014).

7. Concluding remarks and outlook

7.1. Weathering indices

Based on element data available from analyses with ITRAX XRF core-scanners, the weathering indices Rb/Sr, Ba/Sr and Rb/K are investigated. In addition, Ca/Sr documenting the loss of primary CaCO₃ is considered as an index for the strength of secondary calcification in this thesis as Ca is predominantly leached during weathering but also prevailing during secondary calcification (Bokhorst et al., 2009). In case of secondary calcification, this results in constant Ca/Sr values between loess and paleosols. Rb/Sr and Ba/Sr represent “Sr-type” weathering indices (Bugge et al., 2011). They are adversely affected by secondary calcification dynamics (Bugge et al., 2011) and thus require the ratio Ca/Sr or micromorphological investigations for evaluation of secondary calcification dynamics in paleosols. Rb/Sr and Ba/Sr provide reliable information about weathering intensity only when secondary calcification is absent (Bugge et al., 2011). Rb/K represents a proxy for the weathering of K-bearing minerals that usually occur after the weathering of Ca-bearing minerals in humid temperate climates (Nesbitt and Young, 1984). However, possible K-fixation may reduce Rb/K values and affects weathering intensities derived from Rb/K dynamics negatively (Bugge et al., 2011). Besides WD-XRF data that allows examining the A-CN-K plot for K-feldspar weathering and K-fixation (Fedo et al., 1995; Nesbitt and Young, 1984, 1989), detailed clay mineralogical studies would be necessary to corroborate possible K-fixation processes. Additionally, difficulties in detecting small changes of K with the ITRAX XRF scanner may distort Rb/K results as well.

Despite these challenges, Rb/Sr and Ba/Sr are able to identify paleosols except for some of the Remagen soils at Schwalbenberg II and the P-P3 soil on Susak. The latter shows an increase in Ca/Sr compared to loess, clearly originating from strong secondary carbonates observed in the form of rhizoconcretions. Since Schwalbenberg II is generally affected by secondary calcification, the fairly constant line of Ca/Sr corroborates its theoretical behavior under secondary calcification conditions. According to micromorphology, the Sinzig Soils S1 and S2 show the weakest secondary calcification along the paleosols at Schwalbenberg II. Consequently, the actual weathering patterns for most paleosols are likely similar to those identified for the Sinzig Soils S1 and S2 but obscured in the Rb/Sr and Ba/Sr profiles due to Sr-dynamics. At Süttő, negative excursions of Ca/Sr confirm micromorphological analyses that reveal the absence of secondary carbonates in the MIS 5e and MIS 5c-related paleosols.

The comparison of XRF scanning with WD-XRF data obtained from the samples at the LPS Süttő documents erroneous measurements of K with the ITRAX XRF scanner. Therefore, conclusions drawn on Rb/K at Schwalbenberg II and Susak have to be revised and rejected. Although Rb/K is not affected by secondary calcification, the measurement difficulties for typical concentration ranges of K present in LPS dismantle Rb/K as a robust weathering proxy. Hence, the best strategy to describe weathering intensity along a LPS by the aid of XRF scanning data is the combined interpretation of Rb/Sr and Ba/Sr with Ca/Sr. Careful

interpretation of the latter identifies sections likely affected by secondary calcification and thus evaluates Rb/Sr and Ba/Sr revealed weathering dynamics. According to interferences between Ca and K (Potts, 1992) likely being responsible for the adverse measurement of K, these results may also point to substantial consequences for XRF scanning results from other environmental samples characterized by large concentration changes in Ca and comparatively small concentration changes in K.

New insights into the chronology at Nussloch (Moine et al., 2017) challenge the correlation of one of the Sinzig soils at Schwalbenberg II with the Lohne Soil at Nussloch as suggested in previous studies (Kadereit et al., 2013; Kadereit and Wagner, 2014) and in this thesis (Profe et al., 2016). In addition, these insights document likely time periods required for paleosol formation during MIS 3 and MIS 2 (Rousseau et al., 2017a). Earthworm calcite granule-derived ^{14}C ages position the Lohne Soil at Nussloch into GIS 8 consistent with stratigraphic considerations (Moine et al., 2017; Rousseau et al., 2017a). Thus, a correlation of one of the Sinzig Soils (correlation of S2 and S3 with GIS 6 and 5) with the Lohne Soil at Nussloch appears unlikely, although a beginning formation of the Sinzig Soil S1 during GIS 8 cannot be ruled out due to missing chronological tie points (cf. Frechen and Schirmer, 2011). Since there are archived samples from the Schwalbenberg II profile stored at the Ruhr museum, a new project may focus on dating the Schwalbenberg II LPS by using earthworm calcite granules in order to resolve the question whether the paleosols identified by W. Schirmer (Schirmer, 2000b, 2012) are in-situ soil formations or not. Since single soil formations at Nussloch are related to corresponding GIS unambiguously (Moine et al., 2017), it appears likely that the paleosols at Schwalbenberg II are indeed in-situ formations. Only, the ascribed soil types probably need revision according to the findings at Nussloch. Schirmer (2012) identifies eight cambisols while Rousseau et al. (2017a) describe three arctic brown soils for the considered time period. Given the fact that the earthworms producing such granules are assumed to live in the uppermost decimeters of a soil (Prud'Homme et al., 2015), the original paleosol age might be preserved as long as the reworked paleosol was covered by loess prior to earthworm colonization.

In the literature, MS is the standard parameter to identify pedogenesis along an LPS (cf. Zöller, 2010 and references therein). Correlations between weathering indices, individual elements and MS at Schwalbenberg II and Süttő show only weak correlations. Nonetheless, Schwalbenberg II seems to be dominated by truncation-induced signal loss of MS in paleosols while Süttő tends to be dominated by neoformation of magnetic particles during pedogenesis. Consequently, Units 10 and 12 representing weak soil formations, are recognized in the MS record but not in the elemental record. Furthermore, there are no XRF-derived elements suitable as reliable proxy for organic carbon. This is exemplified on Schwalbenberg II and Susak by discussing Br as proxy for TOC according to their strong correlation in the marine realm.

In conclusion, weathering dynamics are best tracked from qualitative XRF scanning data by a combination of Rb/Sr and Ba/Sr with Ca/Sr. Despite secondary calcification adversely influencing Rb/Sr and Ba/Sr, this study highlights their usefulness in reliably detecting weathering dynamics by evaluation with micromorphology and WD-XRF data. In contrast,

there are no XRF scanning-derived element ratios suitable as robust proxies for MS or TOC. Finally, a horizon of 6 cm thickness (N-P1-2 on Susak) being well-characterized by XRF scanning data, emphasizes the need for spatial high-resolution geochemical data. This horizon could have been missed by commonly applied sampling strategies for geochemistry with a spatial resolution of 10 cm at best.

7.2. Provenance indices

Weathering-inert elements reflect changes in dust provenance and sedimentation dynamics. The Al-Ti-Zr ternary diagram is able to identify sediment sorting and recycling, the latter based on Zr enrichment (Garcia et al., 1991; Mongelli et al., 2006). Ti and Al might be controlled by long-distance transport fractionation (Chen et al., 2013) and the parent material composition (Muhs et al., 2003). In contrast, Zr originates from the mineral zircon only (Muhs, 2018; Stiles et al., 2003) and strongly accumulates as a residual during weathering in recycled sediments (e.g. Mongelli et al., 2006). Since Al and Ti are associated with fine particles while Zr is related to coarse particles (Mongelli et al., 2006; Stiles et al., 2003), grain-size effects need to be considered for a reliable interpretation of Al-Ti-Zr dynamics with regard to sediment recycling.

At Schwalbenberg II, Ti/Al and Ti/Zr indicate a dust source change at the transition from MIS 3 to MIS 2. The Al-Ti-Zr documents a recycling-affected sorting effect towards the Zr apex for the early MIS 2. Assuming large-scale erosion during the transition period from MIS 3 to MIS 2 implies transport of large amounts of already weathered material into the river Rhine. The entered material is transported by the river and leaves behind coarser Zr particles close to the location where it was previously eroded from due to density fractionation. Being a braided river system at the time of MIS 2, there were large and dry areas where occasional floods deposited material which was then available for deflation. During eolian transport, another cycle of density-fractionation occurs causing Zr particles to deposit first on the slopes of the Middle Rhine valley. In case of Schwalbenberg, these particles are likely deposited at the same position from which they had previously eroded. Enhanced flood activity during the early MIS 2 in the Eifel region (Brunck et al., 2016) support this conceptual model. The conceptual model explains the observed Zr dynamics. Although literature about the Hardcastle sequence was not known by the author at the time of publication of the Schwalbenberg II article (Chapter 4, Profe et al., 2016), the suggested conceptual model reflects two additional cycles of transport and deposition in terms of the Hardcastle sequence. Accordingly, previous loess deposits follow the scheme P1-T1-D1-T2-D2 (Smalley and Fagg, 2015). T1 and D1 refer to fluvial transport and deposition while T2 and D2 refer to eolian transport and deposition. The loess attributed to early MIS 2 experienced a longer event sequence that can be described as P1-T1-D1-T2-D2-(C)-T3-D3-T4-D4. C stands for the likely occurrence of pedogenesis followed by tentative slope processes prior to T3. T3 summarizes the transport of the material into the river as well as the transport in the river. The deposition on the braided river floodplain is represented by

D3, T4 and D4 refer to the final stages of eolian transport and deposition of the already weathered (D2) and transport-induced-fractionated (T3, T4) material.

On Susak, Ti/Al and Ti/Zr ratios show a rather constant profile except for the sand layer P-S1 attributed to MIS 4. Therefore, the indices confirm that loess deposits on Susak originate from one dominant dust source for the considered time period MIS 7 to MIS 4 – the paleo Po floodplain. Raw element counts indicate a strong depletion in Zr followed by depletion in Ti and constancy in Al. In analogy to findings in North America that regard Zr depletion as a function of distance to a river (Muhs and Bettis III, 2000), Al, Ti and Zr dynamics on Susak indicate long-distance fluvial transport that fractionate Zr, Ti and Al according to particle density and size. The same holds true for subsequent eolian transport where sand particles are transported over short distances only and consequently become further fractionated in the eolian domain. Since zircon has a density in the range from 4.0 to 4.7 g/cm³ (Holland and Gottfried, 1955), it is likely that zircon and thus Zr is deposited first in both the fluvial and eolian domain due to its high density. This idea is supported by ultradense minerals being abundant in Northern Italy proximal to their source (Ferraro, 2009) and rare on Susak distant to their source (Mikulčić Pavlaković et al., 2011). However, this line of argumentation is only valid if there is no additional proximal input of Zr-rich material into the paleo Po floodplain large enough to influence the general elemental composition determined by fluvially transported Alpine material. Therefore, Ti/Zr is challenged as straightforward proxy for dust provenance. It may also indicate transport distance-superimposed changes in wind activity (Susak) or sediment sorting-induced recycling effects (Schwalbenberg II).

At Süttő, XRF scanning-derived Al-Ti-Zr dynamics reveal a pattern similar to but noisier than that at Schwalbenberg II. Comparing the ternary plot indicative of sediment sorting and recycling with WD-XRF-derived Zr/metal ratios supports the hypothesis of sediment recycling at Süttő. However, in contrast to Schwalbenberg, the strongest Zr addition occurs in the oldest loess attributed to MIS 6. Since floodplain sediments of the river Danube are the major dust source over time with potential minor contributions of local sources, it is unlikely that this Zr dynamic is driven by a major change of the dust source. Although there is a fining trend towards the top of the sequence, the correlation between Al, Ti, Zr and the grain-size fractions sand, silt and clay is weak ($|\rho| \leq 0.34$), thus ruling out grain-size as main driver. Therefore, tectonics are assumed to cause the fining upward trend and the observed Zr addition in the oldest loess since the LPS was uplifted by 70 m during the past 150 ka relative to the elevation of the Danube. Increasing the transport distance leads to a deposition of smaller and lighter particles in case all other parameters remain constant. Instead of increasing the horizontal transport distance which is reported to be accompanied by Zr depletion (Muhs and Bettis III, 2000), at Süttő the vertical distance was increased which favored density-fractionation of Zr during short-distance eolian transport. Together with expected milder climatic condition during the last glacial-/interglacial cycle compared to the penultimate glacial period, potential changes in wind activity favor the transport and deposition of fine material and thus explain the observed Zr dynamics. If Zr addition was due to the same reasons as at Schwalbenberg II, i.e. large-scale erosion of weathered sediment followed by local recycling in fluvial and eolian domains prior to final eolian

deposition at the position where the sediment has previously been eroded from, a cyclic pattern for MIS 6, MIS 4 and MIS 2 would be expected.

To test this hypothesis, transects of LPS at Danube terraces of different elevations should be studied. Assuming that each of the studied LPS started to form at a time where their specific terrace levels corresponded to the terrace level vertically closest to the Danube, each LPS should exhibit the same vertical distance to the Danube at its bottom. Consequently, if tectonics is the major driver of Zr addition, at least the trend of most Zr addition at the bottom of each studied LPS should be identical. If this is not the case, either contributions of local dust sources are larger than expected or particles available for deflation from the Danube floodplains may have a different origin. High-resolution heavy mineral, bulk and clay mineral investigations would complement such a study to identify different dust sources and to confirm Zr addition due to sediment recycling by enrichment of heavy minerals.

In conclusion, Al-Ti-Zr dynamics are valuable parameters to unravel loess history. Although careful interpretation is required with regard to site-specific grain-size effects, dust source changes and presumable transport patterns, especially Zr dynamics are able to explain multiple cycles of transport and deposition, framed under the term “sediment recycling”. In addition, dominant dust sources might be traced by Zr whenever sufficient information is available about the occurrence of ultradense minerals along the expected transport path. Since it is common to identify sediment sorting and recycling patterns by the Al-Ti-Zr ternary plot, relative changes between these three elements along a profile are of interest. Consequently, quantitative data are not necessary while qualitative data are correlated with concentration changes. For Al, Ti and Zr this is usually the case so that XRF scanning data is perfectly suitable to identify and track sediment recycling dynamics.

7.3. Grain-size indices

Geochemical grain-size indices rely on the principle that certain elements fractionate with certain particle sizes. Standard grain-size-related element ratios deduced from Chinese LPS are Zr/Rb and Si/Al (Chen et al., 2006; Liang et al., 2013). While Zr and Si fractionate with quartz in coarse silt or sand particles (Stiles et al., 2003), Rb and Al are associated with the grain-size fractions fine silt and clay (Chen et al., 2006; Mongelli et al., 2006). Testing these element ratios as grain-size proxies on the LPS Schwalbenberg II, Susak and Süttő reveals that none of them strongly correlates with grain-size fractions or derived grain-size ratios. This indicates that other processes of similar importance influence Zr/Rb and Si/Al. In addition to grain-size, Zr and thus Zr/Rb is mainly affected by sediment recycling whereas Si/Al is also suggested as a provenance indicator due to the occurrence of Si and Al in weathering residuals (Klasen et al., 2015). Even though Si/Al dominantly reflects grain-size changes as demonstrated by the sand layer P-S1 on Susak, only Si shows moderate positive (negative) correlations with sand (silt) at Süttő. Based on PCA and biplot analyses, Si/K is identified as best suited element ratio to document grain-size variations at Süttő.

However, this is likely due to the aforementioned difficulties in reliably measuring K with the ITRAX XRF scanner resulting in rather constant K values marginally influencing the Si signal. Consequently, the investigated XRF scanning-derived element ratios do not tend to be universally applicable grain-size proxies. Instead, this thesis demonstrates ambiguous correlations of commonly applied geochemical grain-size proxies. Further research may focus on correlations between elements and grain-size fractions at European LPS to establish an end-member based modeling approach in order to predict grain-size distributions along LPS from geochemistry.

7.4. Chemostratigraphy and multivariate statistics

Chemostratigraphy describes the identification of geochemical homogeneous units along a sediment sequence (Ramkumar, 2015). Thus, chemostratigraphy can be compared with lithostratigraphy in order to identify differences that may need particular focus in further analyses. The use of multivariate statistics enables the consideration of several parameters at once. In this study, chemostratigraphies are established by hierarchical clustering. The number of clusters is determined by their relative linkage distances and expert knowledge about the expected number of different clusters derived from field observations (cf. Martin-Puertas et al., 2017). Subsequent PCA and biplot analyses (cf. Martin-Puertas et al., 2017) allow determination of element ratios that are adequate to represent dominant processes along a LPS.

On Susak, complex and stratigraphic incomplete profiles challenge the establishment of a straightforward and comprehensive lithostratigraphy. Therefore, three profiles are investigated that together cover the oldest studied deposits ranging from MIS 7 to MIS 4. Establishing a chemostratigraphic framework helps to correlate paleosols and loess layers across individual profiles. Applying the Ward algorithm (Ward, 1963), hierarchical clustering based on Al, Si, K, Ca, Ti, Mn, Fe, Rb, Sr and Zr together with a preset number of five clusters reveal one cluster corresponding to loess (cluster 5), one cluster corresponding to the sand layer P-S1 (cluster 3) and three clusters corresponding to paleosols (clusters 1, 2, 4). Comparing the derived paleosol clusters with element ratios, indicates that cluster 1 reflects the strongest pedogenesis followed by clusters 2 and 4, which both reflect weaker pedogenesis. Accordingly, the established chemostratigraphy confirms one dominant dust source for the time period MIS 7 to MIS 4. P-S1 denotes the only stratigraphic unit that is represented by cluster 3 highlighting its unique geochemistry. This geochemistry results from the coarse grain-size of PS-1 in combination with transport-induced changes in the elemental composition. Underlying processes might be the regression of the Adriatic Sea on the way to full glacial conditions during MIS 4, coupled with glacial-isostatic adjustment and enhanced wind activity.

Paleosol clusters are predominantly determined by secondary calcification dynamics. They resemble the tripartite structure of N-P1 and identify O-P1 as pedocomplex due to its representation by four different clusters. This is in line with observed element and grain-size

alterations as well as TOC maxima which suggest at least three phases of pedogenesis preserved in O-P1. Stratigraphic refinement allows correlation of the subunit O-P1-2 with P-P1 according to its assignment to the same cluster. N-P1-1 may also correspond to O-P1-2 and/or P-P1 due to its attribution to the same cluster. However, luminescence ages argue against such a correlation because they date N-P1 to MIS 7 and bracket O-P1 to MIS 5. Although robust stratigraphic correlations require a combination of micromorphological and paleopedological investigations with independent numerical age control, the example of Susak demonstrates how a high-resolution XRF scanning-derived chemostratigraphic framework facilitates correlation of paleosols across different profiles and the identification of pedocomplexes. These are promising results for further studies aiming at recovering sediment (“loess”) cores from the plateau-like area on Susak. Such sediment cores could serve as a basis to exploit the full potential of XRF scanning down to a resolution of 200 μm in order to understand more holistically the paleoenvironmental record of Susak.

Based on the lessons learned from Susak, the chemostratigraphic approach at Süttő is coupled with PCA and biplot analyses in order to identify element ratios that best reflect dominant element-influencing processes. According to the different lithologies present at Süttő, the number of clusters is set to seven. Among the seven clusters, five clusters are related to loess whereas two clusters represent paleosols. Loess and paleosols can be separated best by chemostratigraphy, although Units 10 and 12, attributed to weak pedogenesis during MIS 5a, are not identified. The oldest loess is different from younger loess since the cluster assigned to the oldest loess does not occur at any other position along the LPS Süttő. This suggests a dust source change between MIS 6 and younger MIS. However, weathering-inert elements indicate enhanced Zr addition, and thus sediment recycling, as a cause for the difference between MIS 6 and younger loess. Chemostratigraphy does not distinguish MIS 5e, MIS 5c paleosols and the modern soil but distinguishes them from the MIS 3 paleosol. This indicates that climatic conditions during the last interglacial were similar to today.

PCA reveals pedogenesis and grain-size as main drivers controlling element dynamics at Süttő. Checking this against correlation of single elements with grain-size data, verifies Si to represent grain-size variations. In contrast, K is not correlated with any other element rather than reflecting grain-size dynamics due to difficulties in reliably measuring K with the ITRAX XRF scanner. Nonetheless, according to multivariate statistics Ca/Ti and Si/K element ratios are the best proxies for pedogenesis and grain-size variability. This supports the idea that there might be no universal element ratio suitable as grain-size proxy for LPS. Instead, individual factors such as sediment recycling require careful investigation of site-specific processes and interactions to identify suitable element ratios e.g. for grain-size variability on the basis of PCA and biplot analyses. Examining inner-cluster variabilities by performing PCA and biplot analyses for each cluster individually removes the dominant processes. Therefore, elements abundant in low concentrations and thus prone to increased noise might be identified, such as Ba in cluster 3 (MIS 6 loess). In addition, element correlations within one cluster may point to weathering and sediment recycling dynamics that need to be verified by dedicated element ratios. For this purpose, it is

advisable to validate conclusions drawn from high-resolution XRF scanning data with quantitative data due to their higher chemical resolution.

Furthermore, since element data need to be log-transformed and often standardized prior to multivariate statistical analysis (Aitchison, 1986), qualitative data are sufficient as long as quality control guarantees reliable measurements. Replicate measurements document excellent data precision $\leq 2.5\%$ for most studied elements. Al, Ba, Br and Cl are exceptions due to their low detectability or predominant occurrence in low concentrations. Correlation of qualitative and quantitative element data reveal $R^2 \geq 0.52$ for the elements considered at Süttő. This highlights the reliability of XRF scanning of discrete samples in comparison to XRF scanning results derived from U-channels taken from Chinese LPS which exhibit weaker correlations with $R^2 \geq 0.20$ (Liang et al., 2012; Sun et al., 2016). In contrast to U-channels, XRF scanning of discrete samples uses homogenized and dry samples, minimizing interference caused by differences in grain-size or water content (Zolitschka et al., 2014). However, to ensure a smooth flat surface required for XRF analysis, the samples were compacted by hand with a plunger. As variations in porosity and surface roughness adversely affect XRF measurements, compaction by different persons may also influence data precision negatively. Therefore, the study on Susak checks data precision against sample preparation by different persons. The so-called compaction test documents negligible effects on data precision. Consequently, the robustness of XRF scanning of discrete samples is underlined.

In conclusion, this PhD thesis benchmarks XRF scanning of discrete samples as a valuable, cost- and time-efficient geochemical screening tool for LPS. This technique supplements other proxy data and contributes to a fast understanding of fundamental processes (weathering and sedimentation dynamics) potentially active at unknown LPS. Nevertheless, knowledge about limitations is indispensable to correctly interpret XRF scanning-derived element data. Although validation of XRF scanning data against other proxy data is a mandatory step, the application of this method helps to identify important transition zones or pedocomplexes. These zones require detailed time- and cost-intensive investigations (e.g. heavy mineral analysis and clay mineralogy, micromorphology and conventional XRF analyses) to comprehensively unravel paleoenvironmental dynamics recorded in LPS – being one of the most important terrestrial archives. Established chemostratigraphies in comparison with lithostratigraphies complement stratigraphical considerations across subprofiles that are often the only way to construct composite profiles due to inaccessibility of complete stratigraphical successions. This thesis highlights applications of XRF scanning of discrete samples to unravel paleoenvironmental conditions from LPS in different climatic regions (oceanic, continental, Mediterranean) and discusses methodological advantages and limitations. Therefore, these findings may contribute to the advancement of XRF scanning in terrestrial paleoenvironmental reconstructions.

8. References

- Ahmad, I., Chandra, R., 2013. Geochemistry of loess-paleosol sediments of Kashmir Valley, India: Provenance and weathering. *Journal of Asian Earth Sciences* 66, 73-89.
- Aitchison, J., 1986. *The statistical analysis of compositional data*. Chapman and Hall, London, UK, p. 416.
- Amorosi, A., Colalongo, M.L., Fiorini, F., Fusco, F., Pasini, G., Vaiani, S.C., Sarti, G., 2004. Palaeogeographic and paleoclimatic evolution of the Po Plain from 150-kyr core records. *Global and Planetary Change* 40, 55-78.
- Andersen, K.K., Svensson, A., Johnsen, S.J., Rasmussen, S.O., Bigler, M., Röthlisberger, R., Ruth, U., Siggaard-Andersen, M.-L., Peder Steffensen, J., Dahl-Jensen, D., 2006. The Greenland Ice Core Chronology 2005, 15-42 ka. Part 1: constructing the time scale. *Quaternary Science Reviews* 25, 3246-3257.
- Antoine, P., Coutard, S., Guerin, G., Deschodt, L., Goval, E., Loch, J.-L., Paris, C., 2016. Upper Pleistocene loess-palaeosol records from Northern France in the European context: Environmental background and dating of the Middle Palaeolithic. *Quaternary International* 411, 4-24.
- Antoine, P., Rousseau, D.-D., Degeai, J.-P., Moine, O., Lagroix, F., kreutzer, S., Fuchs, M., Hatté, C., Gauthier, C., Svoboda, J., Lisá, L., 2013. High-resolution record of the environmental response to climatic variations during the Last Interglacial–Glacial cycle in Central Europe: the loess-palaeosol sequence of Dolní Věstonice (Czech Republic). *Quaternary Science Reviews* 67, 17-38.
- Antoine, P., Rousseau, D.-D., Moine, O., Kunesch, S., Hatté, C., Lang, A., Tissoux, H., Zöller, L., 2009. Rapid and cyclic aeolian deposition during the Last Glacial in European loess: a high-resolution record from Nussloch, Germany. *Quaternary Science Reviews* 28, 2955-2973.
- Antoine, P., Rousseau, D.D., Zöller, L., Lang, A., Munaut, A.-V., Hatté, C., Fontugne, M., 2001. High-resolution record of the last Interglacial-glacial cycle in the Nussloch loess-paleosol sequences, Upper Rhine Area, Germany. *Quaternary International* 76/77, 211-229.
- Bábek, O., Chlachula, J., Grygar, T.M., 2011. Non-magnetic indicators of pedogenesis related to loess magnetic enhancement and depletion: Examples from the Czech Republic and southern Siberia. *Quaternary Science Reviews* 30, 967-979.
- Babić, L., Zupanič, J., Vidović, J., Razum, I., Lužar-Oberiter, B., Crnjaković, M., 2013. Preservation of hanging aeolian deposits in insular karst depressions: Sediment sources and implications for the Pleistocene palaeogeography of the SE Adriatic archipelago. *Aeolian Research* 11, 171-189.
- Bambynek, W., Crasemann, B., Fink, R.W., Freund, H.U., Mark, H., Swift, C.D., Price, R.E., Rao, P.V., 1972. X-Ray Fluorescence Yields, Auger, and Coster-Kronig Transition Probabilities. *Reviews of Modern Physics* 44, 716-813.
- Banak, A., Mandić, O., Sprovieri, M., Lirer, F., Pavelić, D., 2016. Stable isotope data from loess malacofauna: Evidence for climate changes in the Pannonian Basin during the Late Pleistocene. *Quaternary International* 415, 15-24.
- Barta, G., 2014. Paleoenvironmental reconstruction based on the morphology and distribution of secondary carbonates of the loess-paleosol sequence at Süttő, Hungary. *Quaternary International* 319, 64-75.

- Bartington, 2016. Operation Manual for MS2 Magnetic Susceptibility System. Bartington Instruments Ltd., Oxford, UK, p. 72.
- Baumgart, P., Hambach, U., Meszner, S., Faust, D., 2013. An environmental magnetic fingerprint of periglacial loess: Records of Late Pleistocene loess–palaeosol sequences from Eastern Germany. *Quaternary International* 296, 82-93.
- Bayat, O., Karimi, A., Khademi, H., 2017. Stable isotope geochemistry of pedogenic carbonates in loess-derived soils of northeastern Iran: Paleoenvironmental implications and correlation across Eurasia. *Quaternary International* 429, 52-61.
- Bearden, J.A., 1967. X-Ray wavelengths. *Reviews of Modern Physics* 39, 78-124.
- Beck, M., Boning, P., Schuckel, U., Stiehl, T., Schnetger, B., Rullkötter, J., Brumsack, H.J., 2013. Consistent assessment of trace metal contamination in surface sediments and suspended particulate matter: a case study from the Jade Bay in NW Germany. *Marine Pollution Bulletin* 70, 100-111.
- Begét, J.E., Hawkins, D.B., 1989. Influence of orbital parameters on Pleistocene loess deposition in central Alaska. *Nature* 337, 151-153.
- Begét, J.E., Stone, D.B., Hawkins, D.B., 1990. Paleoclimatic forcing of magnetic susceptibility variations in Alaskan loess during the late Quaternary. *Geology* 18, 40-43.
- Bernet, M., Brandon, M.T., Grarver, J.I., Molitor, B., 2004. Downstream changes of Alpine zircon fission-track ages in the Rhône and Rhine rivers. *Sedimentary Geology* 74, 82-94.
- Beuselinck, L., Govers, G., Poesen, J., Degraer, G., Froyen, L., 1998. Grain-size analysis by laser diffractometry: comparison with the sieve-pipette method. *Catena* 32, 193-208.
- Biskaborn, B.K., Herzschuh, U., Bolshiyarov, D.Y., Schwamborn, G., Diekmann, B., 2013. Thermokarst processes and depositional events in a tundra lake, Northeastern Siberia. *Permafrost and Periglacial Processes* 24, 160-174.
- Blaauw, M., 2012. Out of tune: the dangers of aligning proxy archives. *Quaternary Science Reviews* 36, 38-49.
- Black, B.A., Neely, R.R., Manga, M., 2015. Campanian Ignimbrite volcanism, climate, and the final decline of the Neanderthals. *Geology* 43, 411-414.
- Bloemendal, J., Liu, X., Sun, Y., Li, N., 2008. An assessment of magnetic and geochemical indicators of weathering and pedogenesis at two contrasting sites on the Chinese Loess plateau. *Palaeogeography, Palaeoclimatology, Palaeoecology* 257, 152-168.
- Bloemsma, M.R., 2015. Development of a Modelling Framework for Core Data Integration using XRF Scanning. PhD thesis, Delft University of Technology, Delft, Netherlands, p. 229.
- Bognar, A., Schweitzer, F., Szöör, G., 2003. Susak - Environmental reconstruction of a loess island in the Adriatic. Geographical Research Institute, Hungarian Academy of Science, Budapest, Hungary, p. 141.
- Bokhorst, M.P., Beets, C.J., Marković, S.B., Gerasimenko, N.P., Matviishina, Z.N., Frechen, M., 2009. Pedo-chemical climate proxies in Late Pleistocene Serbian–Ukrainian loess sequences. *Quaternary International* 198, 113-123.
- Bösken, J., Sümegi, P., Zeeden, C., Klasen, N., Gulyás, S., Lehmkuhl, F., 2017. Investigating the last glacial Gravettian site ‘Ságvár Lyukas Hill’ (Hungary) and its paleoenvironmental and geochronological context using a multi-proxy approach. *Palaeogeography, Palaeoclimatology, Palaeoecology*, <https://doi.org/10.1016/j.palaeo.2017.08.010>.

- Brady, N.C., Weil, R.R., 2004. Elements of the nature and properties of soils. Pearson, Upper Saddle River, New Jersey, USA, p. 606.
- Bronk Ramsey, C., 2009. Bayesian analysis of radiocarbon dates. *Radiocarbon* 51, 337-360.
- Brunck, H., Sirocko, F., Albert, J., 2016. The ELSA-Flood-Stack: A reconstruction from the laminated sediments of Eifel maar structures during the last 60000 years. *Global and Planetary Change* 142, 136-146.
- Buggle, B., Glaser, B., Hambach, U., Gerasimenko, N., Marković, S., 2011. An evaluation of geochemical weathering indices in loess–paleosol studies. *Quaternary International* 240, 12-21.
- Buggle, B., Glaser, B., Zöller, L., Hambach, U., Marković, S., Glaser, I., Gerasimenko, N., 2008. Geochemical characterization and origin of Southeastern and Eastern European loesses (Serbia, Romania, Ukraine). *Quaternary Science Reviews* 27, 1058-1075.
- Buggle, B., Zech, M., 2015. New frontiers in the molecular based reconstruction of Quaternary paleovegetation from loess and paleosols. *Quaternary International* 372, 180-187.
- Caracciolo, L., Le Pera, E., Muto, F., Perri, F., 2011. Sandstone petrology and mudstone geochemistry of the Peruc–Korycany Formation (Bohemian Cretaceous Basin, Czech Republic). *International Geology Review* 53, 1003-1031.
- Chen, H.-F., Yeh, P.-Y., Song, S.-R., Hsu, S.-C., Yang, T.-N., Wang, Y., Chi, Z., Lee, T.-Q., Chen, M.-T., Cheng, C.-L., Zou, J., Chang, Y.-P., 2013. The Ti/Al molar ratio as a new proxy for tracing sediment transportation processes and its application in aeolian events and sea level change in East Asia. *Journal of Asian Earth Sciences* 73, 31-38.
- Chen, J., Chen, Y., Liu, L., Ji, J., Balsam, W., Sun, Y., Lu, H., 2006. Zr/Rb ratio in the Chinese loess sequences and its implication for changes in the East Asian winter monsoon strength. *Geochimica et Cosmochimica Acta* 70, 1471-1482.
- Cofflet, L., 2005. Paläomagnetische Untersuchungen im Rheinischen Löss. PhD thesis, Heinrich Heine University Düsseldorf, Germany, p. 153.
- Condie, K.C., 1993. Chemical composition and evolution of the upper continental crust: Contrasting results from surface samples and shales. *Chemical Geology* 104, 1-37.
- Cremaschi, M., 1990. Stratigraphy and palaeoenvironmental significance of the loess deposits on Susak Island (Dalmatian Archipelago). *Quaternary International* 5, 97-106.
- Cremaschi, M., Zerboni, A., Nicosia, C., Negrino, F., Rodnight, H., Spötl, C., 2015. Age, soil-forming processes, and archaeology of the loess deposits at the Apennine margin of the Po plain (northern Italy): New insights from the Ghiardo area. *Quaternary International* 376, 173-188.
- Croudace, I.W., Rindby, A., Rothwell, R.G., 2006. ITRAX: description and evaluation of a new multi-function X-ray core scanner, in: Rothwell, R.G. (Ed.), *New techniques in sediment core analysis*. Geological Society, London, Special Publications 267, pp. 51-63.
- Cullers, R.L., 2000. The geochemistry of shales, siltstones and sandstones of Pennsylvanian-Permian age, Colorado, USA: implications for provenance and metamorphic studies. *Lithos* 51, 181-203.
- Darmody, R.G., Thorn, C.E., Allen, C.E., 2005. Chemical weathering and boulder mantles, Kärkevagge, Swedish Lapland. *Geomorphology* 67, 159-170.

- Davies, S.J., Lamb, H.F., Roberts, S.J., 2015. Micro-XRF core scanning in palaeolimnology: recent developments, in: Croudace, I.W., Rothwell, R.G. (Eds.), *Micro-XRF studies of sediment cores*. Springer, Dordrecht, Netherlands, pp. 189-226.
- de Vries, J.L., Vrebos, B.A.R., 2002. Quantification of infinitely thick specimens by XRF analysis, in: Van Grieken, R.E., Markowicz, A.A. (Eds.), *Handbook of X-ray spectrometry*. Marcel Dekker Inc., New York, Basel, pp. 341-406.
- Dearing, J.A., 1994. *Environmental Magnetic Susceptibility - Using the Bartington MS2 system*. Chi Publishing, Kenilworth, UK, p. 104.
- Dearing, J.A., Dann, R.J.L., Hay, K., Lees, J.A., Loveland, P.J., Maher, B.A., O'Grady, K., 1996. Frequency-dependent susceptibility measurements of environmental materials. *Geophysical Journal International* 124, 228-240.
- Dietrich, S., Seelos, K., 2010. The reconstruction of easterly wind directions for the Eifel region (Central Europe) during the period 40.3–12.9 ka BP. *Climate of the Past* 6, 145-154.
- DiLabio, R.N.W., 1989. Terrain geochemistry in Canada, in: Fulton, R.J. (Ed.), *Quaternary Geology of Canada and Greenland*. Canadian Government Publishing Centre, Ottawa, Canada, pp. 645-663.
- Duller, G.A.T., 2008. *Luminescence dating: guidelines on using luminescence dating in archaeology*. English Heritage, Swindon, UK, p. 42.
- Durn, G., 2003. Terra Rossa in the Mediterranean region: parent materials, composition and origin. *Geologia Croatia* 56/1, 83-100.
- Durn, G., Rubinić, V., Wacha, L., Patekar, M., Frechen, M., Tsukamoto, S., Tadej, N., Husnjak, S., 2017a. Polygenetic soil formation on Late Glacial Loess on the Susak Island reflects paleo-environmental changes in the Northern Adriatic area. *Quaternary International*, <https://doi.org/10.1016/j.quaint.2017.06.072>.
- Durn, G., Wacha, L., Bartolin, M., Rolf, C., Frechen, M., Tsukamoto, S., Tadej, N., Husnjak, S., Li, Y., Rubinić, V., 2017b. Provenance and formation of the red paleosol and lithified terra rossa-like infillings on the Island of Susak: A high-resolution and chronological approach. *Quaternary International*, <https://doi.org/10.1016/j.quaint.2017.11.040>.
- Evans, M.E., Rutter, N.W., Catto, N., Chlachula, J., Nyvit, D., 2003. Magnetoclimatology: Teleconnection between the Siberian loess record and North Atlantic Heinrich events. *Geology* 31, 537-540.
- Fassbinder, J.W.E., Stanjek, H., Vali, H., 1990. Occurrence of magnetic bacteria in soil. *Nature* 343, 161-163.
- Fedo, C.M., Nesbitt, H.W., Young, G.M., 1995. Unraveling the effects of potassium metasomatism in sedimentary rocks and paleosols, with implications for paleoweathering conditions and provenance. *Geology* 23, 921-924.
- Feng, Z.-D., 1997. Geochemical characteristics of a loess-soil sequence in Central Kansas. *Soil Science Society of America Journal* 61, 534-541.
- Ferraro, F., 2009. Age, sedimentation, and soil formation in the Val Sorda loess sequence, Northern Italy. *Quaternary International* 204, 54-64.
- Fitzsimmons, K.E., Hambach, U., Veres, D., Iovita, R., 2013. The Campanian Ignimbrite eruption: new data on volcanic ash dispersal and its potential impact on human evolution. *PloS one* 8, e65839.
- Fitzsimmons, K.E., Marković, S.B., Hambach, U., 2012. Pleistocene environmental dynamics recorded in the loess of the middle and lower Danube basin. *Quaternary Science Reviews* 41, 104-118.

- Floyd, P.A., Winchester, J.A., Park, R.G., 1989. Geochemistry and tectonic setting of Lewisian clastic metasediments from the early Proterozoic Loch Maree Group of Gairloch, NW Scotland. *Precambrian Research* 45, 203-214.
- Förster, M.W., Sirocko, F., 2016. The ELSA tephra stack: Volcanic activity in the Eifel during the last 500,000 years. *Global and Planetary Change* 142, 100-107.
- Frechen, M., 1999. Upper Pleistocene loess stratigraphy in Southern Germany. *Quaternary Geochronology* 18, 243-269.
- Frechen, M., 2003. Loess in Europe - mass accumulation rates during the Last Glacial Period. *Quaternary Science Reviews* 22, 1835-1857.
- Frechen, M., Horváth, E., Gábris, G., 1997. Geochronology of Middle and Upper Pleistocene loess sections in Hungary. *Quaternary Research* 48, 291-312.
- Frechen, M., Schirmer, W., 2011. Luminescence Chronology of the Schwalbenberg II Loess in the Middle Rhine Valley. *E & G - Quaternary Science Journal* 60, 78-89.
- Frechen, M., Zander, A., Čílek, V., Ložek, V., 1999. Loess chronology of the Last Interglacial/Glacial cycle in Bohemia and Moravia, Czech Republic. *Quaternary Science Reviews* 18, 1467-1493.
- Fuchs, M., Kreutzer, S., Rousseau, D.-D., Antoine, P., Hatté, C., Lagroix, F., Moine, O., Gauthier, C., Svoboda, J., Lisá, L., 2013. The loess sequence of Dolní Věstonice, Czech Republic: A new OSL-based chronology of the Last Climatic Cycle. *Boreas* 42, 664-677.
- Fujimoto, C.K., Sherman, G.D., 1948. Behavior of Manganese in the soil and the Manganese cycle. *Soil Science* 66, 131-146.
- Gábris, G., Horváth, E., Novothny, Á., Ruszkiczay-Rüdiger, Z., 2012. Fluvial and aeolian landscape evolution in Hungary – results of the last 20 years research. *Netherlands Journal of Geosciences* 91, 111-128.
- Gábris, G., Nádor, A., 2007. Long-term fluvial archives in Hungary: response of the Danube and Tisza rivers to tectonic movements and climatic changes during the Quaternary: a review and new synthesis. *Quaternary Science Reviews* 26, 2758-2782.
- GADM, 2015. GADM. www.gadm.org (accessed 5 October 2017).
- Gallagher, T.M., Sheldon, N.D., 2013. A new paleothermometer for forest paleosols and its implications for Cenozoic climate. *Geology* 41, 647-650.
- Gallet, S., Jahn, B.-m., Torii, M., 1996. Geochemical characterization of the Luochuan loess-paleosol sequence, China, and plaeoclimatic implications. *Chemical Geology* 133, 67-88.
- Gallet, S., Jahn, B.-m., Van Vliet Lanoe, B., Dia, A., Rossello, E., 1998. Loess geochemistry and its implications for particle origin composition of the upper continental crust. *Earth and Planetary Science Letters* 156, 157-172.
- Garcia, D., Coelho, J., Perrin, M., 1991. Fractionation between TiO₂ and Zr as a measure of sorting within shale and sandstone series (Northern Portugal). *European Journal of Mineralogy* 3, 404-414.
- Garcia, D., Fontelles, M., Moutte, J., 1994. Sedimentary fractionations between Al, Ti and Zr and the genesis of strongly peraluminous granites. *The Journal of Geology* 102, 411-422.
- Gerritse, R.G., George, R.J., 1988. The role of soil organic matter in the geochemical cycling of chlorine and bromine. *Journal of Hydrology* 101, 83-95.
- Gocke, M., Hambach, U., Eckmeier, E., Schwark, L., Zöller, L., Fuchs, M., Löscher, M., Wiesenberg, G.L.B., 2014. Introducing an improved multi-proxy approach for paleoenvironmental reconstruction of loess–paleosol archives applied on the Late

- Pleistocene Nussloch sequence (SW Germany). *Palaeogeography, Palaeoclimatology, Palaeoecology* 410, 300-315.
- Goldschmidt, V.M., 1937. The principles and distribution of chemical elements in minerals and rocks. *Journal of the Chemical Society (Resumed)*, 655-673.
- Goodfriend, G.A., Hood, D.G., 1983. Carbon isotope analysis of land snail shells: implications for carbon sources and radiocarbon dating. *Radiocarbon* 25, 810-830.
- Google-Earth, 2017. Google Earth v. 7.1.8. Data sources for subfigure a: Data SIO, NOAA, U.S. Navy, NGA, GEBCO, Image Landsat / Copernicus, for subfigure b: Data SIO, NOAA, U.S. Navy, GEBCO, Image CNES / Airbus, Digital Globe, for subfigure c: Image: Digital Globe, 2017.
- Grootes, P.M., Stuiver, M., 1997. Oxygen 18/16 variability in Greenland snow and ice with 10^{-3} - to 10^5 -year time resolution. *Journal of Geophysical Research* 102, 26455.
- Haase, D., Fink, J., Haase, G., Ruske, R., Pécsi, M., Richter, H., Altermann, M., Jäger, K.D., 2007. Loess in Europe - its spatial distribution based on a European Loess Map, scale 1:2,500,000. *Quaternary Science Reviews* 26, 1301-1312.
- Hahn, A., Kliem, P., Oehlerich, M., Ohlendorf, C., Zolitschka, B., 2014. Elemental composition of the Laguna Potrok Aike sediment sequence reveals paleoclimatic changes over the past 51 ka in southern Patagonia, Argentina. *Journal of Paleolimnology* 52, 349-366.
- Hahn, A., Kliem, P., Ohlendorf, C., Zolitschka, B., Rosén, P., 2013. Climate induced changes as registered in inorganic and organic sediment components from Laguna Potrok Aike (Argentina) during the past 51 ka. *Quaternary Science Reviews* 71, 154-166.
- Hambach, U., Rolf, C., Schnepf, E., 2008. Magnetic dating of Quaternary sediments, volcanites and archaeological materials: an overview. *E & G - Quaternary Science Journal* 57, 25-51.
- Hardcastle, J., 1889. Origin of the loess deposit of the Timaru plateau. *Transactions and Proceedings of the New Zealand Institute* 22, 406-414.
- Hardcastle, J., 1890. On the Timaru loess as a climate register. *Transactions and Proceedings of the New Zealand Institute* 23, 324-332.
- Harnois, L., 1988. The CIW Index: A new chemical index of weathering. *Sedimentary Geology* 55, 319-322.
- Hatté, C., Pessenda, L.C., Lang, A., Paterne, M., 2001. Development of accurate and reliable ^{14}C chronologies for loess deposits: application to the loess sequence of Nussloch (Rhine Valley, Germany). *Radiocarbon* 43, 611-618.
- Heller, F., Xiuming, L., Tungsheng, L., Tongchun, X., 1991. Magnetic susceptibility of loess in China. *Earth and Planetary Science Letters* 103, 301-310.
- Hennekam, R., de Lange, G., 2012. X-ray fluorescence core scanning of wet marine sediments: methods to improve quality and reproducibility of high-resolution paleoenvironmental records. *Limnology and Oceanography: Methods* 10, 991-1003.
- Hill, T.C., 2005. Geochemical evidence for weathering in northwestern European loess on a sub-millennial scale during the last Ice Age, Faculty of Environment and Leisure. PhD thesis, University of Gloucestershire, Gloucestershire, UK, p. 253.
- Holland, H.D., Gottfried, D., 1955. The effect of nuclear radiation on the structure of zircon. *Acta Crystallographica* 8, 291-300.
- Horiba, 2017. X-Ray Fluorescence - The Basic Process. <http://www.horiba.com/scientific/products/x-ray-fluorescence-analysis/tutorial/x-ray-fluorescence-the-basic-process/> (accessed 8 December 2017).

- Horváth, E., Bradák, B., 2014. Sárga föld, lösz, lös: Short historical overview of loess research and lithostratigraphy in Hungary. *Quaternary International* 319, 1-10.
- Hošek, J., Hambach, U., Lisá, L., Grygar, T.M., Horáček, I., Meszner, S., Knésl, I., 2015. An integrated rock-magnetic and geochemical approach to loess/paleosol sequences from Bohemia and Moravia (Czech Republic): Implications for the Upper Pleistocene paleoenvironment in central Europe. *Palaeogeography, Palaeoclimatology, Palaeoecology* 418, 344-358.
- Huang, J.-J., Löwemark, L., Chang, Q., Lin, T.-Y., Chen, H.-F., Song, S.-R., Wei, K.-Y., 2016. Choosing optimal exposure times for XRF core-scanning: Suggestions based on the analysis of geological reference materials. *Geochemistry, Geophysics, Geosystems* 17, 1558-1566.
- Hughes, P., Woodward, J., Gibbard, P., 2006. Late Pleistocene glaciers and climate in the Mediterranean. *Global and Planetary Change* 50, 83-98.
- Hughes, P.D., Woodward, J.C., van Calsteren, P.C., Thomas, L.E., 2011. The glacial history of the Dinaric Alps, Montenegro. *Quaternary Science Reviews* 30, 3393-3412.
- Ibáñez, J.J., Zinck, J.A., Dazzi, C., 2013. Soil geography and diversity of the European biogeographical regions. *Geoderma* 192, 142-153.
- Iriondo, M.H., Kröhling, D.M., 2007. Non-classical types of loess. *Sedimentary Geology* 202, 352-368.
- Jarvis, S., Croudace, I.W., Rothwell, R.G., 2015. Parameter optimization for the ITRAX XRF core scanner, in: Croudace, I.W., Rothwell, R.G. (Eds.), *Micro-XRF studies of sediment cores*. Springer, Dordrecht, Netherlands, pp. 535-562.
- Jefferson, I.F., Evstatiev, D., Karastanev, D., Mavlyanova, N.G., Smalley, I.J., 2003. Engineering geology of loess and loess-like deposits: a commentary on Russian literature. *Engineering Geology* 68, 333-351.
- Jenkins, R., 1988. X-ray fluorescence spectrometry, in: Winefordner, J.D., Kolthoff, I.M. (Eds.), *Chemical Analysis - A series of monographs on analytical chemistry and its applications*. Vol. 99. John Wiley & Sons, Inc., New York, USA, p. 175.
- Kadereit, A., Kind, C.-J., Wagner, G.A., 2013. The chronological position of the Lohne Soil in the Nussloch loess section – re-evaluation for a European loess-marker horizon. *Quaternary Science Reviews* 59, 67-86.
- Kadereit, A., Wagner, G.A., 2014. Geochronological reconsideration of the eastern European key loess section at Stayky in Ukraine. *Climate of the Past* 10, 783-796.
- Kalugin, I., Daryin, A., Smolyaninova, L., Andreev, A., Diekmann, B., Khlystov, O., 2007. 800-yr-long records of annual air temperature and precipitation over Southern Siberia inferred from Teletskoye Lake sediments. *Quaternary Research* 67, 400-410.
- Keiluweit, M., Nico, P.S., Kleber, M., Fendorf, S., 2016. Are oxygen limitations under recognized regulators of organic carbon turnover in upland soils? *Biogeochemistry* 127, 157-171.
- Klasen, N., Fischer, P., Lehmkuhl, F., Hilgers, A., 2015. Luminescence dating of loess deposits from the Remagen-Schwalbenberg site, Western Germany. *Geochronometria* 42, 67-77.
- Knoll, G.F., 2010. Radiation detection and measurement. John Wiley & Sons, Inc., Hoboken, USA, p. 830.
- Koeniger, P., Barta, G., Thiel, C., Bajnóczi, B., Novothny, Á., Horváth, E., Techmer, A., Frechen, M., 2014. Stable isotope composition of bulk and secondary carbonates from the Quaternary loess-paleosol sequence in Süttő, Hungary. *Quaternary International* 319, 38-49.

- Kronberg, B.I., Fyfe, W.S., Leonardos Jr., O.H., Sanots, A.M., 1979. The chemistry of some Brazilian soils: element mobility during intense weathering. *Chemical Geology* 24, 211-229.
- Kronberg, B.I., Nesbitt, H.W., 1981. Quantification of weathering, soil geochemistry and soil fertility. *Journal of Soil Science* 32, 453-459.
- Kühn, P., Techmer, A., Weidenfeller, M., 2013. Lower to middle Weichselian pedogenesis and palaeoclimate in Central Europe using combined micromorphology and geochemistry: the loess-paleosol sequence of Alsheim (Mainz Basin, Germany). *Quaternary Science Reviews* 75, 43-58.
- Kukla, G., 1977. Pleistocene land-sea correlations I. Europe. *Earth-Science Reviews* 13, 307-374.
- Kukla, G., 1987. Loess stratigraphy in Central China. *Quaternary Science Reviews* 6, 191-219.
- Lavelle, P., Spain, A., Blouin, M., Brwon, G., Decaëns, T., Grimaldi, M., Jiménez, J.J., McKey, D., Mathieu, J., Velasquez, E., Zangerlé, A., 2016. Ecosystem engineers in a self-organized soil: A review of concepts and future research questions. *Soil Science* 181, 91-109.
- Lechner, P., Eckbauer, S., Hartmann, R., Krisch, S., Hauff, D., Richter, R., Soltau, H., Strüder, L., Fiorini, C., Gatti, E., Longoni, A., Sampietro, M., 1996. Silicon drift detectors for high resolution room temperature X-ray spectroscopy. *Nuclear Instruments and Methods in Physics Research Section A* 377, 346-351.
- Lechner, P., Fiorini, C., Hartmann, R., Kemmer, J., Krause, N., Leutenegger, P., Longoni, A., Soltau, H., Stötter, D., Stötter, R., Strüder, L., Weber, U., 2001. Silicon drift detectors for high count rate X-ray spectroscopy at room temperature. *Nuclear Instruments and Methods in Physics Research Section A* 458, 281-287.
- Leger, M., 1990. Loess landforms. *Quaternary International* 7/8, 53-61.
- Lehmkuhl, F., Zens, J., Krauß, L., Schulte, P., Kels, H., 2016. Loess-paleosol sequences at the northern European loess belt in Germany: Distribution, geomorphology and stratigraphy. *Quaternary Science Reviews* 153, 11-30.
- Leonhard, K.C.v., 1824. *Charakteristik der Felsarten: Gleichartige und scheinbar gleichartige Gesteine*. Engelmann, Heidelberg, Germany, p. 367.
- Leri, A.C., Mayer, L.M., Thornton, K.R., Ravel, B., 2014. Bromination of marine particulate organic matter through oxidative mechanisms. *Geochimica et Cosmochimica Acta* 142, 53-63.
- Leri, A.C., Myneni, S.C.B., 2010. Organochlorine turnover in forest ecosystems: The missing link in the terrestrial chlorine cycle. *Global Biogeochemical Cycles* 24, GB4021.
- Leri, A.C., Myneni, S.C.B., 2012. Natural organobromine in terrestrial ecosystems. *Geochimica et Cosmochimica Acta* 77, 1-10.
- Leri, A.C., Ravel, B., 2015. Abiotic bromination of soil organic matter. *Environmental Science and Technology* 49, 13350-13359.
- Liang, L., Sun, Y., Beets, C.J., Prins, M.A., Wu, F., Vandenberghe, J., 2013. Impacts of grain size sorting and chemical weathering on the geochemistry of Jingyuan loess in the Northwestern Chinese Loess Plateau. *Journal of Asian Earth Sciences* 69, 177-184.
- Liang, L., Sun, Y., Yao, Z., Liu, Y., Wu, F., 2012. Evaluation of high-resolution elemental analyses of Chinese loess deposits measured by X-ray fluorescence core scanner. *Catena* 92, 75-82.

- Lindé, K., Mycielska-Dowgiallo, E., 1980. Some experimentally produced microtextures on grain surfaces of quartz sand. *Geografiska Annaler: Series A, Physical Geography* 62, 171-184.
- Lisiecki, L.E., Raymo, M.E., 2005. A Pliocene-Pleistocene stack of 57 globally distributed benthic $\delta^{18}\text{O}$ records. *Paleoceanography* 20, PA1003.
- Litholex, 2013. Lithostratigraphische Einheiten Deutschlands. <http://litholex.bgr.de/> (accessed 16 March 2016).
- Liu, Q., Jin, C., Hu, P., Jiang, Z., Ge, K., Roberts, A.P., 2015. Magnetostratigraphy of Chinese loess–paleosol sequences. *Earth-Science Reviews* 150, 139-167.
- Liu, T., 1988. *Loess in China*. China Ocean Press, Beijing, China, p. 224.
- Liu, W., Huang, Y., 2005. Compound specific D/H ratios and molecular distributions of higher plant leaf waxes as novel paleoenvironmental indicators in the Chinese Loess Plateau. *Organic Geochemistry* 36, 851-860.
- Liu, Z., Colin, C., Trentesaux, A., Siani, G., Frank, N., Blamart, D., Farid, S., 2005. Late Quaternary climatic control on erosion and weathering in the eastern Tibetan Plateau and the Mekong Basin. *Quaternary Research* 63, 316-328.
- Löfverström, M., Caballero, R., Nilsson, J., Kleman, J., 2014. Evolution of the large-scale atmospheric circulation in response to changing ice sheets over the last glacial cycle. *Climate of the Past* 10, 1453-1471.
- Lovley, D.R., Stolz, J.F., Nord, G.L., Phillips, E.J.P., 1987. Anaerobic production of magnetite by a dissimilatory iron-reducing microorganism. *Nature* 330, 252-254.
- Löwemark, L., Chen, H.F., Yang, T.N., Kylander, M., Yu, E.F., Hsu, Y.W., Lee, T.Q., Song, S.R., Jarvis, S., 2011. Normalizing XRF-scanner data: A cautionary note on the interpretation of high-resolution records from organic-rich lakes. *Journal of Asian Earth Sciences* 40, 1250-1256.
- Ludwig, P., Pinto, J.G., Raible, C.C., Shao, Y., 2017. Impacts of surface boundary conditions on regional climate model simulations of European climate during the Last Glacial Maximum. *Geophysical Research Letters* 44, 5086-5095.
- Lyell, C., 1833. *Principles of Geology* Vol. 3. John Murray, London, UK, p. 602.
- Maher, B.A., 2011. The magnetic properties of Quaternary aeolian dusts and sediments, and their palaeoclimatic significance. *Aeolian Research* 3, 87-144.
- Maher, B.A., Thompson, R., Zhou, L.P., 1994. Spatial and temporal reconstructions of changes in the Asian paleomonsoon: A new mineral magnetic approach. *Earth and Planetary Science Letters* 125, 461-471.
- Marković, S.B., Fitzsimmons, K.E., Sprafke, T., Gavrilović, D., Smalley, I.J., Jović, V., Svirčev, Z., Gavrilov, M.B., Bešlin, M., 2016. The history of Danube loess research. *Quaternary International* 399, 86-99.
- Marković, S.B., Stevens, T., Kukla, G.J., Hambach, U., Fitzsimmons, K.E., Gibbard, P., Buggle, B., Zech, M., Guo, Z., Hao, Q., Wu, H., O'Hara Dhand, K., Smalley, I.J., Újvári, G., Sümegi, P., Timar-Gabor, A., Veres, D., Sirocko, F., Vasiljević, D.A., Jary, Z., Svensson, A., Jović, V., Lehmkuhl, F., Kovács, J., Svirčev, Z., 2015. Danube loess stratigraphy - Towards a pan-European loess stratigraphic model. *Earth-Science Reviews* 148, 228-258.
- Marshall, D., 1996. Ternplot: an excel spreadsheet for ternary diagrams. *Computers & Geosciences* 22, 697-699.
- Martin-Puertas, C., Tjallingii, R., Bloemsa, M., Brauer, A., 2017. Varved sediment responses to early Holocene climate and environmental changes in Lake Meerfelder

- Maar (Germany) obtained from multivariate analyses of micro X-ray fluorescence core scanning data. *Journal of Quaternary Science* 32, 427-436.
- Maselli, V., Hutton, E.W., Kettner, A.J., Syvitski, J.P.M., Trincardi, F., 2011. High-frequency sea level and sediment supply fluctuations during Termination I: An integrated sequence-stratigraphy and modeling approach from the Adriatic Sea (Central Mediterranean). *Marine Geology* 287, 54-70.
- Maynard, J.B., 1992. Chemistry of modern soils as a guide to interpreting Precambrian paleosols. *The Journal of Geology* 100, 279-289.
- McLennan, S.M., 1993. Weathering and global denudation. *The Journal of Geology* 101, 295-303.
- McLennan, S.M., 2001. Relationships between the trace element composition of sedimentary rocks and upper continental crust. *Geochemistry, Geophysics, Geosystems* 2, 2000GC000109.
- McLennan, S.M., Hemming, S., McDaniel, D.K., Hanson, G.N., 1993. Geochemical approaches to sedimentation, provenance, and tectonics, in: Johnsson, M.J., Basu, A. (Eds.), *Processes controlling the composition of clastic sediments*. Geological Society of America Special Paper 284, Boulder, Colorado, pp. 21-40.
- Meszner, S., Kreuzer, S., Fuchs, M., Faust, D., 2013. Late Pleistocene landscape dynamics in Saxony, Germany: Paleoenvironmental reconstruction using loess-paleosol sequences. *Quaternary International* 296, 94-107.
- Mikulčić Pavlaković, S., Crnjaković, M., Tibljaš, D., Šoufek, M., Wacha, L., Frechen, M., Lacković, D., 2011. Mineralogical and geochemical characteristics of Quaternary sediments from the Island of Susak (Northern Adriatic, Croatia). *Quaternary International* 234, 32-49.
- Miller, J.N., 1991. Basic statistical methods for analytical chemistry part 2. Calibration and regression methods - A review. *Analyst* 116, 3-14.
- Moine, O., Antoine, P., Hatte, C., Landais, A., Mathieu, J., Prud'homme, C., Rousseau, D.D., 2017. The impact of Last Glacial climate variability in West-European loess revealed by radiocarbon dating of fossil earthworm granules. *Proceedings of the National Academy of Sciences of the United States of America* 114, 6209-6214.
- Mongelli, G., Critelli, S., Perri, F., Sonnino, M., Perrone, V., 2006. Sedimentary recycling, provenance and paleoweathering from chemistry and mineralogy of Mesozoic continental redbed mudrocks, Peloritani mountains, southern Italy. *Geochemical Journal* 40, 197-209.
- Moseley, H.G.J., 1914. The high-frequency spectra of the elements. Part II. *The London, Edinburgh, and Dublin Philosophical Magazine and Journal of Science* 27, 703-713.
- MSU, 2017. Analytical Fees. <https://ees.natsci.msu.edu/about/facilities/xrf-lab/#fees> (accessed 8 November 2017).
- Muhs, D.R., 2013. The geologic records of dust in the Quaternary. *Aeolian Research* 9, 3-48.
- Muhs, D.R., 2018. The geochemistry of loess: Asian and North American deposits compared. *Journal of Asian Earth Sciences* 155, 81-115.
- Muhs, D.R., Ager, T.A., Bettis III, E.A., McGeehin, J.P., Been, J.M., Begét, J.E., Pavich, M.J., Stafford Jr., T.W., Stevens, D.A.S.P., 2003. Stratigraphy and palaeoclimatic significance of Late Quaternary loess-palaeosol sequences of the Last Interglacial-Glacial cycle in Central Alaska. *Quaternary Science Reviews* 22, 1947-1986.

- Muhs, D.R., Benedict, J.B., 2006. Eolian additions to Late Quaternary Alpine soils, Indian peaks wilderness area, Colorado Front Range. *Arctic, Antarctic, and Alpine Research* 38, 120-130.
- Muhs, D.R., Bettis III, E.A., 2000. Geochemical variations in Peoria loess of Western Iowa indicate paleowinds of midcontinental North America during last glaciation. *Quaternary Research* 53, 49-61.
- Muhs, D.R., Bettis III, E.A., 2003. Quaternary loess-paleosol sequences as examples of climate-driven sedimentary extremes, in: Chan, M.A., Archer, A.W. (Eds.), *Extreme depositional environments: Mega end members in geological time*. Geological Society of America Special Paper 370, Boulder, Colorado, USA, pp. 53-74.
- Murton, J.B., Goslar, T., Edwards, M.E., Bateman, M.D., Danilov, P.P., Savvinov, G.N., Gubin, S.V., Ghaleb, B., Haile, J., Kanevskiy, M., Lozhkin, A.V., Lupachev, A.V., Murton, D.K., Shur, Y., Tikhonov, A., Vasil'chuk, A.C., Vasil'chuk, Y.K., Wolfe, S.A., 2015. Palaeoenvironmental interpretation of Yedoma Silt (Ice Complex) deposition as cold-climate loess, Duvanny Yar, Northeast Siberia. *Permafrost and Periglacial Processes* 26, 208-288.
- Nesbitt, H.W., Markovics, G., Price, R.C., 1980. Chemical processes affecting alkalis and alkaline earths during continental weathering. *Geochimica et Cosmochimica Acta* 44, 1659-1666.
- Nesbitt, H.W., Young, G.M., 1982. Early Proterozoic climates and plate motions inferred from major element chemistry of lutites. *Nature* 299, 715-717.
- Nesbitt, H.W., Young, G.M., 1984. Prediction of some weathering trends of plutonic and volcanic rocks based on thermodynamic and kinetic considerations. *Geochimica et Cosmochimica Acta* 48, 1523-1534.
- Nesbitt, H.W., Young, G.M., 1989. Formation and diagenesis of weathering profiles. *The Journal of Geology* 97, 129-147.
- Nesbitt, H.W., Young, G.M., McLennan, S.M., Keays, R.R., 1996. Effects of chemical weathering and sorting on the petrogenesis of siliciclastic sediments, with implications for provenance studies. *The Journal of Geology* 104, 525-542.
- Novothy, Á., Frechen, M., Horváth, E., Bradák, B., Oches, E.A., McCoy, W.D., Stevens, T., 2009. Luminescence and amino acid racemization chronology of the loess-paleosol sequence at Süttő, Hungary. *Quaternary International* 198, 62-76.
- Novothy, Á., Frechen, M., Horváth, E., Krbetschek, M., Tsukamoto, S., 2010. Infrared stimulated luminescence and radiofluorescence dating of aeolian sediments from Hungary. *Quaternary Geochronology* 5, 114-119.
- Novothy, Á., Frechen, M., Horváth, E., Wacha, L., Rolf, C., 2011. Investigating the penultimate and last glacial cycles of the Süttő loess section (Hungary) using luminescence dating, high-resolution grain size, and magnetic susceptibility data. *Quaternary International* 234, 75-85.
- Öberg, G.M., 2003. The biogeochemistry of Chlorine in soil, *The Handbook of Environmental Chemistry*. Springer, Berlin, Heidelberg, Germany, pp. 43-62.
- Obreht, I., Hambach, U., Veres, D., Zeeden, C., Bosken, J., Stevens, T., Markovic, S.B., Klasen, N., Brill, D., Burow, C., Lehmkuhl, F., 2017. Shift of large-scale atmospheric systems over Europe during late MIS 3 and implications for Modern Human dispersal. *Scientific Reports* 7, 5848.
- Obreht, I., Zeeden, C., Hambach, U., Veres, D., Markovic, S.B., Bosken, J., Svircev, Z., Bacevic, N., Gavrilov, M.B., Lehmkuhl, F., 2016. Tracing the influence of

- Mediterranean climate on Southeastern Europe during the past 350,000 years. *Scientific Reports* 6, 36334.
- Obreht, I., Zeeden, C., Schulte, P., Hambach, U., Eckmeier, E., Timar-Gabor, A., Lehmkuhl, F., 2015. Aeolian dynamics at the Orlovat loess–paleosol sequence, Northern Serbia, based on detailed textural and geochemical evidence. *Aeolian Research* 18, 69-81.
- Ohlendorf, C., 2018. A sample carrier for measuring discrete powdered samples with an ITRAX XRF core scanner. *X-Ray Spectrometry* 47, 58-62.
- Ohlendorf, C., Wennrich, V., Enters, D., 2015. Experiences with XRF-scanning of long sediment records, in: Croudace, I.W., Rothwell, R.G. (Eds.), *Micro-XRF studies of sediment cores*. Springer, Dodrecht, Netherlands, pp. 351-372.
- OSM, 2015. OpenStreetMap. <https://www.openstreetmap.de/> (accessed 28 November 2015).
- Pécsi, M., 1982. The most typical loess profiles in Hungary, in: Pécsi, M. (Ed.), *Quaternary Studies in Hungary*. Geographical Research Institute, Budapest, Hungary, pp. 145-169.
- Pécsi, M., 1990. Loess is not just the accumulation of dust. *Quaternary International* 7/8, 1-21.
- Peng, S., Hao, Q., Wang, L., Ding, M., Zhang, W., Wang, Y., Guo, Z., 2016. Geochemical and grain-size evidence for the provenance of loess deposits in the Central Shandong Mountains region, Northern China. *Quaternary Research* 85, 290-298.
- Perri, F., Critelli, S., Martín-Algarra, A., Martín-Martín, M., Perrone, V., Mongelli, G., Zattin, M., 2013. Triassic redbeds in the Malaguide Complex (Betic Cordillera - Spain): Petrography, geochemistry and geodynamic implications. *Earth-Science Reviews* 117, 1-28.
- Pind, N., 1984. Standard-addition procedure for the determination of traces of lead in solid samples by X-ray fluorescence spectrometry. *Talanta* 31, 1118-1120.
- Potts, P.J., 1992. *A hand book of silicate rock analysis*. Blackie & Son Limited, Glasgow, UK, p. 622.
- Preusser, F., Degering, D., Fuchs, M., Hilgers, A., Kadereit, A., Klasen, N., Krbetschek, M., Richter, D., Spencer, J.Q.G., 2008. Luminescence dating: basics, methods and applications. *E & G - Quaternary Science Journal* 57, 95-149.
- Profe, J., Neumann, L., Novothny, Á., Barta, G., Rolf, C., Frechen, M., Ohlendorf, C., Zolitschka, B., under review. Paleoenvironmental conditions and sedimentation dynamics in Central Europe inferred from geochemical data of the loess-paleosol sequence at Süttő (Hungary). *Quaternary Science Reviews*.
- Profe, J., Wacha, L., Frechen, M., Ohlendorf, C., Zolitschka, B., 2018. XRF scanning of discrete samples – A chemostratigraphic approach exemplified for loess-paleosol sequences from the Island of Susak, Croatia. *Quaternary International*, <https://doi.org/10.1016/j.quaint.2018.05.006>.
- Profe, J., Zolitschka, B., Schirmer, W., Frechen, M., Ohlendorf, C., 2016. Geochemistry unravels MIS 3/2 paleoenvironmental dynamics at the loess–paleosol sequence Schwalbenberg II, Germany. *Palaeogeography, Palaeoclimatology, Palaeoecology* 459, 537-551.
- Prud'Homme, C., Antoine, P., Moine, O., Turpin, E., Huguenard, L., Robert, V., Degeai, J.-P., 2015. Earthworm calcite granules: a new tracker of millennial-timescale environmental changes in Last Glacial loess deposits. *Journal of Quaternary Science* 30, 529-536.

- Prud'homme, C., Lécuyer, C., Antoine, P., Hatté, C., Moine, O., Fourel, F., Amiot, R., Martineau, F., Rousseau, D.-D., 2018. $\delta^{13}\text{C}$ signal of earthworm calcite granules: A new proxy for palaeoprecipitation reconstructions during the Last Glacial in Western Europe. *Quaternary Science Reviews* 179, 158-166.
- Pye, K., 1984. Loess. *Progress in Physical Geography* 8, 176-217.
- Pye, K., 1995. The nature, origin and accumulation of loess. *Quaternary Science Reviews* 14, 653-667.
- Raczyk, J., Jary, Z., Korabiewski, B., 2015. Geochemical properties of the Late Pleistocene loess-soil sequence in Dankowice (Niemcza-Strzelin Hills). *Landform Analysis* 29, 49-61.
- Ramkumar, M., 2015. Toward standardization of terminologies and recognition of chemostratigraphy as a formal stratigraphic method, in: Ramkumar, M. (Ed.), *Chemostratigraphy Concepts, Techniques, and Applications*. Elsevier Inc., Amsterdam, Netherlands, pp. 1-21.
- Rasmussen, S.O., Andersen, K.K., Svensson, A.M., Steffensen, J.P., Vinther, B.M., Clausen, H.B., Siggaard-Andersen, M.L., Johnsen, S.J., Larsen, L.B., Dahl-Jensen, D., Bigler, M., Röthlisberger, R., Fischer, H., Goto-Azuma, K., Hansson, M.E., Ruth, U., 2006. A new Greenland ice core chronology for the last glacial termination. *Journal of Geophysical Research* 111, D06102.
- Reese, R.A., 2005. Boxplots. *significance* 2, 134-135.
- Reimer, P.J., Bard, E., Bayliss, A., Beck, J.W., Blackwell, P.G., Bronk Ramsey, C., Buck, C.E., Cheng, H., Lawrence Edwards, R., Friedrich, M., Grootes, P.M., Guilderson, T.P., Hafliðason, H., Hajdas, I., Hatté, C., Heaton, T.J., Hoffmann, D.L., Hogg, A.G., Hughen, K.A., Kaiser, K.F., Kromer, B., Manning, S.W., Niu, M., Reimer, R.W., Richards, D.A., Scott, E.M., R., S.J., Staff, R.A., Turney, C.S.M., Van der Plicht, J., 2013. IntCal13 and Marine13 radiocarbon age calibration curves 0-50,000 years cal BP. *Radiocarbon* 55, 1869-1887.
- Retallack, G.J., 2001. *Soils of the Past: An introduction to paleopedology*. Blackwell Science Ltd, Oxford, UK, p. 404.
- Richthofen, F.v., 1882. On the mode of origin of the loess. *Geological Magazine* 9, 293-305.
- Rindby, A., 2007. *The Itrax Core Scanner - a personal presentation*. Cox Analytical Systems, Mölndal, Sweden, p. 33.
- Roberts, H.M., 2008. The development and application of luminescence dating to loess deposits: a perspective on the past, present and future. *Boreas* 37, 483-507.
- Rochette, P., 1987. Magnetic susceptibility of the rock matrix related to magnetic fabric studies. *Journal of Structural Geology* 9, 1015-1020.
- Rohling, E.J., Hibbert, F.D., Williams, F.H., Grant, K.M., Marino, G., Foster, G.L., Hennekam, R., de Lange, G.J., Roberts, A.P., Yu, J., Webster, J.M., Yokoyama, Y., 2017. Differences between the last two glacial maxima and implications for ice-sheet, $\delta^{18}\text{O}$, and sea-level reconstructions. *Quaternary Science Reviews* 176, 1-28.
- Rolf, C., Hambach, U., Novothny, Á., Horváth, E., Schnepf, E., 2014. Dating of a Last Glacial loess sequence by relative geomagnetic palaeointensity: A case study from the Middle Danube Basin (Süttő, Hungary). *Quaternary International* 319, 99-108.
- Rollinson, H.R., 1993. *Using geochemical data: Evaluation, presentation, interpretation*. Pearson Education Asia (Pte) Ltd., Singapore, p. 352.
- Rothwell, R.G., Croudace, I.W., 2015a. Micro-XRF studies of sediment cores: A perspective on capability and application in the environmental sciences, in: Croudace, I.W.,

- Rothwell, R.G. (Eds.), *Micro-XRF studies of sediment cores*. Springer, Dordrecht, Netherlands, pp. 1-21.
- Rothwell, R.G., Croudace, I.W., 2015b. Twenty years of XRF core scanning marine sediments: what do geochemical proxies tell us?, in: Croudace, I.W., Rothwell, R.G. (Eds.), *Micro-XRF Studies of sediment cores*. Springer, Dordrecht, Netherlands, pp. 25-102.
- Rothwell, R.G., Rack, F.R., 2006. New techniques in sediment core analysis: an introduction, in: Rothwell, R.G. (Ed.), *New techniques in sediment core analysis*. Geological Society, London, Special Publications 267, pp. 1-29.
- Rousseau, D.-D., Boers, N., Sima, A., Svensson, A., Bigler, M., Lagroix, F., Taylor, S., Antoine, P., 2017a. (MIS3 & 2) millennial oscillations in Greenland dust and Eurasian aeolian records – A paleosol perspective. *Quaternary Science Reviews* 169, 99-113.
- Rousseau, D.-D., Svensson, A., Bigler, M., Sima, A., Steffensen, J.P., Boers, N., 2017b. Eurasian contribution to the last glacial dust cycle: how are loess sequences built? *Climate of the Past* 13, 1181-1197.
- Rousseau, D.D., Antoine, P., Gerasimenko, N., Sima, A., Fuchs, M., Hatté, C., Moine, O., Zoeller, L., 2011. North Atlantic abrupt climatic events of the last glacial period recorded in Ukrainian loess deposits. *Climate of the Past* 7, 221-234.
- Rousseau, D.D., Chauvel, C., Sima, A., Hatté, C., Lagroix, F., Antoine, P., Balkanski, Y., Fuchs, M., Mellett, C., Kageyama, M., Ramstein, G., Lang, A., 2014. European glacial dust deposits: Geochemical constraints on atmospheric dust cycle modeling. *Geophysical Research Letters* 41, 7666-7674.
- Ruszkiczay-Rüdiger, Z., Fodor, L., Bada, G., Leél-Össy, S., Horváth, E., Dunai, T.J., 2005. Quantification of Quaternary vertical movements in the Central Pannonian Basin: A review of chronologic data along the Danube River, Hungary. *Tectonophysics* 410, 157-172.
- Ruszkiczay-Rüdiger, Z., Kern, Z., 2016. Permafrost or seasonal frost? A review of paleoclimate proxies of the last glacial cycle in the East Central European lowlands. *Quaternary International* 415, 241-252.
- Ruxon, B.P., 1968. Measures of the degree of chemical weathering of rocks. *The Journal of Geology* 76, 518-527.
- Schatz, A.-K., Scholten, T., Kühn, P., 2015. Paleoclimate and weathering of the Tokaj (Hungary) loess-paleosol sequence. *Palaeogeography, Palaeoclimatology, Palaeoecology* 426, 170-182.
- Schatz, A.-K., Zech, M., Buggle, B., Gulyás, S., Hambach, U., Marković, S.B., Sümegi, P., Scholten, T., 2011. The late Quaternary loess record of Tokaj, Hungary: Reconstructing palaeoenvironment, vegetation and climate using stable C and N isotopes and biomarkers. *Quaternary International* 240, 52-61.
- Scheffer, F., Schachtschabel, P., 2002. *Lehrbuch der Bodenkunde*. Spektrum Akademischer Verlag GmbH, Heidelberg, Berlin, Germany, p. 593.
- Schirmer, W., 1995. Mittelrhein Basin and Lower Mittelrhein, in: Schirmer, W. (Ed.), *Quaternary field trips in Central Europe*. Pfeil, Munich, Germany, pp. 524-537.
- Schirmer, W., 2000a. Eine Klimakurve des Oberpleistozäns aus dem rheinischen Löss. *E & G - Quaternary Science Journal* 50, 25-49.
- Schirmer, W., 2000b. Rhein loess, ice cores and deep-sea cores during MIS 2-5. *Zeitschrift der Deutschen Geologischen Gesellschaft* 151, 309-332.
- Schirmer, W., 2010. Interglacial complex and solcomplex. *Central European Journal of Geosciences* 2, 32-40.

- Schirmer, W., 2012. Rhine loess at Schwalbenberg II - MIS 4 and 3. *E & G - Quaternary Science Journal* 61, 32-47.
- Schirmer, W., 2016. Late Pleistocene loess of the Lower Rhine. *Quaternary International* 411, 44-61.
- Schirmer, W., Iking, A., Nehring, F., 2012. Die terrestrischen Böden im Profil Schwalbenberg/Mittelrhein. *Mainzer Geowissenschaftliche Mitteilungen* 40, 53-78.
- Schirrmeister, L., Froese, D., Tumskoy, V., Grosse, G., Wetterich, S., 2013. Yedoma: Late Pleistocene ice-rich syngenetic permafrost of Beringia, in: Elias, S.A. (Ed.), *The Encyclopedia of Quaternary Science*, vol. 3. Elsevier Inc., Amsterdam, Netherlands, pp. 542-552.
- Schnetger, B., Brumsack, H.J., Schale, H., Hinrichs, J., Dittert, L., 2000. Geochemical characteristics of deep-sea sediments from the Arabian Sea: a high-resolution study. *Deep-Sea Research II* 47, 2735-2768.
- Scholze, F., Procop, M., 2009. Modelling the response function of energy dispersive X-ray spectrometers with silicon detectors. *X-Ray Spectrometry* 38, 312-321.
- Schoonjans, T., Vincze, L., Solé, V.A., Sanchez del Rio, M., Brondeel, P., Silversmit, G., Appel, K., Ferrero, C., 2012. A general Monte Carlo simulation of energy dispersive X-ray fluorescence spectrometers - Part 5. *Spectrochimica Acta Part B: Atomic Spectroscopy* 70, 10-23.
- Schulte, P., Lehmkuhl, F., Steininger, F., Loibl, D., Lockot, G., Protze, J., Fischer, P., Stauch, G., 2016. Influence of HCl pretreatment and organo-mineral complexes on laser diffraction measurement of loess-paleosol-sequences. *Catena* 137, 392-405.
- Sebe, K., Csillag, G., Ruzkiczay-Rüdiger, Z., Fodor, L., Thamó-Bozsó, E., Müller, P., Braucher, R., 2011. Wind erosion under cold climate: A Pleistocene periglacial megaradg system in Central Europe (Western Pannonian Basin, Hungary). *Geomorphology* 134, 470-482.
- Sebe, K., Roetzel, R., Fiebig, M., Lüthgens, C., 2015. Pleistocene wind system in Eastern Austria and its impact on landscape evolution. *Catena* 134, 59-74.
- Sheldon, N.D., 2006. Abrupt chemical weathering increase across the Permian-Triassic boundary. *Palaeogeography, Palaeoclimatology, Palaeoecology* 231, 315-321.
- Sheldon, N.D., Tabor, N.J., 2009. Quantitative paleoenvironmental and paleoclimatic reconstruction using paleosols. *Earth-Science Reviews* 95, 1-52.
- Sial, A.N., Gaucher, C., Ferreira, V.P., Pereira, N.S., Cezario, W.S., Chiglino, L., Lima, H.M., 2015. Isotope and elemental chemostratigraphy, in: Ramkumar, M. (Ed.), *Chemostratigraphy Concepts, Techniques, and Applications*. Elsevier Inc., Amsterdam, Netherlands, pp. 23-64.
- Sierralta, M., Kele, S., Melcher, F., Hambach, U., Reinders, J., van Geldern, R., Frechen, M., 2010. Uranium-series dating of travertine from Süttő: Implications for reconstruction of environmental change in Hungary. *Quaternary International* 222, 178-193.
- Sima, A., Kageyama, M., Rousseau, D.D., Ramstein, G., Balkanski, Y., Antoine, P., Hatté, C., 2013. Modeling dust emission response to North Atlantic millennial-scale climate variations from the perspective of East European MIS 3 loess deposits. *Climate of the Past* 9, 1385-1402.
- Sirocko, F., Dietrich, S., Veres, D., Grootes, P.M., Schaber-Mohr, K., Seelos, K., Nadeau, M.-J., Kromer, B., Rothacker, L., Röhner, M., Krbetschek, M., Appleby, P., Hambach, U., Rolf, C., Sudo, M., Grim, S., 2013. Multi-proxy dating of Holocene maar lakes and

- Pleistocene dry maar sediments in the Eifel, Germany. *Quaternary Science Reviews* 62, 56-76.
- Sirocko, F., Knapp, H., Dreher, F., Förster, M.W., Albert, J., Brunck, H., Veres, D., Dietrich, S., Zech, M., Hambach, U., Röhner, M., Rudert, S., Schwibus, K., Adams, C., Sigl, P., 2016. The ELSA-Vegetation-Stack: Reconstruction of Landscape Evolution Zones (LEZ) from laminated Eifel maar sediments of the last 60,000 years. *Global and Planetary Change* 142, 108-135.
- Smalley, I., Fagg, R., 2015. John Hardcastle looks at the Timaru loess: Climatic signals are observed, and fragipans. *Quaternary International* 372, 51-57.
- Smalley, I., Jary, Z., 2004. A random walk towards a definition of loess. *New Zealand Soil News* 52, 142-146.
- Smalley, I., Kels, H., 2018. Leonard Horner and an enthusiasm for Loess. *Aeolian Research* 31, 85-90.
- Smalley, I., Markovic, S.B., 2017. Controls on the nature of loess particles and the formation of loess deposits. *Quaternary International*, <https://doi.org/10.1016/j.quaint.2017.08.021>.
- Smalley, I., Markovic, S.B., 2018. Four loess pioneers: Charles Lyell, F. von Richthofen, V.A. Obruchev, L.S. Berg. *Quaternary International* 469, 4-10.
- Smalley, I., O'Hara-Dhand, K., Kwong, J., 2014. China: Materials for a loess landscape. *Catena* 117, 100-107.
- Smalley, I., O'Hara-Dhand, K., Wint, J., Machalett, B., Jary, Z., Jefferson, I., 2009. Rivers and loess: The significance of long river transportation in the complex event-sequence approach to loess deposit formation. *Quaternary International* 198, 7-18.
- Smalley, I.J., 1966. The properties of glacial loess and the formation of loess deposits. *Journal of Sedimentary Petrology* 36, 669-676.
- Smalley, I.J., Jefferson, I.F., Dijkstra, T.A., Derbyshire, E., 2001. Some major events in the development of the scientific study of loess. *Earth-Science Reviews* 54, 5-18.
- Smalley, I.J., Leach, J.A., 1978. The origin and distribution of the loess in the Danube Basin and associated regions of east-central Europe - a review. *Sedimentary Geology* 21, 1-26.
- Sorace, J.M., Zhan, M., 2003. A data review and re-assessment of ovarian cancer serum proteomic profiling. *BMC Bioinformatics* 4, 24.
- Spearman, C., 1904. The proof and measurement of association between two things. *American Journal of Psychology* 15, 72-101.
- Sprafke, T., Obreht, I., 2016. Loess: Rock, sediment or soil – What is missing for its definition? *Quaternary International* 399, 198-207.
- Sprafke, T., Thiel, C., Terhorst, B., 2014. From micromorphology to palaeoenvironment: The MIS 10 to MIS 5 record in Paudorf (Lower Austria). *Catena* 117, 60-72.
- Stevens, T., Marković, S.B., Zech, M., Hambach, U., Sümegi, P., 2011. Dust deposition and climate in the Carpathian Basin over an independently dated last glacial–interglacial cycle. *Quaternary Science Reviews* 30, 662-681.
- Stiles, C.A., Mora, C.I., Driese, S.G., 2003. Pedogenic processes and domain boundaries in a Vertisol climosequence: evidence from titanium and zirconium distribution and morphology. *Geoderma* 116, 279-299.
- Stockmann, U., Minasny, B., McBratney, A.B., 2011. Quantifying processes of pedogenesis, in: Sparks, D.L. (Ed.), *Advances in Agronomy*. Elsevier Inc., Sydney, New South Wales, Australia, pp. 1-71.

- SU, 2017. <http://www.geo.su.se/index.php/sv/resources-at-igv/analytical-resources/list-of-all-analytical-equipments/1315-itrax-xrf-core-scanner> (accessed 8 November 2017).
- Sümeği, P., Krolopp, E., 2002. Quaternary malacological analyses for modeling of the Upper Weichselian palaeoenvironmental changes in the Carpathian Basin. *Quaternary International* 91, 53-63.
- Sun, Y., Clemens, S.C., Morrill, C., Lin, X., Wang, X., An, Z., 2012. Influence of Atlantic meridional overturning circulation on the East Asian winter monsoon. *Nature Geoscience* 5, 46-49.
- Sun, Y., He, L., Liang, L., An, Z., 2011. Changing color of Chinese loess: Geochemical constraint and paleoclimatic significance. *Journal of Asian Earth Sciences* 40, 1131-1138.
- Sun, Y., Liang, L., Bloemendal, J., Li, Y., Wu, F., Yao, Z., Liu, Y., 2016. High-resolution scanning XRF investigation of Chinese loess and its implications for millennial-scale monsoon variability. *Journal of Quaternary Science* 31, 191-202.
- Svensson, A., Andersen, K.K., Bigler, M., Clausen, H.B., Dahl-Jensen, D., Davies, S.M., Johnsen, S.J., Muscheler, R., Parrenin, F., Rasmussen, S.O., Röthlisberger, R., Seierstad, I., Steffensen, J.P., Vinther, B.M., 2008. A 60000 year Greenland stratigraphic ice core chronology. *Climate of the Past* 4, 47-57.
- Svensson, A., Andersen, K.K., Bigler, M., Clausen, H.B., Dahl-Jensen, D., Davies, S.M., Johnsen, S.J., Muscheler, R., Rasmussen, S.O., Röthlisberger, R., 2006. The Greenland Ice Core Chronology 2005, 15-42 ka. Part 2: comparison to other records. *Quaternary Science Reviews* 25, 3258-3267.
- Szalai, S., Konkolyné, B.Z., Lakatos, M., Szentimrey, T., 2005. Magyarország éghajlatának néhány jellemzője 1901-től napjainkig. *Országos Meteorológiai Szolgálat, Hungary*, p. 12.
- Targulian, V.O., Krasilnikov, P.V., 2007. Soil system and pedogenic processes: Self-organization, time scales, and environmental significance. *Catena* 71, 373-381.
- Taylor, S.N., Lagroix, F., Rousseau, D.D., Antoine, P., 2014. Mineral magnetic characterization of the Upper Pleniglacial Nussloch loess sequence (Germany): an insight into local environmental processes. *Geophysical Journal International* 199, 1463-1480.
- Taylor, S.R., McLennan, S.M., 1985. *The continental crust: its composition and evolution*. Blackwell Scientific Publications Ltd., Oxford, UK, p. 312.
- Taylor, S.R., McLennan, S.M., McCulloch, M.T., 1983. Geochemistry of loess, continental crust composition and crustal model ages. *Geochimica et Cosmochimica Acta* 47, 1897-1905.
- Terhorst, B., Frechen, M., Reitner, J., 2002. Chronostratigraphische Ergebnisse aus Lössprofilen der Inn- und Traun-Hochterrassen in Oberösterreich. *Zeitschrift für Geomorphologie Supplement Band* 127, 213-232.
- Terhorst, B., Sedov, S., Sprafke, T., Peticzka, R., Meyer-Heintze, S., Kühn, P., Solleiro Rebolledo, E., 2015. Austrian MIS 3/2 loess-palaeosol records - Key sites along a west-east transect. *Palaeogeography, Palaeoclimatology, Palaeoecology* 418, 43-56.
- Thiel, C., Horváth, E., Frechen, M., 2014. Revisiting the loess/palaeosol sequence in Paks, Hungary: A post-IR IRSL based chronology for the 'Young Loess Series'. *Quaternary International* 319, 88-98.
- Thomson, J., Croudace, I.W., Rothwell, R.G., 2006. A geochemical application of the ITRAX scanner to a sediment core containing eastern Mediterranean sapropel units, in:

- Rothwell, R.G. (Ed.), *New techniques in sediment core analysis*. Geological Society, London, Special Publications 267, pp. 65-77.
- Tjallingii, R., Röhl, U., Kölling, M., Bickert, T., 2007. Influence of the water content on X-ray fluorescence core-scanning measurements in soft marine sediments. *Geochemistry, Geophysics, Geosystems* 8, Q02004.
- Török, Á., Mindszenty, A., Claes, H., Kele, S., Fodor, L., Swennen, R., 2017. Geobody architecture of continental carbonates: "Gazda" travertine quarry (Süttő, Gerecse Hills, Hungary). *Quaternary International* 437, 164-185.
- Tripathi, J.K., Rajamani, V., 1999. Geochemistry of the loessic sediments on Delhi Ridge, Eastern Thar Desert, Rajasthan: implications for exogenic processes. *Chemical Geology* 155, 265-278.
- Tsoar, H., Pye, K., 1987. Dust transport and the question of desert loess formation. *Sedimentology* 34, 139-153.
- Tzedakis, P.C., Hooghiemstra, H., Pälike, H., 2006. The last 1.35 million years at Tenaghi Philippon: revised chronostratigraphy and long-term vegetation trends. *Quaternary Science Reviews* 25, 3416-3430.
- Újvári, G., Kok, J.F., Varga, G., Kovács, J., 2016. The physics of wind-blown loess: Implications for grain size proxy interpretations in Quaternary paleoclimate studies. *Earth-Science Reviews* 154, 247-278.
- Újvári, G., Varga, A., Balogh-Brunstad, Z., 2008. Origin, weathering, and geochemical composition of loess in Southwestern Hungary. *Quaternary Research* 69, 421-437.
- Újvári, G., Varga, A., Raucsik, B., Kovács, J., 2014. The Paks loess-paleosol sequence: A record of chemical weathering and provenance for the last 800 ka in the mid-Carpathian Basin. *Quaternary International* 319, 22-37.
- USGS, 2003. Shuttle Radar Topography Mission. <https://pubs.usgs.gov/fs/2003/0071/report.pdf> (accessed 21 September 2017).
- van den Boogaart, K.G., Tolosana-Delgado, R., 2008. "compositions": A unified R package to analyze compositional data. *Computers & Geosciences* 34, 320-338.
- Van Espen, P., 2002. Spectrum Evaluation, in: Van Grieken, R.E., Markowicz, A.A. (Eds.), *Handbook of X-ray spectrometry*. Marcel Dekker Inc., New York, USA, pp. 239-340.
- Vandenberghe, J., 2013. Grain size of fine-grained windblown sediment: A powerful proxy for process identification. *Earth-Science Reviews* 121, 18-30.
- Vandenberghe, J.F., Múcher, H.J., Roebroeks, W., Gemke, D., 1985. Lithostratigraphy and palaeoenvironment of the Pleistocene deposits at Maastricht-Belvédère, southern Limburg. *Mededelingen Rijks geologische Dienst* 39, 7-29.
- Varga, A., Újvári, G., Raucsik, B., 2011. Tectonic versus climatic control on the evolution of a loess–paleosol sequence at Beremend, Hungary: an integrated approach based on paleoecological, clay mineralogical, and geochemical data. *Quaternary International* 240, 71-86.
- Varga, G., 2011. Similarities among the Plio–Pleistocene terrestrial aeolian dust deposits in the World and in Hungary. *Quaternary International* 234, 98-108.
- Varga, G., Cserhádi, C., Kovács, J., Szalai, Z., 2016. Saharan dust deposition in the Carpathian Basin and its possible effects on interglacial soil formation. *Aeolian Research* 22, 1-12.
- Vinther, B.M., Clausen, H.B., Johnsen, S.J., Rasmussen, S.O., Andersen, K.K., Buchardt, S.L., Dahl-Jensen, D., Seierstad, I.K., Siggaard-Andersen, M.L., Steffensen, J.P., Svensson, A., Olsen, J., Heinemeier, J., 2006. A synchronized dating of three

- Greenland ice cores throughout the Holocene. *Journal of Geophysical Research* 111, D13102.
- Von Eynatten, H., Barceló-Vidal, C., Pawlowsky-Glahn, V., 2003. Composition and discrimination of sandstones: a statistical evaluation of different analytical methods. *Journal of Sedimentary Research* 73, 47-57.
- Wacha, L., Galović, L., Koloszár, L., Magyar, Á., Chikán, G., Marsi, I., 2013. The chronology of the Šarengrad II loess-palaeosol section (Eastern Croatia). *Geologia Croatica* 66, 191-203.
- Wacha, L., Mikulčić Pavlaković, S., Frechen, M., Crnjaković, M., 2011a. The Loess Chronology of the Island of Susak, Croatia. *E & G - Quaternary Science Journal* 60, 153-169.
- Wacha, L., Mikulčić Pavlaković, S., Novothny, Á., Crnjaković, M., Frechen, M., 2011b. Luminescence dating of Upper Pleistocene loess from the Island of Susak in Croatia. *Quaternary International* 234, 50-61.
- Wacha, L., Rolf, C., Hambach, U., Frechen, M., Galović, L., Duchoslav, M., 2017. The Last Glacial aeolian record of the Island of Susak (Croatia) as seen from a high-resolution grain-size, rock and palaeo-magnetic analysis. *Quaternary International*, <https://doi.org/10.1016/j.quaint.2017.08.016>.
- Wang, N., Jiang, D., Lang, X., 2018. Northern westerlies during the Last Glacial Maximum: Results from CMIP5 simulations. *Journal of Climate* 31, 1135-1153.
- Ward, J.H., 1963. Hierarchical grouping to optimize an objective function. *Journal of the American Statistical Association* 58, 236-244.
- Weltje, G.J., Bloemsmá, M.R., Tjallingii, R., Heslop, D., Röhl, U., Croudace, I.W., 2015. Prediction of geochemical composition from XRF core scanner data: A new multivariate approach including automatic selection of calibration samples and quantification of uncertainties, in: Croudace, I.W., Rothwell, R.G. (Eds.), *Micro-XRF studies of sediment cores*. Springer, Dordrecht, Netherlands, pp. 507-534.
- Weltje, G.J., Tjallingii, R., 2008. Calibration of XRF core scanners for quantitative geochemical logging of sediment cores: Theory and application. *Earth and Planetary Science Letters* 274, 423-438.
- WISE, 2012. WISE Large rivers and large lakes. <https://www.eea.europa.eu/data-and-maps/data/wise-large-rivers-and-large-lakes> (accessed 5 October 2017).
- WRB, I.W.G., 2015. World reference base for soil resources 2014, update 2015, International soil classification system for naming soils and creating legends for soil maps, *World Soil Resources Reports No. 106*. FAO, Rome, Italy, p. 192.
- Wright, J., 2001a. "Desert" loess versus "glacial" loess: quartz silt formation, source areas and sediment pathways in the formation of loess deposits. *Geomorphology* 36, 231-256.
- Wright, J., 2001b. Making loess-sized quartz silt: data from laboratory simulations and implications for sediment transport pathways and the formation of 'desert' loess deposits associated with the Sahara. *Quaternary International* 76/77, 7-19.
- Wright, J., Smith, B., 1993. Fluvial comminution and the production of loess-sized quartz silt. *Geografiska Annaler: Series A, Physical Geography* 75, 25-34.
- Wright, J., Smith, B., Whalley, B., 1998. Mechanisms of loess-sized quartz silt production and their relative effectiveness: laboratory simulations. *Geomorphology* 23, 15-34.
- Yamada, Y., 1968. Occurrence of bromine in plants and soil. *Talanta* 15, 1135-1141.

- Yang, S., Ding, F., Ding, Z., 2006. Pleistocene chemical weathering history of Asian arid and semi-arid regions recorded in loess deposits of China and Tajikistan. *Geochimica et Cosmochimica Acta* 70, 1695-1709.
- Yu, K., Hartmann, K., Nottebaum, V., Stauch, G., Lu, H., Zeeden, C., Yi, S., Wünnemann, B., Lehmkuhl, F., 2016. Discriminating sediment archives and sedimentary processes in the arid endorheic Ejina Basin, NW China using a robust geochemical approach. *Journal of Asian Earth Sciences* 119, 128-144.
- Yuita, K., 1983. Iodine, bromine and chlorine contents in soils and plants of Japan. *Soil Science and Plant Nutrition* 29, 403-428.
- Yuita, K., Tanaka, T., Abe, C., Aso, S., 1991. Dynamics of iodine, bromine, and chlorine in soil I. Effect of moisture, temperature, and pH on the dissolution of the triad from soil. *Soil Science and Plant Nutrition* 37, 61-73.
- Zander, A., 2000. Vergleich verschiedener Lumineszenzmethoden zur Datierung von Löss, Institute of Geology. PhD thesis, University of Cologne, Cologne, Germany, p. 92.
- Zander, A., Duller, G.A.T., Wintle, A.G., 2000. Multiple and single aliquot luminescence dating techniques applied to quartz extracted from Middle and Upper Weichselian loess, Zemechy, Czech Republic. *Journal of Quaternary Science* 15, 51-60.
- Zecchin, M., Donda, F., Forlin, E., 2017. Genesis of the Northern Adriatic Sea (Northern Italy) since early Pliocene. *Marine and Petroleum Geology* 79, 108-130.
- Zech, M., Krause, T., Meszner, S., Faust, D., 2013a. Incorrect when uncorrected: Reconstructing vegetation history using n-alkane biomarkers in loess-paleosol sequences – A case study from the Saxonian loess region, Germany. *Quaternary International* 296, 108-116.
- Zech, M., Zech, R., Zech, W., Glaser, B., Brodowski, S., Amelung, W., 2008. Characterisation and palaeoclimate of a loess-like permafrost palaeosol sequence in NE Siberia. *Geoderma* 143, 281-295.
- Zech, R., Zech, M., Marković, S., Hambach, U., Huang, Y., 2013b. Humid glacials, arid interglacials? Critical thoughts on pedogenesis and paleoclimate based on multi-proxy analyses of the loess-paleosol sequence Crvenka, Northern Serbia. *Palaeogeography, Palaeoclimatology, Palaeoecology* 387, 165-175.
- Zeeden, C., Hambach, U., Veres, D., Fitzsimmons, K., Obrecht, I., Böskén, J., Lehmkuhl, F., 2017. Millennial scale climate oscillations recorded in the Lower Danube loess over the last glacial period. *Palaeogeography, Palaeoclimatology, Palaeoecology*, <https://doi.org/10.1016/j.palaeo.2016.12.029>.
- Zeeden, C., Kels, H., Hambach, U., Schulte, P., Protze, J., Eckmeier, E., Marković, S.B., Klasen, N., Lehmkuhl, F., 2016. Three climatic cycles recorded in a loess-palaeosol sequence at Semlac (Romania) – Implications for dust accumulation in South-Eastern Europe. *Quaternary Science Reviews* 154, 130-142.
- Zerboni, A., Trombino, L., Frigerio, C., Livio, F., Berlusconi, A., Michetti, A.M., Rodnight, H., Spötl, C., 2014. The loess-paleosol sequence at Monte Netto: a record of climate change in the Upper Pleistocene of the central Po Plain, northern Italy. *Journal of Soils and Sediments* 15, 1329-1350.
- Zhang, J., Rolf, C., Wacha, L., Tsukamoto, S., Durn, G., Frechen, M., under review. Luminescence dating and paleomagnetic age constraints of a last glacial loess-paleosol sequence from Istria, Croatia. *Quaternary International*.
- Zhang, M., Karathanasis, A.D., 1997. Characterization of Iron-Manganese concretions in Kentucky alfisols with perched water tables. *Clays and Clay Minerals* 45, 428-439.

- Zhang, Z., Zhao, M., Eglinton, G., Lu, H., Huang, C., 2006. Leaf wax lipids as paleovegetational and paleoenvironmental proxies for the Chinese Loess Plateau over the last 170 kyr. *Quaternary Science Reviews* 25, 575-594.
- Ziegler, M., Jilbert, T., de Lange, G.J., Lourens, L.J., Reichert, G.-J., 2008. Bromine counts from XRF scanning as an estimate of the marine organic carbon content of sediment cores. *Geochemistry, Geophysics, Geosystems* 9, Q05009.
- Zolitschka, B., Rolf, C., Bittmann, F., Binot, F., Frechen, M., Wonik, T., Froitzheim, N., Ohlendorf, C., 2014. Pleistocene climatic and environmental variations inferred from a terrestrial sediment record – the Rodderberg Volcanic Complex near Bonn, Germany. *Zeitschrift der Deutschen Gesellschaft für Geowissenschaften* 165, 407-424.
- Zöller, L., 2010. New approaches to European loess: a stratigraphic and methodical review of the past decade. *Central European Journal of Geosciences* 2, 19-31.
- Zöller, L., Semmel, A., 2001. 175 years of loess research in Germany - long records and "unconformities". *Earth-Science Reviews* 54, 19-28.
- Zou, K.H., Tuncalli, K., Silverman, S.G., 2003. Correlation and simple linear regression. *Radiology* 227, 617-622.

Acknowledgements

First of all, I would like to thank my supervisor Prof. Dr. Bernd Zolitschka for giving me the opportunity to work on this PhD thesis, for his encouragement and the confidence in my research in combination with the freedom to visit two summer schools and numerous conferences. Special thanks go to Prof. Dr. Markus Fuchs for being the second referee and for his interest in my work.

Furthermore, Christian Ohlendorf, I really appreciate our countless discussions and your scientific advice while having a coffee after lunch. Additionally, I am much obliged to the other members and student helpers of the GEOPOLAR working group at the University of Bremen for continuous support (Lena Neumann, Kim Peis, Britta Schülzke, Carsten Smidt, Sabine Stahl, Katrin Wagner). The same is true for the members of the new working group “Climate Lab” at the University of Bremen contributing to a comfortable working atmosphere and living next door to us.

Thank you Lara Wacha and Mihovil Brlek for the unforgettable field trip to Susak in spring 2015! Moreover, I am much obliged to my co-authors for the collaborative and positive cooperation (Gabriella Barta, Manfred Frechen, Ágnes Novothny, Christian Rolf, Wolfgang Schirmer, Lara Wacha).

During my visits to conferences and workshops, I met many people and I really like to thank some of them for in-depth discussions of my work (Tobias Fischer, Jyh-Jaan Huang, Kim Jakob, Andrea Junge, Sascha Meszner, Simon Meyer-Heintze, Manuel Pappusch, Denis-Didier Rousseau, Christoph Schmidt, Tobias Sprafke, Raphael Steup, Rik Tjallingii, Christian Zeeden). One of my best experiences in my scientific life was the opportunity to attend the “Urbino Summer School of Paleoclimatology” in 2016 – many thanks to all participants and lecturers. Finally, I would like to thank Bernhard Höfle for mental support during dark times working on my PhD.

On the private side of life, I am indebted to my friends and parents. Without them (Christoph, Durk, Fabi, Ines, Kerstin, Martin, Sabine, Theresa and Vicky), I would have probably never finished this thesis. For example, I keep the weekends playing Skat and Straßenboßeln in good memory; thank you Durk. Finally, special thanks go to my parents who are the backbone of support in any situation.

Erklärung

Hiermit erkläre ich, dass ich diese Arbeit selbständig ohne unerlaubte Hilfe verfasst und keine anderen als die angegebenen Quellen und Hilfsmittel verwendet habe. Ich habe wörtlich oder inhaltlich entnommene Stellen aus anderen Werken als solche kenntlich gemacht. Ich erkläre ferner, dass ich an keiner anderen Universität ein Promotionsverfahren begonnen habe.

Diese Dissertation ist eine kumulative Dissertation. Meine Anteile an den wissenschaftlichen Publikationen sind im jeweiligen Kapitel gekennzeichnet.

Bremen, Dezember 2017